1981

Applications of vibrating wire electrodes to electroanalysis

Kenneth W. Pratt Jr.
Iowa State University

PRATT, Jr., Kenneth W.

APPLICATIONS OF VIBRATING WIRE ELECTRODES TO ELECTROANALYSIS.

Iowa State University Ph.D. 1981

Applications of vibrating wire electrodes to electroanalysis

by

Kenneth W. Pratt, Jr.

A Dissertation Submitted to the
Graduate Faculty in Partial Fulfillment of the
Requirements for the Degree of
DOCTOR OF PHILOSOPHY

Department: Chemistry
Major: Analytical Chemistry

Approved:

Signature was redacted for privacy.

In Charge of Major Work

Signature was redacted for privacy.

For the Major Department

Signature was redacted for privacy.

For the Graduate College

Iowa State University
Ames, Iowa

1981

TABLE OF CONTENTS

LIST OF FIGURES

LIST OF TABLES

LIST OF ACRONYMS

AAS	Atomic absorption spectroscopy
AC	Alternating current
AM	Amplitude modulation
ASV	Anodic stripping voltammetry
CE	Counter electrode
CMRR	Common-mode rejection ratio
CSTER	Continuously stirred tank electrochemical reactor
DC	Direct current
DPASV	Differential pulse anodic stripping voltammetry
DPDT	Double-pole, double-throw
DTA	Diethylenetriamine
DVM	Digital voltmeter
FET	Field-effect transistor
FIA	Flow-injection analysis
FM	Frequency modulation
HMVE(AM)	Hydrodynamic modulation at the vibrating electrode by modulation of the vibrational amplitude
HMVE(FM)	Hydrodynamic modulation at the vibrating electrode by modulation of the vibrational frequency
LED	Light emitting diode
LIA	Lock-in amplifier
LP	Low-pass
LSW	Lake Superior water
PAR	Princeton Applied Research
PLL	Phase-locked loop

PM	Permanent magnet
RC	Resistance-capacitance
RDE	Rotating disc electrode
RMS	Root-mean-square
RPM	Revolutions per minute
SCE	Saturated calomel electrode
SPDT	Single-pole, double-throw
SPST	Single-pole, single-throw
TDW	Triply distilled water
USA	United States of America
USSR	Union of Soviet Socialist Republics
VCO	Voltage-controlled oscillator
VR	Voltage regulator
WE	Working electrode

LIST OF SYMBOLS

A	Surface area (centimeters^2)
a	Peak vibrational amplitude (centimeters)
a_{obs}	Observed vibrational amplitude, peak-to-peak (centimeters)
a_{pp}	Peak-to-peak vibrational amplitude (centimeters)
a_w	Proportionality constant related to vibrational amplitude (centimeters^2)
B	Breadth of plate (centimeters)
$C(t)$	Instantaneous concentration of analyte (moles liter^{-1})
$C(\tau)$	Instantaneous concentration of analyte at time τ (moles liter^{-1})
C^b	Bulk concentration (moles liter^{-1})
C_c	Capacitor in carrier oscillator of AM/FM generator (farads)
C_f	Capacitor in integrator (farads)
C_{init}	Initial concentration of analyte in bulk electrolysis (moles liter^{-1})
C_{new}	Values of capacitors in LIA for operation at $f_o = f_{new}$ (farads)
C_o	Concentration of analyte in sample plug (moles liter^{-1})
C_{osc}	Capacitor in 10-Hz oscillator (farads)
C^s	Surface concentration (moles liter^{-1})
C_{ss}	Steady-state concentration in FIA (moles liter^{-1})
dC	Incremental concentration in FIA (moles liter^{-1})
$(dC/dx)_{x=0}$	Concentration gradient at surface of electrode (moles liter^{-1} centimeter^{-1})
D	Diffusion coefficient (centimeters^{2}second^{-1})
d_e	Diameter of electrode (centimeters)

E_{dis}	Initial potential of Au electrode in rest potential studies (volts vs. SCE)
E_{in}	Input voltage to loudspeaker (volts RMS)
E_{lim}	Limit voltage of triangular waveform generator (volts)
E_{peak}	Peak potential of triangular waveform applied to Schmitt trigger (volts)
E_{ref}	Amplitude of square-wave reference waveform in LIA (volts)
E_s	Peak amplitude of input signal to phase-selective detector in LIA (volts)
E_{sat}	Saturation potential of operational amplifier (volts)
E_{sw}	Switching threshold of Schmitt trigger (volts)
E_{WE}	Potential of working electrode (volts vs. SCE)
$e(t)$	Triangular waveform applied to Schmitt trigger (volts)
$e_I(\theta)$	DC output of LIA for in-phase measurement of $e_s(t)$ (volts)
e_{in}	Input voltage (volts)
e_o	Output voltage (volts)
$e_o(\phi)$	DC output of LIA as a function of phase difference between signal and reference waveforms (volts)
$e_{o,max}$	DC output of LIA with signal and reference waveforms in phase (volts)
$e_Q(\theta)$	DC output of LIA for quadrature measurement of $e_s(t)$ (volts)
$e_s(t)$	Signal waveform applied to input of phase-selective detector in LIA (volts)
F	Faraday constant (96487 coulombs equivalent^{-1})
f	Frequency (Hertz)
f_c	Carrier frequency of AM or FM signal (Hertz)
f_{new}	Frequency of operation of modified LIA (Hertz)
f_o	Resonant frequency (Hertz)
G	Internal voltage gain of LIA (dimensionless)

$[Hg(II)]$	Concentration of Hg(II) (moles liter^{-1})
I	Current (amperes)
I_{coul}	Coulometric current in FIA (amperes)
I_l	Limiting current (amperes)
$I_l(t)$	Instantaneous limiting current in FIA (amperes)
$I_l(\tau)$	Instantaneous limiting current in FIA at time τ (amperes)
$I_{l,ss}$	Steady-state limiting current (amperes)
I_{peak}	Peak current in FIA (amperes)
I_r	Relative, time-dependent limiting current in FIA (amperes)
ΔI	10-Hz component of I in HMVE(AM) and HMVE(FM) (amperes, peak-to-peak)
ΔI_{dp}	Differential current in DPASV (amperes)
ΔI_l	10-Hz component of I_l in HMVE(AM) and HMVE(FM) (amperes, peak-to-peak)
$\Delta I_l(t)$	Instantaneous 10-Hz component of $I_l(t)$ in HMVE(AM) (amperes, peak-to-peak)
ΔI_l^{2f}	AC component of I_l at a frequency of 2f (amperes RMS)
$\Delta I_{l,pp}^{2f}$	Peak-to-peak value of ΔI_l^{2f} (amperes, peak-to-peak)
ΔI_{peak}	10-Hz component of I_{peak} for HMVE(AM) in FIA (amperes, peak-to-peak)
ΔI_{strip}	Peak differential stripping current in DPASV (amperes)
pI_{peak}	$-\log I_{peak}$
$[I^-]$	Concentration of I^- (moles liter^{-1})
pI^-	$-\log [I^-]$
J_D'	Dimensionless mass transfer coefficient (dimensionless)
k, k', k''	Proportionality constants
k_m	Mass transfer coefficient (centimeters second^{-1})
L	Length (centimeters)

L_{F-S}	Length of electrode from fulcrum to seal (centimeters)
L_{F-T}	Length of electrode from fulcrum to tip (centimeters)
L_{S-T}	Length of electrode from seal to tip (centimeters)
Nu	Nusselt number (dimensionless)
dN_{cell}	Incremental quantity of analyte accumulating in flow-through cell (moles)
dN_{elec}	Incremental quantity of analyte reacting at electrode (moles)
dN_{in}	Incremental quantity of analyte entering flow-through cell (moles)
dN_{out}	Incremental quantity of analyte leaving flow-through cell (moles)
$(dN/dt)_{elec}$	Flux of electroactive species to electrode (moles second^{-1})
n	Number of electrons in reaction (equivalents mole^{-1})
P	Current sensitivity of potentiostat (amperes volt^{-1})
p	Constant in general differential equation
Q	Quality factor of bandpass amplifier (dimensionless)
Q_{ox}	Quantity of charge required for oxidation of Au surface (coulombs centimeter^{2})
q	Constant in general differential equation
R_c	Resistor in carrier oscillator of AM/FM generator (ohms)
R_{ext}	Resistor connected to summing junction of control amplifier in potentiostat for external input (ohms)
R_{in}	Input resistor of integrator (ohms)
R_{osc}	Resistor in 10-Hz Wien-bridge oscillator (ohms)
Re	Reynolds number (dimensionless)
Re_v	Vibrational Reynolds number (dimensionless)
r	Radius of polar plot (centimeters)
S	Sensitivity of potentiostat-LIA combination (amperes volt^{-1})

Sc	Schmidt number (dimensionless)
Sh_v	Vibrational Sherwood number (dimensionless)
T	Setting of AC Gain control on LIA (turns)
T_p	Thickness of plate (centimeters)
t	Time (seconds)
t_{dep}	Deposition time in DPASV (seconds)
dt	Increment of time (seconds)
u^*	Friction velocity (centimeters second^{-1})
V_{cell}	Volume of flow-through cell (milliliters)
V_s	Volume of sample plug in FIA (milliliters)
dV	Incremental volume (milliliters)
$v(t)$	Instantaneous velocity (centimeters second^{-1})
v_{avg}	Average velocity (centimeters second^{-1})
v_f	Volume flow rate (milliliters second^{-1})
$x(t)$	Position of vibrating electrode as a function of time (centimeters)
$y(t)$	Time-dependent function in general differential equation
z	Exponential dependence of heat- or mass-transport parameters on vibrational parameters (dimensionless)
δ	Thickness of diffusion layer (centimeters)
ϵ	Fractional conversion (dimensionless)
θ	Phase lag of signal waveform relative to reference waveform (degrees)
θ_e	Angular swing of electrode (radians)
θ_ℓ	Angular variable in polar plot (degrees)
θ_{tot}	Total phase lag of signal waveform during quadrature measurements of $e_s(t)$ (degrees)
ν	Kinematic viscosity (centimeters^{2}second^{-1})

ρ	Density (grams centimeter^3)
τ	Length of sample plug in time units (seconds)
ϕ	Phase lead of signal waveform in LIA (degrees)
ϕ_{disp}	Setting of Phase control on LIA (degrees)
ψ	Flow function (dimensionless)
ω	Angular frequency (radians second^{-1})
ω_{app}	Apparent "rotation speed" of vibrating electrode (radians second^{-1})
ω_r	Rotation speed of RDE (radians second^{-1})

I. INTRODUCTION

Recent technological, environmental, and legal developments have created a need for analytical determinations at concentrations far below those previously encountered. This requirement for methods having increased sensitivity has been a major driving force in the development of instrumental analytical methodology. Such research has also been aided immeasurably by the concurrent development of improved electronic devices and techniques of signal processing.

Electroanalytical techniques possess distinct advantages for many trace-level analytical determinations. Among the most useful electroanalytical methods is voltammetry. In voltammetry, a working or indicating electrode is maintained at a potential by means of a potentiostat. The potentiostat also monitors the current passing through the working electrode, which is directly related to the concentration of electroactive species being oxidized or reduced at the electrode.

The relationship between the current at the working electrode and the concentration of electroactive species, or analyte, in the bulk solution may be derived from fundamental electrochemical considerations. The relationship of electrode current to the flux of electroactive species at the electrode is given by Equation I-1.

$$I = nF(dN/dt)_{elec} \qquad (I\text{-}1)$$

The flux, $(dN/dt)_{elec}$, results from the processes of migration, convection, and diffusion. Solutions used in voltammetry generally contain, in addition to the analyte, a large excess of an inert or supporting

electrolyte, which serves to reduce migrational flux to a negligible value. Mass transport in voltammetry is thus restricted to the processes of convection and diffusion.

Convection, which results from physical displacement of solution, is far more efficient than diffusion as a means of mass transport. Diffusion is the predominant mode of flux in voltammetry only in the thin layer of solution which adheres to the surface of the electrode and remains stationary, relative to the position of the electrode. Since diffusion is the only mode of mass transport in this layer, the flux of electroactive species to the surface of the electrode may be described by Fick's Law, the basic relationship describing diffusional processes, which is given in Equation I-2. The flux, $(dN/dt)_{elec}$, is expressed in mmoles sec^{-1} for $(dC/dx)_{x=0}$ in M cm^{-1}.

$$(dN/dt)_{elec} = AD(dC/dx)_{x=0} \qquad \text{(I-2)}$$

According to the model developed by Nernst (1), the concentration gradient at the surface of the electrode, $(dC/dx)_{x=0}$, may be approximated by a linear function over the region from x = 0, the surface of the electrode, to x = δ, the point at which convection becomes the dominant mode of mass transport. This mathematical approximation for the concentration gradient is given in Equation I-3. The variable δ represents the thickness of the diffusion layer.

$$(dC/dx)_{x=0} = (C^b - C^s)/\delta \qquad \text{(I-3)}$$

Equations I-1, I-2, and I-3 may be combined to give the basic equation for voltammetry, shown in Equation I-4. In Equation I-4 and succeeding

equations, the current, I, is expressed in mA for concentrations, C^b and C^s, expressed in M.

$$I = nFAD(C^b - C^s)/\delta \qquad \text{(I-4)}$$

In cases where the electrode is operated at a potential such that the concentration of the substance being oxidized or reduced becomes essentially zero at the surface of the electrode, the electrode current assumes a maximum value. The current in this case is referred to as the limiting current, I_l, and is given in Equation I-5.

$$I_l = nFADC^b/\delta \qquad \text{(I-5)}$$

Wherever possible, analytical determinations using voltammetry are performed under conditions described by Equation I-5. It will be noted that I_l is proportional to C^b, the concentration of the analyte in the bulk solution. This proportionality forms the basis for all analytical applications of voltammetry. Equation I-5 is frequently given in an alternate, simplified form, shown in Equation I-6.

$$I_l = nFAk_mC^b \qquad \text{(I-6)}$$

The variable k_m in Equation I-6 is referred to as the "mass transfer coefficient" and is frequently encountered in the literature; k_m is equal to the quantity D/δ in Equation I-5.

It must be emphasized that Equations I-2 through I-6 apply only to electrochemical reactions whose rate of electron transfer is fast compared to the rate of mass transport to the surface of the electrode. Such reactions are referred to as being reversible. Except as noted,

the electrochemical reactions described in this dissertation are reversible.

Consideration of Equation I-5 suggests possible techniques which may be used to effect an increase in the sensitivity of voltammetric determinations. To obtain the greatest sensitivity, the analytical variable, I_l, must be maximized for a given concentration of analyte, C^b, contained in the sample. Elementary algebra shows that the limiting current will increase for an increase in the values of n, F, A, or D, or for a decrease in the value of δ. Faraday's constant, F, is a fundamental physical constant and cannot be varied. The number of electrons involved in the reaction, n, and the diffusion constant of the electroactive species, D, are determined by the analyte and are therefore also fixed. Thus, the only factors which may be varied in order to effect an increase in I_l are A and δ.

Increasing the area of the working electrode will result in an increase in the limiting current observed for a given concentration of analyte. However, unwanted background currents also increase in direct proportion to the area of the electrode. Such background currents result from breakdown of the supporting electrolyte and from surface reactions of the electrode material itself. The detection limit in voltammetric analysis ultimately depends upon the signal-to-noise ratio of the analytical variable, I_l, to these background currents. Since both the numerator and denominator of the signal-to-noise ratio are directly proportional to the surface area of the electrode, a change in this area will not effect an increase in the sensitivity of voltammetric analyses.

From the preceding argument, it is evident that reduction of the thickness of the diffusion layer is the only method which may be used to obtain lower detection limits in voltammetry. The value of δ is inversely related to any motion of the electrolyte with respect to the electrode, and any method of achieving such motion will result in a decrease in δ and a consequent increase in voltammetric sensitivity.

Motion of the electrolyte past a stationary electrode has been used to effect a reduction in the value of δ. The most obvious method of achieving this motion is to stir the electrolyte, into which the stationary electrode is immersed. Experimentation shows that reproducible hydrodynamic conditions are not readily obtained with such stirring, and the limiting currents observed are therefore unstable. Stirring has found considerable application in anodic stripping voltammetry, however, in which short-term variations in the limiting current for deposition may be averaged out over the comparatively long period of deposition.

A second method of moving the electrolyte past the electrode surface is to place the electrode in a flowing stream. The most familiar application of this principle is the tubular electrode, introduced by Blaedel, et al. (2). The hydrodynamic conditions prevailing in the tubular electrode are those of laminar flow and may be evaluated mathematically, resulting in an explicit expression for δ as a function of the experimental parameters. Blaedel, et al. substituted this expression into the basic voltammetric equation and obtained the equation relating the limiting current observed at a tubular electrode to the length of the electrode and the volume flow rate.

$$I_l = 5.24 \times 10^5 \, nD^{2/3} L^{2/3} v_f^{1/3} C^b \qquad \text{(I-7)}$$

The principle of placing the electrode in a flowing stream also forms the basis for flow-injection analysis, which will be discussed later in this work.

Motion of the electrode through a stationary electrolyte also has been used to increase the sensitivity of voltammetric determinations. The rotating disc electrode (RDE), the most frequently used solid voltammetric electrode, makes use of this principle. The RDE is a circular disc which rotates about an axis passing through its center and perpendicular to its surface. The hydrodynamic equations pertaining to laminar flow in this system were first evaluated by Levich (3). He also derived the basic voltammetric equation for the RDE, shown in Equation I-8.

$$I_l = 0.62nFAD^{2/3} \nu^{-1/6} \omega_r^{1/2} C^b \qquad \text{(I-8)}$$

Relative motion of an electrode through an electrolyte may also be effected by vibration of the electrode. Although vibrating electrodes have found comparatively few applications in voltammetry, they offer certain advantages which have not been fully exploited in electroanalytical chemistry. This dissertation explores new applications of vibrating wire microelectrodes to voltammetric analysis and uses the basic advantages of vibrating electrodes to extend the usable range of electroanalytical determinations to the lowest levels yet achieved. The hydrodynamic behavior of vibrating wire electrodes is also studied in greater detail than heretofore possible. The design and operation of

original electronic circuitry and instrumentation which has made these investigations possible is explained. Equations describing the behavior of vibrating electrodes in flow-injection analysis are derived and experimentally verified, and their applicability to similar systems using rotating disc electrodes is evaluated.

II. LITERATURE REVIEW

A. Introduction

The literature pertaining to electrochemical applications and fundamental studies of solid vibrating electrodes is reviewed here. This review covers all articles on this topic which have appeared in the literature from 1948 through 1979. It is noteworthy that almost all work with vibrating electrodes has been performed outside the USA; of 81 references reviewed here, only 6 are from the USA.

The paucity of electrochemical work performed with vibrating electrodes in the USA is most likely a result of 2 factors. First, the technique is somewhat empirical and is not amenable to mathematical treatment. Second, the method is extremely inexpensive. Both these factors combine to make work with vibrating electrodes unattractive to many American researchers.

Delahay (4) in 1954 briefly discussed vibrating electrodes in his well-known text on electrochemistry. This reference provided the stimulus for the present work. The only true review article which has appeared to date on the topic of vibrating electrodes is that of Facsko (5), which is in German. Facsko's article is a thorough review of all work which had appeared in the literature up to 1961. The present work is the only review of vibrating electrodes to appear since that time and is the first review of this topic to appear in the English language.

B. Analytical Applications

Vibrating electrodes were first used in voltammetry by Harris and Lindsey (6) in 1948. They obtained reproducible polarograms using a Pt microelectrode vibrated at 100 Hz and at "an amplitude considerably greater than its linear dimensions." This article is the first reference to vibrating electrodes in electrochemistry. Roberts and Meek (7) used a dual Pt electrode, vibrated by a speaker, for the polarographic analysis of alkyl peroxides. The dual electrode was used to minimize the effects of fouling. Linear calibration curves were obtained over ranges of 2×10^{-4} M to 2×10^{-3} M for the reduction of Cd^{2+} and 1×10^{-4} M to 1×10^{-3} M for the reduction of ethyl peroxide.

Dirscherl and Otto (8, 9) used a vibrating Pt electrode for the reduction of O_2 and the oxidation of I^- over a range of 1×10^{-4} M to 1×10^{-3} M. The authors found that the limiting current for both reactions decreased for repeated voltammograms of the same solution. Concurrently with the decrease in the anodic current for the oxidation of I^-, the authors noted a corresponding increase in the cathodic current observed at potentials more negative than the I^-/I_2 wave. This cathodic current was attributed to the reduction of I_2 formed from the oxidation of I^- at the electrode during previous polarograms. The consumption of electroactive species by the vibrating Pt electrode was found to be 10 to 20 times more rapid than at a dropping mercury electrode, and the limiting currents observed both for the oxidation of I^- and the reduction of O_2 were found to decay according to a first-order exponential relationship.

Oehme and Noack (10) studied the application of vibrating electrodes to the reduction of Cd^{2+} and Tl^{+} on amalgamated Ag and to the oxidation of ascorbic acid on Pt. Irreproducible results encountered in the analyses of solutions of Cd^{2+} and Tl^{+} at higher concentrations were attributed to the accumulation of electrodeposited Cd and Tl; these difficulties were not found for the reduction of oxygen and aromatic nitro compounds, whose reaction products did not deposit on the electrode. Vlček (11) applied vibrating electrodes to polarographic studies of $Co_2(CO)_8$. Leont'ev and Fedotov (12) used vibrating Pt electrodes for polarographic analyses of solutions containing Fe^{3+} and H_2O_2. In both cases, the limiting currents observed at the vibrating electrode were 3 to 3.5 times larger than those observed at a stationary electrode. Kalvoda (13) analyzed solutions containing micromolar quantities of Au(III), Ag(I), and Hg(I) using oscillographic polarography with a vibrating Pt electrode.

Facsko and Poraicu (14) found that the limiting currents for the oxidation of $Fe(CN)_6^{4-}$ at vibrating Pt and Ni electrodes were proportional to concentration. The limiting current increased tenfold when the electrode was vibrated. The same authors found similar results for the reduction of Ce(IV) at Pb and Pt electrodes and for the oxidation of Tl(I) at Pt electrodes (15). Pint and Flengas (16) obtained polarograms for the reduction of Cu^{2+}, Pb^{2+}, and Cd^{2+} in aqueous solution at W electrodes and for the reduction of Ag^{+} at Pt electrodes in a KNO_3-$NaNO_3$ melt. Linear calibration curves were given for Pb^{2+} at 2×10^{-3} M to 1×10^{-2} M and for Ag^{+} at 5×10^{-3} to 5×10^{-2} mole percent. Magjer and Branica (17) employed a stationary glassy-carbon electrode situated

next to a vibrating, conically perforated disc for the determination of Zn, Cd, Pb, and Cu in seawater using differential pulse anodic stripping voltammetry. The detection limit for Cd was given as 0.1 ng L^{-1}, and analyses at the 1 ng L^{-1} level were demonstrated. Analyses for Zn, Pb, and Cu at the 100 ng L^{-1} level were also illustrated. The glassy-carbon disc was plated <u>in situ</u> with a Hg film obtained from the reduction of 4 x 10^{-5} M $HgCl_2$ added to the seawater sample. Finally, Moorhead, et al. (18) used resonant vibrating wires for the reduction of $Fe(CN)_6^{3-}$ at W and for the reduction of IO_3^-, catalyzed by I_2, at Pt electrodes. Linear calibration curves were obtained in both cases.

Vibrating electrodes were frequently employed in amperometric titrations, particularly in early work. Rosenberg, et al. (19) used a vibrating Pt electrode in the amperometric determination of cysteine and glutathione with $AgNO_3$. The electrode responded to excess Ag^+ present after the endpoint. Harris and Lindsey used vibrating Pt electrodes in the titration of As(III) and $S_2O_3^{2-}$ with iodine, with the electrode responding to excess I_2 (20). In a following article (21), the same authors used vibrating electrodes in the titration of As(III) and Sb(III) with $KBrO_3$. The electrode responded to Br_2 which was formed from the reaction between excess BrO_3^-, present after the endpoint, with Br^- formed during the reaction as a reaction product.

Alimarin and Gallai (22) employed a vibrating electrode in the titration of Fe^{2+} with $K_2Cr_2O_7$. They particularly emphasized the applicability of the technique to titrations using small volumes, e.g., 1 to 2 mL. The electrode responded to Fe^{2+} present prior to the endpoint; the expected linearity was observed between I_1 and the

concentration of Fe^{2+}. The vibrating wire electrode was found to be only half as sensitive as a rotated wire electrode, likely due to the small amplitude of vibration used in the experiment. Jenšovský (23) used a vibrating Pt electrode in percuprimetric (sic) titrations, with the electrode responding to excess Cu(III) present after the endpoint. A well-defined polarographic wave was obtained, with the limiting current proportional to the concentration of Cu(III) from 2×10^{-4} M to 1×10^{-3} M.

Sarkar and Sivaraman (24) used a vibrating Pt electrode for the amperometric titration of cysteine; cystine was also determined following prereduction to cysteine. The titrant was $AgNO_3$, with the electrode responding to excess Ag^+. Titrations were performed using total volumes as small as 0.8 mL. Tikhomirova (25) performed amperometric titrations of As(III) with I_2, using a vibrating Pt electrode which detected excess I_2. She also used the vibrating electrode in an amperometric titration of Fe^{2+} with $KMnO_4$. The electrode was held at a potential of + 0.5 V vs. SCE and responded to excess MnO_4^- present after the endpoint. A measurable current was observed in solutions containing 10^{-7} M MnO_4^-. Although the reduction of MnO_4^- under these conditions was irreversible, the limiting current was observed to increase with increased amplitude of vibration. The vibrating wire electrode was found to be 1.5 to 2 times as sensitive as the rotated wire electrode.

Vibrating electrodes have found use in the electrochemical determination of dissolved oxygen for studies of respiratory oxygen demand. Küster (26) applied a vibrating Pt electrode to studies of respiration

of plants. The electrode was calibrated by addition of known volumes of air-saturated, buffered electrolyte into a cell of constant volume, simultaneously displacing an equivalent volume of deaerated electrolyte. A mathematical expression was derived for the concentration of O_2 following each such addition. The calibration curves obtained showed significant deviations from linearity; the limiting currents observed at higher concentrations of O_2 were lower than the expected values calculated from linear extrapolation of data obtained at lower concentrations.

Liese, et al. (27) employed a vibrating Au electrode for studies of mitochondria. The electrode used was a Au disc, approximately 1 mm in diameter, which was sealed into a glass tube with epoxy. The electrode was coated with collodium for protection against fouling from proteins in the sample. This work is the only reference to vibrating Au electrodes in the literature.

In the USSR, Shurukhin, et al. (28) applied a vibrating Pt electrode to studies of respiratory activity of enzyme preparations. Rudichenko and Rudichenko (29) employed a vibrating Pt electrode to determine the respiration rates of mitochondria <u>in vitro</u> and <u>in vivo</u>.

Passwaters (30) investigated the application of vibrating electrodes to flowing systems. Using a Pt disc electrode, he studied the effect of flow rate on the limiting current observed for the oxidation of 0.01 M $Fe(CN)_6^{4-}$ in the flowing stream. His data show that the limiting current was less dependent on flow rate when the electrode was vibrated at 80 Hz and 0.05-cm amplitude than when the electrode was stationary. Passwaters drew the following conclusions from his work:

"1. Mass transport is not increased using a vibrating electrode when the flow velocity exceeds the electrode linear velocity.

2. ... concurrent use of two forced convection systems to increase mass transport is superfluous.

3. ... as the vibration frequency increases, the effect of changes in the flow rate decreases.

4. Thus, while there is little advantage in using a vibrating electrode at flow velocities exceeding the electrode velocity, at lower velocities the moving electrode enjoys the advantage of increased analytical sensitivity with minimal error introduced by undetected flow velocity changes."

No data were presented for the application of vibrating electrodes to flow-injection analysis, and all experiments were performed under steady-state conditions. Equations relating the steady-state current to the oxidation of $Fe(CN)_6^{4-}$ in this system were not derived.

C. Fundamental Studies

Popov and Rybyanets (31) found that the limiting currents observed using a planar electrode vibrated perpendicular to its surface were 2 to 3 times larger than those obtained using the same electrode vibrated at the same frequency and amplitude but parallel to its surface. They concluded that the motion of liquid around the electrode was turbulent in the case of perpendicular vibration and laminar in the case of parallel vibration. The chemical polarization for the reduction of Cd^{2+} and Cu^{2+} was not changed. Facsko and Radoi supported this latter conclusion in studies of the passivation of Fe electrodes (32). Vibration increased the critical current density for passivation but had no effect on the thermodynamic aspects of the passivation.

Radoi (33) stressed the need for reproducible hydrodynamic conditions in all applications of vibrating and rotating wire electrodes. Gibert and Angelino (34) compared vibration of a spherical electrode to pulsation of the solution past a stationary sphere. The limiting currents observed for the 2 cases, using the same sphere, agreed to within 10% for corresponding vibrational parameters. Ross and Aspin (35) found that surface roughness affected the rate of ionic mass transfer only at low vibrational velocities.

Podesta, et al. investigated the nature of mass transport to a vibrating disc electrode (36). At low vibrational amplitudes, less than 0.55 mm at 50 Hz, solution flow was observed only in the region actually traversed by the disc. At higher amplitudes, streaming of the solution from the electrode to the bulk of the solution was noted. Also, the limiting current contained an alternating-current (AC) component, whose frequency was that of the vibration (50 Hz), with an amplitude equal to 1.5% of the average limiting current. The oscillogram shown in the article indicated that a significant component was also present at the second harmonic, 100 Hz. The limiting current was proportional to the square root of the Schmidt number (Sc) over the range of 852 to 19218.

The effects of vibrational amplitude and frequency on the rate of mass transfer have been studied by many investigators. The results of these studies are summarized in Table II-1. The numerical values for the dependence of mass transport upon frequency, amplitude, and vibrational Reynolds number represent the exponential dependence of I_l, k_m, or Sh_v on each of these parameters. Verbal descriptions of these

relationships are given in cases where no exponential dependence was noted.

Table II-2 summarizes equations given in the literature which relate the limiting current or mass transport rate observed at various types of vibrating electrodes to the vibrational amplitude, a, and frequency, f. The equations are given in the original form. Variables are designated in accordance with the nomenclature employed in this dissertation. References from the Indian literature use the dimensionless parameter J_D' to characterize the mass transport. J_D' is related to more familiar parameters by Equation II-1.

$$J_D' = k_m v_{avg}^{-1} Sc^{2/3} \qquad \text{(II-1)}$$

The vibrational Reynolds number, which is a dimensionless quantity used to characterize the hydrodynamics of vibrating bodies, is given by Equation II-2.

$$Re_v = v_{avg} d_e / \nu \qquad \text{(II-2)}$$

The vibrational Sherwood number, Sh_v, is a second dimensionless quantity and is used to characterize the mass transport to a vibrating electrode. It is related to the limiting current and diameter of the electrode by Equation II-3.

$$I = (nFADC^b/d_e)Sh_v \qquad \text{(II-3)}$$

By comparison of Equations II-3 and I-5, it may be seen that the vibrational Sherwood number is given by the quotient of the diameter of the electrode and the thickness of the diffusion layer:

Table II-1. Exponential dependence of mass transport upon vibrational parameters

Electrode	Mode of vibration	Dependence of M.T.[a] on a, f, Re_v	Range studied	Ref.
Ni disc	Normal	Re_v, proportional	a: 0-2.5 mm f: 0-100 Hz	35
Ni disc	Normal	Re_v, 0.88	$Re_v^{0.88}Sc^{0.5}$ = 10000-30000	35
Pt disc	Normal	a: 0.75 f: 0.75 Re_v: 0.75	a: 0.0635-0.55 mm f: 20-100 Hz	36
W, Pt disc	Normal	f: linear increase	a: 2.5 mm f: 0-3 Hz	16
Pt disc[b]	Angular transverse	f: 0.64	a: 0.25 mm f: 20-110 Hz	29
Cu, steel plate[c]	Normal	a: increases	a: not noted f: 0-100 Hz	37
Ni plate	Normal; parallel	a: 0.9 (normal) a: 0.6 (parallel)	a: 0-0.9 mm f: 100 Hz	31

[a] M.T. = mass transport.

[b] I_1 decreased sporadically at f > 95 Hz. Attributed to cavitation for $v_{avg} > 17.8$ cm sec^{-1}.

[c] Mass transport was further enhanced at mechanical resonance of plate.

Table II-1. Continued

Electrode	Mode of vibration	Dependence of M.T.[a] on a, f, Re_v	Range studied	Ref.
Cu plate	Normal; parallel	Re_v: 0.74 (normal) Re_v: 0.56 (parallel)	a: 1.3-19.88 mm f: 1.67-23.3 Hz	38
Cu plate[c]	Parallel	a: 0.42 f: 1.09	a: 0-8 mm f: 0-48 Hz	39, 40
Pt sphere	–	a: 1.0 (theoret.)	a: 0-0.002 mm f: 82 kHz	41
Ni sphere	–	Re_v: 0.538	a: 0-24 mm f: 0.4-3.3 Hz	34
Cu, steel cylinder	Transverse	a: 0.62 f: 0.62 Re_v: 0.62	a: 2.43-37.09 mm f: 1.67-15 Hz	42
Cu cylinder	Axial	Re_v: 0.62 ($Re_v < 150$) Re_v: 0.87 ($Re_v > 150$)	a: 0.54-7.7 mm f: 3.33-41.7 Hz Re_v: 18.27-959	43
Cu cylinder	Angular transverse	f: 0.57	θ_e: 0.01063-0.1452 radians f: 1.67-23.3 Hz	44

Table II-1. Continued

Electrode	Mode of vibration	Dependence of M.T.[a] on a, f, Re_v	Range studied	Ref.
Pt wire[d]	Axial	f: linear to 40 Hz (at a = 0.9 mm); constant at f > 40 Hz a: linear to 0.4 mm (at f = 100 Hz); constant at a > 0.4 mm	a: 0-0.9 mm f: 0-120 Hz	45
Pt wire	Angular transverse	a: 0.5	a: 0-3.5 mm f: 50 Hz	8, 9
Pt wire	Transverse	a: I_1 incr. 33% from 0.2 mm to 0.5 mm f: I_1 incr. 33% from 50 Hz to 150 Hz	a: 0.2-0.5 mm f: 50-150 Hz	22
Pt wire	Axial	a: I_1 incr. with incr. a up to 4 mm	a: 0-4 mm f: 50 Hz	25
Pt wire	Axial	a: increases; two linear regions. Transition at a = 0.6 mm	a: 0-3.5 mm f: 35 Hz	5

[d] I_1 independent of a, f for all $4af > 15.9$ cm sec^{-1}.

$$Sh_v = d_e/\delta \qquad \text{(II-4)}$$

D. Electrodeposition and Electrosynthesis

Facsko (46) reviewed applications of vibrating electrodes in the electrogravimetric determinations of Bi, Cu, Pb, Sb, and Zn.

Vibrating electrodes have been used by several investigators in the electrodeposition, electrorefining, and electrogravimetric determination of Cu (31, 39, 47-56). Increases in the maximum allowable current density and in the current efficiency were stressed by Facsko and coworkers (47, 48, 51, 52, 54, 55). These increases resulted from the increase in the mass-transport limited rate for the reduction of Cu^{2+} ions relative to the rate for H_2 formation resulting from solvent breakdown. Electrodeposited Cu retained a microcrystalline character at higher current densities when deposited at a vibrating cathode than when deposited at a stationary cathode (54, 55).

Other metals which have been electrodeposited onto vibrating electrodes include Bi (57), Cd (28), Cr (58, 59), Ni (58, 60), Pb as PbO_2 (61), Sb (62), and Zn (63, 64). In all cases, significant increases were noted in the limiting current density or in the maximum allowable current density.

Facsko and Radoi used the vibrating electrode in internal electrolysis (49, 65, 66). A large, cylindrical cage of Pt gauze was used as the vibrating cathode, and a small, stationary Zn rod served as the anode. As a result of the vibration, the polarization of the cathode decreased, and the polarization of the anode consequently increased.

Table II-2. Equations from the literature relating mass transport to vibrational parameters

Electrode	Mode of vibration	Equation	Ref.
Disc	Normal	$k_m = 0.00927Re_v$	35
Disc	Normal	$Sh_v = 0.00118Re_v^{0.88}Sc^{0.5}$	35
Disc	Normal	$I_1 = 0.07nFAD^{1/2}f^{3/4}a^{3/4}\nu^{-1/4}d_e^{-1/4}C^b$	36
Plate[a]	Normal	$J_D' = 0.486Re_v^{-0.44}(1 + (L/B)^{-0.7})$	38
	Parallel	$J_D' = 0.437Re_v^{-0.26}(T_p/B)^{-0.5}$	
Sphere[b]	Pulsation of sol'n.	$Sh_vSc^{-1/3} = 0.624(Re_v(a_{pp}/d_e)^{1/2})^{0.538}$ $Sh_vSc^{-1/3} = 0.711Re_v^{0.538}$	34
Sphere[b]	Vibration of sphere	$Sh_vSc^{-1/3} = 0.593(Re_v(a_{pp}/d_e)^{1/2})^{0.538}$ $Sh_vSc^{-1/3} = 0.661Re_v^{0.538}$	34
Cylinder	Transverse	$J_D' = 0.41Re_v^{-0.38}$	42
Cylinder	Axial	$J_D' = 0.24Re_v^{-0.38}$ for $Re_v < 150$ $J_D' = 0.066Re_v^{-0.13}$ for $Re_v > 150$	43
Cylinder[c]	Angular transverse	$J_D' = 0.54Re_v^{-0.43}$	44

[a] L, T_p, and B designate length, thickness, and breadth of plate, respectively.

[b] Upper equation for $(a_{pp}/d_e) \leq 150$; lower equation for $(a_{pp}/d_e) > 150$.

[c] $Re_v = (2Ld_e\theta_e f\rho)/\nu$, where L = length of electrode and θ_e = angular swing of electrode in radians.

Cementation of the analyte at the anode therefore could not occur, and the internal electrolysis could be performed without a diaphragm. Thus, the time required for the electrolysis was decreased, and the maximum permissible concentration of analyte was increased.

The vibrating electrode has also found application in the electroplating industry (67-71). Khnykin and Ogol applied vibrating electrodes to the electrogravimetric analysis of nonferrous metals (72).

Facsko and co-workers have investigated applications of vibrating electrodes to the electrosynthesis of ferricyanide (14), chromate (73), and permanganate (74). In each case, increases in the current efficiency were noted.

E. Chronopotentiometry and Electrode Kinetics

Rowe and Nyborg (41) used chronopotentiometry to study the reactions of O_2 and H_2 on spherical Pt electrodes vibrated at ultrasonic frequencies. They concluded that mass transport of O_2 and H_2 resulted from the acoustic streaming induced by the vibration. Radoi used chronopotentiometry at vibrating electrodes to study the reductions of Cu^{2+} (75, 76), Fe^{3+} (76), and nitrobenzene and related compounds (77). The chronopotentiometric transition times observed for these reductions were studied as a function of the vibrational Reynolds number for the electrode. The transition time was smallest at stationary electrodes and increased over a range of $Re_v = 0$ to 50. At approximately $Re_v = 50$, the transition time became infinite, which Radoi interpreted as indicative of the onset of turbulence. He also concluded that the concentra-

tion overvoltage was eliminated at Re_v values greater than 50. A Tafel plot for the reduction of Cu^{2+} at an electrode vibrated under such conditions was presented (76).

Vibrating electrodes have been applied to electrochemical studies of heterogeneous kinetics. Hoover (60) studied the kinetics of the Ni^{2+} reduction at a Ni electrode in boric acid solutions. Facsko and Poraicu used vibrating electrodes in studies of the kinetics of the Fe^{3+}/Fe^{2+} and $Ce(IV)/Ce^{3+}$ couples (78) and of the Ti^{3+}/Tl^{+} couple (79). Passwaters studied the kinetics of the $Ce(IV)/Ce^{3+}$ and $Fe(CN)_6^{3-}/Fe(CN)_6^{4-}$ couples at vibrating Pt and carbon paste electrodes (30). Both Facsko and Passwaters applied the vibrating electrode to kinetic studies of electrochemical reactions having heterogeneous rate constants from 10^{-3} to 10^{-5} cm sec^{-1}.

F. Vibrators

Electrodes have been vibrated by means of ultrasonic techniques (41, 58), vibrating stirrers (19, 80), relays (22, 81, 82), buzzers (24), doorbells (22, 25), solenoids (30), cranks (16, 43), massage vibrators (27, 45), speakers (7, 36), an external vibrating disc (17), and a Scotch yoke (34). Electromagnetic vibrators of custom design have also been popular (8, 9, 10, 12, 31, 47, 60, 62, 83). One investigator (18) used a resonant wire, supported at both ends in a strong magnetic field, which was vibrated by passing an alternating current through the wire at its resonant frequency. Those vibrators of interest to the present work are discussed below.

Facsko and Golumbioschi (62) described a polarized electromagnetic vibrator, which was very similar to a permanent magnet (PM) loudspeaker. The electromagnet was a movable coil, which was centered in the gap of an annular, permanent magnet by means of 6 flexible membranes. In common with actual speakers, this design had the advantage of being polarized, meaning that the frequency of vibration was equal to that of the applied current. The polarized vibrator also operated at greater efficiency than nonpolarized units, as exemplified by the designs of Lindsey (83), and of Popov and Rybyanets (31).

Loudspeakers have been used as vibrators by Roberts and Meek (7), and by Podesta, et al. (36). Roberts and Meek employed an electrodynamic speaker, similar in design to those used in the USA prior to World War II, which was modified by removing the cone and supporting framework. A guide and support for the electrode were then affixed to the center of the spider used for centering the voice coil.

Podesta, et al. used a modern, 7-in. PM loudspeaker and affixed a large supporting cone to the original, acoustic cone. The electrode was located at the apex of the supporting cone. The entire assembly was inverted, and the speaker doubled as a cell cover.

G. Patents

Several workers have applied for patents relating to vibrating electrodes. Lindsey (83) applied for a British patent on his nonpolarized electromagnetic vibrator. In the USSR, Khnykin and Ogol (72) were issued a patent relating to uses of vibrating electrodes in

electrogravimetric determinations. A second Soviet patent (56) and a South African patent (84) were issued to Petrov, et al. on applications of vibrating electrodes in the electrorefining of copper.

III. ENGINEERING

A. Microelectrodes

The research described in this dissertation was performed with microelectrodes made from 28, 30, or 32-gauge (Brown and Sharpe) Au or Pt wire and 5-μL disposable micropipets. The micropipets were Drummond Microcaps®, obtained in lots of 100 from Chemistry Stores, Iowa State University. Tests with 1, 2, 5, 10, and 20-μL disposable micropipets proved that the 5-μL size was best suited to the construction of vibrating microelectrodes using 28 through 32-gauge wire, due to its small size combined with relatively high ridigity. The 2-μL size possessed suitable dimensions but insufficient rigidity, and the 1-μL micropipets, although ideal for wire sizes below 32-gauge, had an inside diameter smaller than the diameter of 32-gauge wire. Micropipets larger than 5 μL were too large for use in microelectrodes.

The major difficulty encountered in the construction of solid voltammetric electrodes is the production of a sturdy insulator-to-metal seal which is free from capillary leaks. Pt has a thermal coefficient of expansion which closely approximates that of soft glass, and the formation of a platinum-to-glass seal meeting the above requirements is, thus, a fairly simple matter. Au possesses a lower melting point than Pt, and the thermal coefficient of expansion of Au differs considerably from that of glass. The manufacture of a gold-to-glass seal of high quality is, consequently, extremely difficult and is impossible on the small scale required for this application.

The Pt wire microelectrodes for the present work were manufactured

according to a procedure adapted from Parr and Hendley (85). A 39-mm length of Pt wire was cut and one end was polished with 6-μm diamond paste. This wire was rotated by hand as the polished end was heated in the flame of a type 3A orthodontic blowpipe, manufactured by the Veriflo Corp., Richmond, CA. One end of a 5-μL micropipet was simultaneously heated in the flame until the end fused to form a sphere approximately 1 mm in diameter. The molten glass sphere and the heated, rotating Pt wire were then brought into contact at a point 5 mm from the end of the wire, and a "thread" of molten glass was wound around the Pt wire for approximately 2 revolutions of the wire. When correctly performed, this procedure resulted in a Pt wire with a glass bead approximately 1.5 mm in diameter, which surrounded the wire evenly and left a 5 mm length of wire exposed from the edge of the sphere to the tip of the electrode. The wire was then removed from the flame and allowed to cool. At this point, the longer end of the wire was inserted into a second 5-μL micropipet until the glass sphere touched the end of the micropipet. The sphere and end of the micropipet were carefully reheated in the flame until a smooth joint was formed. The flame was then lowered in temperature by shutting off the flow of air to the blowpipe, and the glass-to-metal seal was annealed for 10 min in this fuel-rich flame. After annealing, the electrode was slowly removed from the flame and allowed to cool. When correctly manufactured according to the above procedure, the glass-to-metal seal was clear and uniform, with no cracks visible in the glass.

The Au electrodes were manufactured by sealing the Au wire into 5-μL micropipets with epoxy resin. The wire was cut and polished ac-

cording to the procedure given above for Pt wire. The resin used, Epon 828®, and the curing agent, diethylenetriamine (DTA), were both products of the Shell Chemical Co., Houston, TX, and were obtained as free samples from the Miller-Stephenson Chemical Co., Danbury, CT. Batches of epoxy were mixed according to the stoichiometric ratio of 11 parts DTA to 100 parts resin (w/w) as suggested by the manufacturer. This epoxy proved superior to the 5-Minute Epoxy manufactured by the Devcon Corp., Danvers, MA, which softened in H_2SO_4 solution and did not maintain a leak-free seal with Au electrodes. The gap between the Au wire and the micropipet was first filled with epoxy, which was allowed to cure for 24 hours. The actual gold-to-insulator seal was then produced by forming an epoxy sphere at the end of the pipet, allowing 5 mm of Au wire to remain exposed. The seal was permitted to cure for 24 hours prior to testing the electrode. Correctly manufactured gold-to-epoxy seals were free from bubbles entrapped in the epoxy.

The completed microelectrodes (see Figure III-1) were 39 mm in overall length with 5 mm of Pt or Au wire exposed from the tip of the electrode to the insulator-to-metal seal. At the top of the electrode, a 1 mm length of wire was exposed to permit connection to the upper pivot of the mounting assembly. The insulator-to-metal seal was ellipsoidal in shape and approximately 1 mm in diameter.

The Pt and Au electrodes were tested by obtaining residual voltammograms in 1.0 M H_2SO_4, using voltage limits of + 1.4 V and - 0.25 V vs. the saturated calomel electrode (SCE) for Pt electrodes and + 1.7 V and + 0.2 V vs. SCE for Au electrodes. If necessary, the electrodes were preconditioned for up to 2 hours by cycling the electrode between

Figure III-1. Mounting assembly for vibrating electrodes

See Table III-2 for designations of lettered parts A through M.

Scale 1:1.

Side view

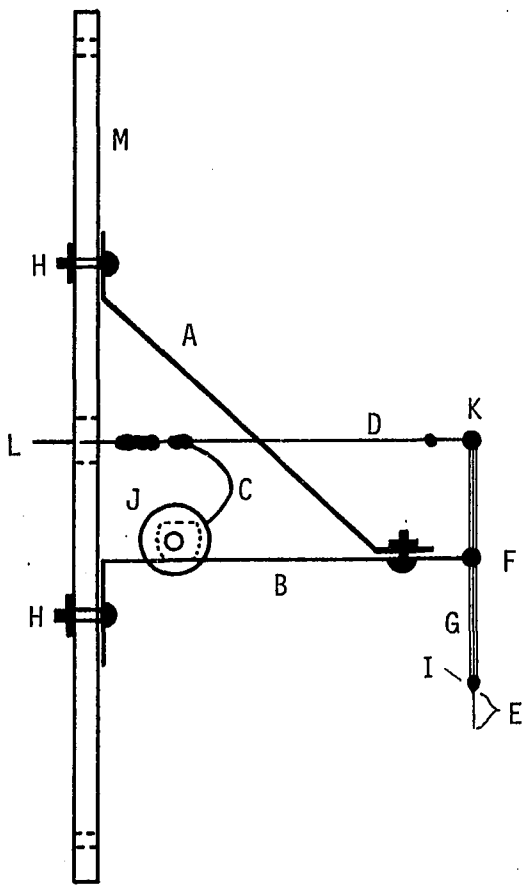

Top view

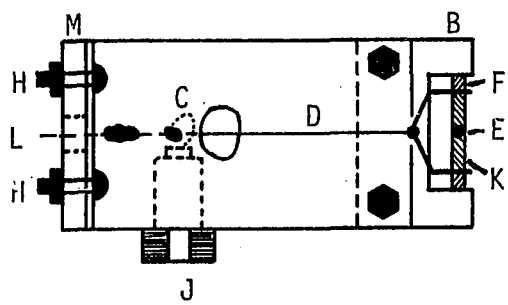

the above limits. Electrodes not yielding reproducible voltammograms similar in appearance to those shown in Figures 1 (Pt) and 26 (Au) of Bélanger and Vijh (86) were rejected. The dimensions of the electrodes which were used in this work are given in Table III-1.

B. Mounting Assembly for Electrodes

Each microelectrode described in the previous section was mounted in an assembly as indicated in Figure III-1. This assembly was designed to allow vibration of the electrode at the maximum frequency and amplitude permissible under the constraints set by the electrode and speaker. The microelectrode and associated portions of the mounting assembly, designated by parts A through K of Figure III-1, formed a removable module. Individual microelectrodes were readily interchanged by unsoldering the linking wire from the driving fork, removing the mounting hardware, and replacing the mounting assembly with a second, similar assembly holding a different electrode.

The materials used in the construction of the mounting assembly are listed in Table III-2. The connecting wire, chosen for maximum flexibility, was formed into a semicircular loop which permitted the driving fork to vibrate freely. A drop of epoxy fastened the bottom end of the loop to the bracket. The linking wire and driving fork overlapped for 3 mm to facilitate soldering. The angular brace was fastened to the bracket at its electrode end with 2-56 brass hardware. Both the knee (upper) and fulcrum (central) pivots for the vibrating electrode were formed using torsion bearings made from 1.5-mm strips of 3-mil

Table III-1. Dimensions of vibrating electrodes used in this work

Electrode	Wire	Dimensions (mm)[a]			
		d_e	L_{S-T}	L_{F-T}	L_{F-S}
A	28 ga. Pt	0.291	5.083	22.976	17.892
B	28 ga. Pt	0.305	5.193	23.807	18.614
C	28 ga. Pt	0.30	4.237	23.424	19.187
D	32 ga. Pt	0.191	5.0	23.0	18.0
E	30 ga. Au	0.250	4.806	23.715	18.909
F	28 ga. Au	0.30	5.0	23.0	18.0

[a] F = fulcrum; S = seal; T = tip.

Table III-2. Construction materials and designations of parts used in the mounting assembly

Letter in Figure III-1	Designation	Material or item used
A	Angular brace	16-gauge Cu sheet
B	Bracket	16-gauge Cu sheet
C	Connecting wire	4-cm length of Belden 8599 wire (7 x 40 ga., insulated)
D	Driving fork	20-gauge Cu wire, soldered at junction of arms
E	Electrode (active surface area)	Pt or Au wire; see Section III-A
F	Fulcrum pivot	See text
G	Glass sheath of electrode	5-μL micropipet; see Section III-A
H	Hardware for mounting	4 4-36 brass screws and brass nuts
I	Insulator-to-metal seal	See Section III-A
J	Jack for connection to potentiostat	Banana jack, epoxied to bracket
K	Knee (upper) pivot	See text
L	Linking wire	18-gauge Cu wire
M	Mounting plate	1/8-in. Al sheet

phosphor bronze stock, obtained from the Physics Instrument Shop, Iowa State University. To install these pivots, the ends of a 5-cm by 1.5-mm predrilled strip of phosphor bronze stock were first soldered to 20-gauge Cu strips which were wrapped around the projections on the arms of a dual buret clamp. The spring in the buret clamp maintained a suitable tension on the phosphor bronze strip during its installation in the mounting assembly. This strip was then carefully soldered to the pretinned projections of the bracket, making certain that the hole for the electrode was centered between the projections. The knee pivot on the driving fork was assembled in similar fashion, except that the bronze strip was soldered to the pretinned arms of the fork. The electrode passed through the hole in the bronze strip forming the fulcrum and was fastened to it with a small portion of epoxy. At the top of the electrode, the Pt or Au wire was carefully soldered to the bronze strip forming the knee pivot, after which the top of the glass micropipet was fastened to the bronze strip with epoxy. The procedure described above produced torsion bearings of uniformly high quality, and reproducible performance was obtained over periods exceeding 6 months under constant usage without replacement of parts.

Torsion bearings were chosen as the pivots for the vibrating electrodes because they were free from mechanical "play" encountered with normal bearings. This property was desired in the present work because the vibrating electrodes were generally operated at small amplitudes and high frequencies, at which such "play" would affect the reproducibility of vibration. Also, the use of a conducting torsion bearing in the knee pivot, together with the flexible connecting wire,

obviated the need for moving contacts such as those used with rotating disc electrodes. This frequent source of electrical noise was thus eliminated. The torsion bearings were also more rugged than mechanical pivots and did not require the exacting alignment demanded by small mechanical bearings.

The geometry of the vibrating electrode and its mounting assembly was analogous to that described by Oehme and Noack (10), although these authors employed mechanical pivots, a crude vibrator, and much larger electrodes than those used in this work. The use of torsion bearings in Torbal® analytical balances in place of the customary knife edges exemplified the reproducibility and sensitivity of this technology to the present author and suggested its application to vibrating electrodes.

C. Loudspeaker

The vibrator employed in this research was an acoustic suspension loudspeaker, Realistic part No. 40-1197, obtained from Radio Shack, Ames, IA. This speaker was modified for use as a vibrator by gluing a metal cone, 23 mm in diameter, to the cardboard dome covering the voice coil. This metal cone was formed from a 25-mm circle of 3-mil phosphor bronze stock which was cut along a radius. The edges of this cut were overlapped until the apex angle of the cone so formed measured 135 degrees and were then soldered. A linking wire, 32 mm in length, was then soldered to the apex of the cone. The modified speaker was mounted on a vertical piece of 1/2-in. Al stock, 7 in. high and 6 in. wide, which had a circular hole, 3-5/8 in. in diameter, centered 2-5/16 in.

below the top of the support and 3 in. from either side. The speaker was affixed to the rear side of this support and was centered in the circular hole, with the linking wire protruding normal to the plane of the hole. The mounting plate shown in Figure III-1 was fastened to the front side of the support with its long dimension vertical, and the linking wire was centered in the 1/4-in. hole in this plate. The vertical support was mounted on a base of 1/4-in. Al stock measuring 6 in. by 6-1/2 in. such that the rear face of the speaker magnet was flush with the shorter side.

Loudspeakers possess several advantages relative to other types of vibrators which have found application to vibrating electrodes. The amplitude of vibration is directly proportional to the value of the alternating-current (AC) input voltage. Speakers vibrate over a wider range of frequencies than other types of vibrators previously used with voltammetric electrodes. These 2 properties are fundamental requirements for high-fidelity sound reproduction, and much research has been performed to design loudspeakers which most closely approach these goals. Such engineering and design research was exploited to advantage in the present application. The amplitude and frequency of vibration of the electrode are determined by the voltage and frequency on the input signal to the speaker, and the vibrational parameters thus may be changed rapidly and reproducibly by means of appropriate changes in the characteristics of the input signal. Loudspeakers are also inexpensive and readily available, and they require minimal modification for use as vibrators.

The acoustic suspension loudspeaker used in this research featured

a 200-g magnet and cloth-roll suspension and had high compliance. The diameter of the cone excluding the cloth roll was 3-1/2 in. The amplitude of vibration which resulted from a given AC input voltage was thus very large, and the mechanical power available to drive the vibrating electrode was more than sufficient to achieve the desired vibrational parameters with minimal loading of the speaker.

D. Mechanical Evaluation of the Vibrating Electrode

The electrode system described in the previous sections could be vibrated at frequencies from 5 Hz to 500 Hz at amplitudes up to 3 mm, peak-to-peak. The upper limit to the frequency of vibration was set by the natural resonance of that portion of the microelectrode below the fulcrum pivot. This resonance occurred at approximately 550 Hz for the microelectrodes used in this work. At the frequency corresponding to natural resonance, a small excitation of the electrode by the speaker induced vibrations of large amplitude in the lower half of the microelectrode. The glass micropipet no longer behaved as a rigid member but bent at the fulcrum and consequently fractured at or near the fulcrum. This nonideal behavior was not observed at vibrational frequencies below 500 Hz, which were sufficiently removed from the resonant frequency to ensure safe operation. The lower limit of 5 Hz was determined by the frequency limitations of the instrumentation used to drive the speaker.

The only resonance displayed by the electrode system in the usable frequency range of 5 Hz to 500 Hz was a lateral resonance of the driving

fork and torsion bearings. This resonance occurred at approximately 300 Hz and resulted in elliptical motion of the vibrating electrode, as contrasted to the desired reciprocal motion. The lateral response had no deleterious effects on the electrode, and this frequency could be avoided in studies requiring pure reciprocal motion. The speaker displayed a highly damped natural resonance at approximately 75 Hz which did not affect the mechanics of vibration.

The amplitude of vibration was measured with a travelling microscope constructed from a model M101A microscope with M204 scale eyepiece micrometer, products of the Gaertner Scientific Corp., Chicago, IL, and a micrometer slide, part No. 469M, manufactured by the L. S. Starrett Co., Athol, MA. The micrometer slide was capable of measurements with an accuracy of $\pm$ 0.001 mm and was used to calibrate the eyepiece micrometer by moving the image of a stationary object across the field of vision, which was approximately 3.3 mm in diameter. Those electrodes whose measurements are given in Table III-1 to an accuracy of 0.001 mm were measured using the travelling microscope in its usual fashion. The vibrational amplitude was measured using the calibrated eyepiece micrometer to observe the distance traversed by the image of the thin, bright reflection from the polished surface of the Pt or Au wire forming the active surface of the working electrode. Light was provided by a high-intensity lamp positioned so as to maximize the intensity of this thin reflection. The maximum vibrational amplitude in the research was limited to 3.3 mm, which was the diameter of the field of vision of the eyepiece micrometer.

The observed vibrational amplitude, a_{obs}, was measured at a point 0.069 mm above the tip of the Au or Pt wire. The corresponding value for the peak-to-peak vibrational amplitude of the tip of the electrode, a_{pp}, was calculated from each value of a_{obs} by means of Equation III-1.

$$a_{pp} = 2L_{F-T}\sin^{-1}[a_{obs}/(2L_{F-T} - 0.069)] \qquad \text{(III-1)}$$

Unless otherwise stated, all values for a_{pp} and related quantities cited in this dissertation were calculated from experimental values for a_{obs} using Equation III-1 and, consequently, refer to the conditions prevailing at the tip of the electrode. Equation III-1 was derived from the basic geometric and trigonometric relationships governing the motion of a point through an arc of a circle, which is the motion described by the tip of the electrode. Since this arc is of small amplitude relative to the length of the electrode, the motion of the tip of electrode closely approximates the ideal of linear simple harmonic motion.

Figure III-2 illustrates typical calibration curves for the peak-to-peak vibrational amplitude (a_{pp}) of the tip of the electrode as a function of the input voltage to the speaker (E_{in}). The vibrational amplitude is directly proportional to the input voltage to within 2% at 240 Hz and 1% at 80 Hz. Greater deviations were observed at higher vibrational amplitudes, not shown in these calibration curves. The vibrational amplitudes covered by these curves, however, exceed those used in the electrochemical work, thus ensuring the desired linearity in all electrochemical investigations. The input voltage to the speaker

Figure III-2. Calibration curves for Electrode A

■ 80 Hz; ▲ 120 Hz; ● 240 Hz.

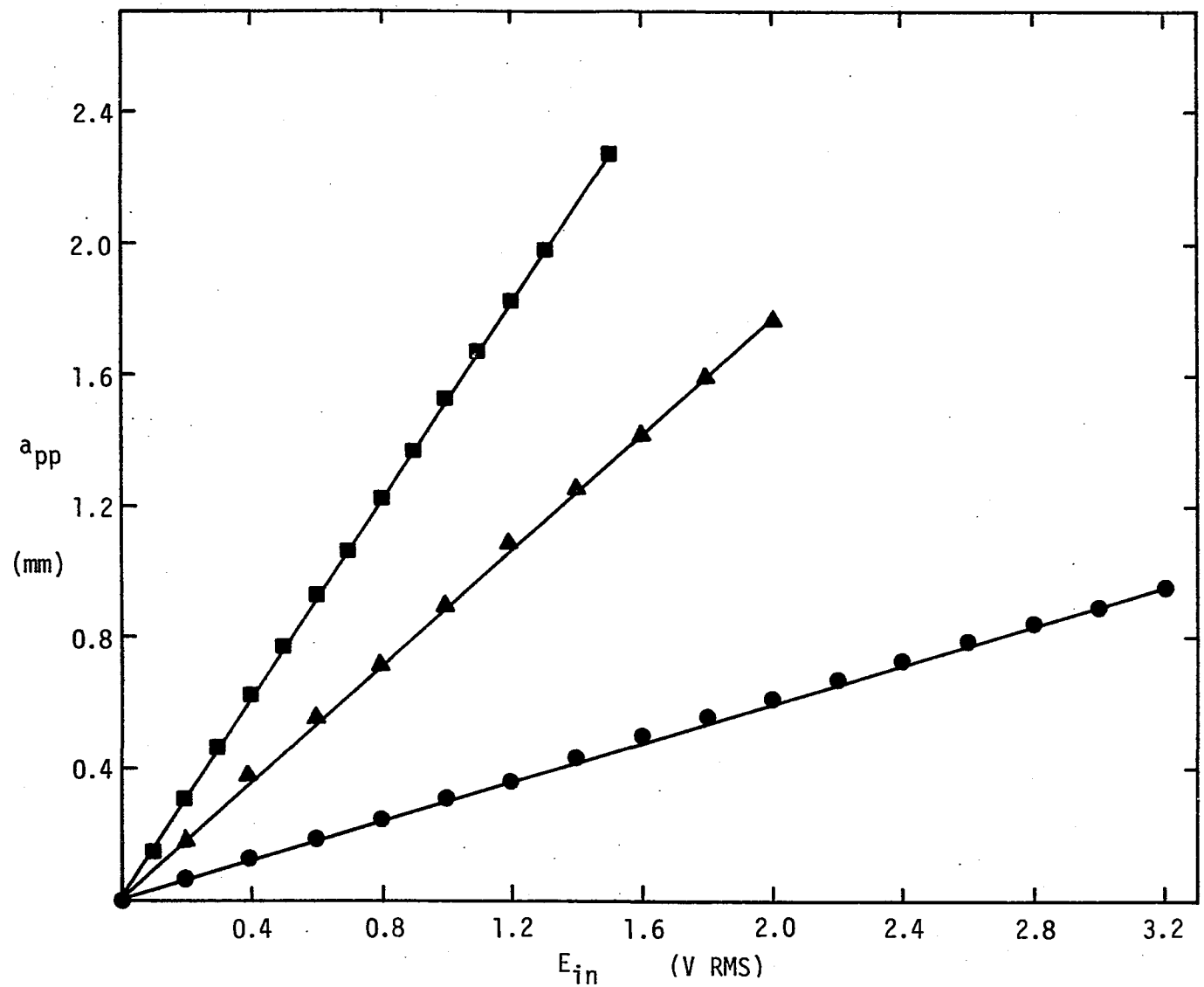
2.4
2.0
1.6
a_{pp}
1.2
(mm)
0.8
0.4
0.4
0.8
1.2
1.6
2.0
2.4
2.8
3.2
E_{in} (V RMS)

was measured in volts RMS using a Simpson model 461 digital multimeter, manufactured by the Simpson Electric Co., Elgin, IL.

Figure III-3 illustrates the frequency response of a vibrating electrode from 30 Hz to 510 Hz. The peak-to-peak amplitude of vibration is plotted as a function of the frequency for a constant input voltage of 1.000 V RMS. The amplitude obtained at a given input voltage decreases with increasing frequency up to approximately 400 Hz. Above this frequency, a slow increase is noted. This increase represents the low-frequency shoulder of the peak resulting from natural resonance of the lower portion of the electrode and indicates that the electrode is no longer behaving as a rigid member.

The amplitude measurements for the calibration curves shown in Figures III-2 and III-3 were obtained with the lower portion of the electrode immersed in a square spectrophotometric cuvet filled with deionized water. Surprisingly, the vibration amplitudes observed with the electrode immersed in water were approximately 3% greater than those observed under identical conditions but with the electrode vibrating in air. Measurements of a stationary object of known dimensions established that this difference was not due to refractive effects of the water.

E. Calculation of Re_v from the Experimental Data

Knowledge of the vibrational Reynolds number is fundamental to the characterization of the flow pattern around vibrating electrodes. The vibrational Reynolds number, Re_v, may be readily calculated from Equation II-2 if the average velocity, v_{avg}, and diameter, d_e, of the electrode

Figure III-3. Frequency response of Electrode C

E_{in} = 1.000 V RMS.

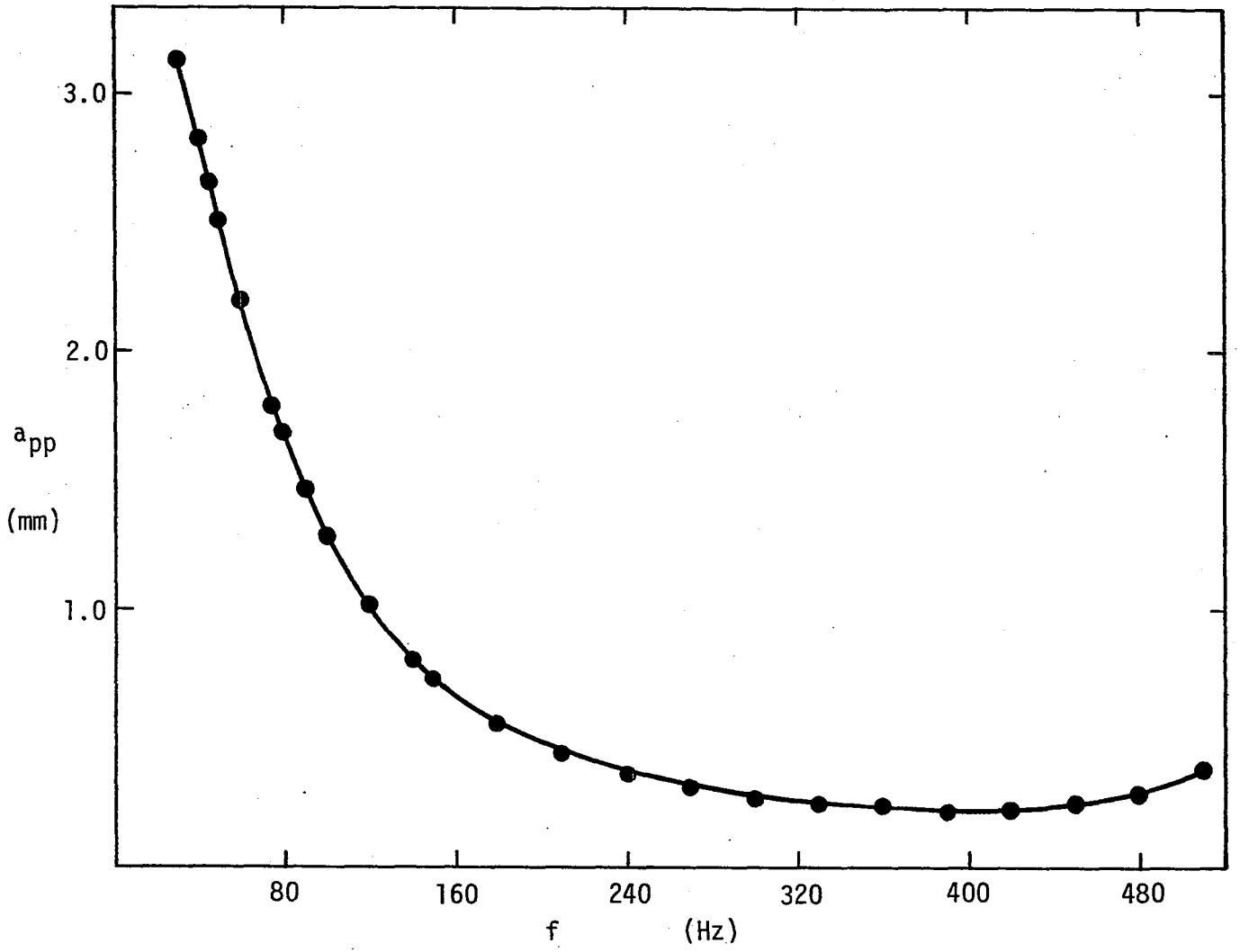
3.0
2.0
1.0
a_{pp}
(mm)
80
160
240
320
400
480
f
(Hz)

are known. The kinematic viscosity, ν, of the solution must also be known.

The kinematic viscosity of a liquid is defined as the ratio of the viscosity of the liquid to its density. For 0.5 M H_2SO_4 at a temperature of 25 C, the supporting electrolyte used in the studies of I_1 as a function of Re_v, these values are 0.01092 g $cm^{-1}sec^{-1}$ for the viscosity and 1.0273 g cm^{-3} for the density (calculated from data in 87). The kinematic viscosity of 0.5 M H_2SO_4 is thus 0.01063 cm^2sec^{-1}.

The diameters of the electrodes used in this work appear in Table III-1.

The average velocity of the vibrating electrode may be calculated from the basic equation defining simple harmonic motion, Equation III-2, in which x(t) represents the location of the vibrating body as a function of time.

$$x(t) = a \cos \omega t \qquad \text{(III-2)}$$

The velocity of this body as a function of time, v(t), is obtained from differentiation of Equation III-2 with respect to time. Since the effect of motion of the electrode is the same in both directions of vibration, the absolute value of the velocity, $|v(t)|$, is the parameter of interest:

$$|v(t)| = |dx/dt| = |- a\omega \sin \omega t| \qquad \text{(III-3)}$$

Equation III-3 is familiar to the reader as the relationship describing the voltage observed at the output of a full-wave rectifier, prior to filtering, in a direct-current (DC) power supply.

From the periodic nature of the graph of Equation III-3, it is evident that v_{avg} is most expeditiously obtained by averaging $|v(t)|$ over the region from $\omega t = 0$ to $\omega t = \pi$. This average value is given by Equation III-4.

$$v_{avg} = (1/\pi) \int_0^{\pi} a\omega \sin \omega t \, d(\omega t) = 2a\omega/\pi \qquad \text{(III-4)}$$

The angular frequency of vibration ω, is related to the frequency, f, by Equation III-5.

$$\omega = 2\pi f \qquad \text{(III-5)}$$

The relationship between v_{avg} and the vibrational parameters is obtained by combining Equations III-4 and III-5.

$$v_{avg} = 4af = 2a_{pp}f \qquad \text{(III-6)}$$

Equations III-6 and II-2 may be combined to give the basic relationship between Re_v and the experimentally determined parameters a and f, Equation III-7. The value of a in Equations III-6 and III-7 is equal to half the value of a_{pp} as defined in this dissertation.

$$Re_v = 4afd_e/\nu = 2a_{pp}fd_e/\nu \qquad \text{(III-7)}$$

The average vibrational velocity for electrode C as a function of the frequency of vibration is shown in Figure III-4. Each point on the graph was calculated from the corresponding datum shown in Figure III-3 using Equation III-6. When presented in this manner, the data show the increases in relative mechanical efficiency of the vibrating system at 75 Hz, due to the natural resonance of the speaker, and at the upper

Figure III-4. Average vibrational velocity for Electrode C as a function of frequency E_{in} = 1.000 V RMS.

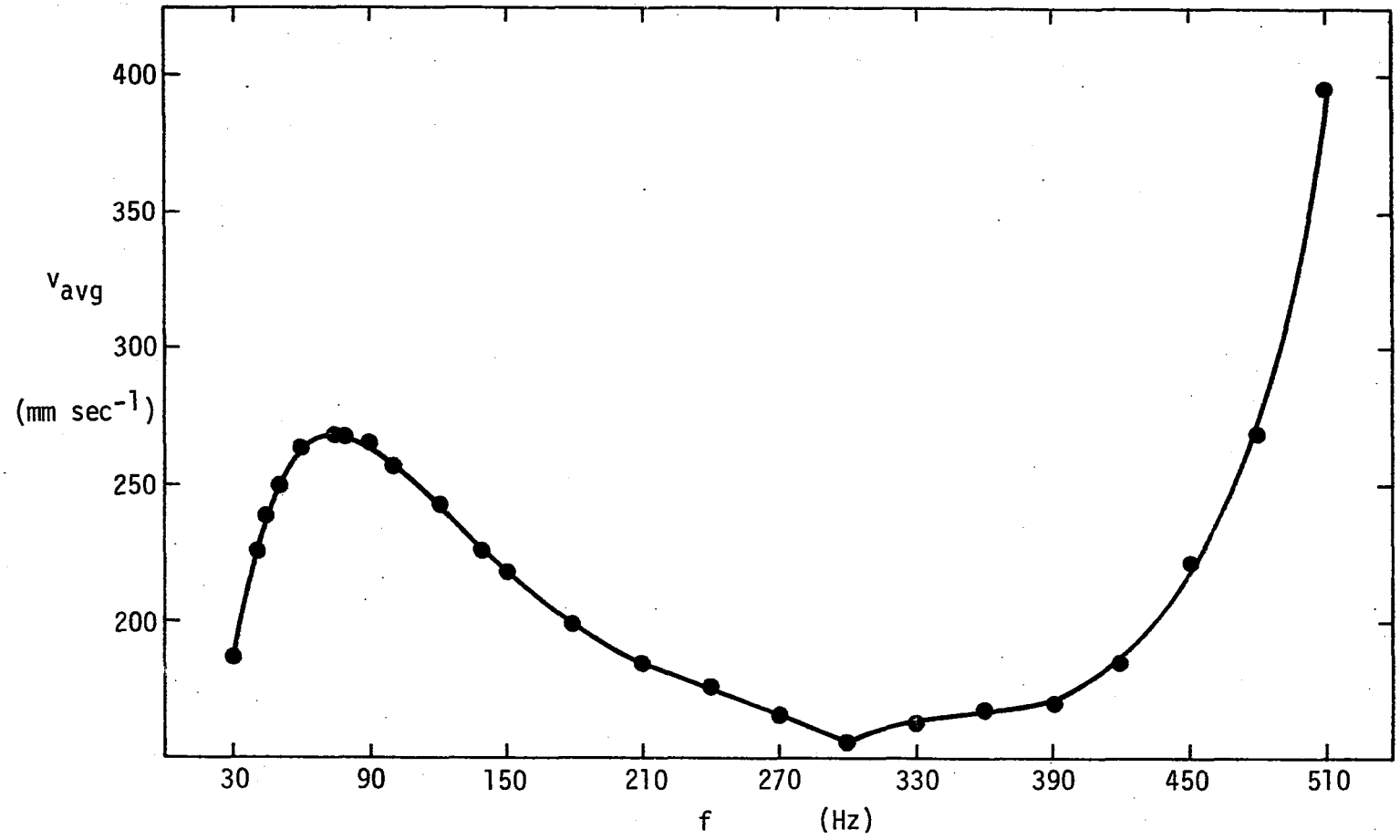
400
350
300
250
200
v_{avg}
(mm sec^{-1})
30
90
150
210
270
330
390
450
510
f (Hz)

frequency limit, at which the natural resonance of the electrode is approached. The slight decrease in efficiency at 300 Hz results from the lateral resonance of the mounting assembly.

F. Cell

The cell employed for all experiments described in this dissertation, with the exception of those employing flow-injection analysis, was constructed from a square bottle, model 13537, manufactured by the Hach Chemical Co., Ames, IA. This bottle was originally designed for use in an apparatus for water analysis in which sample preparation and spectrophotometric analysis were both conducted in the same vessel. For this reason, the bottle is more rugged than spectrophotometric cuvets but optically of higher quality than similar bottles designed solely for storage of reagents. As supplied, the bottle had 2 clear sides and 2 frosted sides and had a capacity of 25 mL, indicated by a frosted mark on one of the clear sides. For use as the electrochemical cell in the present work, the portion of the bottle above the frosted mark was sawed off, and 2 fritted glass discs (Corning part No. 31001-10, medium porosity) were attached to the 2 frosted sides of the square bottle, with the centers of the frits 1.5 cm above the bottom of the bottle and the tubes (supplied with the frits) projecting horizontally outward. Following completion of this step, both tubes were bent until they projected vertically upward at a distance of 2.5 cm from the side of the cell, and excess tubing was removed such that the ends of the tubes were flush with the top of the sawed-off bottle. These 2 tubes

served as the compartments for the counter and reference electrodes. The vibrating electrode was immersed in the central, 2.4-cm square compartment of the completed cell. This compartment had a capacity of approximately 28 mL.

For experiments requiring removal of O_2 from the solution, the central compartment of the cell was covered with a shield made from a 3.0 x 3.0 x 0.3-cm piece of Teflon which was provided with 2 2-mm holes located in the center and right rear corner of the shield. Deaeration of the solution in the central compartment was readily effected by bubbling a stream of N_2 gas through a Pasteur pipet inserted in the corner hole. The vibrating electrode was inserted into the solution through the center hole.

The completed cell permitted observation of the vibrating electrode in situ by means of the travelling microscope. Because the optical quality of this cell was not as high as that of a spectrometric cuvet, the image of the vibrating electrode was slightly blurred. Hence, the calibration curves of a_{pp} vs. E_{in} for the vibrating electrodes were obtained using cuvets as previously described.

IV. INSTRUMENTATION

The research described in this dissertation was performed with the aid of electronic instrumentation whose design and operation are presented in this chapter. Emphasis is given to those circuits which have not previously appeared in the literature. Much of the circuitry employs operational amplifiers, whose principles of operation and electrochemical applications are discussed by Deboo and Burrous (88), and by Bard and Faulkner (89), respectively.

A. General Guidelines

Unless otherwise noted, the following guidelines apply to all circuits presented in this section. Resistors are 1% metal film units. Resistances in the figures are given in ohms, with K and M signifying thousand and million, respectively. Capacitors shown in the diagrams without indication of polarity are Mylar units with capacitances noted in microfarads (μF). Electrolytic capacitors have their capacitances (in μF), polarities, and rated voltages noted in the schematic diagrams. Except as noted, the operational amplifiers have offset potentiometers, connected and adjusted in accordance with the manufacturers' recommendations (90, 91). These offset potentiometers are not shown in the schematic diagrams. The connections from the operational amplifiers to the power supply also follow standard practice and are not depicted in the diagrams. Circled letters denote connections to other circuits, as noted for each figure. All offset potentiometers and connections to the power supply are shown for integrated circuits other than operational

amplifiers. All circuits were constructed on perforated fiberboard. Voltage, current, and resistance measurements were performed with a Simpson model 461 digital multimeter, manufactured by the Simpson Electric Co., Elgin, IL. Waveform observations and measurements were performed on a model 122A oscilloscope, manufactured by the Hewlett-Packard Co., Palo Alto, CA. Frequency measurements were performed on this oscilloscope by applying the signal of unknown frequency to the vertical amplifier and a 10-V RMS, 60.00-Hz standard signal, obtained from the 115-V power line using a Bell transformer, to the horizontal amplifier. The patterns so obtained were of the type first described by Bowditch (92) in 1815 and today are known as Lissajous figures. Their application to frequency measurements is reviewed in the literature (pp. 168-71 of 93). The unknown frequency was adjusted such that a stationary Lissajous pattern of the desired order was obtained. This technique was applicable to unknown frequencies from 10 Hz to 510 Hz, which were employed in this research.

B. Potentiostat

A schematic diagram of the potentiostat used in this research is presented in Figure IV-1. The circuit is of standard design and is similar to that shown in Bard and Faulkner (Figure 13.4.5 of 89). In the present circuit, however, the current passing through the working electrode (WE) is monitored indirectly by employing an instrumentation amplifier, composed of operational amplifiers OA3 and OA4, to measure the voltage drop across a standard resistance placed in the lead to the

Figure IV-1. Schematic diagram of potentiostat

OA1, OA3, OA4, OA5 – National Semiconductor LM741 operational amplifier; OA2 – Analog Devices AD540 FET input operational amplifier; R1 – 10-turn trimmer potentiometer; S_1 – single-pole, 5 position rotary switch.

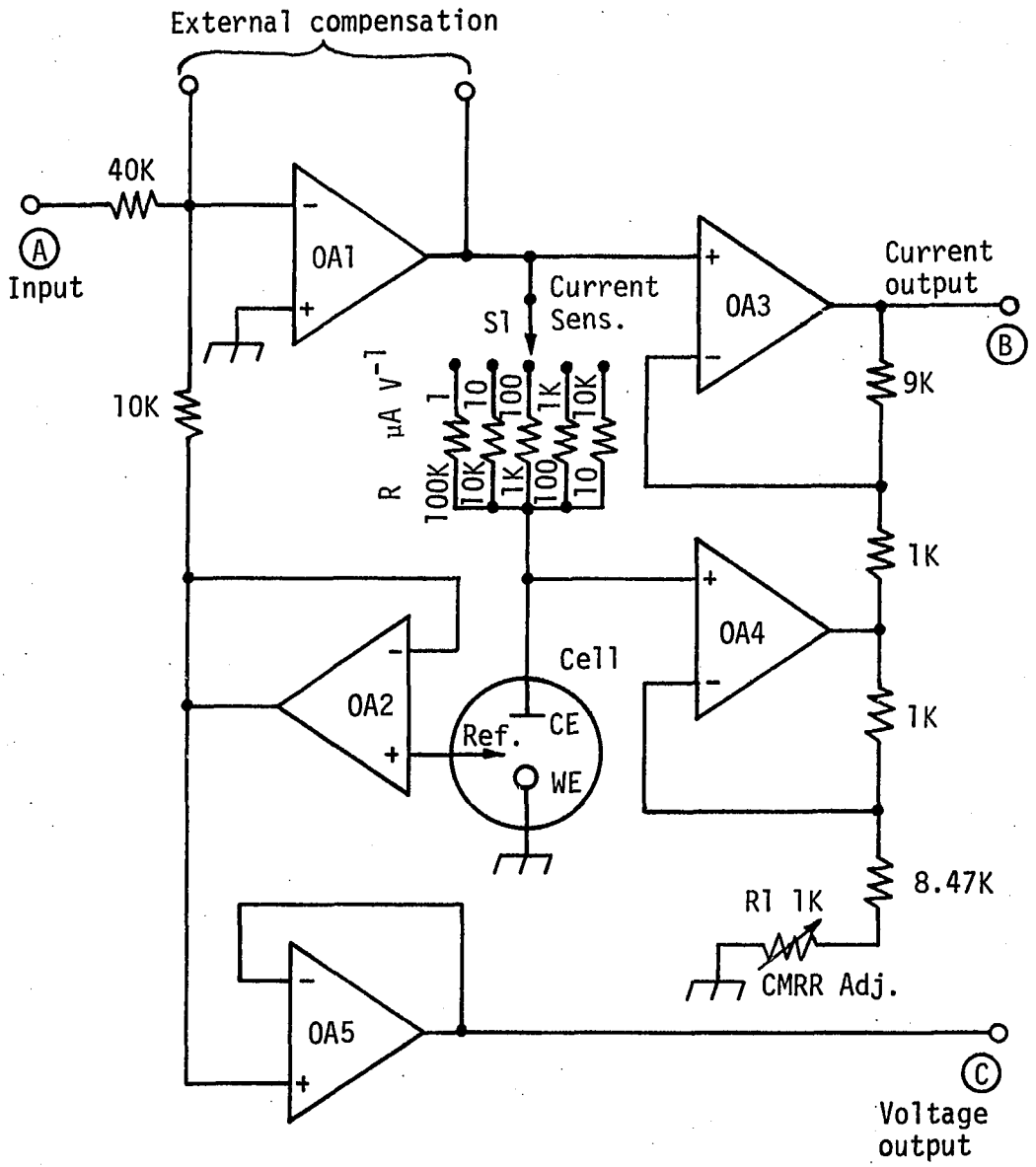
External compensation
40K
A
Input
OA1
10K
S1
Current
Sens.
R μA V⁻¹
1
10
100
1K
10K
100K
10K
1K
100
10
OA3
Current
output
B
9K
1K
OA4
1K
OA2
Cell
Ref.
CE
WE
8.47K
R1 1K
CMRR Adj.
OA5
C
Voltage
output

the counter electrode (CE). This approach has found previous application (94). The instrumentation amplifier was taken from Malmstadt, et al. (p. 30 of 93). In contrast to normal practice, this modification to the standard circuit allows the working electrode to be grounded directly and consequently eliminates the introduction of unwanted noise through stray coupling to the working electrode. The elimination of such noise was of prime concern in this research. The modified potentiostat suffers from the disadvantage that the range of potentials which may be assumed by the counter electrode is limited by the common-mode restrictions of the instrumentation amplifier and not by the less stringent output restrictions of the control amplifier, OA1. In the aqueous solutions studied in this research, however, these limits were not approached.

An operational amplifier having FET input is used at OA2, the voltage follower for the reference electrode (Ref). OA5 is connected as a voltage follower and isolates the voltage output of the potentiostat, point C, from the feedback loop. The ratio of the 2 resistors connected to the summing junction of OA1 provides an attenuation of the input signal from the triangular waveform generator by a factor of 4. This attenuation reduces the effects of drift and noise from the waveform generator by a like factor. External voltages, such as sinusoidal signals for AC polarography or switched DC potentials for voltage-step applications, may be applied to the potentiostat through resistors connected to the summing junction of OA1. These external voltages are attenuated by a factor of $(R_{ext}/10)$, where R_{ext} represents the resistance of the added resistor in kilohms.

The common-mode rejection ratio (CMRR) of the instrumentation

amplifier is optimized by removing OA1 and connecting the noninverting input of OA3 alternately to potentials of + 5.0 V and - 5.0 V. The setting of the CMRR Adj. potentiometer, R1, is then adjusted until the output potential of OA3 remains 0.000 V for both input values.

The potentiostat is wired such that the potential appearing at the voltage output is equal to - E_{WE} and the potential appearing at the current output, point B, is positive for cathodic currents. This choice permits voltammograms to be obtained on an X-Y recorder with the axes presented in the standard electrochemical presentation (negative potentials to the right, cathodic currents upward). The X-Y recorder need not have its input leads reversed nor be used upside-down to achieve this format. Use of the output potential from OA5 for the voltage axis also provides a foolproof indication of saturation in the potentiostat. Since the output of OA2 (and thus OA5) is equal to - E_{WE}, the potential observed at the voltage output during saturation of the potentiostat remains fixed at the potential at which such saturation occurs. Most commercial potentiostats obtain their voltage output directly from the waveform generator and therefore give no indication of saturation in the potentiostat.

In cases where additional frequency compensation for the control amplifier is required, an external capacitor may be connected between the 2 terminals noted in Figure IV-1. For the experiments described in this dissertation, a 680-pF silver mica capacitor was used to assure freedom from unwanted oscillations.

C. Triangular Waveform Generator

A schematic diagram of the triangular waveform generator designed for this research is shown in Figure IV-2. The circuit is based on 3 operational amplifiers and uses electronic switching in place of mechanical switching at the voltage scan limits. The waveform generator features independent control of the positive and negative scan limits, the facility for manual reversal of scan direction, and automatic termination of the voltage scan at either scan limit.

For analysis, the waveform generator may be considered as having 3 stages: an integrator of standard design made from an operational amplifier with FET input, OA3, 2 voltage comparators made from general-purpose operational amplifiers, OA1 and OA2, and a diode switching network. Diodes D1-D6 comprise the switching network. All electrical components are considered to be ideal devices, which is a satisfactory approximation for their application in this circuit.

An analysis of the circuit begins most conveniently with the integrator, which functions according to Equation IV-1.

$$e_o = - \frac{1}{R_{in}C_f} \int e_{in} dt, \qquad \text{(IV-1)}$$

where e_{in}, e_o, R_{in} and C_f are, respectively, the input voltage, output voltage, input resistor, and feedback capacitor indicated in Figure IV-2. The value of e_o is represented by a positive linear ramp ($de_o/dt > 0$) for a negative value of e_{in} and <u>vice versa</u>. From the orientation of diodes D2 and D4 shown in Figure IV-2, it can be seen that the negative value of e_{in} needed for a positive ramp originates

Figure IV-2. Schematic diagram of triangular waveform generator

OA1, OA2 – National Semiconductor LM747C dual operational amplifier; OA3 – Analog Devices AD540 FET input operational amplifier; D1 to D6 – 1N914 diodes; VR – voltage regulator; 4 1N914 diodes and 1N747 Zener diode; P1, P3, P5 – 10-turn potentiometers with calibrated dials; P2, P4, P6 – 10-turn trimmer potentiometers; S1, S2 – normally-open push button switches; S3 – double pole on-off-on switch; S4 – single pole on-off-on switch; S5, S6 – SPDT switches.

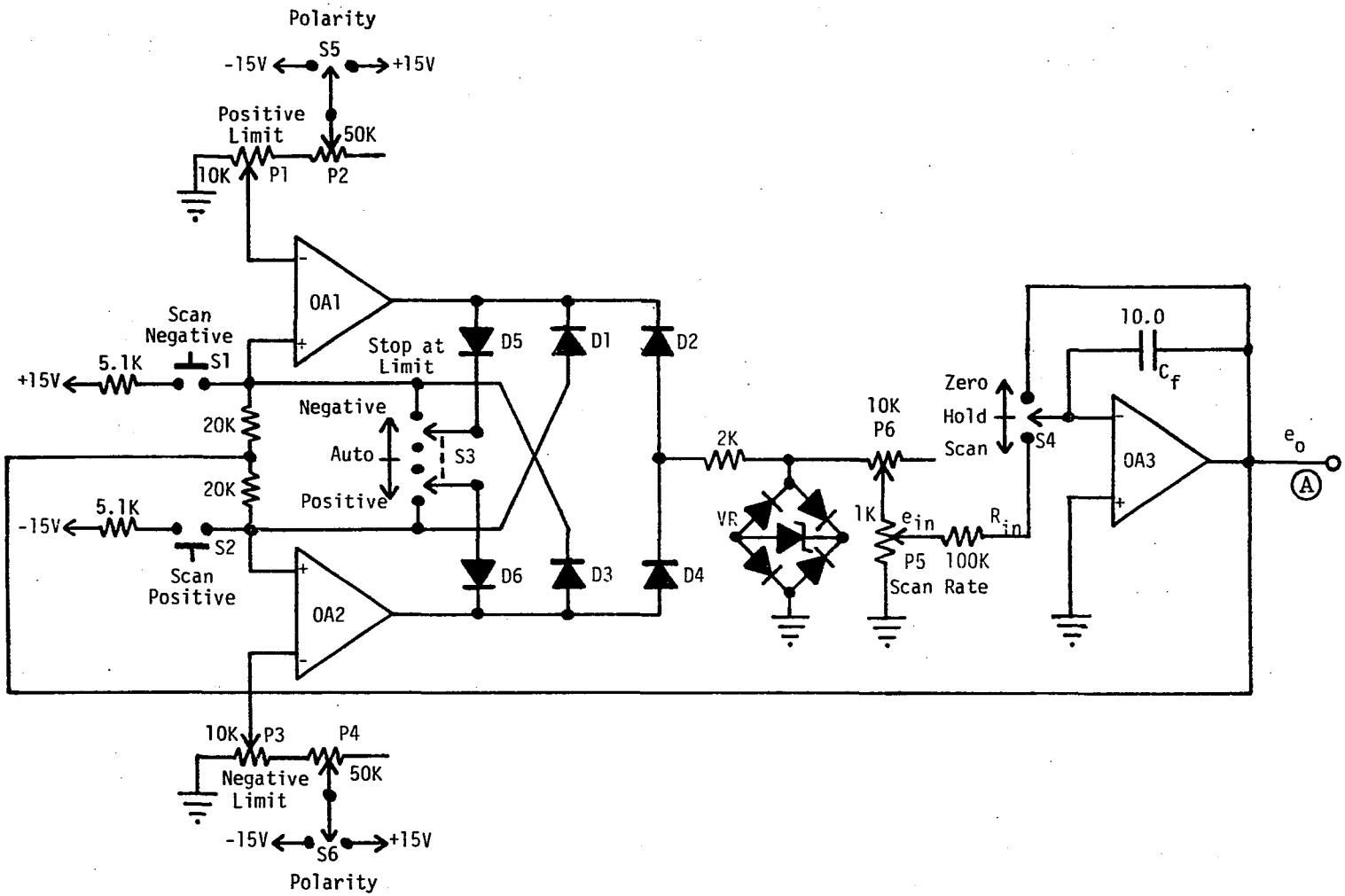
Polarity
S5
-15V
+15V
Positive Limit
50K
10K
P1
P2
OA1
Scan Negative
S1
5.1K
+15V
Stop at Limit
D5
D1
D2
Negative
Auto
Positive
S3
20K
20K
5.1K
-15V
S2
Scan Positive
D6
D3
D4
OA2
2K
VR
10K
P6
1K
ein
Rin
P5
100K
Scan Rate
Zero
Hold
Scan
S4
10.0
Cf
OA3
eo
A
10K
P3
P4
50K
Negative Limit
-15V
+15V
S6
Polarity

from comparator amplifier OA1 and that the positive value of e_{in} required for a negative ramp originates from comparator amplifier OA2. The limits for the positive and negative voltage scans are determined by potentiometers P1 and P3, respectively. The scan rate is determined by potentiometer P5. Potentiometers P2, P4, and P6 are for calibration adjustments.

The functioning of the switching diodes D1-D4 is most readily understood by following the operation of the circuit through one cycle of the output waveform. Assume that the integrator starts on a positive scan. This means that the output of OA1 is at negative saturation, $- E_{sat}$, and diodes D1 and D2 are conducting. Since D1 is conducting, OA2 "sees" $- E_{sat}$ from OA1 at the noninverting input. This voltage is less than the negative scan limit obtained from P3, and OA2 is forced to negative saturation. Hence, diodes D3 and D4 are nonconducting so that OA2 influences neither the integrator input voltage nor the voltage present at the noninverting input of OA1. Furthermore, the voltage at the noninverting input of OA1 is equal to the integrator output voltage, e_o. When the integrator output voltage reaches the positive scan limit, set at P1, the output of OA1 switches to positive saturation, $+ E_{sat}$, and D1 and D2 become nonconducting. The signal now at the noninverting input of OA2 is e_o. Since e_o is greater than the negative scan limit at this time, OA2 switches to positive saturation. Diodes D3 and D4 are now conducting, so that the integrator output changes to a negative scan. OA1 has a voltage of $+ E_{sat}$ at the noninverting input and is thereby forced to positive saturation. As a result, D1 and D2 are nonconducting so the output of OA1 is isolated both from OA2 and

from the integrator input. This state continues until the integrator output reaches the negative scan limit. At this instant OA2 switches to negative saturation, D3 and D4 become nonconducting, and OA1 again "sees" the integrator output voltage, e_o, at the noninverting input. OA1 then switches to negative saturation, D1 and D2 conduct, and the integrator output changes to a positive scan. This completes one cycle of the triangular waveform. This process will repeat itself indefinitely unless interrupted by the manual activation of switches S1, S2, or S3.

S2 and S1 are the Scan Positive and Scan Negative switches. These are normally-open pushbutton units which when pressed introduce a pulse to the noninverting input of the comparator amplifier controlling the scan. This pulse is of appropriate polarity and sufficient amplitude to cause the comparator output to switch state. The opposite comparator then takes over as described above and disables the first comparator; this results in a reversal of the scan direction. If the Scan Positive switch (S2) is pressed during a positive scan, OA2 is already in a disabled state, and the switch has no effect on the scan direction. The same holds for the Scan Negative switch (S1) during a negative scan.

S3 is the Stop at Limit switch. Operation of S3 is most easily explained by consideration of a latching comparator as shown in Figure IV-3 for comparator OA1. If the Latch switch is open, the circuit functions normally as described above. If the Latch switch is closed when e_o is less than E_{lim}, the comparator remains at negative saturation, and D5 is nonconducting. As soon as e_o exceeds E_{lim}, the comparator switches to positive saturation, and D5 conducts, placing a

Figure IV-3. Latching comparator

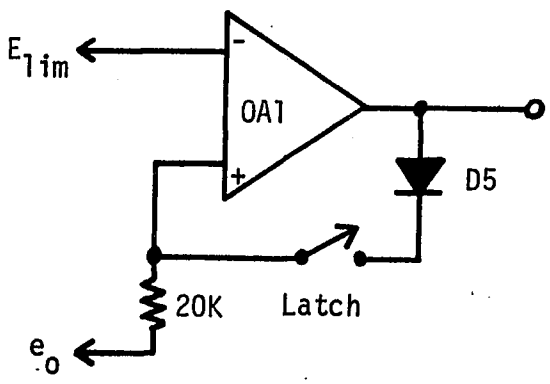
E_{lim}
OA1
D5
20K
Latch
e_o

voltage of + E_{sat} at the noninverting input. The comparator is now latched and will remain at positive saturation regardless of e_o until the Latch switch is opened. If the Latch switch is closed when e_o is greater than E_{lim}, the comparator latches immediately. In the sweep generator, OA1 is at positive saturation during the negative scan. If the Stop at Limit switch is put in the Negative position, at this time, OA1 becomes latched. Comparator OA2 controls the output scan until the negative scan limit is reached and then switches to negative saturation. Diodes D1, D2, D3 and D4 are now all nonconducting since OA1 is latched at positive saturation and cannot switch state at the negative scan limit, as normally occurs. The value of e_{in} to the integrator is thus zero, and the scan "holds" ($de_o/dt = 0$) at the negative scan limit. If the Stop at Limit switch is put in the Negative position during the positive scan, OA1 is at negative saturation and the comparator does not latch. When the positive scan limit is reached, OA1 switches to positive saturation and the comparator latches. The generator then scans to the negative scan limit and "holds" as described above. The operation of the Stop at Limit switch in the Positive position is entirely analogous to that described above except that all polarities are reversed and the latch is on OA2. It should be noted that the Stop at Limit switch can be put in either of the limit positions during either scan direction without affecting the scan until the corresponding limit is reached. This is a major advantage of this circuit.

When the Stop at Limit switch is returned to the Auto position after the generator has stopped at the corresponding limit, the latched

comparator switches state and takes control of the scan; normal operation resumes. If the Stop at Limit switch is momentarily switched from either limit position to Auto and then returned to its original position, one complete scan from that limit to the opposite limit and back will be produced. A half scan can be produced by switching from one limit to the opposite limit.

Manual interruption of the scanning operation can be made at any time by switching S4 from the Scan position to the Hold position. When S4 is switched to the Zero position, e_o goes to zero volts. Returning S4 to the Scan position from either the Hold or Zero positions allows the resumption of the scanning operation.

The operational amplifiers used for the comparators must be capable of withstanding a differential input voltage of $\pm$ 15 V. The feedback capacitor, C_f, is a Mylar unit or comparable type having low leakage. Capacitors of smaller value may be wired in parallel if necessary to obtain the given value of C_f. Electrolytic capacitors are not suitable for this application. The diodes used in the switching network should have high reverse resistance to assure correct operation of the switching and latching functions. The 4 bridge diodes in the voltage regulator (VR) network should be matched for forward voltage drop. High switching speed in the comparator amplifiers and for the switching network is not necessary for the scan rates less than 40 V min^{-1} which were required for this research. The 2 20 KΩ and 2 5.1 KΩ resistors shown are 5% composition units, and the 2 KΩ and 100 KΩ resistors in the integrator circuit are 1% metal film units.

All electrochemical data cited in this dissertation, with the ex-

ception of the data for the differential pulse anodic stripping voltammetry (DPASV) of Hg, were obtained with the potentiostat and triangular waveform generator described in this chapter. A single power supply, model AD902 from Analog Devices, Inc., Norwood, MA, was used to power both circuits.

Original circuits for triangular waveform generators have been published in numerous articles during the last 15 years. The use of operational amplifiers in triangular waveform generators was pioneered by Buck and Eldridge (95). Sherwood (96) has reviewed the literature of triangular waveform generators through 1975. Most of the circuits are more complex than that presented in this work and employ digital logic in the switching functions. The circuit presented in this section has not appeared in the literature and is likely the simplest possible circuit which fulfills the design criteria set forth at the beginning of this section.

D. Lock-in Amplifier

1. Introduction

Portions of this research, to be presented in Chapters V and VI of this dissertation, deal with the application of hydrodynamic modulation (97) to voltammetry at rotating disc and vibrating electrodes. In hydrodynamic modulation, the mass transport rate to the surface of the working electrode is varied sinusoidally about an average value by appropriate alteration of the rotation speed or vibrational parameters. For electrochemical reactions whose rate is limited by the rate of

mass transport to the surface of the electrode, hydrodynamic modulation results in a corresponding AC component to the current at the working electrode. The amplitude of this AC component is proportional to the concentration of the electroactive species. Phase selective detection of this AC component is required to ascertain whether the electrochemical reaction taking place is an oxidation or a reduction. In addition, the circuitry which processes the AC component must reject hum and noise from the potentiostat, which is frequently larger in amplitude than the desired signal.

A block diagram of the lock-in amplifier (LIA) constructed for this purpose is presented in Figure IV-4. The LIA is designed to isolate the low-amplitude 10-Hz component present in the output of the potentiostat and to produce a DC output signal which is proportional to the amplitude of this AC component and is dependent on the phase of this AC component relative to the phase of a 10-Hz reference signal. The frequency of the hydrodynamic modulation, 10 Hz, was fixed by physical limitations of the rotator, model MSR, manufactured by Pine Instruments, Grove City, PA. This rotator was used with the rotating disc electrodes (RDEs) employed in this research. The LIA is divided into 4 sections, as indicated in Figure IV-4: the 10-Hz amplifier, the phase-selective detector, the phase shifter, and the reference generator. In Figure IV-4, a capacitor placed between 2 stages indicates that AC coupling is used at the corresponding point in the actual circuit. Offset potentiometers are not used in those stages which are AC coupled to succeeding stages (OA1, OA2, OA10), in the comparators (OA4, OA11), or in the first 2 stages following the 4-quadrant multiplier (OA5, OA6).

Figure IV-4. Block diagram of lock-in amplifier

Nomenclature of stages: OA1 – Voltage follower; OA2, OA3 – 10-Hz tuned amplifier; OA4 – Warning comparator; IC1 – 4-quadrant multiplier; OA5 – Level shifter; OA6, OA7 – 4-pole Butterworth LP filter; OA8 – Voltage follower for phase shifter; OA9 – Phase shifter; PLL – Phase-locked loop; OA10 – Voltage follower with variable gain; OA11 – Schmitt trigger with adjustable threshold.

Designations for the 4 subsections of the LIA and references to the corresponding figures for detailed schematic diagrams are given in the figure.

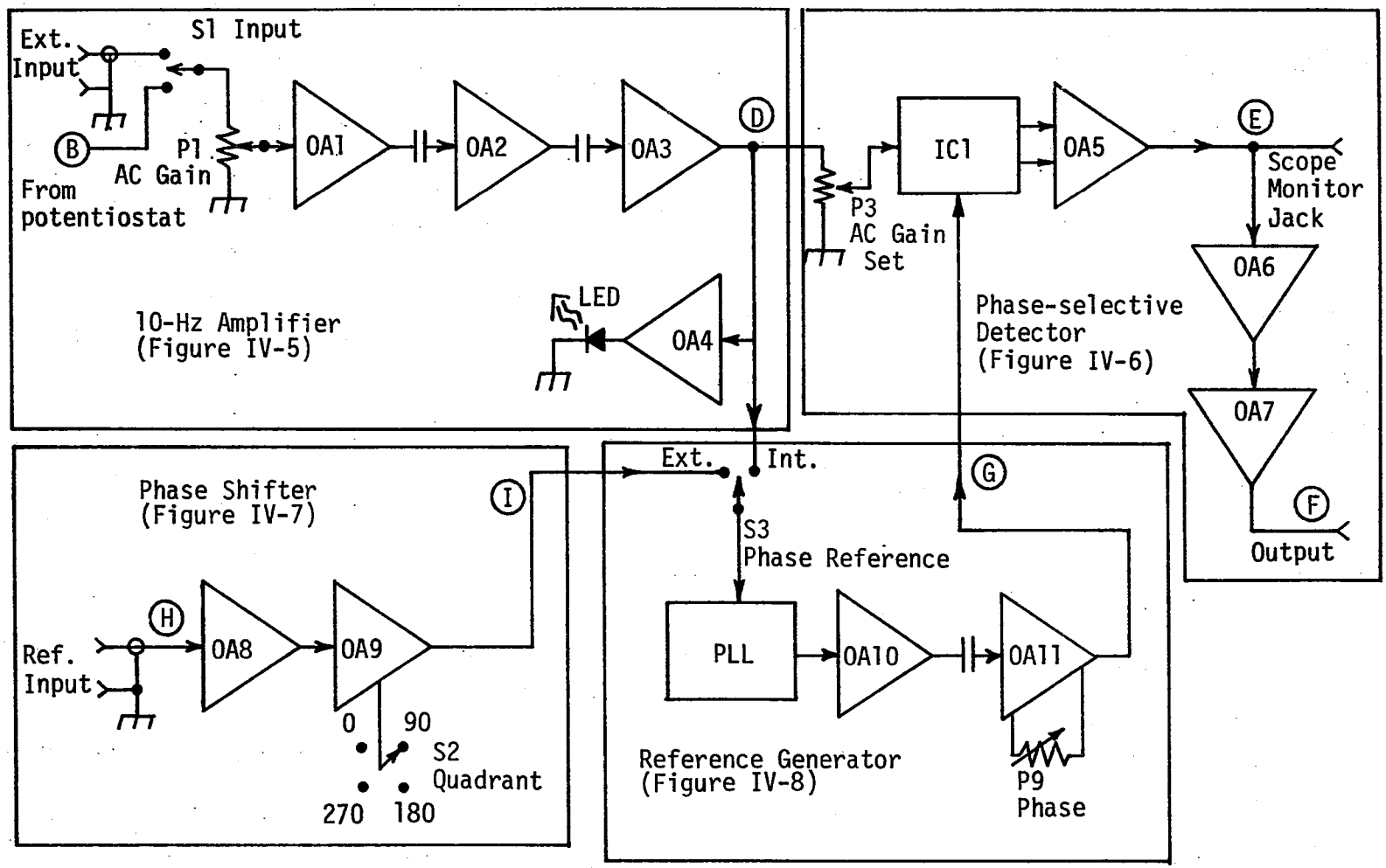
Ext.
Input
S1 Input
B
P1
AC Gain
From
potentiostat
OA1
OA2
OA3
D
10-Hz Amplifier
(Figure IV-5)
LED
OA4
IC1
OA5
E
Scope
Monitor
Jack
P3
AC Gain
Set
OA6
Phase-selective
Detector
(Figure IV-6)
OA7
F
Output
Phase Shifter
(Figure IV-7)
I
H
Ref.
Input
OA8
OA9
0
90
S2
Quadrant
270
180
Ext.
Int.
G
S3
Phase Reference
PLL
OA10
OA11
P9
Phase
Reference Generator
(Figure IV-8)

All external controls and switches are noted in Figure IV-4. The entire LIA is powered by an Analog Devices AD902 power supply (± 15 V at 100 mA); current drain is approximately 60 mA from each side of the supply. The LIA, with its power supply, and the triangular waveform and potentiostat, with their power supply, were both mounted in a 17 x 6 x 3-in. Al chassis, which was covered by an Al bottom plate. All circuitry was thus housed in a shielded enclosure. The 3 connections from the potentiostat to the cell and the 2 inputs to the LIA were made with 4 BNC-type coaxial connectors. The chassis was connected to the circuitry and to a water-pipe ground at the outside contact of the input jack for the reference electrode. The 2 outputs from the potentiostat and the LIA output were brought to a multi-pin connector, which permitted connection to the X-Y recorder with a single, 3-wire shielded cable.

2. 10-Hz amplifier

The schematic diagram of the 10-Hz amplifier is shown in Figure IV-5. The 10-Hz component of the input signal to the LIA is selectively amplified in this section. The circuit consists of a voltage follower, OA1, 2 stages of 10-Hz tuned amplification, OA2 and OA3, and a warning comparator, OA4. Switch S1 connects the input of the LIA to either the current output of the potentiostat or to the external input. The AC Gain potentiometer, P1, sets the overall gain of the 10-Hz amplifier; it thus determines the sensitivity of the LIA. The linear relationship desired between the setting of P1 and the gain of the 10-Hz amplifier is ensured by the high input impedance presented by OA1.

OA2 and OA3 are connected as multiple-feedback resonators. The

Figure IV-5. Schematic diagram of 10-Hz tuned amplifier

OA1 – LM741 operational amplifier; OA2, OA3 – LM747 dual operational amplifier; OA4 – 1 section of LM747 dual operational amplifier, OA10 is the other section; LED – Light emitting diode (red); P1 – 10-turn precision potentiometer with calibrated dial; P2 – 10-turn trimmer potentiometer; S1 – SPDT switch.

Variable resistors for RC networks: R1, R3 – 10K 1% resistor and 10K trimmer potentiometer in series; R2, R4 – 100K 1% resistor and 100K trimmer potentiometer in series.

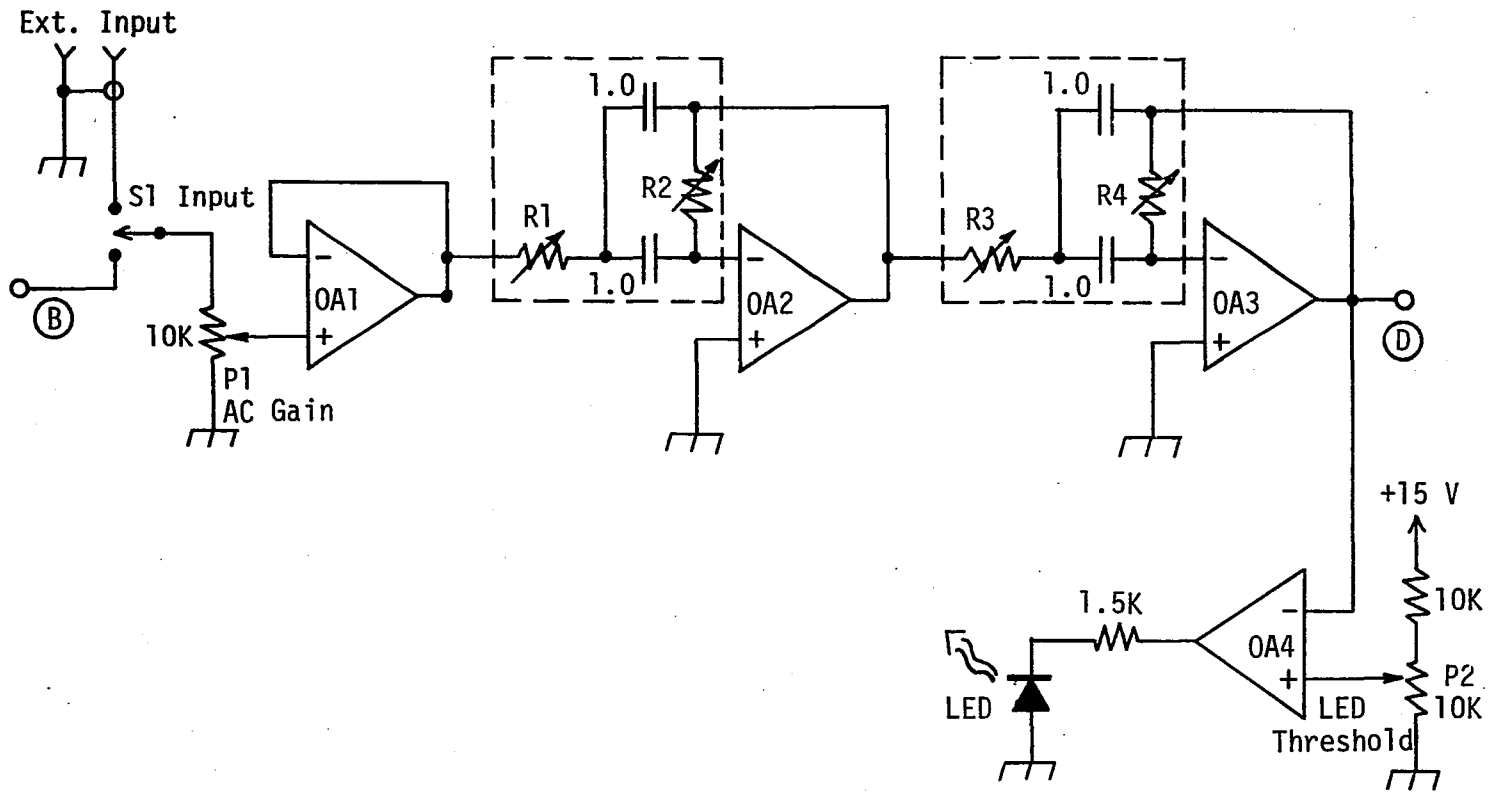
Ext. Input
S1 Input
B
10K
P1
AC Gain
OA1
1.0
R1
R2
1.0
OA2
1.0
R3
R4
1.0
OA3
D
+15 V
10K
1.5K
OA4
P2
10K
LED
LED
Threshold

design equations and principles of operation of this circuit are given by Williams (98). In the present application, the component values were chosen for a voltage gain (per stage) of 50, a resonant frequency, f_o, of 10 Hz, and a Q factor (resonant frequency divided by bandwidth at 3-dB points) of 5.0. For the 2-stage tuned amplifier used in the LIA, the overall voltage gain is thus 2500 (68 dB) and the overall Q is 9.8 (3-dB bandwidth 1.0 Hz). The RC networks for each stage, outlined by broken lines in Figure IV-5, are constructed as removable subassemblies, to facilitate changes in f_o. The alignment procedure for the 10-Hz tuned amplifier is based on the property that the multiple-feedback resonator displays a phase shift of 180 deg at the resonant frequency. To align the RC network, R2 and R4 are first set to the theoretical value for f_o = 10 Hz, 159 KΩ, prior to installation of the RC subassemblies into the circuit. The subassemblies are then connected to the circuit and the LIA is turned on. A 50-mV RMS, 10.00-Hz signal is connected to the external input of the LIA and to the horizontal input of the oscilloscope. The vertical input of the oscilloscope is connected to the output of OA2, and the AC Gain control is set to 10.0 turns. R1 is then adjusted to give a 1:1 Lissajous figure with a phase angle of 180 deg (line of slope - 1). The vertical input of the oscilloscope is then moved to the output of OA3, and the setting of the AC Gain control is changed to 0.2 turns. R3 is then adjusted to give a 1:1 Lissajous figure at a phase angle of 0 deg (line of slope + 1). The 10-Hz amplifier is now aligned.

The light emitting diode (LED), driven by comparator OA4, provides a visual indication of overload of the LIA. The LED illuminates when-

ever the output of OA3 exceeds 10 V_{pp}. To adjust the LED Threshold potentiometer, a 10.00-Hz signal is connected to the external output, and the AC Gain control is advanced until the output of OA3 is 10.0 V_{pp}, as measured with the oscilloscope. The LED Threshold potentiometer is then adjusted until the LED commences flashing at 10 Hz.

3. Phase-selective detector

The schematic diagram of the phase-selective detector is given in Figure IV-6. The circuits for the 4-quadrant multiplier and level shifter were taken from the Motorola data manual (99) and were modified for increased linearity as described in the manual. The offset potentiometers, P4, P5, and P6, were adjusted in accordance with the procedures given in the Motorola manual. The monitor jack, which is connected to the output of OA5, is used during alignment of the LIA and permits observation of the unfiltered output of the LIA on an oscilloscope. The waveforms present at the output of OA5 for in-phase and out-of-phase operation of the phase-selective detector are similar to those shown in Malmstadt, et al. (pp. 75, 124 of 100) and are used to verify correct functioning and alignment of the LIA.

The output signal from OA5 is applied to the input of a 4-pole Butterworth low-pass (LP) filter (101) constructed from OA6, OA7, and associated circuitry. The values for the resistors are obtained from Hilburn and Johnson (p. 37 of 101), based on a chosen cutoff frequency of 2.0 Hz, capacitor value of 1.0 μF, DC gain of 4.0, and K-value (constant in the transfer function) of 50. The cutoff frequency of 2.0 Hz is chosen to maximize the response time of the LIA to the

Figure IV-6. Schematic diagram of phase-selective detector

IC1 – Motorola MC1595 4-quadrant multiplier; OA5, OA6, OA7 – LM741 operational amplifier; P3, P4, P5, P6 – 10-turn trimmer potentiometers.

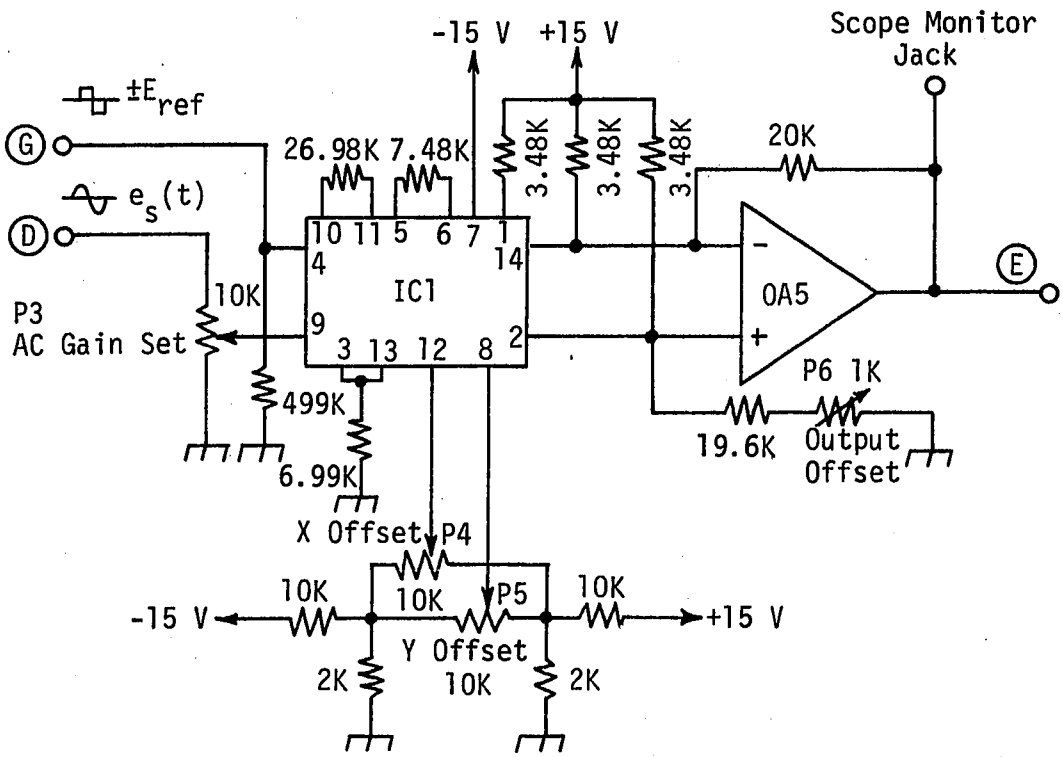
-15 V
+15 V
Scope Monitor Jack
±E ref
e s (t)
G
D
26.98K
7.48K
3.48K
3.48K
3.48K
20K
10 11 5 6 7 1
4
14
IC1
9
3 13 12 8 2
10K
P3
AC Gain Set
499K
6.99K
OA5
E
P6 1K
19.6K
Output Offset
X Offset P4
10K
10K
P5
10K
-15 V
+15 V
Y Offset
10K
2K
2K

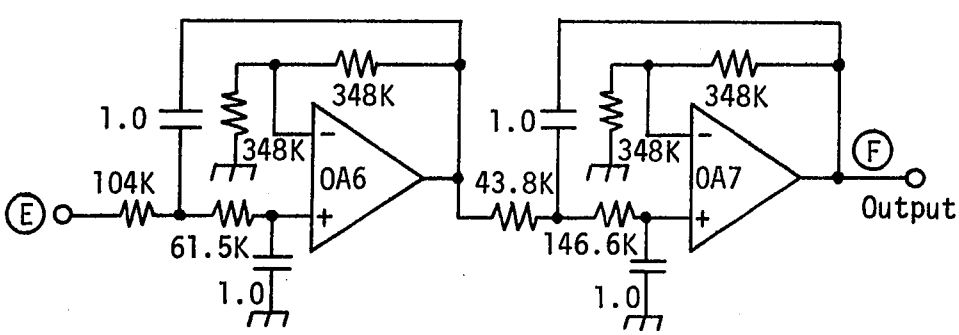
1.0
348K
348K
104K
OA6
E
61.5K
1.0
1.0
348K
348K
43.8K
OA7
F
Output
146.6K
1.0

greatest extent possible, consistent with adequate filtering of the 10- and 20-Hz ripple present at the output of OA5. With the circuit as shown in Figure IV-6, a maximum ripple voltage of 3 mV_{pp} is observed for 10.00 V DC output from the LP filter. The response time observed for 99% response to a 4-mV_{pp} signal at the input to the LIA was 1.2 sec. This response was determined principally by the step response of the 10-Hz tuned amplifier.

The AC Gain Set potentiometer, P3, is used to set the overall maximum gain of the phase selective detector. It is set so that a 10.00-V_{pp} signal at the output of OA3 results in a 10.00 V DC signal at the output of OA7.

4. Phase shifter

The schematic diagram of the phase shifter is illustrated in Figure IV-7. This circuit products a sinusoidal output signal, which is shifted 0, 90, 180, or 270 deg in phase from that of the input signal. An external 10-Hz oscillator, which also generates the 10-Hz sine wave used for producing the hydrodynamic modulation, produces the sinusoidal signal which is applied to the input of OA8, a voltage follower. The output of OA8 is connected to the phase shifter, a hybrid circuit. The operation of this circuit depends on the position of S2, the Quadrant switch. With S2 in the 0 deg position, OA9 operates as a voltage follower, and its output is in phase with the input signal. When S2 is in the 180 deg position, OA9 is connected as an inverting amplifier, and its output is consequently 180 deg out of phase from the input. When S2 is in the 90 deg position, OA9 is connected as a

Figure IV-7. Schematic diagram of phase shifter

OA8, OA9 — LM747 dual operational amplifier; S2 — 2-pole, 5-position rotary switch.

Variable resistor for R5: 10K 1% resistor in series with 10K trimmer potentiometer.

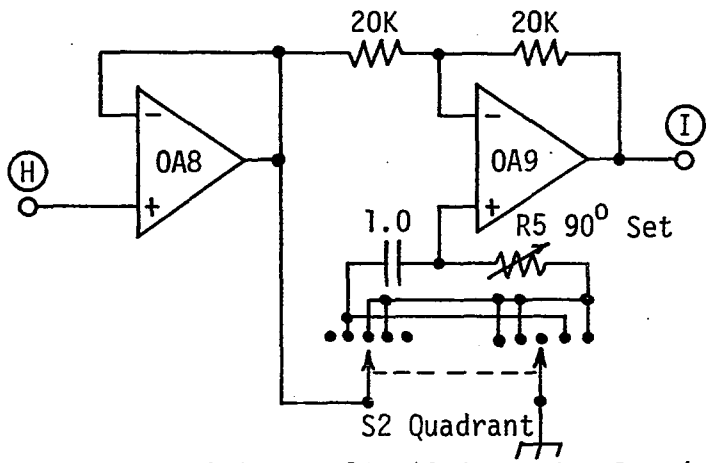
20K
20K
H
OA8
OA9
I
1.0
R5 90° Set
S2 Quadrant
Positions: 180 270 0 90 180 (deg)

constant amplitude phase shifter, based on the circuit from Deboo and Burrous (88). If the resistance of R5 is equal to the magnitude of the reactance of the 1.0-μF capacitor, 15.9 KΩ at 10 Hz, the output of OA9 lags 90 deg in phase behind that of the input. When the positions of the resistor and capacitor in this circuit are interchanged, as effected by moving S2 to the 270 deg position, the output of OA9 lags the input by 270 deg. Thus, by moving S2 over its 4 positions, the 10-Hz output signal may be shifted over the 4 quadrants of the complex plane, without affecting its amplitude.

To align the phase shifter, a sinusoidal input signal (10.00 Hz, 10 V_{pp}) is applied to the input of OA8. With S2 in the 90 deg position, R5 is adjusted until the phase shift observed at the output of OA9 is exactly 90 deg.

5. Reference generator

The schematic diagram of the reference generator is shown in Figure IV-8. The function of this section is to produce the 10-Hz square wave which serves as the reference signal for the phase-selective detector. The reference generator consists of a phase-locked loop (PLL), a voltage follower with variable gain, OA10, and a Schmitt trigger with adjustable threshold, OA11.

The circuit for the phase-locked loop is adapted from representative circuits published by National Semiconductor (102). In the present application, the PLL is used to generate a 10-Hz triangular wave which is locked in frequency and phase to that of the input signal to the PLL. The PLL is able to lock onto a 10-Hz signal of low amplitude in the

Figure IV-8. Schematic diagram of reference generator

PLL – National semiconductor LM565 phase-locked loop; OA10 – one section of LM747 dual operational amplifier; OA4 is the other section; OA11 – LM301 operational amplifier; D1, D2 – 1N957B Zener diodes (6.8 V, 5%); VR – Voltage regulator; 4 1N914 diodes and 1N747 Zener diode; P7, P8, R8 – 10-turn trimmer potentiometers; P9 – 10-turn precision potentiometer with calibrated dial; S3a, S3b – DPDT switch.

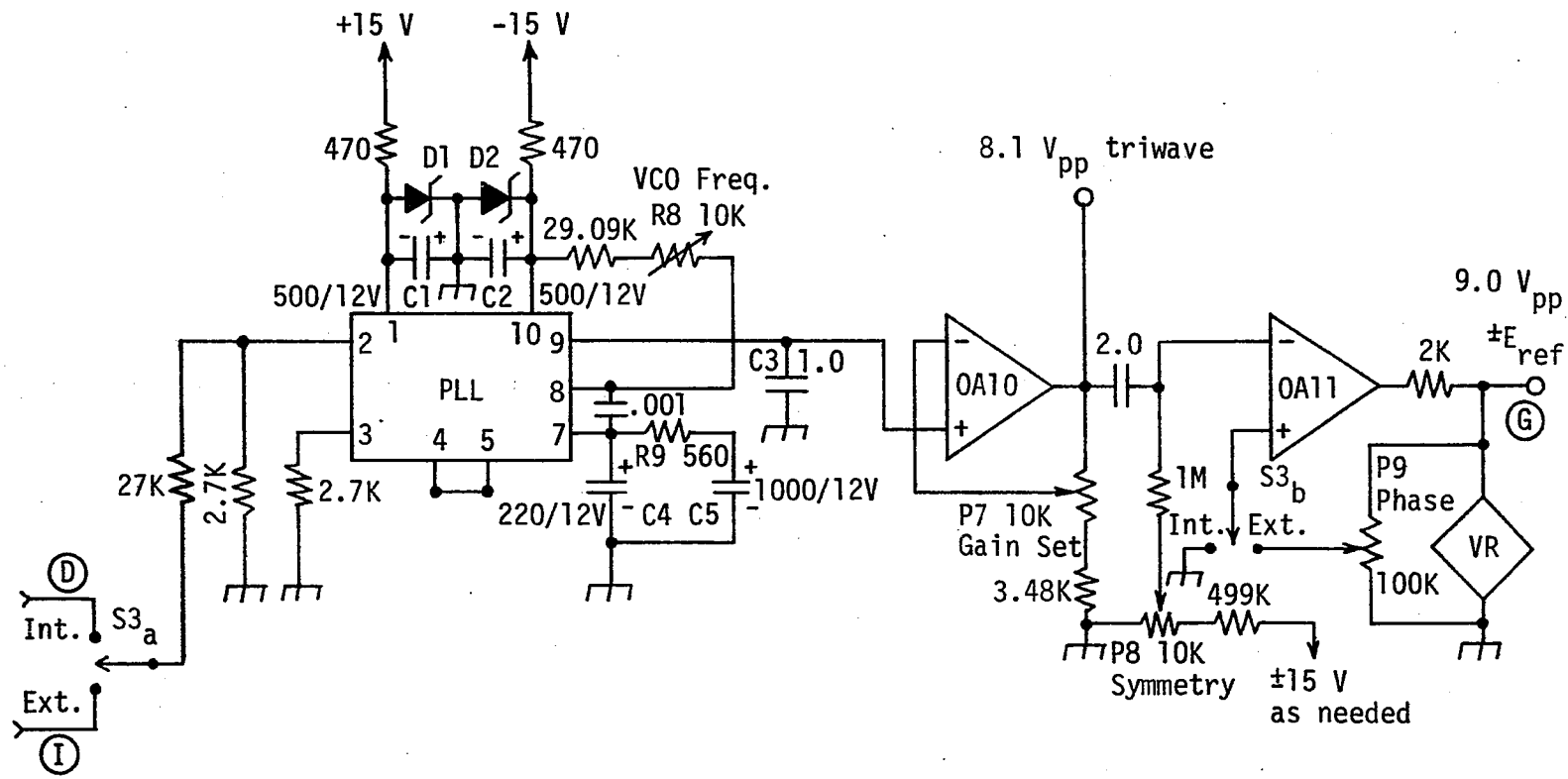
+15 V
-15 V
470
D1 D2
470
VCO Freq.
R8 10K
29.09K
500/12V
C1
C2
500/12V
2 1
10 9
PLL
8
3
4 5
7
.001
R9 560
C3 1.0
27K
2.7K
2.7K
220/12V
C4 C5
1000/12V
8.1 Vpp triwave
OA10
2.0
OA11
2K
±Eref
9.0 Vpp
P7 10K
Gain Set
1M
S3b
Int.
Ext.
P9
Phase
VR
100K
3.48K
499K
P8 10K
Symmetry
±15 V
as needed
D
Int.
S3a
Ext.
I
G

presence of an unwanted signal of a different frequency (e.g., 60 Hz) and much higher amplitude. This feature is important in cases where the PLL is used to generate an internal reference signal from an input signal having a poor signal-to-noise ratio.

The LM565 chip is powered from a $\pm$ 6.8-V regulated supply constructed from C1, C2, D1, D2, R6, and R7. The free-running frequency of the voltage-controlled oscillator (VCO) in the PLL is set by R8 and C3. C4, C5, and R9 comprise the loop filter for the PLL, which is designed according to the formulas and procedure published by the manufacturer (103). The loop filter is designed for a natural loop frequency of 0.382 Hz, a damping factor of 0.722, and a loop bandwidth of 0.204 Hz. These values are chosen to provide minimum lock-in time for the PLL to applied signals consistent with sufficient filtering of the error signal. The reader is referred to the literature for further discussion of loop filters for PLLs (102).

The free-running frequency of the VCO is set to 10.00 Hz in the absence of an input signal to the LIA. This ensures that the VCO is running at its natural frequency. R8 is adjusted until the triangular wave observed at the output of OA10 has a frequency of 10.00 Hz.

All resistors in the PLL circuit are 5% fixed composition units, with the exception of R10, which is a 1% metal film resistor. C1, C2, C4, and C5 are Al electrolytic capacitors.

The voltage follower, OA10, amplifies the triangular wave generated by the PLL and provides the high input impedance necessary to ensure linearity of the waveform. The gain of this stage is governed by the setting of the Gain Set potentiometer, P7. The triangular wave has an

amplitude of 2.2 V_{pp} at pin 9 of the LM565 and 8.1 V_{pp} at the output of OA10. OA10 is AC coupled to OA11, the Schmitt trigger with adjustable threshold. The triangular wave present at the output of OA10 is exactly in phase with the input signal to the PLL.

OA11 produces the 10-Hz square wave which is applied to the phase-selective detector as the reference signal. The voltage regulator (VR) at the output of OA11 clamps the positive and negative portions of the square wave at equal and opposite potentials, $\pm E_{ref}$. With S3b in the Int. position, OA11 functions as a normal comparator, and the square wave generated is 180 deg out of phase from the input signal to the PLL. Since S3a and S3b are linked, the input signal to the PLL is obtained from the output of OA3, the second 10-Hz tuned amplifier. The PLL thus tracks the phase of the input signal to the LIA, and the phase-selective detector functions as a full-wave rectifier. In the phase-selective detector, OA5 is connected to the 4-quadrant multiplier such that a maximum positive output is obtained when the signal and reference waveforms are 180 deg out of phase. The output from OA7 thus is proportional to the absolute peak-to-peak magnitude of the input signal to the LIA. The Symmetry control, P8, is set such that the positive and negative portions of the square wave observed at point G are of equal duration.

With S3b in the Ext. position, OA11 functions as a Schmitt trigger. The switching threshold of this Schmitt trigger, $\pm E_{sw}$, is directly proportional to the setting of the Phase potentiometer, P9. The input signal to the Schmitt trigger is a triangular wave with no DC component. By definition, the triangular waveform possesses alternately positive-

going and negative-going linear segments of equal and opposite slope. During the negative-going segment of the triangular wave, the Schmitt trigger switches state at that point where the potential of the triangular wave becomes lower than - E_{sw}. Analogously, the Schmitt trigger switches state during the positive-going segment of the triangular wave at that point where the potential of the triangular wave exceeds + E_{sw}. The triangular wave applied to the input of the Schmitt trigger, e(t), changes from e(t) = 0 to its peak values, e(t) = $\pm$ E_{peak}, over a period of 1/4 cycle. Increasing the switching threshold of the Schmitt trigger from E_{sw} = 0 to E_{sw} = $\pm$ E_{peak} therefore moves the points on the triangular waveform at which the Schmitt trigger changes state from the zero crossing points to the positive and negative peaks of the triangular wave, an effective increase in phase shift from 180 deg to 270 deg. Intermediate values of E_{sw} result in proportionately lower phase shifts. For values of E_{sw} greater than $\pm$ E_{peak}, the Schmitt trigger ceases to function, since the triangular wave fails to reach the switching threshold.

Use of a 10-turn potentiometer with dial for the Phase control permits direct display of the phase shift introduced by the Schmitt trigger. To align the circuit, the Phase control is set to 9.00 turns and P7, the Gain Set potentiometer, is advanced until OA11 fails to trigger. P7 is then turned back until OA11 just starts to produce a stable square wave. When multiplied by 10, the reading of the dial of the Phase control represents the phase shift introduced by the Schmitt trigger.

For use in other quadrants, the phase shifts introduced by the

phase shifter (indicated by the setting of the Quadrant switch) and the phase shift introduced by the Schmitt trigger (read on the Phase control) are summed.

6. Evaluation and testing

Tables IV-1 through IV-3 present the results of experiments designed to verify the performance of the lock-in amplifier described in this chapter. Table IV-1 shows the linearity of the response of the LIA to 10-Hz input signals with the Quadrant switch in the 0, 180, and 270 deg positions. Signals in quadrature to the reference phase are rejected by a ratio of 167 to 1, or 44 dB. The linearity of the AC Gain control, P1, is displayed in Table IV-2. The output of the LIA, with the reference and signal waveforms in phase, is presented as a function of the setting of P1 over its range. Linearity to within 2 parts per thousand was observed in both experiments.

The output voltage from a lock-in amplifier as a function of the phase difference between the signal and reference waveforms is readily predicted from theoretical considerations. Maximum output is obtained from a phase-selective detector when the signal and reference waveforms are in phase. The unfiltered output of the phase-selective detector operated under such conditions, using a sinusoidal signal of amplitude E_s and a reference square wave of amplitude E_{ref}, is identical to that of a full-wave rectifier. The average DC value, $e_{o,max}$, of this unfiltered signal is given by Equation IV-2.

$$e_{o,max} = kE_sE_{ref}(2/\pi) \qquad \text{(IV-2)}$$

Table IV-1. Linearity of LIA response to 10-Hz signals[a]

e_o from 10-Hz oscillator (V_{pp})	e_{in} to LIA[b] (mV_{pp})	e_o of LIA (V DC) at quadrant		
		0 deg	180 deg	270 deg
0.00	0.000	- 0.005	0.007	0.00
0.100	0.498	0.983	- 0.998	
0.200	0.995	1.98	- 2.00	
0.300	1.49	2.98	- 3.00	
0.400	1.99	3.98	- 4.00	
0.500	2.49	4.98	- 5.00	- 0.03
0.600	2.98	5.98	- 6.00	
0.700	3.48	6.98	- 7.00	
0.800	3.98	7.98	- 8.00	
0.900	4.48	8.98	- 9.00	
1.000	4.98	9.99	- 10.00	- 0.06

[a]AC Gain = 8.29 turns; Phase = 0 deg; Quadrant as noted.

[b]Input signal to LIA fed through a 2.00 MΩ resistor for attenuation. Values of e_{in} calculated on basis of 10.0 KΩ/2.00 MΩ voltage divider so formed.

Table IV-2. Linearity of AC Gain control on LIA[a]

AC Gain setting (turns)	e_o of LIA (V DC)
0.00	- 0.005
1.00	0.977
2.00	1.98
3.00	2.98
4.00	3.99
5.00	5.00
6.00	6.00
7.00	7.01
8.00	8.01
9.00	9.01
10.00	10.00

[a] e_{in} to LIA = 0.837 V_{pp} through 10.0 KΩ/2.00 MΩ voltage divider; Quadrant = 0 deg; Phase = 0° deg.

Table IV-3. Phase linearity of Schmitt trigger with adjustable threshold

ϕ_{disp} (deg) (from P9 setting)	Calculated values for ϕ (deg); Quadrant as noted			
	0 + ϕ	90 + ϕ	180 + ϕ	270 + ϕ
0.0	0.00	- 0.06	0.00	- 0.34
5.0	5.73	4.82	5.13	4.58
10.0	9.94	9.85	9.93	9.50
20.0	19.95	19.82	20.05	19.45
30.0	29.89	29.80	29.89	29.47
40.0	39.91	39.79	39.91	39.42
45.0	44.93	44.83	44.93	44.42
50.0	49.91	49.91	49.91	49.38
60.0	59.93	59.88	59.93	59.43
70.0	69.94	69.88	69.94	69.23
80.0	80.04	80.06	79.97	79.11
85.0	84.95	84.87	84.95	83.72
90.0	90.00	90.00	90.00	86.38

Equation IV-2 results from the same averaging procedure derived in Equations III-2 through III-4 in the preceding chapter. The factor kE_sE_{ref} in Equation IV-2 results from the multiplication which occurs in the 4-quadrant multiplier. The constant k is the scaling factor of the 4-quadrant multiplier.

The average value of the output from a phase-selective detector may also be calculated for cases where the signal and reference waveforms are not in phase. In such cases, it is advantageous to use the reference waveform as the frame of reference for the time variable, ωt. In cases where a phase lag is artificially imposed on the reference waveform, the sinusoidal signal may be considered to lead the reference waveform by a phase constant, ϕ. The signal waveform is thus expressed by Equation IV-3:

$$e_s(t) = E_s \sin(\omega t + \phi) \tag{IV-3}$$

For the period from $\omega t = 0$ to $\omega t = \pi$, the reference waveform, a square wave, has a value of E_{ref}. The average value of the output signal, $e_o(\phi)$, is obtained by multiplication of the signal and reference waveforms, as shown in Equation IV-4.

$$e_o(\phi) = (1/\pi)kE_sE_{ref} \int_0^{\pi} \sin(\omega t + \phi)\, d(\omega t) \tag{IV-4}$$

Evaluation of the integral in Equation IV-4 and simplification of the result using the trigonometric identity $\cos(\pi + \phi) = -\cos\phi$ yields the average value as a function of the phase shift, ϕ:

$$e_o(\phi) = (2/\pi)kE_sE_{ref}\cos\phi \tag{IV-5}$$

The value of $e_o(\phi)$ relative to the maximum value, $e_{o,max}$, is obtained by combination of Equations IV-2 and IV-5:

$$e_o(\phi)/e_{o,max} = \cos \phi \qquad \text{(IV-6)}$$

The calculated phase angle, which is tabulated in Table IV-3, is obtained by a simple transformation of Equation IV-6, as shown in Equation IV-7.

$$\phi = \cos^{-1}[e_o(\phi)/e_{o,max}] \qquad \text{(IV-7)}$$

This calculated phase angle, which represents the actual phase shift imparted to the reference waveform, may be compared to the displayed phase shift, ϕ_{disp}, indicated by the setting of P9.

Data obtained in this manner using the LIA are summarized in Table IV-3. The phase shifts observed were within 1 deg of those predicted from theory for the Schmitt trigger, with the exception of the final 2 values. It should be noted that the errors in these latter 2 data resulted from corresponding errors of only 2 parts per thousand in the actual output of the LIA. The calculated values for phase shifts greater than 180 deg were obtained by application of elementary trigonometric identities to Equation IV-7. Prior to recording the data from which the values of ϕ shown in Table IV-3 were calculated, the AC Gain control on the LIA was set such that $e_{o,max}$ was 10.00 V DC.

The application of the LIA to measurement of the phase of the signal waveform is discussed in Section F of Chapter V of this dissertation.

From the data presented in Tables IV-1 and IV-2, an expression for the sensitivity of the LIA was obtained. This expression was

multiplied by the current sensitivity of the potentiostat to obtain the overall sensitivity of the system comprising the LIA and potentiostat. The relationship among the experimental variables is summarized by Equation IV-8:

$$S = 10P/GT \qquad \text{(IV-8)}$$

In Equation IV-8, S represents the overall sensitivity of the system in $\mu A_{pp} V^{-1}$ and P represents the current sensitivity of the potentiostat in $\mu A\ V^{-1}$. T denotes the setting of the AC Gain control in turns, and G represents the internal voltage gain of the LIA. Prior to each experiment, G was experimentally verified by observing the DC output voltage, e_o, from the LIA for a known AC input voltage, e_{in}, expressed in V_{pp}. G was then readily calculated from Equation IV-9:

$$G = 10e_o/e_{in}T \qquad \text{(IV-9)}$$

7. Preparation for experiments

Prior to performing experimental work with the LIA, the external 10-Hz oscillator which generates the sinusoidal signal used for hydrodynamic modulation and as the reference phase must be centered in the passband of the 10-Hz tuned amplifier in the LIA. Either of 2 alignment procedures may be employed to effect this goal. In either procedure, the 10-Hz oscillator is first connected to the Ref. Phase and Ext. Input jacks on the LIA. Switch S1 is set to the Ext. Input position, switch S3 to the Int. position, and the output of the 10-Hz oscillator and/or the setting of the AC Gain control are adjusted to obtain a DC output voltage of 8 to 9 V. The frequency of the oscillator is then

adjusted according to either of the 2 procedures given below. Both alignment procedures yield equivalent results.

In the first alignment procedure, the vertical input of an oscilloscope is connected to the Scope Monitor Jack, and the horizontal input of the oscilloscope is connected to the output of the external 10-Hz oscillator. The pattern displayed on the oscilloscope will appear as a vee-shaped figure with loops for the 2 legs of the vee. The frequency of the external 10-Hz oscillator is then adjusted until each loop collapses, forming a straight line. The pattern displayed by the oscilloscope now appears as a perfect vee with straight, linear legs. This perfect vee indicates correct adjustment of the LIA and 10-Hz oscillator.

An alternate alignment procedure dispenses with the need for an oscilloscope. In this procedure, the Quadrant switch is set to 90 deg. With the Phase control set to 0.00 deg, switch S3 is moved to the Ext. position. The DC output of the LIA decreases from the original value of 8 to 9 V to a lower value, normally less than 1 V. The frequency of the 10-Hz oscillator is then adjusted until the DC output of the LIA is 0.00 V. This null condition indicates correct alignment of the LIA. For in-phase operation, the Quadrant switch is returned to the 0 deg position.

For operation of the LIA with the MSR rotator, the reference phase must be further adjusted to compensate for the phase shift introduced by the rotator. With the external 10-Hz oscillator connected to the MSR rotator as described in the following section, the signal input to the LIA is moved from the 10-Hz oscillator to the Output jack on the MSR rotator. The voltage at this jack is derived from the tachometer

output of the rotator and, consequently, is in phase with the actual variations in rotation speed of the electrode. With S3 on the LIA in the Int. position, the AC Gain control is adjusted to obtain a DC output voltage of 8 to 9 V for a 0.10 V_{pp} input signal to the MSR rotator. The Quadrant switch is moved to the 90 deg position, and S3 is moved to the Ext. position. Without changing the frequency of the 10-Hz oscillator, the Phase control is adjusted until the DC output of the LIA is 0.00 V. The phase shift displayed on the dial of the Phase control represents the phase lag introduced by the MSR rotator. Experimentally, this value is observed to be 25.6 to 26.2 deg at 10.0 Hz. For in-phase operation of the LIA, the Quadrant switch is returned to the 0 deg position.

The LIA may be modified to operate at frequencies other than 10 Hz. This is most readily effected by changing the values of the 1.0-μF capacitors in the 2 multiple-feedback resonators, the phase shifter, and the PLL circuit (C3). These modifications adjust the resonant frequency of the tuned amplifier, the free-running frequency of the VCO in the PLL, and the frequency for quadrature operation of the phase shifter. Since each of these frequencies is inversely proportional to the values of these capacitors, and each capacitor in the present circuit has a value of 1.0 μF, the capacitors all must be changed to a single new value, C_{new}, given by Equation IV-10, where f_{new} is the new frequency.

$$C_{new} = (10/f_{new})\mu F \qquad \text{(IV-10)}$$

The modified LIA retains the same gain and operational capabilities as the present unit, and the alignment procedures, except for the

substitution of f_{new} for 10 Hz, remain unchanged. The external oscillator must be modified to operate at f_{new} as well. The LIA, when modified in this manner, is well-suited to use in AC polarography and related applications in the 10-1000 Hz range. For operation at these higher frequencies, the cutoff frequency of the LP filter and the loop frequency of the PLL also may be proportionally increased, with corresponding decreases in the response time of the LIA.

E. 10-Hz Oscillator

The schematic diagram of the 10-Hz oscillator constructed for this work is shown in Figure IV-9. OA1 and associated components are connected as a Wien-bridge oscillator, with amplitude stabilization provided by Q1, an N-channel FET. The design is adapted from published circuits for similar Wien-bridge oscillators (104, 105). The output frequency of the Wien-bridge oscillator is given by Equation IV-11, where R_{osc} and C_{osc} are the resistances and capacitances noted in Figure IV-9.

$$f = 1/2\ R_{osc}C_{osc} \qquad \text{(IV-11)}$$

R1 and P1 control the feedback stabilization of the oscillator. In this circuit, R1 and P1 are adjusted until a stable, undistorted sine wave having an amplitude of 10.0 V_{pp} is observed at point H. The high input impedance presented by OA2, a voltage follower, ensures linearity of e_o, measured at point J, as a function of the setting of P2, the Output Level control. R2 is adjusted to give a 1.00-V_{pp} signal at the

Figure IV-9. Schematic diagram of 10-Hz oscillator

OA1, OA2 — LM741 operational amplifiers; D1 — 1N914 diode; Q1 — 2N3819 N-channel FET; P1, R1, R2 — 10-turn trimmer potentiometers; P2 — 10-turn precision potentiometer with calibrated dial; R3 — 2 sections of 100K dual linear taper potentiometer (Allen-Bradley part No. JD1N200P104UA); R4 — 2 sections of 1K dual linear taper potentiometer (Allen-Bradley part No. JD1N200P102UA).

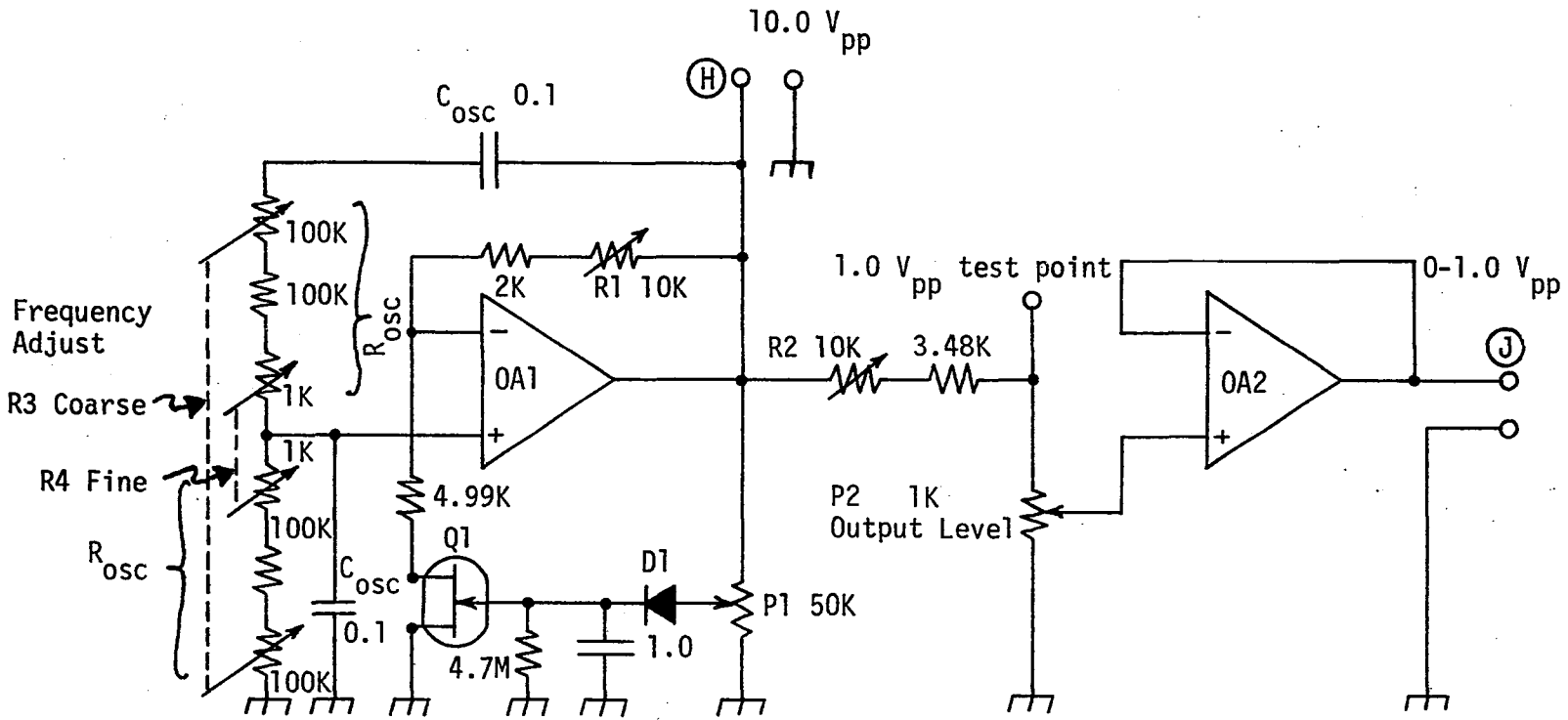
10.0 V_{pp}
H
C_{osc} 0.1
100K
100K
Frequency Adjust
R3 Coarse
1K
1K
R4 Fine
100K
R_{osc}
100K
C_{osc}
0.1
R_{osc}
2K
R1 10K
OA1
4.99K
Q1
4.7M
D1
1.0
P1 50K
1.0 V_{pp} test point
R2 10K
3.48K
P2 1K
Output Level
OA2
0-1.0 V_{pp}
J

ungrounded end of P2, as measured with an oscilloscope. P3 and P4, the Coarse and Fine frequency adjustments, are both dual, linear-taper potentiometers.

For use with the LIA, the 10-Hz oscillator produces both the 0-1.0 V_{pp} signal used to produce the hydrodynamic modulation of the vibrating or rotating electrode and the 10-V_{pp} signal used as the phase reference for the LIA. The 10-V_{pp} output of the oscillator, point H, is connected to the input of the phase shifter in the LIA. In experiments using hydrodynamic modulation at RDEs, the 0-1.0 V_{pp} output of the 10-Hz oscillator, point J, is connected to the Input jack of the MSR rotator.

F. AM/FM Generator

A schematic diagram of the AM/FM generator, which produces the waveforms used to drive the vibrating electrode, is shown in Figure IV-10. The designations used in this diagram and its description follow the established nomenclature (106) applied to radiotelephony employing amplitude modulation (AM) and frequency modulation (FM). The circuit consists of 4 sections: a sine-wave generator, IC1; a variable-gain voltage follower, OA3; a summing amplifier, OA4; and an amplitude modulator, based on a 4-quadrant multiplier, IC2. Offset potentiometers are not used with OA3 and OA4. The AM/FM generator and the 10-Hz oscillator were both mounted in an 8 x 6 x 5-in. steel box. Both circuits were powered by an Analog Devices model AD-904 power supply ($\pm$ 15 V at 50 mA).

Figure IV-10. Schematic diagram of AM/FM generator

IC1 — Intersil 8038 function generator chip; IC2 — Analog Devices ZM605 4-quadrant multiplier; OA3, OA4 — LM741 operational amplifier; P3, P12 — 10-turn precision potentiometers with calibrated dials; R5, R7 — 1-turn linear-taper potentiometers; P4, P5, P6, P7, P8, P9, P10, P11, R6 — 10-turn trimmer potentiometers; J1 — Miniature, closed-circuit phone jack.

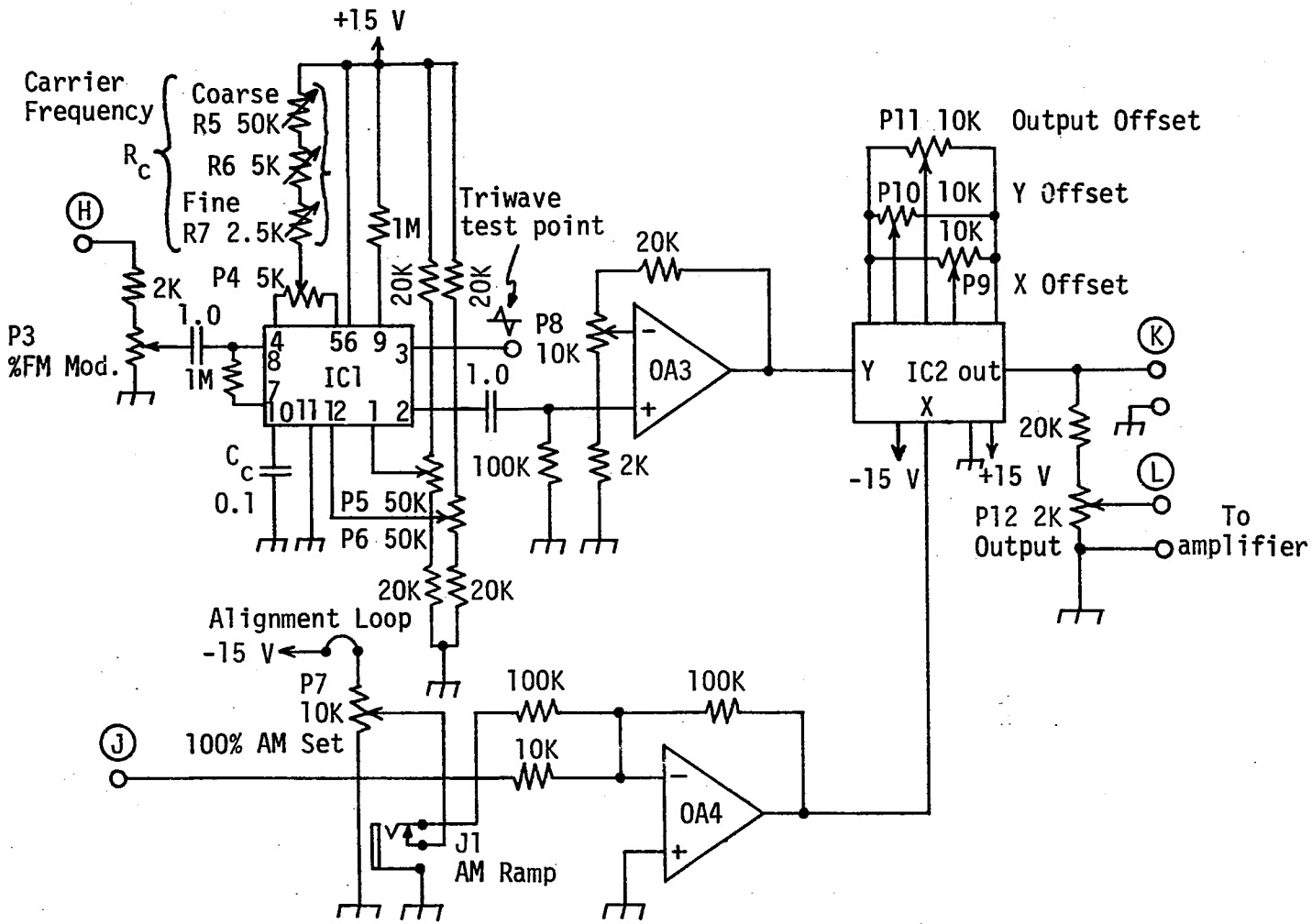
+15 V
Carrier Frequency
R_c
Coarse R5 50K
R6 5K
Fine R7 2.5K
H
2K
P4 5K
1.0
P3 %FM Mod.
1M
IC1
1M
20K
20K
Triwave test point
P8 10K
20K
OA3
1.0
100K
2K
C_c 0.1
P5 50K
P6 50K
20K
20K
Alignment Loop
-15 V
P7 10K
100% AM Set
J
100K
100K
10K
OA4
J1 AM Ramp
P11 10K Output Offset
P10 10K Y Offset
10K
P9 X Offset
Y IC2 out X
-15 V
+15 V
K
20K
L
P12 2K Output
To amplifier

The circuit for the sine-wave generator, which employs an Intersil 8038 integrated circuit, was adapted from representative circuits given in the data sheet for the integrated circuit (107). The data sheet was provided by Poly Paks, Inc., South Lynnfield, MA, the supplier for the 8038. The sine-wave generator consists of a triangular-wave VCO and a shaping network. The shaping network converts the triangular waveform into a close approximation of a sine wave. The frequency of oscillation, f_c, depends on the values of R_c and C_c, which are denoted in Figure IV-10. The relationship between R_c, C_c, and f_c is given by Equation IV-12:

$$f_c = 0.15/R_c C_c \qquad \text{(IV-12)}$$

Application of a 10-Hz signal to point H introduces an AC signal to the VCO via pin 8 of the 8038. The output of the sine-wave oscillator thus becomes an FM signal, modulated at 10 Hz, with a center frequency of f_c. The frequency deviation of the FM signal is proportional to the amplitude of the AC signal applied to pin 8 of the 8038, which is determined by the setting of P3. The maximum value of f_c is set to 510 Hz by adjustment of R6. R5 and R7 provide coarse and fine adjustment, respectively, of f_c. The minimum value of f_c is approximately 26 Hz, with component values as shown.

Adjustment of P4 varies the symmetry of the triangular and sinusoidal waveforms produced by the 8038. In this circuit, P4 is adjusted such that the triangular wave observed at pin 3 of the 8038 possesses positive- and negative-going portions of equal and opposite slope. This minimizes distortion of the sinusoidal waveform. P5 and P6 determine

the characteristics of the sinusoidal shaping network and are adjusted to minimize distortion of the sine wave observed at pin 2 of the 8038.

OA3 is a voltage follower which amplifies the sinusoidal output of IC1 to a level of 10 V_{pp}. The output of OA3 is the carrier signal which is applied to the 4-quadrant multiplier. OA4 is a summing amplifier which combines the 10-Hz and DC components required to produce an AM signal at the output of the 4-quadrant multiplier (p. 68 of 100). The modulation percentage of the AM signal is directly proportional to the amplitude of the 10-Hz signal applied to point J. P7 is adjusted such that a 1.0-V_{pp} signal at point J produces an AM signal with 100% modulation at the output of the 4-quadrant multiplier, point K. After P7 has been set, P8 is adjusted such that the output signal from the 4-quadrant multiplier has an amplitude of 10 V_{pp} in the absence of amplitude modulation.

The 4-quadrant multiplier, IC2, is connected according to the recommendations of the manufacturer, Zeltex, Inc., Concord, MA (108). The modulating signal, generated by the 10-Hz oscillator, is applied to the X axis of the 4-quadrant multiplier, and the carrier signal, generated by IC1, is applied to the Y axis. The product of these 2 signals appears as an AM signal at the output. P9, P10, and P11 are the X, Y, and Output offset potentiometers, respectively. To adjust P9, the noninverting input of OA3 is grounded and a 1.0-V_{pp}, 10-Hz signal is applied to point J. P9 is then adjusted until no 10-Hz component is observed at the output of IC2, point K. The connection grounding the noninverting input of OA3 is then removed, the aligmment loop connecting P7 to the - 15 V line is temporarily disconnected, and the 10-Hz signal

applied to OA4 is reduced to 0 V_{pp}. P10 is then adjusted until no AC component at the carrier frequency is noted at point K, and P11 is adjusted such that the DC level of the output of IC2 is 0.000 V. After P11 is adjusted, the alignment loop is reconnected. The adjustments described for P7 and P8 in the preceding paragraph are then repeated, completing the alignment of the AM/FM generator.

Table IV-4 summarizes the observed percentages of modulation for the output signal from the AM/FM generator as a function of the setting of the Output Level control, P2, in the 10-Hz oscillator. The percentages were calculated from measurements of the trapezoidal patterns formed by application of the 10-Hz modulating signal and the AM output signal to the horizontal and vertical inputs of an oscilloscope, respectively. Such trapezoidal patterns are routinely used for evaluation of the performance of AM transmitters, and their characteristics and interpretation are discussed in the literature (pp. 369, 375, 376 of 92). For the AM/FM generator, the percentage of modulation is directly proportional to the setting of P2 to within 0.6%, as is evident from inspection of Table IV-4. Errors in the measurement of the trapezoidal pattern displayed on the oscilloscope contributed significantly to the observed deviations from linearity.

Following suitable amplification, such AM signals may be applied to the speaker, which functions as the vibrator for the vibrating electrode. By means of this technique, hydrodynamic modulation results from the modulation of the vibrational amplitude. The technique is accordingly referred to as HMVE(AM) and is evaluated in Chapter VI of this dissertation.

Table IV-4. Observed percentages of modulation vs. setting of Output Level control (P2)

P2 setting (turns)	Percentage of modulation of AM output signal (%)[a]
0.00	0.0
1.00	10.0
2.00	20.3
3.00	30.4
4.00	40.6
5.00	50.4
6.00	60.5
7.00	70.4
8.00	80.2
9.00	89.9
10.0	100.0

[a] f_c = 240.0 Hz.

The AM and FM characteristics of the output signal from the AM/FM generator may be independently varied by adjustment of P2 and P3, respectively. The AM/FM generator is constructed such that the output signal resulting from simultaneous AM and FM is characterized by minimum instantaneous frequency at periods of minimum carrier amplitude (troughs of the modulation envelope) and by maximum instantaneous frequency at periods of maximum carrier amplitude (peaks of the modulation envelope).

Following amplification, this composite AM/FM signal is applied to the speaker. At the vibrating electrode, pure FM vibrations of constant amplitude are produced, and hydrodynamic modulation results in this case from the modulation of the vibrational frequency. The technique is consequently referred to as HMVE(FM). The AM component of the input signal to the speaker compensates for the frequency response of the vibrating electrode, which has been illustrated in Figure III-3. In order to achieve constant vibrational amplitude by AM compensation, the range of vibrational frequencies covered by the FM signal must be sufficiently small such that the corresponding portion of the graph shown in Figure III-3 is linear. To set the AM compensation to the correct value, the frequency deviation of the FM signal is set to the desired value, and the Output Level control, P2, is adjusted until the extremes of vibration cease to "tremble" at 10 Hz and become stationary.

The AM Ramp jack, J1, permits a DC ramp to be applied to the summing amplifier, OA4, in place of the DC component normally obtained from P7. Using the DC ramp, the carrier voltage at the output of the 4-quadrant multiplier, and consequently the vibrational amplitude, may be linearly increased from zero to a desired maximum value as a function

of time. Application of the DC ramp and the current output of the potentiostat to the X and Y axes, respectively, of an X-Y recorder permits recording of the limiting current at a vibrating electrode as a function of the vibrational amplitude or vibrational Reynolds number. This procedure may be applied in the presence or absence of an AM component to the vibration.

The level of output signal applied to the audio amplifier, which is connected to point L, is determined by the setting of potentiometer P12.

G. Audio Amplifier

The amplifier employed in this work was a model 215 stereo amplifier which was purchased in kit form from Southwest Technical Products Corp., San Antonio, TX. Only 1 of the 2 channels was used in this work. For the determinations of Hg described in Section IX, a model 540 stereo amplifier from the same manufacturer was used. The 540 amplifier was modified to permit simultaneous and independent operation of 2 vibrating electrodes and was driven by a VIZ model WA-504B signal generator, which served as the sine-wave oscillator. The signal generator was purchased from Fordham Radio, Farmingdale, NY.

The maximum power output required for the operation of the vibrating electrodes described in this work was 1.5 W RMS, and the choice of audio amplifier was therefore not critical.

V. HYDRODYNAMIC BEHAVIOR

As has been mentioned in Chapter I of this dissertation, the increased sensitivity of vibrating electrodes in electroanalysis results from the decrease in the thickness of the diffusion layer produced by the motion of the solution past the surface of the electrode. This motion arises from the hydrodynamic flow patterns which are established in the vicinity of the electrode as a result of its vibration. An understanding of the hydrodynamic behavior of vibrating electrodes is, therefore, of fundamental importance to the application of vibrating electrodes to quantitative, trace-level analyses. This chapter presents the results of experiments which were undertaken in an attempt to provide insight into the hydrodynamic behavior of vibrating electrodes and into the nature of the flow patterns induced by the vibration of the electrode.

A. Literature

The circulation of air prevailing in the vicinity of vibrating reeds and cylinders has been studied by West (109), who observed 3 separate regimes of circulation. According to West, the first flow regime occurs at low vibrational velocities and is analogous to the flow which takes place "when a lamina moves forward in a perfect fluid." It is characterized by 2 elliptical sets of streamlines which are centered laterally opposite the plane of vibration. At somewhat higher Re_v values, not specified in the article, a gradual transition to the second flow regime takes place.

The second regime occurs at Re_v values up to approximately 40 and is characterized by circulation in the form of a 4-leaved rose about the vibrating reed or cylinder, with the 4 lobes centered at angles, θ_ℓ, of 45, 135, 225, and 315 degrees from the direction of vibration. West accordingly models the circulation in polar coordinates by Equation V-1.

$$\psi = (a_w/r^2)\sin 2\theta_\ell \qquad \text{(V-1)}$$

In Equation V-1, ψ is the flow function, a_w is a constant which is proportional to the amplitude of vibration, and r is the distance on the polar plot from the center of the electrode at the center of vibration. Photographs of the experimentally observed flow patterns of smoke particles entrained in air circulating about vibrating reeds and cylinders supported this model.

The third regime of circulation is similar to the second except that each of the 4 lobes described above shrinks to the immediate vicinity of the reed, and each lobe is bounded by a second, similar lobe at the same angle from the direction of vibration. Each of these 4 outer lobes is much larger than the inner lobes and circulates in a direction opposite to that of the corresponding inner lobe. The intensity of circulation is far greater than that observed in the inner lobes. The appearance of these outer lobes marks the onset of the third flow regime and is described by West as "catastrophic." The onset of this third regime occurs at Re_v values from 40 to 45.

Radoi has compared the hydrodynamic behavior of vibrating cylinders to that of stationary cylinders subjected to linear flow perpendicular

to the axis of the cylinder (33, 75, 110, 111). The Reynolds number, Re, used to characterize such flow, is identical to Re_v except that the velocity of the linear flow is substituted for the average vibrational velocity, v_{avg}. According to Radoi (75, 112) and Eck (113), the flow about the cylinder at Re values from 1 to 32 is characterized by the existence of 2 Föppl vortices which are held captive behind the cylinder. At Re = 10, these Föppl vortices "cover the entire rear surface of the cylinder." The 2 vortices remain fixed behind the cylinder at increasing Re values up to 32, at which point they begin to be alternately torn away from the rear surface of the cylinder, forming "turbulence elements" in the backwash of the cylinder. These turbulence elements first appear at Re = 32 and become stable, taking on a turbulent character, at Re = 50. For Re values greater than 60, a strongly periodic, alternating character to these turbulence elements is noted, forming a Kármán vortex street in the backwash of the cylinder.

Radoi (112) also studied the angular dependence of the mass transport to a rectangular microelectrode situated flush with the surface of a nonconducting cylinder. The cylinder was placed in a flowing stream of electrolyte, and the placement of the microelectrode relative to the direction of flow could be varied from 0 to 180 deg in a clockwise or counterclockwise direction by rotation of the cylinder. The observed relationship between the limiting current density and the angular placement of the electrode was presented in polar coordinates, and the resulting graphs were butterfly-shaped, with an axis of symmetry passing through the center of the cylinder in the direction of flow. At Re = 110, the maximum limiting current density was observed

at angles of 40 to 70 deg from the direction of flow, and a minimum value was observed at 105 to 115 deg. A secondary maximum was observed at 130 to 150 deg. At Re = 400, the 3 regions occurred at 40 to 70, 95 to 115, and 115 to 125 deg, respectively.

Homann (114) has also studied the hydrodynamic flow patterns prevailing at cylinders in flowing streams. According to his photographs and description, the formation of Föppl vortices is not visible at Re values less than 6. The captive pair of Föppl vortices remains fixed at the rear of the cylinder at Re values from 6 to 25 or 30. At slightly higher Re values, the relative size of each vortex begins to oscillate. Each vortex alternately grows in size at the expense of the other. The backwash of the cylinder oscillates at the corresponding frequency. At Re values greater than 37, the vortices are alternately shed from the cylinder, forming the Kármán vortex street.

Blevins (115) also describes the behavior of cylinders in flowing streams. For Re values less than 300, Blevins distinguishes 6 regimes of flow. Unseparated, fully laminar flow occurs at Re values less than 5. A pair of fixed Föppl vortices at the rear of the cylinder is characteristic of the region commencing at Re = 5 to 15 and extending to Re = 40. Within this region, the 2 vortices elongate with increasing Re values. At about Re = 40, the longer of the 2 vortices breaks away, commencing the alternate shedding of vortices described above. This process continues at a periodic rate, forming the Kármán vortex street. The periodic alternate shedding of laminar vortices is characteristic of 2 regimes of flow, which extend from Re = 40 to 90 and from Re = 90 to 150, respectively. The transition to turbulence in the

vortex street occurs in the region form Re = 150 to 300. Above Re = 300, the vortex street is fully turbulent. Blevins notes that the transition to turbulence in the boundary layer of the cylinder occurs at Re values on the order of 3×10^5.

Studies of the dependence of the heat transfer from rods and cylinders in flowing gaseous and liquid streams were performed by Ulsamer (116) and Hilpert (117). In the results of these studies, the Nusselt number was expressed as an exponential function of Re, according to Equation V-2:

$$Nu = kRe^z \qquad (V-2)$$

The Nusselt number, Nu, is related to the heat transfer in the same manner as the Sherwood number, Sh, is related to the mass transfer (117). Hence, the results of these experiments indicate the expected exponential dependence of the mass transport to a cylindrical electrode on the Reynolds number. Table V-1 summarizes the results of the experiments of Ulsamer and Hilpert.

Evidence for the existence of transitions in the hydrodynamic flow patterns produced by vibrating electrodes has been cited in Chapter II of this dissertation (5, 29, 34, 36, 43, 45).

B. Enhancement of Mass Transport

A measure of the enhancement of the mass transport effected by vibration of an electrode may be gathered by comparison of the experimentally observed limiting current for the reaction of a given

Table V-1. Exponential dependence of Nusselt number on Reynolds number

Re range	z in Equation V-2	Fluid	Ref.
0.1-4	0.305	Air	116
4-50	0.41	Air	116
50-1000	0.50	Air	116
0.1-50	0.385	Liquid	116
50-10000	0.50	Liquid	116
1-4	0.330	Air	117
4-40	0.385	Air	117
40-4000	0.466	Air	117

electroactive species at a vibrating electrode to the corresponding limiting current which is predicted by the Levich equation, Equation I-8, for an RDE of the same surface area. To perform this comparison, it is most instructive to calculate an "apparent rotation speed," ω_{app}, for the vibrating electrode. The value of ω_{app} is calculated from the experimental values of I_l and A for the vibrating electrode. These experimental values and the values of n, D, and C^b for the electroactive species, as well as the value of ν for the solution, are substituted into Equation I-8, which is then solved for ω_r. The value of ω_r so calculated is designated ω_{app} and represents the speed at which an RDE of the same area as the vibrating electrode would have to rotate in order to achieve the same value of I_l with the same solution used with the vibrating electrode.

An experiment employing 1.018 mM I^- in 0.5 M H_2SO_4 was performed in this manner with Electrode A. The solution was deaerated with N_2 to minimize oxidation of the I^- by atmospheric oxygen. The potential of the electrode was maintained at 0.0 V vs. SCE except during the brief measurements of I_l, which were conducted at + 0.800 V vs. SCE for each frequency of vibration. This procedure minimized the oxidation of I^- by the electrode, which otherwise would have seriously affected the results through deletion of the I^- in the bulk of the solution. The surface area of the vibrating electrode was calculated from Equation V-2.

$$A = \pi d_e L_{S-T} + \pi d_e^2/4 \qquad \text{(V-2)}$$

This area, A, represents the geometric surface area of the working

electrode. The value of D for I^-, 1.56×10^{-5} $cm^2 sec^{-1}$, was determined experimentally with an RDE (118), and the value for ν used was that noted previously, 0.01063 $cm^2 sec^{-1}$. The maximum stable value of I_1 for Electrode B was obtained at f = 240.0 Hz and Re_v = 100, as indicated in Figure V-2. The value of ω_{app} calculated from the above data was 2.61×10^3 rad sec^{-1} or 2.49×10^4 revolutions per minute (RPM).

An analogous experiment employing 0.200 mM $Cr_2O_7^{2-}$ in 0.5 M H_2SO_4 was performed with Electrode E. The value used for D, 1.07×10^{-5} $cm^2 sec^{-1}$, was that given for CrO_4^{2-} by Kolthoff and Lingane (119). The observed value of I_1 was 125.4 μA at f = 240.0 Hz and Re_v = 130, and the corresponding value calculated for ω_{app} of this Au electrode was 1.94×10^3 rad sec^{-1} or 1.85×10^4 RPM. The value is somewhat lower than that for I^- at the Pt electrode due to the decay of I_1 for the reduction of Cr(VI) to Cr(III) at a Au electrode.

The data from these 2 experiments indicate that the maximum value for the mass transport to a vibrating electrode is approximately equal to that which would be observed at an RDE rotating at 20,000 RPM, assuming that laminar flow prevailed at the RDE at that speed of rotation. As a result, the sensitivity of the vibrating electrode may be expected to be at least 1.5 times greater than the maximum sensitivity observed for RDEs, which normally find application at speeds of rotation less than 10,000 RPM. It must be emphasized that ω_{app} is a purely fictitious parameter and is useful only for purposes of comparison of vibrating electrodes with RDEs.

C. Studies at Constant Re_v

The rate of mass transport to any electrode can be characterized on the basis of the Sherwood number, Sh, which was defined in Equations II-3 and II-4. The Sherwood number, and thus the mass transport, is a function of the vibrational Reynolds number, Re_v, and the Schmidt number, Sc (112, 120). The Schmidt number is defined as the ratio of the kinematic viscosity of the solution to the diffusion coefficient of the electroactive species (120) and is, thus, independent of the vibrational parameters. Therefore, the relationship between the mass transport to a vibrating electrode and its vibrational parameters is theoretically characterized solely by Re_v, which was defined in Equations II-2 and III-7.

Inspection of Equation III-7 reveals that the vibrational amplitude and frequency may be varied without altering the value of Re_v, provided that the product of the amplitude and frequency remains constant. From the discussion presented in the preceding paragraph, the value of I_l at a vibrating electrode should remain constant under such conditions. The results of 2 experiments designed to verify this prediction are presented in Tables V-2 and V-3. Both experiments were performed with Electrode D. For the data presented in Table V-2, v_{avg} was held constant at 30.0 cm sec^{-1}, corresponding to $Re_v = 53.8$, over a frequency range of 40 to 480 Hz. This value of Re_v was chosen to permit the widest possible range of frequencies to be studied; it also was representative of the values for Re_v employed in much of the analytical work. The results indicate that I_l remains constant within

Table V-2. I_l as a function of a_{pp} and f at v_{avg} = 30.0 cm sec^{-1}; $Re_v = 53.8$[a]

f (Hz)	a_{pp} (mm)	I_l (μA)
40.0	3.75	73.4
60.0	2.497	76.2
90.0	1.664	80.2
120.0	1.249	86.3
150.0	0.999	92.0
180.0	0.836	91.3
240.0	0.624	92.9
360.0	0.415	91.5
480.0	0.312	72.6

[a]Electrode A; 1.018 mM I^- in 0.5 M H_2SO_4; E_{WE} = +0.800 V vs. SCE.

Table V-3. I_l as a function of a_{pp} and f at v_{avg} = 15.0 cm sec^{-1}; Re_v = 26.9[a]

f (Hz)	a_{pp} (mm)	I_l (μA)
30.0	2.497	54.3
40.0	1.873	55.7
60.0	1.249	59.8
90.0	0.836	63.1
120.0	0.624	61.8
150.0	0.499	58.2
180.0	0.415	53.9
240.0	0.312	46.3
360.0	0.209	27.0
480.0	0.166	18.1

[a]Electrode A; 1.018 mM I^- in 0.5 M H_2SO_4; E_{WE} = + 0.800 V vs. SCE.

$\pm$ 3% from 100 Hz to 400 Hz and within $\pm$ 10% over the range of frequencies covered by the experiment. Table V-3 presents data from a similar experiment, which was performed at v_{avg} = 15.0 cm sec^{-1}, corresponding to Re_v = 26.9. In this case I_1 remained constant within $\pm$ 5% from 30 Hz to 180 Hz, and a distinct rolloff was noted at higher frequencies. The value of I_1 measured at 480 Hz in this experiment was only 25% of that found at 150 Hz.

The results of these 2 experiments indicate that the value of Re_v based on the diameter of the working electrode is an adequate characterization of the mass transport from 100 Hz to 400 Hz at values of Re_v used in the analytical work. At lower Re_v values, other factors apparently reduce the mass transport to the electrode at vibrational frequencies above approximately 180 Hz. In view of these results, a frequency of 240 Hz was chosen for most of the analytical determinations performed with vibrating electrodes. The failure of the correlation between Re_v based on the diameter of the working electrode and the rates of mass transport at lower values of Re_v is possibly due to influences of the glass sheath of the microelectrode on the flow patterns induced by the working electrode.

D. Hydrodynamic Frequency Response

As was noted in Chapter II of this dissertation, Podesta, et al. (36) observed an AC component to the limiting current at a vibrating disc electrode. The results of an analogous experiment designed to ascertain the AC frequency response of the boundary layer at a vibrating

wire electrode by electrochemical means are presented in Figure V-1. The data in Figure V-1 were obtained by measuring the relative amplitudes of the AC and DC components present at the current output of the potentiostat as a function of the frequency of vibration of the electrode. These measurements were performed with the Model 461 digital voltmeter, which was connected to the current output of the potentiostat. The meter was AC coupled on the AC voltage ranges and therefore did not respond to the DC component of I_1 in the AC measurement. The relative value of the AC component was obtained by dividing the measured value for the AC component, designated by ΔI_1^{2f}, by the measured value for the DC component, designated by I_1. This ratio was multiplied by 2.828 to change the RMS value of ΔI_1^{2f} to the peak-to-peak value, $\Delta I_{1,pp}^{2f}$, and then by 100 to yield a percentage, the logarithm of which is plotted in Figure V-1. The superscript 2f in ΔI_1^{2f} and $\Delta I_{1,pp}^{2f}$ denotes that the AC component being measured has a frequency which is twice that of the frequency of vibration. This 2:1 relationship arises from the symmetrical nature of the vibration and the resultant equivalence of the flow patterns induced by motion of the electrode in either direction.

During the experiment, the vertical and horizontal inputs of the oscilloscope were connected, respectively, to the current output of the potentiostat and to the signal used to drive the vibrating electrode. A 2:1 Lissajous figure was observed in this manner for all frequencies employed in this experiment, thus verifying the predicted 2:1 relationship of the frequency of ΔI_1^{2f} to the vibrational frequency. The phase shift of ΔI_1^{2f} relative to the AC signal used to drive the speaker in-

Figure V-1. Bode plot of frequency response of vibrating electrode

Re_v = 26.9; v_{avg} = 15.0 cm sec^{-1}; Electrode D; 1.018 mM I^- in 0.5 M H_2SO_4; E_{WE} = + 0.800 V vs. SCE.

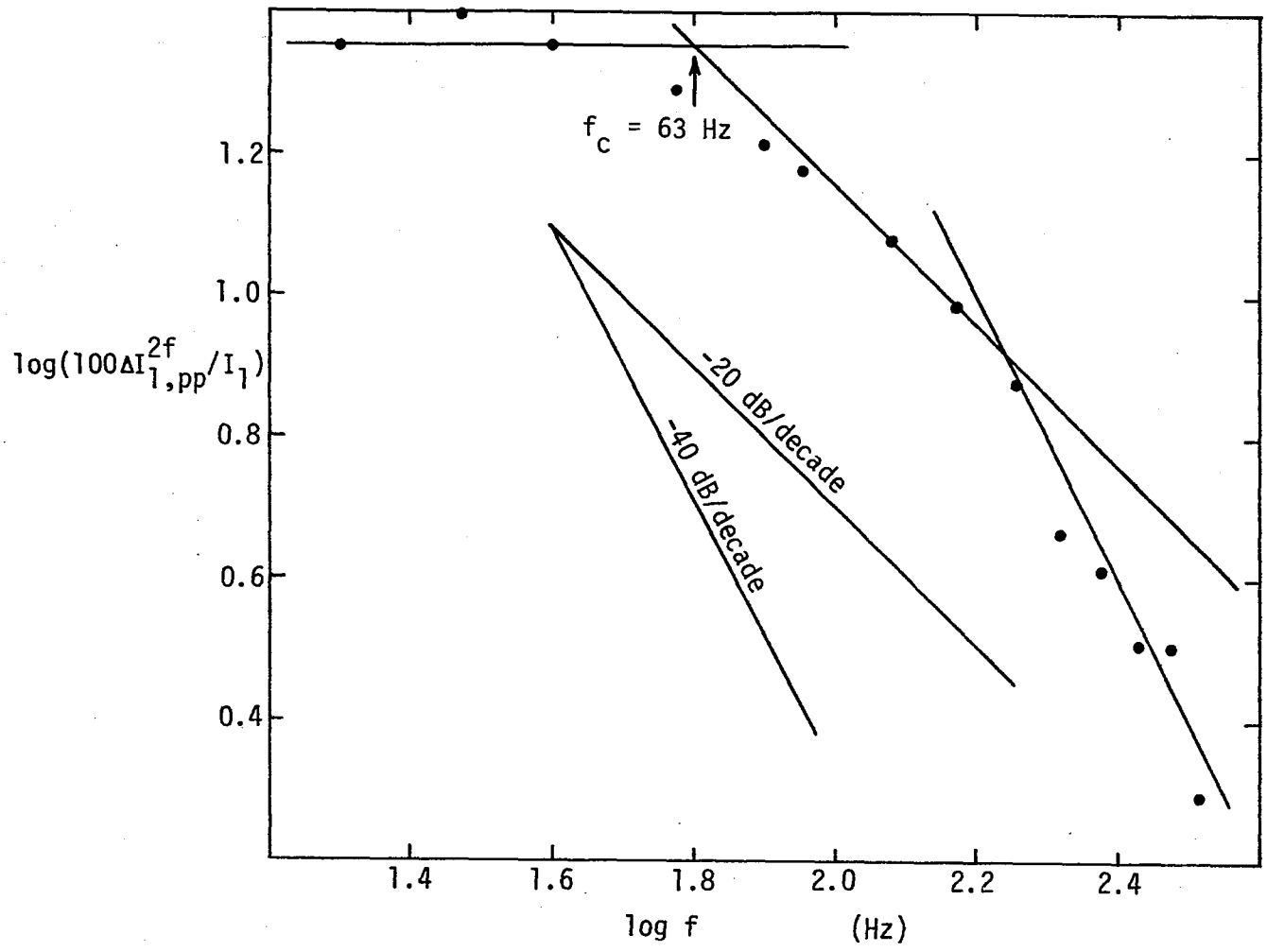
f_c = 63 Hz
-20 dB/decade
-40 dB/decade
1.2
1.0
0.8
0.6
0.4
$\log(100\Delta I^{2f}_{1,pp}/I_1)$
1.4
1.6
1.8
2.0
2.2
2.4
log f (Hz)

creased with increasing frequency. This phase shift was a combined result of the phase shift produced by the speaker and vibrator assembly and that arising from the response of the boundary layer.

The experiment was performed with Electrode D in a 1.018 mM solution of I^- in 0.5 M H_2SO_4 which was deaerated with N_2 to minimize oxidation of the I^- by atmospheric oxygen. The electrode was maintained at a potential of 0.0 V vs. SCE except during the measurements of the values of ΔI_1^{2f} and I_1, which were simultaneously performed at + 0.800 V vs. SCE. All data were obtained at v_{avg} = 15.0 cm sec^{-1}, corresponding to Re_v = 26.9. The range of frequencies studied was 20 Hz to 330 Hz.

The data obtained in the above experiment are plotted in Figure V-1 in a log-log format. The graph of the frequency response is analogous to a Bode plot, which is employed extensively to display the frequency characteristics of electronic circuits (pp. 71-2 of 93). The response of the boundary layer is seen to approximate that of a low-pass filter, which is characterized by a limiting slope of - 20 dB/decade at high frequencies for a first-order filter and - 40 dB/decade for a second-order filter. These slopes are shown in Figure V-1 for reference. The attenuation in excess of - 20 dB/decade noted at higher frequencies is possibly due to the frequency response of the potentiostat combined with that of the boundary layer. Taking - 20 dB/decade as the limiting slope for the Bode plot, a cutoff frequency of approximately 63 Hz is obtained for the vibrating electrode.

The frequency response of electrochemical mass transfer probes in turbulent flow has been studied by Fortuna and Hanratty (121) and by Hanratty and Chorn (122). These studies were directed toward ap-

plication of small, rectangular electrodes to the characterization of the turbulent flow occurring in tubes and pipes. The electrodes were situated flush with the wall of the pipe, with the long dimension parallel to the direction of flow. In particular, the frequency response of the electrodes to rapid changes in the velocity of flow in the vicinity of the electrode was sought. Hanratty and Chorn stated a criterion, couched in dimensionless variables, for the calculation of the frequency at which the response of the boundary layer causes significant attenuation of the signal. When combined with the definitions of these dimensionless variables (121), this criterion is summarized by Equation V-3:

$$2\pi f L^{-1/2} u^{*-2} Sc^{1/2} \cong 1 \qquad \text{(V-3)}$$

In Equation V-3, L represents the characteristic length of the electrode and u* represents the friction velocity, which is an averaged velocity employed in analyses of turbulent flow. Using d_e for Electrode D and 63 Hz for f, a value for u* of 20 cm sec^{-1} is obtained. The values substituted for d_e, ν, and Sc are taken from data cited previously. The calculated value of u* is surprisingly close to the value of v_{avg}, 15.0 cm sec^{-1}, which was chosen for the experiment described in this section. It must be noted that the relationship given in Equation V-3 was not derived for cylindrical electrodes. According to Hanratty and Chorn: "The analyses carried out by Fortuna for wall probes should be extended so as to include cylindrical elements immersed in a fluid..." Also, u* and v_{avg} are not identical.

The dominance of the second harmonic in the AC component to I_1,

which was observed in the above experiment, contrasts significantly with the dominance of the fundamental frequency noted by Podesta, et al. (36). This difference arises from the contrasting natures of the 2 types of vibrating electrodes. In the present work, the vibrating electrode is a cylinder and is vibrated symmetrically from side-to-side. Movement in either direction has an identical effect on the hydrodynamic flow patterns (except for direction) induced by the electrode and on the limiting current. In the system employed by Podesta, et al., a disc electrode was surrounded by a cone, and the hydrodynamic flow patterns differed for the half-cycle corresponding to impingement and that corresponding to withdrawal of the conical assembly in the solution. Thus, a dominant component was noted at the fundamental frequency. A significant contribution from the second harmonic was visible in the oscillogram presented in the article, although this was not noted by the authors.

The small amplitude of $\Delta I_{1,pp}^{2f}$ noted in these experiments precludes its application to analytical determinations in a manner analogous to HMVE(AM) and HMVE(FM), which employ the 10-Hz AC component of I_1, ΔI_1, as the analytical observable.

E. Relationship of I_1 and ΔI_1 to Re_v

The experimental plots of I_1 as a function of Re_v were automatically recorded using the AM/FM generator, potentiostat, and audio amplifier described in Chapter IV. The X-Y recorder employed in this and all succeeding experiments was an Omnigraphic model 2000, manufactured by

the Houston Instrument Co., Bellaire, TX. In the experiments detailed in this section, the X-Y recorder was connected as described in Section F of Chapter IV. The potential applied to the AM Ramp jack in the AM/FM generator was derived from a ramp generator of standard design, which produced an initial potential of 0.000 V and a final potential of 7.000 V with provision for reversal of the direction of scan at the limits. The scan rate employed was 1.9 V min^{-1}.

In order to calibrate the X (Re_v) axes of the experimental plots, it was necessary to characterize the overall function relating the value of Re_v to the potential of the DC ramp. This function is a composite of 3 independent relationships: the dependence of Re_v on the value of a_{pp}, the dependence of a_{pp} on E_{in} applied to the speaker, and the dependence of E_{in} on the voltage of the DC ramp. These 3 relationships are all direct proportionalities, as shown by Equation III-7, Figure III-2, and the quoted characteristics of the 4-quadrant multiplier (108), respectively. Therefore, Re_v is directly proportional to the value of the DC ramp, and the proportionality constant for this overall composite function is given by the product of the proportionality constants for each of the 3 relationships mentioned above. For the present research, the first of these constants was obtained by substitution of the experimental values for f, d_e, and ν into Equation III-7. The second constant was obtained from the slope of the applicable calibration curve for the corresponding electrode and frequency, examples of which have been shown in Figure III-2. The numerical values for the slopes were obtained from the observed data using the least-squares program supplied with the SR-51A calculator,

manufactured by Texas Instruments, Inc., Dallas, TX.

Prior to determining the proportionality constant relating E_{in} to the voltage of the DC ramp, the setting of P12 in the AM/FM generator was adjusted such that the vibrational amplitude obtained for a ramp voltage of 7.0 V was approximately 10% larger than that corresponding to the onset of unsteady values of I_l at the vibrating electrode. Following this, the value of E_{in} corresponding to a ramp voltage of 5 to 7 V DC was measured; the potential of the ramp generator was held constant during the measurement. Both E_{in} and the potential of the DC ramp were measured to an accuracy of $\pm$ 0.001 V. Following this measurement, the plot of I_l vs. Re_v was recorded, starting at a ramp potential of 0.000 V. Normally the value of I_l was recorded for a complete cycle of the ramp generator, thus permitting investigation of flow transitions for increasing and decreasing values of Re_v.

In addition to the plots of I_l vs. Re_v described above, the principle of HMVE(AM) was applied to the study of hydrodynamic flow patterns at vibrating electrodes. In these experiments, a 0.1-V_{pp}, 10-Hz signal was superimposed on the DC ramp used for the I_l graphs. This produced a sinusoidal, 10-Hz perturbation of the otherwise linearly increasing value of Re_v. The percentage of modulation for a 0.1-V_{pp} input from the 10-Hz oscillator was 1.0% at a ramp potential of 5.0 V. The 10-Hz perturbation in Re_v induced a 10-Hz AC component in I_l, designated as ΔI_l, which was processed by the LIA. The DC output of the LIA was recorded as a function of Re_v in a manner analogous to that employed in the plots of I_l vs. Re_v. The corresponding plots of I_l and ΔI_l were generally recorded on the same sheet of graph paper

during successive scans of the ramp generator. Simultaneous recording of both components would be possible on a 2-pen recorder. The degree of perturbation expressed in terms of Re_v was obtained by multiplication of the level of the 10-Hz input signal, 0.1 V_{pp}, by the proportionality constant relating the ramp potential to the value of Re_v.

A typical example of a combined plot displaying both I_1 and ΔI_1 as a function of Re_v is illustrated in Figure V-2. The value of ΔI_1 represents the component of the 10-Hz signal which is in phase with the hydrodynamic modulation of the vibrating electrode. The experiment was performed with Electrode A at a vibrational frequency of 240 Hz. I_1 and ΔI_1 were measured for the oxidation of 1.018 mM I^- in 0.5 M H_2SO_4 at a potential of + 0.800 V vs. SCE. The solution was deaerated with N_2 prior to performing the experiment and was blanketed with N_2 during the scans of Re_v. The potential of the electrode was maintained at 0.0 V vs. SCE except during the actual scan. These precautions minimized unwanted oxidation of I^- to I_2. Analogous experiments were also performed with Electrode A at 40, 80, and 120 Hz; with Electrode B at 120 Hz; and with Electrodes B and E at 240 Hz. I_1 and ΔI_1 for Electrode E were measured for the reduction of 200 μM $Cr_2O_7^{2-}$ in 1.0 M H_2SO_4. In addition, tests were conducted with axial and transverse vibration of Electrode C, which was held by a stiff Cu wire attached to the cone of the speaker; the transverse studies were performed with the exposed Pt wire bent 90 deg at the glass-to-metal seal.

The experiments with Electrode C showed that the value of I_1 observed for axial vibration, i.e., parallel to the axis of the wire, was 1/4 to 1/2 that observed for transverse or angular transverse

Figure V-2. Experimental plot of I_l and ΔI_l vs. Re_v for Electrode A at 240 Hz

A, B, C, D, E, F — key points referred to in text and Table V-5; G — point used in calculation of ω_{app} for Electrode A.

Scan rate of Re_v = 34.1 min^{-1}; f = 240.0 Hz; Electrode A; 1.018 mM I^- in 0.5 M H_2SO_4; E_{WE} = + 0.800 V vs. SCE.

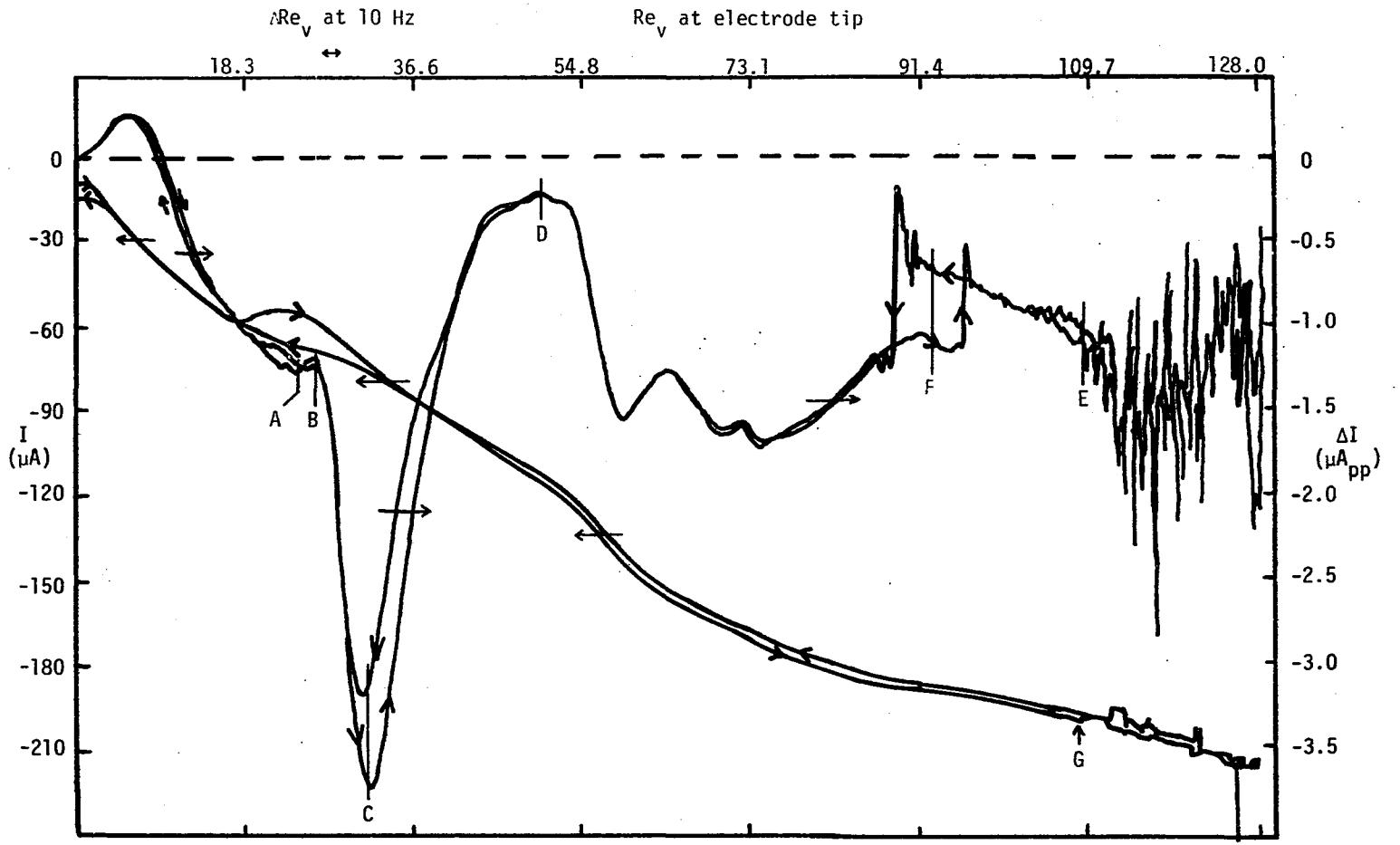
ΔRe$_v$ at 10 Hz
Re$_v$ at electrode tip
18.3
36.6
54.8
73.1
91.4
109.7
128.0
0
-30
-60
-90
-120
-150
-180
-210
I (μA)
0
-0.5
-1.0
-1.5
-2.0
-2.5
-3.0
-3.5
ΔI (μA$_{pp}$)
A
B
C
D
E
F
G

vibration (both perpendicular to the axis of the wire) of the same electrode at corresponding vibrational parameters. The plots of I_l vs. Re_v for normal (linear) transverse and angular transverse vibration were similar in appearance, and both differed from the "smoother" appearance of the axial plot. Whereas the plots of I_l vs. Re_v for transverse vibration were distinctly nonlinear and showed some evidence of fine structure, the analogous plots for axial vibration were much closer to a direct linear relationship between I_l and Re_v.

The general appearance of all plots of I_l vs. Re_v was similar to that seen in Figure V-2. A smooth increase in I_l at low Re_v values was interrupted at approximately Re_v = 13 to 19 by the appearance of a distinct "bump" in the curve. In many cases, including the graph shown in Figure V-2, a short region was even noted in which an increase in the amplitude of vibration produced a decrease in the limiting current. This behavior was noted only in the ramp direction corresponding to increasing values of Re_v. After this region was passed, the current again monotonically increased until the onset of noise occurred, typically at Re_v = 85 to 115, above which the value of I_l became unstable. In most cases a broad "bump" was noted at Re_v values approximately halfway from the start of the plot to the onset of noise. Studies were not conducted at vibrational amplitudes far beyond the onset of noise, because the vibrational parameters approached the maximum values possible with the speaker chosen, and the high noise level precluded application to electroanalytical determinations. The high acoustical noise level produced at large vibrational amplitudes, particularly at frequencies above 120 Hz, also proved objectionable to

the experimenter and to co-workers in the laboratory (123). It should be noted, however, that I_l continued to increase, albeit rather slowly, with increasing amplitudes of vibration beyond that corresponding to the onset of noise. The only feasible analytical application of vibrating electrodes operated in this region would be in anodic stripping voltammetry during the deposition process, in which the long period of deposition would average out the comparatively high-frequency components of the noise. Use of the vibrating electrode at Re_v values below the onset of noise generally ensures that a stable analytical signal is obtained. The only exceptions to this rule were found with Electrode A at frequencies of 80 and 120 Hz and intermediate values of Re_v, in the region of the broad "bump," Re_v = 50 to 70. At times, the value of I_l under these conditions would alternate between 2 stable values, which differed by about 5%. It is likely that an unstable transition between 2 flow patterns at a portion of the electrode caused this behavior.

In Figure V-2, I_l increases in a distinctly nonlinear fashion with increasing values of Re_v. Further characterization of the relationship between I_l and Re_v necessitates the presentation of the data for I_l from Figure V-2 in a log-log format. Such a graph is presented in Figure V-3 for data taken from Figure V-2. Values of I_l and Re_v were taken directly from the I_l-Re_v plot in Figure V-2 at 0.25-V increments in the value of the ramp potential. The values of I_l were uniformly read from the scan in the direction of decreasing Re_v. The slope of this plot, which represents the average exponential dependence of I_l on Re_v, was obtained from the original data by means of the least-squares routine on the SR-51A calculator. The experimental points on

Figure V-3. Log I_l vs. log Re_v for Electrode A at 240 Hz

Data from Figure V-2.

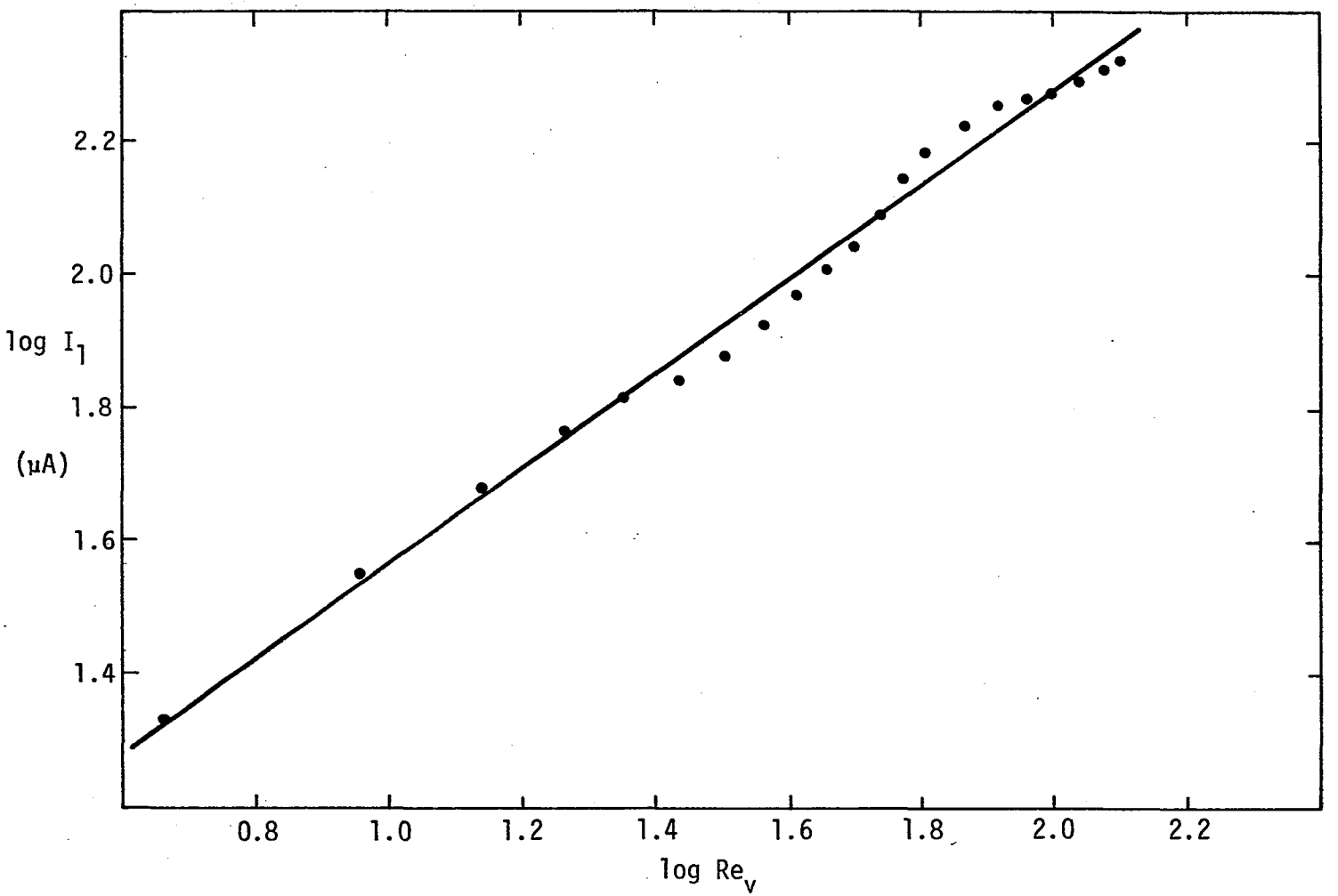
2.2
2.0
1.8
1.6
1.4
log I_1
(μA)
0.8
1.0
1.2
1.4
1.6
1.8
2.0
2.2
log Re_v

the log-log plot do not lie on the calculated line, but oscillate about it. This behavior was characteristic of all plots of log I_l vs. log Re_v for vibrating electrodes and was observed with both Pt and Au electrodes with the electrochemical reactions of I^- and $Cr_2O_7^{2-}$, respectively. It was concluded that the "bumps" in the experimental data result from the hydrodynamic flow patterns induced by the electrode and are not a result of the electrochemical reaction.

The results of analogous experiments conducted at different frequencies and with different electrodes are summarized in Table V-4. The slopes given in Table V-4 represent the exponential dependence of I_l on both Re_v and a_{pp}, because a_{pp} was the experimental variable in these experiments. The observed values for the exponential dependence of I_l on Re_v lie between 0.5 and 0.7, with the exception of one result obtained for Electrode B. The reason for the larger value observed for Electrode B is unknown. All values found experimentally lie within the range of 0.42 to 1.0, which has been reported in the literature (see Table II-1).

Although not employed in this research, direct recording of log I_l vs. log Re_v is theoretically possible with the addition of 2 logarithmic converters to the present experimental apparatus. For this experiment, the DC ramp and the current output of the potentiostat would each be connected to the input of a logarithmic converter, and the corresponding outputs of the converters would be connected to the X and Y axes of the X-Y recorder, respectively. The slope of the graph obtained on the X-Y recorder, when connected for the scaling factors of the converters, would represent the exponential dependence

Table V-4. Exponential dependence of I_l on Re_v and a_{pp} for different electrodes and frequencies

Electrode	f (Hz)	Slope	Re_v range covered
A[a]	40	0.519	4-80
A[a]	80	0.636	5-85
A[a]	120	0.614	5-110
A[a]	240	0.712	5-128
B[a]	240	0.962	8-117
E[b]	240	0.679	9-145

[a] 1.018 mM I^- in 0.5 M H_2SO_4; E_{WE} = + 0.800 V vs. SCE.

[b] 200 μM $Cr_2O_7^{2-}$ in 1.0 M H_2SO_4; E_{WE} = + 0.300 V vs. SCE.

of I_l on Re_v and a_{pp}. This procedure would permit more detailed investigation of the exponential dependence.

The exponential dependence of I_l on the vibrational frequency, f, was also calculated from the data obtained in the experiments with Electrode A. Since direct recording of I_l vs. f at constant a_{pp} was not possible, the value of I_l at a chosen amplitude of 0.685 mm_{pp} was calculated from the 4 plots of I_l vs. Re_v. The corresponding values of Re_v ranged from 15 at f = 40 Hz to 90 at f = 240 Hz. The data are presented graphically in a log-log format in Figure V-4. The slope of this graph, 0.664, represents the exponential dependence of I_l on f for Electrode A. This value lies within the range of 0.57 to 1.09, which has been reported in the literature (see Table II-1).

As stated previously, the mass transport to a vibrating electrode is characterized solely by Re_v for a given solution and electroactive species. The relationship between the rate of mass transport and Re_v may be expressed in exponential form (112, 117, 120), as shown in Equation V-4.

$$Sh_v = kRe_v^z \qquad (V\text{-}4)$$

In Equation V-4, the rate of mass transport is defined by the vibrational Sherwood number, Sh_v, and k is a proportionality constant. The exponential dependence of Sh_v on Re_v is represented in Equation V-4 by z. This relationship may be extended to I_l by combining Equations V-4 and II-3:

$$I_l = k'Re_v^z \qquad (V\text{-}5)$$

Figure V-4. Log I_1 vs. log f for Electrode A at a_{pp} = 0.685 mm
1.018 mM I^- in 0.5 M H_2SO_4; E_{we} = + 0.800 V vs. SCE.

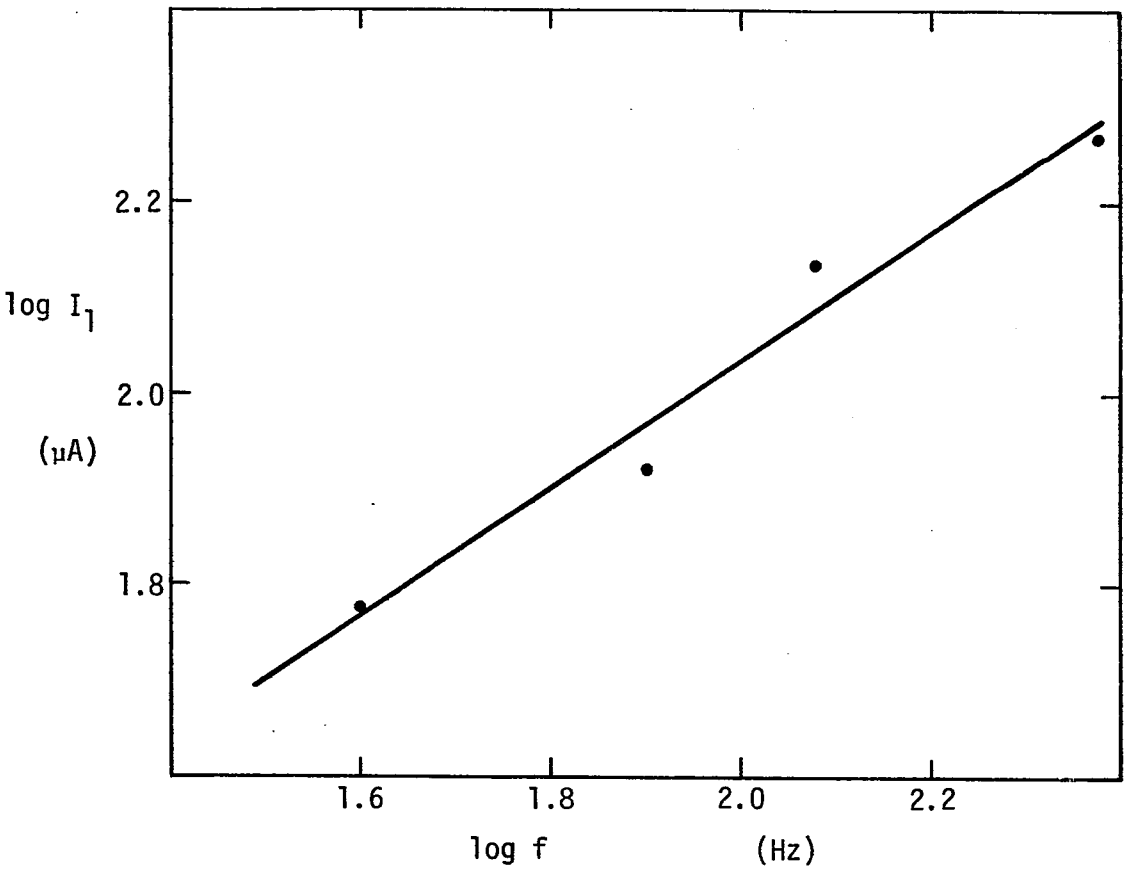
2.2
2.0
1.8
log I_l
(μA)
1.6
1.8
2.0
2.2
log f
(Hz)

In Equation V-5, k' represents a proportionality constant composed of constants from Equations V-4 and II-3. The theoretical relationship between I_1 and the vibrational amplitude and frequency is now readily obtained by combination of Equations V-5 and III-7, which yields Equation V-6. The constant k" represents the overall proportionality constant.

$$I_1 = k''a^z f^z \tag{V-6}$$

Taking the logarithm of both sides of Equation V-6 yields Equation V-7:

$$\log I_1 = \log k'' + z \log a + z \log f \tag{V-7}$$

From Equation V-7, it is evident that graphs of log I_1 vs. log a at constant f and of log I_1 vs. log f at constant a should theoretically have identical slopes, represented by z, the exponential dependence of I_1 on a or f.

The values for the exponential dependence of I_1 on a and f as experimentally determined were 0.620 and 0.664, respectively. The former value is the mean of the 4 values for Electrode A given in Table V-4, and the latter value is the slope of the graph in Figure V-4. These values are in close agreement and provide support to the theory developed in the preceding paragraph.

The experimental plots of ΔI_1 vs. Re_v provided interesting insights into the nature of the flow transitions occurring at vibrating electrodes. In all cases, the graph of ΔI_1 presented a 3-bumped appearance, as seen in Figure V-2. The second or middle bump was always largest and was usually quite narrow. In most cases the first bump,

observed at low Re_v values, was better developed than in Figure V-2; in certain cases it was as much as half the height of the second bump. The third bump was always the broadest and ended with the transition to noisy, unstable values of ΔI_1, which occurred at $Re_v = 85$ to $Re_v = 115$. The end of the first bump coincided with the dip in the graph of I_1, where present, and the onset of noise occurred at similar points in the graphs of I_1 and ΔI_1. The noise at high values of Re_v was much larger in the ΔI_1 graph. This is a natural result of the nature of ΔI_1, which is produced by small variations in the thickness of the diffusion layer. Whereas I_1 depends on the overall value of δ, the value of ΔI_1 depends on the value of these small variations.

In certain cases a sharp transition in the value of ΔI_1 was noted near the end of the third bump. This transition is noted by point F in Figure V-2 and is likely related to the bistable transition in I_1 noted previously.

The plot of ΔI_1 vs. Re_v for Electrode C vibrated in the axial mode was found to differ significantly from the 3-bumped graphs observed in the angular transverse mode of vibration. In the axial case, the value of ΔI_1 roughly paralleled the increasing value of I_1 with the exception of a rather abrupt dip at $Re_v \cong 20$. The contrasting natures of the graphs of ΔI_1 vs. Re_v for axial and transverse vibration show that the hydrodynamic flow patterns induced by the electrode are fundamentally different for the 2 modes.

Several points were chosen as characteristic of the 3-bumped graphs of ΔI_1 vs. Re_v. These key points are depicted in Figure V-2, and the Re_v values corresponding to the positions of analogous points

in other scans are noted in Table V-5. In each graph, point A represents the peak of the first bump, B the dip between the first and second bumps, C the peak of the second bump, D the minimum between the second and third bumps, and E the transition to noise. Point F, where shown, represents the Re_v value corresponding to the sharp transition in ΔI_1 in the third bump. The values are not totally independent of frequency, and the lower values observed for Electrode D likely reflect the smaller diameter of that electrode. However, the variations in the locations of these points are far smaller than the corresponding variations in the vibrational frequency. From comparison of these Re_v values with values given in the literature for the observed hydrodynamic transitions occurring at cylinders, it is likely that point B corresponds to the establishment of fixed vortices in the region of the electrode. Points E and F likely correspond to the transition between 2 flow regimes noted by Blevins (115) at Re $\cong$ 90. The significance of the other points is not readily interpreted. Since all features of the 3-bumped graphs were observed with both Pt and Au electrodes for the electrochemical reactions of I^-, $Cr_2O_7^{2-}$, and O_2, it was concluded that the features are characteristic of the hydrodynamic behavior of the electrodes.

The degree of fine structure observed in the scans of ΔI_1 vs. Re_v was found to be inversely related to the level of the 10-Hz signal superimposed on the DC ramp. This property is analogous to similar behavior observed in AC polarography and in modulated-wavelength spectroscopy, and it is characteristic of all modulated instrumental techniques. The level of modulation of the DC ramp chosen provided

Table V-5. Characterization of plots of ΔI_1 vs. Re_v by key points

Electrode	f (Hz)	Re_v values of key points[a]					
		A	B	C	D	E	F
A	40	18	20	23	28	73	–
A	80	18	21	26	32	81	–
A	120	20	23	29	36	85	65
A	240	23	26	31	50	108	92
B	240	21	25	46	69	113	90
D	120	13	16	20	23	56	–
E	240	26	31	36	67	137	97

[a]See text and Figure V-2 for designation of points A through F.

a good tradeoff between the resolution of observed fine structure and the noise figure of ΔI_1.

F. Phase of ΔI_1 as a Function of Re_v

To ascertain the phase of ΔI_1, it was necessary to record 2 scans of ΔI_1 vs. Re_v. In the first of these, the LIA was set to measure the component of ΔI_1 in phase with the hydrodynamic modulation of the vibrating electrode, in the manner employed previously. In the second scan, the LIA was set to measure the component of ΔI_1 in quadrature with the hydrodynamic modulation (i.e., 90 deg out of phase from the modulating signal). This was effected by changing the setting of the Quadrant switch on the LIA from the 0 deg position to the 90 deg position. The 2 scans were recorded directly on the X-Y recorder in the normal manner.

The requirement for the second scan of ΔI_1, recorded in quadrature with the hydrodynamic modulation, may be understood by considering the response of the LIA to phase shifts in the input signal. The response of the LIA to sinusoidal input signals which are shifted from the reference waveform by a phase angle ϕ was derived in Chapter IV of this dissertation and is given by Equation IV-6. This equation was derived under the assumption that the phase of the signal <u>led</u> that of the reference. However, an equivalent <u>lag</u> in the signal waveform, which corresponds to a phase lead of $-\phi$ deg, produces the same value of $e_o(\phi)$. This is a result of the fundamental trigonometric identity that $\cos \phi = \cos(-\phi)$. To ascertain whether the signal

waveform leads or lags the reference waveform, it is necessary to perform the second measurement of the component of the signal which is in quadrature with the reference waveform.

The response of the LIA to a signal measured in quadrature with the reference waveform may be elucidated by analysis of the phase relationships existing between the signal and reference waveforms in the LIA. For the purpose of this analysis, the signal waveform, $e_s(t)$, is considered to lag the reference waveform at the reference input by a phase angle of θ. The equation of the signal waveform is thus given by Equation V-8:

$$e_s(t) = E_s \sin (\omega t - \theta) \qquad \text{(V-8)}$$

As has been described in Chapter IV of this dissertation, the processing circuitry for the reference waveform introduces a phase lag of 90 deg with the Quadrant switch set to the 90 deg position. This introduced phase lag of 90 deg between the reference input and the 4-quadrant multiplier is equivalent to an added phase lag of - 90 deg in the signal waveform. The overall lag in the signal waveform relative to the reference waveform (at the reference input) is thus $\theta_{tot} = \theta - 90$. The apparent phase lag "sensed" by the 4-quadrant multiplier is θ_{tot}, and the quadrature output signal of the LIA, designated as $e_Q(\theta)$, is given by Equation V-9.

$$e_Q(\theta)/e_{o,max} = \cos \theta_{tot} \qquad \text{(V-9)}$$

The value of $e_{o,max}$ in Equation V-9 is given by Equation IV-2. Since

$\theta_{tot} = \theta - 90$ and $\cos(\theta - 90) = \sin\theta$, the quadrature response of the LIA is given by Equation V-10:

$$e_Q(\theta)/e_{o,max} = \sin\theta \tag{V-10}$$

The output of the LIA for in-phase measurement of the signal defined in Equation V-8 is given by Equation V-11. The DC output from the LIA in this case is designated as $e_I(\theta)$ to distinguish it from the DC output obtained from the quadrature measurement.

$$e_I(\theta)/e_{o,max} = \cos\theta \tag{V-11}$$

The phase lag of the signal waveform may be ascertained from the values obtained from the in-phase and quadrature measurements of $e_s(t)$ without the need for measurement of $e_{o,max}$. In this case, θ is given by Equation V-12, which results from division of Equation V-10 by Equation V-11.

$$e_Q(\theta)/e_I(\theta) = \tan\theta \tag{V-12}$$

An equivalent form is presented in Equation V-13:

$$\theta = \tan^{-1}[e_Q(\theta)/e_I(\theta)] \tag{V-13}$$

The quadrant of θ is defined by the signs of $e_Q(\theta)$ and $e_I(\theta)$.

As a verification of the above equations, the phase lag introduced by the MSR rotator was determined by measurement of $e_I(\theta)$ and $e_Q(\theta)$. This measurement yielded a result of 26.9 deg, which agreed, within experimental error, with the value obtained by the alternate method described in Chapter IV. The accuracy of the phase shifts calculated

by Equation V-13 was on the order of $\pm$ 1 deg.

The phase of ΔI_1 as a function of Re_v for Electrode D is shown in Figure V-5. The raw data for this graph were obtained from 2 successive scans of ΔI_1 vs. Re_v which were performed with the LIA set to measure the in-phase and quadrature components of ΔI_1, respectively. The graphs of ΔI_1 were obtained for 1.0 mM I^- in 0.5 M H_2SO_4. Values of ΔI_1 were measured at 0.1-V increments of the DC ramp, and corresponding values from the 2 scans were substituted into Equation V-13 to calculate the phase shift, θ. The 10-Hz signal superimposed on the DC ramp had an amplitude of 0.1 V_{pp}.

At most of the values of Re_v in the regions of the first and third bumps of the plot of ΔI_1 vs. Re_v, the phase shift observed is a lag of 20 to 100 deg. These values lie within the range predicted by Fortuna and Hanratty (121) and by Tokuda, et al. (124) for the phase shifts resulting from the phase response of the diffusion layer to sinusoidal perturbations. The phase shifts calculated at Re_v values from 22 to 24 are less accurate due to the low values of $e_Q(\theta)$ and $e_I(\theta)$ produced by the LIA. However, the large change in the phase shift observed in the region of the second bump is not an instrumental artifact and results from a significant change in the phase response of the diffusion layer at the corresponding values of Re_v.

Phase shifts from 20 to 26 deg (lag) were observed for Electrodes A and D for ΔI_1 measured in the same manner using HMVE(AM) at large percentages of modulation, from 33% to 95%. The electrochemical system studied in these experiments was also 1.0 mM I^- in 0.5 M H_2SO_4.

The phase shifts resulting from the response of the diffusion

Figure V-5. Phase of ΔI_1 vs. Re_v for Electrode D

f = 120 Hz; $\Delta Re_v = 1.06_{pp}$; 1.018 mM I^- in 0.5 M H_2SO_4; E_{WE} = + 0.800 V vs. SCE.

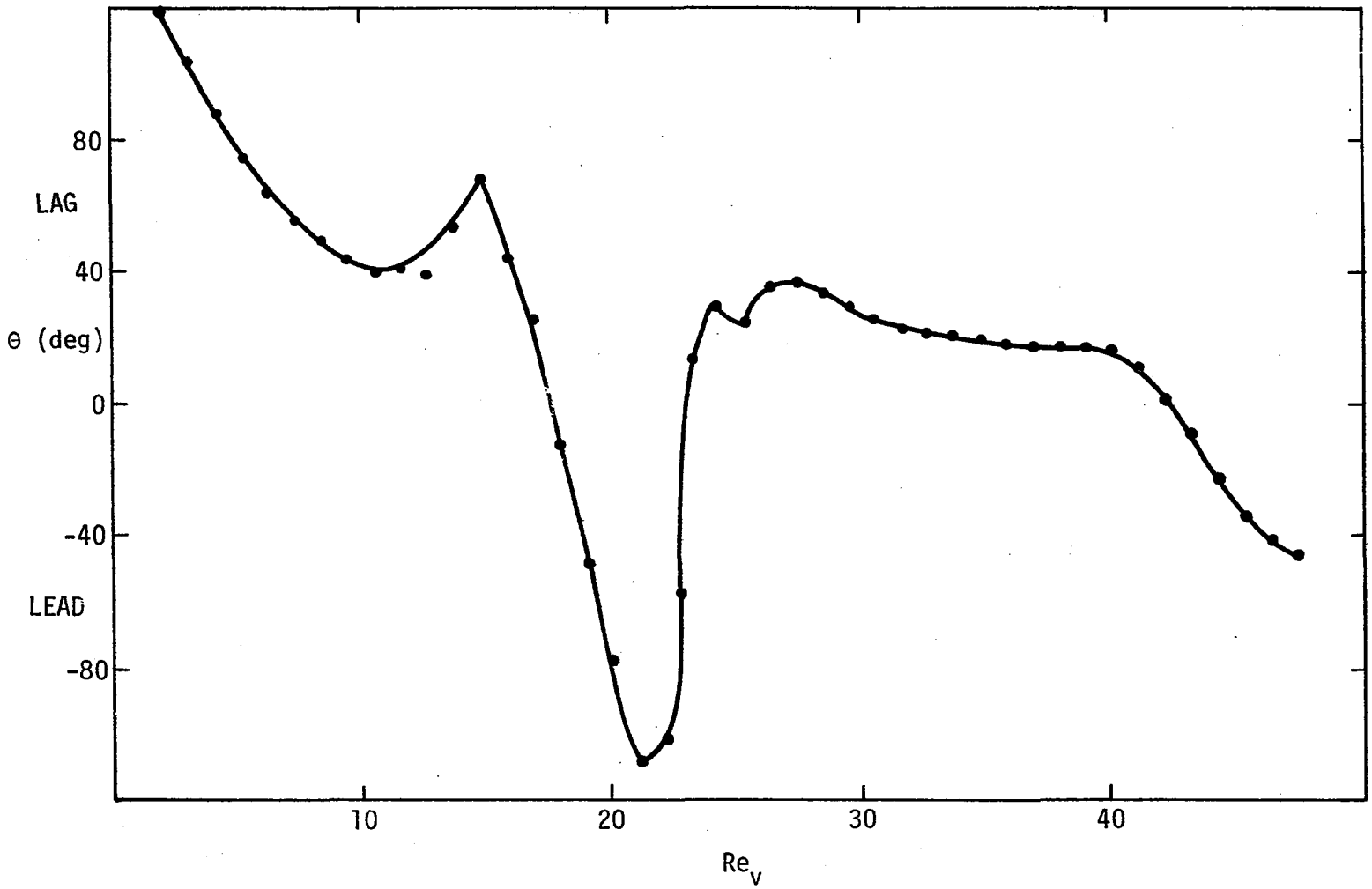
80
LAG
40
Θ (deg)
0
-40
LEAD
-80
10
20
30
40
Re_V

layer to sinusoidal perturbations are related to the relaxation time of the diffusion layer. Since this relaxation time is also related to the frequency response of the diffusion layer, the results of these phase studies complement the studies of frequency response presented in Section D of this chapter. A major difference in these 2 experiments results from the nature of the HMVE(AM) technique. In the study of frequency response, the perturbation in the diffusion layer resulted from the large variation in the instantaneous velocity of the electrode, described by Equation III-3. In the HMVE(AM) experiments, the 10-Hz modulation introduced a small 10-Hz perturbation in the average velocity, the effect of which was studied in the experiments described in this and the preceding section. Both sets of results should be able to be quantitatively described by an extension of the theory of Fortuna and Hanratty (121). The development of such a theory is beyond the scope of this dissertation and is not pursued further in this work. Quite possibly, the complex nature of the flow patterns induced by transverse vibrations of cylindrical bodies precludes development of such a theory. The primary purpose of the experiment described in this section was to demonstrate the application of the LIA to the experimental measurement of phase angles.

G. Visual Evidence of Hydrodynamic Transitions

A simple experiment was conducted with Electrode A at f = 240 Hz in an attempt to correlate the features noted in Figure V-2 and discussed in the preceding sections with the actual flow patterns ob-

served at the vibrating electrode. The flow patterns were made visible by means of entrained H_2 bubbles generated at the vibrating electrode, which was immersed in 1.0 M H_2SO_4. A Pt wire in one of the sidearms of the cell served as the counter (positive) electrode, and power for the electrolysis was supplied by 2 flashlight cells hooked in series (3.0 V). The amplitude of E_{in} applied to the speaker was manually varied, and observations of the nature, position, and movement of the bubbles were noted. These observations are presented here in order of increasing values of Re_v for the vibrating electrode.

At $Re_v = 0$, the bubbles were of comparatively large diameter and rose more or less straight up within 1 electrode diameter from the edge of the electrode. As the value of Re_v was slowly increased, by increasing the value of a_{pp} at constant f, the width of the region traversed by the bubbles at first decreased and reached a minimum of $1.5d_e$ at $Re_v = 11$. Above this point, the bubbles began to move slightly outward from the electrode; this change in the behavior of the bubbles became noticeable at $Re_v = 15$ to 20. The first significant movement of the bubbles outward from the electrode was noted at $Re_v = 23$ to 29, at which point the bubbles moved as far as $4d_e$ away from the electrode, following parabolic curves upward. Actual laminar streaming commenced in the region from $Re_v = 29$ to 51. At $Re_v = 51$, the first <u>horizontal</u> streaming of bubbles away from the electrode was noted; at this point the bubbles moved horizontally outwards for 5 electrode diameters and then began to drift upward, following a parabolic curve. The diameter of the streaming bubbles was noticeably smaller than that of the bubbles produced at lower Re_v values. From $Re_v = 51$ to 78, the horizontal,

laminar streaming intensified, and the diameter of the bubbles became somewhat smaller. Slightly below $Re_v = 78$, the velocity of the laminar, horizontal stream of bubbles became sufficiently great that the stream of bubbles reached the sides of the cell before moving upwards. All streaming from the electrode at $Re_v < 78$ was confined to the plane of vibration of the electrode. At $Re_v = 78$, the first signs of turbulence in the stream of bubbles was noted. This turbulence occurred exclusively in the last third of the distance from the electrode to the wall of the cell and took the form of loops and swirls in the stream of bubbles. At $Re_v = 86$, a distinct change in the nature of the motion of the bubbles was noted. The motion in the region of the electrode became more intense and turbulent, and the streaming became sufficiently intense that the evolved bubbles began to cloud up the solution in the upper third of the cell with H_2 bubbles. This effect was not noted below $Re_v = 86$. The flow pattern which commenced at $Re_v = 86$ became stronger at Re_v values up to 96. At $Re_v = 96$ to 98, the first streaming from the electrode at angles separated from the plane of vibration was noted. The diameter of the evolved bubbles was noticeably smaller, and the solution became sufficiently clouded to obscure the electrode within 20 sec. There was a definite change to greater turbulence at this point, although it was noted that this process could represent merely a continuation and strengthening of the flow pattern which commenced at $Re_v = 86$. Above $Re_v = 98$, all flow observed in the cell was turbulent. The intensity of flow continued to increase, but characterization of the flow pattern was impossible. At $Re_v = 103$, the upper half of the cell became sufficiently clouded to

obscure the electrode within 10 sec of application of power to the electrode.

The above description of the observed flow patterns indicates that definite transitions occur within the range of Re_v values employed in this research. From the results of the present experiment, it is concluded that the significant transitions in the flow patterns induced by the electrode occur for Electrode A at 240 Hz at Re_v = 11, ca. 25, 78, ca. 90, and possibly at Re_v values around 103. It must be emphasized that these observations and conclusions relate to the hydrodynamic behavior observed at significant distances from the electrode. The relationship between this behavior and the thickness and/or character of the diffusion layer, the variable of primary electrochemical interest, is unclear. However, the transition in the flow pattern observed at Re_v = 78 almost certainly has little or no effect on δ, because it was confined to large distances from the electrode.

From comparisons of the present experimental results to the values of the key points observed in the graph of ΔI_l vs. Re_v for the same electrode (see Figure V-2 and Table V-5), it appears that the second transition in the present experiment corresponds to point B and the fourth and fifth transitions correspond to points F and E, respectively. This interpretation lends credence to the interpretation of these key points as indicative of transitions in the hydrodynamic flow patterns induced by the electrode, but it does not explain the 3-bumped appearance of the graphs nor the significance of points A, C, and D, if any. The relationship of the hydrodynamic transitions observed at vibrating electrodes to the thickness and nature of the

diffusion layer constitutes a promising field for future research with vibrating electrodes.

The onset of noise in both the I_1 and ΔI_1 scans is directly related to the extreme turbulence noted visually at corresponding values of Re_v in the present experiment.

H. Conclusion

The relationship between the limiting current observed at a vibrating electrode and the vibrational parameters has been quantitatively determined for a_{pp} = 0 to 3.3 mm, f = 40 to 240 Hz, and Re_v = 0 to 150 at Pt and Au vibrating electrodes. The exponential dependences of I_1 on a_{pp} and f were found to be 0.620 and 0.664, respectively, for a given vibrating electrode. These values lend support to the theoretical prediction of equal values for these 2 exponential dependences. All values calculated for these dependences in this research are within the range previously reported in the literature, although significant differences were observed between different electrodes. The validity of Re_v as a characterization of the mass transport to vibrating electrodes has been tested at frequencies from 30 to 480 Hz and has been found to provide excellent correlations from 100 to 400 Hz at Re_v = 53.8 and good correlations at other values. The frequency and phase responses of vibrating electrodes have been evaluated, and the experimental results have agreed with general theoretical predictions in both cases. The maximum analytically useful rate of mass transport to vibrating electrodes has been experimentally determined, leading to

the prediction that the sensitivity of the vibrating electrode should be at least 1.5 times as sensitive as the RDE for analytical determinations.

The possible application of hydrodynamic modulation to the characterization of mass transport to vibrating electrodes has been studied, and predictions based on these studies have been compared with actual observations of the flow patterns induced by vibrating electrodes, with significant agreement noted between the 2 methods.

Differences in both the electrochemical and hydrodynamic behavior of electrodes vibrated in the axial and transverse modes have been observed and evaluated, and the transverse mode has been found to possess significantly higher analytical sensitivity and more complex hydrodynamic behavior.

Consideration of the angular dependence of the flux of electroactive species to a cylindrical electrode reported by Radoi (112) indicates that the mass transport to a vibrating electrode is not uniform, and the vibrating electrode therefore does not possess the property of uniform accessibility characteristic of the RDE. From summation of the results presented by Radoi for both directions of vibration, the polar plot of the flux to a vibrating electrode should appear somewhat like a 4-leaf clover, with the largest rates of mass transport noted at ca. 45 and 135 deg from the direction of vibration.

A speculative characterization of the flow patterns induced by vibrating electrodes may be formulated from a synthesis of the experimental results and observations from this research and from previous studies reported in the literature. The flow in the region of the

vibrating electrode is totally laminar at Re_v values below 10. From Re_v = 10 to ca. 25, a set of 4 fixed vortices is established, with a structure similar to that observed by West (109). These 4 vortices form the vibrational analog of the Föppl vortices reported in linear flow. Although not directly noted in this work, the presence of these vortices would explain the slight outward motion of the bubbles observed at these Re_v values. From Re_v = 25 to 50, these vortices begin to be shed in a manner analogous to that observed in linear flow. The turbulence in the stream of bubbles at Re_v = 78 is analogous to the establishment of the Kármán vortex street. The major transition observed at Re_v = 86 possibly corresponds to the transition at Re = 90 noted by Blevins (115).

The original instrumental techniques described in this chapter were developed and evaluated for the characterization of the hydrodynamic behavior of vibrating electrodes, and they constitute a significant advance in the technology of vibrating electrodes. They enable far more detailed investigations to be undertaken than have been performed in earlier work, which relied exclusively on point-by-point, manual observations of I_l. These techniques are applicable to other types of vibrating electrodes, and their future use could well lead to more exact knowledge of the hydrodynamics of vibrating bodies.

VI. EVALUATION OF HYDRODYNAMIC MODULATION

Analytical applications of hydrodynamic modulation at RDEs and vibrating electrodes are presented in this chapter, and the merits of these techniques relative to DC voltammetry are evaluated. A comparison of HMVE(AM) and HMVE(FM) is also presented.

A. Literature

The concept of hydrodynamic modulation at RDEs was introduced by Miller, et al. (125) and analytical application of the techniques was first demonstrated by Miller and Bruckenstein (97). In the latter study, voltammograms employing this technique were presented for the reduction of 5×10^{-8} M nitrobenzene and 4×10^{-7} M Tl^{+} at an amalgamated Au RDE and for the reaction of 1×10^{-6} M quinhydrone at a Pt RDE. The techniques were also applied to reactions at wax-impregnated graphite and Ag RDEs. Linear calibration curves of ΔI_1 at the RDE vs. concentration were presented. The relationships between the amplitude and phase of ΔI_1 and the hydrodynamic parameters were predicted from theory for reversible reactions by Tokuda, et al. (124), and experimental results in agreement with the theoretical predictions were observed. In recent publications these and other authors have extended these theoretical predictions and experimental observations to reactions having slower rates of electron transfer (126-129).

Bruckenstein and Miller have summarized the areas of electrochemical investigation which benefit from application of the technique of hydrodynamic modulation at RDEs (130).

Blaedel and Engstrom developed a closely related technique, in which the rotation speed of a glassy carbon RDE was switched between 500 and 1500 RPM (131). A two-fold increase in the difference between the limiting currents observed at these 2 rotation speeds was noted in the presence of 10 nM $Fe(CN)_6^{3-}$, relative to the blank value.

A technique applicable to tubular electrodes which is analogous in principle to hydrodynamic modulation at RDEs was devised by Blaedel and Iverson (132). The difference between the values of I_l observed at a tubular electrode for 2 different flow rates was evaluated as a function of the concentration of $Fe(CN)_6^{3-}$. A linear relationship was observed from 0.1 to 4.0 μM $Fe(CN)_6^{3-}$, with an estimated detection limit of 0.05 μM. Recent publications by Blaedel and Kim (133, 134) have reported improvements in instrumentation for the technique, designated as pulsed flow voltammetry. The response of the AC component of I_l observed in pulsed flow voltammetry at tubular electrodes was studied at frequencies of pulsation from 0.1 to 2.0 Hz (134). Further improvements in the detection limit were not noted, however. Application of pulsed flow voltammetry to electrochemical detection in liquid chromatography was reported (135).

B. Theory

The basic principles of hydrodynamic modulation and the instrumental methodology used to effect such modulation at vibrating electrodes have been presented in Chapters IV and V of this work. The major advantage of hydrodynamic modulation is its ability to discriminate

against components of the total electrode current which are independent of the rate of mass transport to the electrode, viz. currents resulting from nonfaradaic processes, e.g., charging current, and from surface-controlled reactions, such as the oxidation and reduction of noble metal electrodes. Inasmuch as the majority of electrochemical reactions of analytical interest are mass-transport limited, the application of the technique of hydrodynamic modulation results in a significant increase in analytical sensitivity, as noted by Miller and Bruckenstein (97). In fundamental electrochemical investigations, the discrimination against surface-controlled processes afforded by hydrodynamic modulation permits rapid isolation of the components of the electrode current which are dependent on the rate of mass transport to the electrode. This information, which is of theoretical and mechanistic significance, cannot be obtained from a single DC voltammogram by other means.

The techniques of HMVE(AM) and HMVE(FM) have been introduced in Chapter IV of this work. From the predicted exponential dependences of I_1 on a and f summarized in Equation V-6, it follows that corresponding perturbations of the vibrational amplitude or frequency should affect I_1 in an equivalent manner. The choice between the 2 methods may thus be determined solely from instrumental considerations.

C. Comparison of HMVE(AM), HMVE(FM), and DC Voltammetry

Voltammograms of 4.19 μM Br^- in 1.0 M H_2SO_4 recorded using HMVE(AM), HMVE(FM), and DC voltammetry are presented in Figure VI-1. Similar percentages of modulation of v_{avg} (and consequently, Re_v) were employed

Figure VI-1. DC, HMVE(AM), and HMVE(FM) voltammograms of 4.19 μM Br^- in 1.0 M H_2SO_4 at Electrode A

A — DC voltammogram; B — HMVE(AM) voltammogram; C — HMVE(FM) voltammogram.

Scan rate = 2.0 V min^{-1}; DC: f = 350 Hz; Re_v = 76; a_{pp} = 0.397 mm; HMVE(AM): f = 350 Hz; average Re_v = 76; 17.6% modulation; HMVE(FM): f = 350 ± 60 Hz; average Re_v = 76; a_{pp} = 0.397 mm; Quadrant = 180 deg.

Details of DC voltammogram designated by "10X" recorded at 10 times the current sensitivity of primary DC voltammogram.

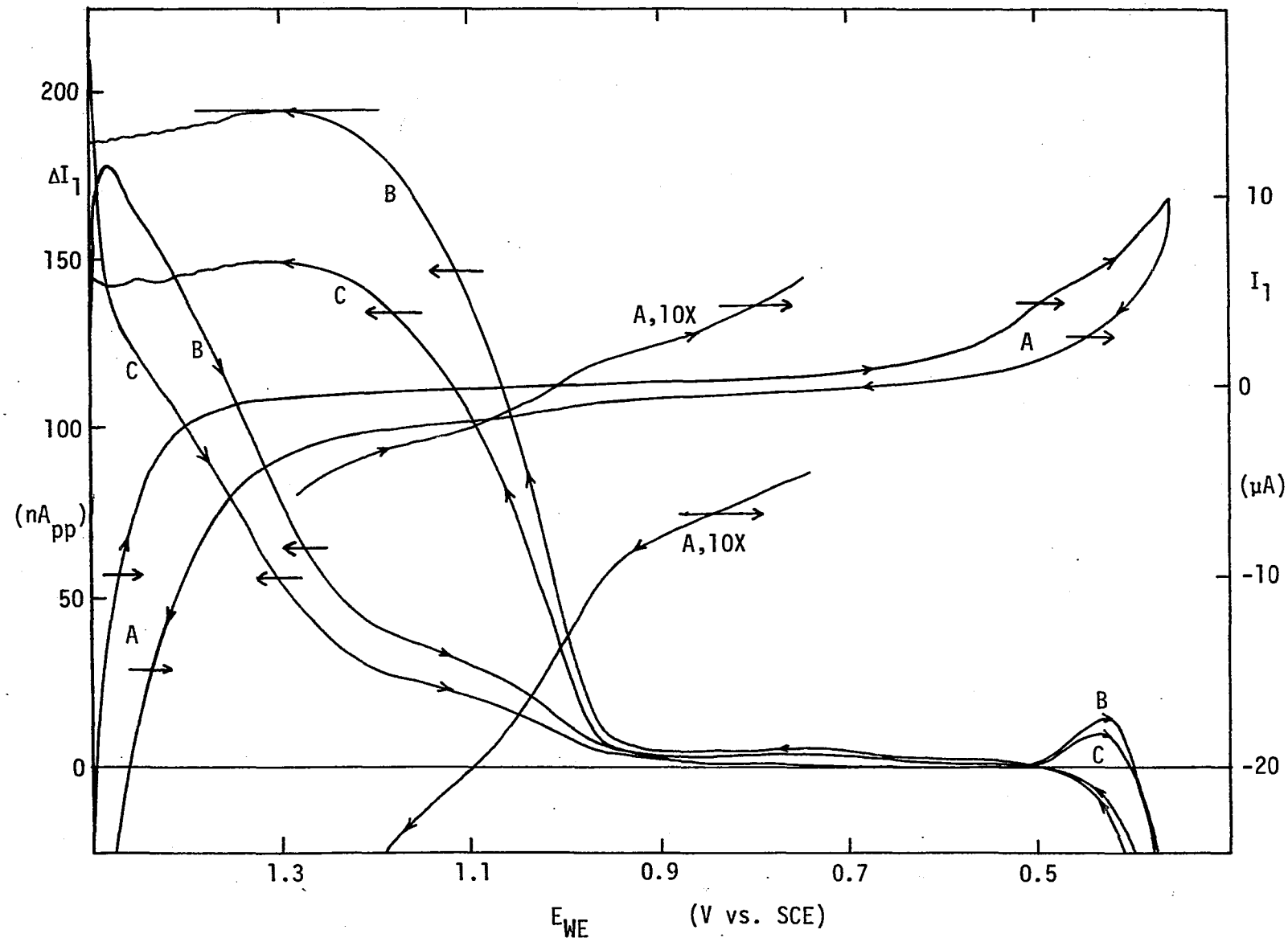
200
ΔI1
150
100
(nApp)
50
0
10
I1
0
(μA)
-10
-20
A
B
C
A,10X
A,10X
1.3
1.1
0.9
0.7
0.5
EWE
(V vs. SCE)

in the HMVE(AM) and HMVE(FM) voltammograms, permitting direct comparison of the 2 techniques. In the DC voltammogram, the wave corresponding to the oxidation of Br^- to Br_2 is not readily resolved from the residual current, which results from the oxidation of the surface of the Pt electrode to PtO. The limiting current for the oxidation of Br^-, which is obtained at potentials greater than + 1.3 V vs. SCE, is totally obscured by the background currents produced by further oxidation of Pt to PtO and by the oxidation of H_2O to O_2. In the voltammograms of ΔI_1 produced by the HMVE(AM) and HMVE(FM) techniques, these background currents are substantially reduced, and both the Br^- wave and the limiting current for the oxidation of Br^- are clearly visible. The peak observed in the value of ΔI_1 at + 1.5 V vs. SCE results from ringing in the 10-Hz bandpass amplifier of the LIA induced by the reversal of the direction of scan and is not indicative of electrochemical processes occurring at this potential. The slight offset of ΔI_1 in the HMVE(AM) and HMVE(FM) voltammograms in the region from + 0.5 to + 0.9 V vs. SCE is not an instrumental artifact, and the nonzero value indicates that a significant, albeit miniscule, component of the residual current at the Pt electrode is mass-transport controlled. This background value in ΔI_1 was noted in all experiments conducted at Pt RDEs and vibrating electrodes in which hydrodynamic modulation at high sensitivities was employed. The values of ΔI_1 noted at potentials less than + 0.5 V vs. SCE result from the mass transport-limited reduction of dissolved O_2 present in the solution, which was not deaerated. Because the Quadrant switch was set to the 180 deg position in this experiment, the directions of the HMVE(AM) and HMVE(FM)

waves are vertically inverted relative to the waves shown in the DC voltammogram (i.e., anodic values of ΔI_1 are positive).

The values of ΔI_1 observed for the Br^- wave relative to the background level of ΔI_1 and to the noise in ΔI_1 indicates that the detection limit for Br^- in this system, defined for a signal-to-noise (background) ratio of 2, is on the order of 4×10^{-7} M Br^-. This concentration lies well below the detection limit for Br^- using DC voltammetry, which is estimated from Figure VI-1 to be roughly 4×10^{-6} M, the concentration employed in the experiment. Even at this concentration, the sloping baseline observed in the DC voltammogram complicates accurate determination of the limiting current. As previously noted, the DC limiting current, I_1, is totally obscured by background processes.

The values of ΔI_1 in the HMVE(FM) voltammogram are approximately 25% lower than corresponding values for ΔI_1 in the HMVE(AM) voltammogram. In all other respects the 2 voltammograms are equivalent. From the theoretical predictions set forth in Chapter V, direct equivalence between the 2 methods is expected. The cause of the reduced amplitude of the HMVE(FM) voltammogram is unknown but possibly originates from the same effect which caused the deviations in the values of I_1 at constant Re_v, which were noted in the experiments described in Section C of Chapter V.

Since the HMVE(AM) and HMVE(FM) voltammograms are equivalent, the detection limit is expected to be identical for both methods. The HMVE(FM) technique offers no advantage over HMVE(AM) at vibrating electrodes and suffers from considerably greater instrumental complexity.

Hence, the simpler HMVE(AM) technique was employed in all further experiments with hydrodynamic modulation described in this dissertation. The only factor favoring the use of HMVE(FM) is its constant vibrational amplitude, which could possibly prove advantageous in applications requiring minimal cell volume (e.g., flow-injection analysis).

The existence of finite background values of ΔI_1, observed in the absence of electroactive species, has been noted. These small, mass-transport controlled currents could possibly originate from the reduction or oxidation of electroactive impurities in the supporting electrolyte or from dissolution of the Pt electrode. To investigate the former possibility, residual voltammograms were recorded both in 0.01 M and 1.0 M H_2SO_4, using hydrodynamic modulation at a Pt RDE. The amplitude and character of the residual values of ΔI_1 did not change appreciably, showing that contamination of the H_2SO_4 was not the cause of these currents. These and succeeding experiments were performed with triply distilled, deionized water (TDW), with the deionization following the first distillation and the second distillation being from alkaline permanganate (0.01 M $KMnO_4$ in 0.1 M KOH). The background currents were therefore ascribed to the dissolution of Pt with the concomitant, mass transport-dependent formation of a soluble species. This hypothesis has also been forwarded by Miller (136). Evidence for the dissolution of Pt electrodes subjected to positive potentials in 1.0 M H_2SO_4 has been cited (137) based on the results of experiments employing collection at rotating ring-disc electrodes and spectrophotometric determination of Pt(IV) in the H_2SO_4 following anodization. The same author also observed slight dif-

ferences in the residual voltammograms obtained at a Pt RDE rotated at 400 and 10,000 RPM. This dependence was independently observed in the present work and is probably directly analogous to the residual values of ΔI_1 observed with hydrodynamic modulation.

A second comparison of HMVE(AM) with DC voltammetry is presented in Figure VI-2. In this experiment, the mass transport-controlled reduction (138) of Cr(VI) to Cr(III) was studied at an iodized Pt vibrating electrode. The DC voltammogram displays no evidence of a reduction wave or limiting plateau for the reduction of Cr(VI), and the positive and negative scans are widely separated due to the large current associated with the charging of the double layer at the electrode. The DC residual curve of the iodized Pt electrode, although not shown, was identical in appearance to the voltammogram obtained in the presence of 7×10^{-8} M $Cr_2O_7^{2-}$. In contrast to these results, the presence of 7×10^{-8} M $Cr_2O_7^{2-}$ was readily observed with HMVE(AM) at the same electrode. On the basis of these results, the detection limit for $Cr_2O_7^{2-}$ using HMVE(AM) is estimated at 1×10^{-8} M. This experiment illustrates the increase in sensitivity afforded by the HMVE(AM) technique in a system in which faradaic surface reactions of the electrode are absent (139).

D. Relationship of ΔI_1 in HMVE(AM) to Percentage of Modulation

For a given concentration of electroactive species, the value of ΔI_1 observed for HMVE(AM) is dependent on the percentage of modulation of a_{pp} for the vibrating electrode. The results of an investigation

Figure VI-2. DC and HMVE(AM) voltammograms of 7.8×10^{-8} M $Cr_2O_7^{2-}$ in 1.0 M H_2SO_4

A – DC voltammogram of 7.0×10^{-8} M $Cr_2O_7^{2-}$ in 1.0 M H_2SO_4; B – HMVE(AM) voltammogram of 1.0 M H_2SO_4; C – HMVE(AM) voltammogram of 7.0×10^{-8} M $Cr_2O_7^{2-}$ in 1.0 M H_2SO_4.

Scan rate = 2.0 V min^{-1}; DC: f = 240 Hz; Re_v = 31; a_{pp} = 0.234 mm; HMVE(AM): f = 240 Hz; average Re_v = 31; 33.3% modulation; Electrode A.

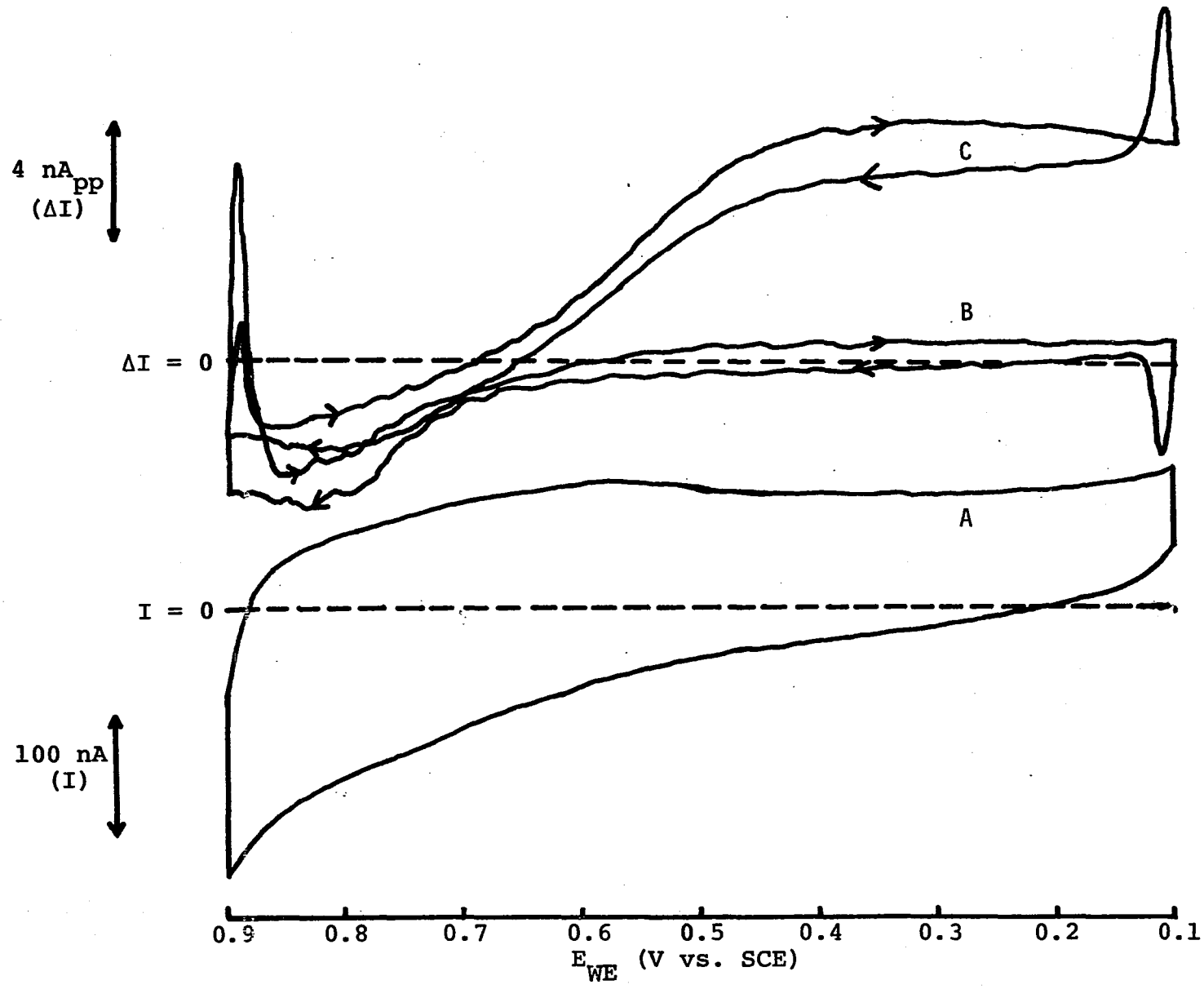
4 nA$_{pp}$
(ΔI)
C
B
ΔI = 0
A
I = 0
100 nA
(I)
0.9
0.8
0.7
0.6
0.5
0.4
0.3
0.2
0.1
E_{WE} (V vs. SCE)

of this dependence are presented in Table VI-1. As predicted from Equation V-6, the value of ΔI_1 increases with increasing modulation of the vibrational amplitude. Therefore, the signal-to-noise ratio of the analytical signal (ΔI_1) relative to electronic noise generated by the instrumentation is most favorable at large percentages of modulation, and the detection limits for determinations limited by electronic noise decrease with an increase in the percentage of modulation. However, the detection limit for HMVE(AM) remains unchanged for trace determinations which are limited by the background level of ΔI_1 resulting from electrochemical processes, because the background and analytical components of ΔI_1 are identically affected by increases in the percentages of modulation.

E. Determination of O_2 by HMVE(AM) and DC Voltammetry

In the research described in this section, HMVE(AM) and DC voltammetry were applied to the determination of dissolved O_2 present at macro and trace levels. For calibration of the electrode, solutions containing standard concentrations of O_2 were produced by bubbling known mixtures of N_2 and O_2 through 0.010 M H_2SO_4, which served as the supporting electrolyte. Each mixture was bubbled from a Pasteur pipet through the solution for a period of 20 min prior to recording the HMVE(AM) and DC voltammograms, and the solution was blanketed with the mixture during the 2 analyses. The standard mixtures were formulated by Air Products and Chemicals, Inc., Allentown, PA, and ranged in O_2 content from 0.100% to 10.0% (v/v) O_2. Voltammograms were also obtained for

Table VI-1. ΔI_1 as a function of percentage of modulation[a]

Modulation (%)	ΔI_1 at f = 240 Hz (μA_{pp})[b]	ΔI_1 at f = 360 Hz (μA_{pp})[c]
5.0	2.48	2.01
10.0	5.19	4.24
15.0	8.10	6.16
20.0	11.2	7.87
25.0	14.8	9.62
30.0	18.4	12.1
35.0	21.9	16.3
40.0	25.8	21.4
45.0	28.6	27.4
50.0	31.8	33.7
55.0	35.0	40.0
60.0	38.1	45.8
65.0	41.1	51.1
70.0	44.0	55.8
75.0	46.7	60.3
80.0	49.2	64.1
85.0	51.4	67.6
90.0	53.3	70.6
95.0	55.2	73.4
100.0	56.8	75.8

[a]Electrode B; 1.0 mM I^- in 1.0 M H_2SO_4; E_{WE} = + 0.800 V vs. SCE.

[b]Average Re_v = 28; average a_{pp} = 0.203 mm.

[c]Average Re_v = 66; average a_{pp} = 0.319 mm.

0.010 M H_2SO_4 saturated with pure O_2 and with air, obtained from the compressed air line in the laboratory. The experimental values of I_1 and ΔI_1 for these mixtures are presented in Table VI-2. Since the values differed for the positive and negative scans of applied potential, these data are noted for both scan directions. Calibration curves were constructed from the data for each scan direction, and these calibration curves were used to calculate the percentage of O_2 in the air, based on the recorded values of I_1 and ΔI_1 noted for the air-saturated solution. The calculated values for the percentage of O_2 in air are tabulated in Table VI-3. Because the currents observed for pure O_2 were smaller than the expected values based on the other standards, the calculated concentrations of O_2 in air were also obtained from extrapolation of the line formed by the current values for the 5 mixtures, omitting the points for pure O_2. These latter calculated percentages are closer to the accepted value, 20.95% (v/v) (140), than those calculated using the calibration curves in which the points for pure O_2 were included. Significant nonlinearity was noted at lower concentrations, as well. Similar nonlinearity was observed with the same system by Küster (26), as previously noted.

The reduction of dissolved O_2 constitutes a significant interference in numerous electroanalytical applications of Pt electrodes, and the complete removal of dissolved O_2 is consequently of great importance in applications of voltammetry to trace analyses. Because of its high sensitivity in the determination of O_2, the HMVE(AM) technique was applied to the evaluation of the effectiveness of deaeration for removal of dissolved O_2 from solution. The concentration of O_2 in

Table VI-2. Experimental data for determination of percentage of O_2 in air[a]

Concentration of O_2 (% v/v)	DC I_1 (μA)		HMVE(AM) ΔI_1 (μA_{pp})	
	Neg. scan	Pos. scan	Neg. scan	Pos. scan
0.1	1.51	0.25	0.717	0.610
0.5	4.77	3.63	3.03	2.77
1.0	8.26	7.08	5.83	5.42
4.0	30.9	29.8	22.8	22.0
10.0	72.0	71.1	54.8	54.1
100.0	664	656	449	472
Air[b]	149.1	149.7	112.9	115.4

[a]Scan rate = 2.0 V min^{-1}; 0.010 M H_2SO_4; DC: f = 120 Hz; Re_v = 47; a_{pp} = 0.681 mm_{pp}; HMVE(AM): f = 120 Hz; average Re_v = 47; 95% modulation; Electrode B; all currents measured at E_{WE} = 0.000 V vs. SCE.

[b]Atmospheric pressure = 983.5 mbar; temperature = 21.2 C.

Table VI-3. Calculated values for percentage of O_2 in air[a,b]

Range of standards (% v/v)	Technique	Calculated percentages (% v/v)	
		Neg. scan	Pos. scan
0.1-10.0	DC	21.1	21.3
0.1-10.0	HMVE(AM)	20.7	21.1
0.1-100.0	DC	21.3	21.9
0.1-100.0	HMVE(AM)	23.5	24.1

[a]Experimental data and conditions shown in Table VI-2.

[b]Accepted value = 20.95 % (v/v) (140).

the deaerated solution was estimated from comparison of the height of the O_2 wave observed in the deaerated solution with that observed in air-saturated 1.0 M H_2SO_4. The ratio of the value of ΔI_1 for the deaerated solution to the value of ΔI_1 for the air-saturated solution was multiplied by the concentration of O_2 in the air-saturated solution, 2.5×10^{-4} M (p. 383 of 141). Analyses performed in this manner demonstrated that deaeration of the covered cell (see Chapter III, Section F) using the Pasteur pipet reduced the concentration of dissolved O_2 to a constant concentration, typically 2×10^{-7} to 4×10^{-7} M, within 20 min. The lowest value obtained was 9.8×10^{-8} M. The detection limit for O_2 using HMVE(AM) was estimated to be 2×10^{-8} M, for a signal-to-noise ratio of 2. In contrast, no clear O_2 wave was noted at an O_2 level of 1×10^{-6} M in the DC voltammogram; only a small offset on the Pt residual voltammogram was observed at potentials from 0 to + 0.2 V vs. SCE.

Extensive attempts were made to further reduce the concentration of dissolved O_2 in the deaerated solutions, without success. Purification systems employing V(II) and Cr(II) solutions in gas scrubbing bottles were inserted into the N_2 stream but failed to reduce the height of the O_2 wave obtained in deaerated solutions (pp. 89-90 of 141, 142). These measures also introduced impurities into the H_2SO_4 which were adsorbed onto the Pt electrodes, producing spurious peaks in the residual voltammograms. From the results of these experiments, it was concluded that the residual level of dissolved O_2 did not originate in an O_2 impurity in the N_2 gas used for deaeration, but resulted instead from incomplete deaeration of the solution and/or diffusion

of O_2 from the outside air through the holes in the Teflon cover of the cell.

F. Conclusion

Comparisons of HMVE(AM), HMVE(FM), and DC voltammetry have shown that the application of hydrodynamic modulation to the determination of electroactive species yields a ten-fold to hundred-fold increase in analytical sensitivity with a corresponding decrease in the detection limit. Residual values of ΔI_1 observed at Pt RDEs and vibrating electrodes have been ascribed to the mass-transport controlled dissolution of Pt from the electrode. These background values correspond directly to the small changes noted in residual voltammograms obtained at a Pt RDE rotated at 400 and 10,000 RPM. The HMVE(AM) and HMVE(FM) techniques produce identical voltammograms, as predicted from theory, although the amplitude of ΔI_1 observed in HMVE(FM) is somewhat reduced from corresponding values observed in HMVE(AM). Because the instrumentation required for production of HMVE(AM) is simpler than that required for HMVE(FM), the former technique is preferred.

The HMVE(AM) technique was applied to the analysis of dissolved O_2, with excellent agreement found between the calculated and accepted values for the percentage of O_2 in air. Application of the same technique in the evaluation of the effectiveness of deaeration showed that small residual levels of dissolved O_2 resulted from diffusion of O_2 from the outside air into the cell. The level of dissolved O_2 achieved in the deaerated solutions was approximately 2×10^{-7} M, corresponding

to 99.9% effectiveness of the deaeration.

Slight nonlinearity in the calibration curves of ΔI_1 vs. concentration of O_2 was noted over the range of 0.1% to 100% (v/v) O_2.

VII. FLOW-INJECTION ANALYSIS

In this chapter the application of vibrating electrodes to flow-injection analysis (FIA) is demonstrated. Equations are derived and verified which describe the response of vibrating electrodes in flowing streams.

A. Literature

The basic principles, literature, and applications of FIA have been reviewed in recent feature articles in Analytical Chemistry (143, 144). The reader unfamiliar with FIA should consult these publications for a general treatment of the topic.

The first application of an electrochemical sensor in a flowing stream was made by Müller (145) in 1947. In recent years, the response of numerous forms of electrochemical detectors in flowing streams has been investigated (146). Recent developments in this laboratory have included the flow-through wire (147) and disc (148) electrodes.

Other investigations related to the present work include the research of Pungor, et al. (149) into the response of potentiometric detectors in FIA. These workers derived equations describing the effect of a mixing chamber inserted between the point of sample injection and the detector.

Wang and Ariel employed RDEs in the determination of trace metals in flowing streams by anodic stripping voltammetry (ASV) (150, 151). Because the systems developed by Wang and Ariel used a conventional RDE, the diameter of the tubing (7 mm) and flow rates employed in the analyses (5-100 mL min^{-1}) were both far greater than values conven-

tionally employed in FIA (typically 0.9 mm and 1.0 mL min^{-1}, respectively). The peak currents obtained in ASV were proportional to the square root of the flow rate when the disc electrode was stationary, and independent of the flow rate when the disc was rotated. At the RDE, the peak currents were proportional to the square root of the rotation speed. In their latter system (151), the authors noted that the peak currents measured under conditions of plug injection were less than the peak currents measured under steady-state conditions for delays of less than 60 sec, measured from the time of arrival of the sample solution at the detector to the initiation of the deposition step. Equations describing this relationship were not derived, however.

Oosterhuis, et al. (152) applied an RDE to the analysis of catecholamines in flowing streams. The RDE was employed both in conventional FIA and as a detector for liquid chromatography at a flow rate of 1.0 mL min^{-1}. A three-fold improvement in the sensitivity was noted for the RDE at ω_r = 1200 RPM relative to the same electrode when stationary, and the detection limit for dopamine was estimated at "a few tenths of a nanogram." The dependence of the peak current on the flow rate was not investigated. Negative deviations from the expected proportionality between the peak current and $\omega_r^{1/2}$ were ascribed to wall effects arising from the use of a small cell (diameter = 9 mm).

Blaedel and Schieffer (153) designed a turbulent tubular electrode, in which a rotating stirrer located within a conventional tubular electrode induced turbulent flow. At low rotation speeds of the stirrer, the limiting current observed in a continuously flowing stream of analyte was dependent on the cube root of the volume flow rate, v_f. At high

rotation speeds, greater than 2000 RPM, the current was independent of the flow rate, and the limiting current depended on the square root of the rotation speed of the stirrer. The detection limit for $Fe(CN)_6^{3-}$ was below 0.1 μM, and a five-fold increase in sensitivity was noted at a stirring rate of 3430 RPM relative to that at 0 RPM.

Johansson (154) designed a coulometric detector for liquid chromatography in which rotation of Pt gauze electrodes aided the mass transport to the working electrode.

The investigations by Passwaters (30) of vibrating electrodes in flowing streams have been discussed in Chapter II of this dissertation.

B. Theory

For the purposes of this theoretical development, the FIA system employed in this research is modeled as a vibrating electrode contained in a cell of constant volume, V_{cell}. The cell is provided with an inlet and an outlet for the flow of solution into and out of the cell, respectively. The following 7 assumptions are postulated regarding the behavior of this system:

1. The rates of inflow and outflow to and from the cell, respectively, are both equal to v_f, the volume flow rate of the FIA system.

2. The background concentration of the electroactive species (analyte) in the supporting electrolyte is zero.

3. A sample plug of volume V_s containing analyte at a concentration C_o is injected into the inlet channel. This plug experiences no

dispersion in the inlet channel and consequently reaches the cell in the form of a "square" plug.

4. The time t = 0 is defined as the point in time at which the leading edge of the sample plug reaches the cell. The length of the plug expressed in units of time is designated as τ, where $\tau = V_s/v_f$.

5. Instantaneous, perfect mixing of the contents of the cell results from the vibration of the electrode. Consequently, the solution in the cell is homogeneous, and each volume increment, dV, of solution flowing into the outlet channel is thus a representative sample of the contents of the cell at the corresponding point in time. Mixing effects do not extend beyond the boundaries of the cell.

6. The vibrating electrode is operated under the mass-transport limited conditions applicable to Equation I-6, i.e., on the limiting plateau for oxidation or reduction of the analyte.

7. The mass transport coefficient for the electrode, k_m, is independent of the value of v_f. The flux of analyte to the vibrating electrode is thus $(dN/dt)_{elec} = Ak_mC(t)$, where C(t) represents the instantaneous concentration of analyte in the cell.

The validity of assumptions 3, 5, and 7 as applied to the FIA system developed for this research is discussed in Section D of this chapter.

The mathematical relationships describing the behavior of the vibrating electrode in FIA are readily derived through application of the principle of material balance, which is widely employed in chemical engineering (155). Analyte entering the cell through the inlet channel may either remain in the cell, leave the cell through the outlet

channel, or react at the electrode. For a given increment of time dt, the quantity of analyte accumulating in the cell equals the quantity entering the cell minus the sum of the quantities leaving the cell or reacting at the electrode. Expressing these 4 quantities as incremental numbers of moles yields Equation VII-1, the fundamental material balance for this system.

$$dN_{cell} = dN_{in} - (dN_{out} + dN_{elec}) \qquad \text{(VII-1)}$$

Utilization of the basic relationship between quantity, volume, and concentration permits these incremental quantities of analyte to be expressed in terms of incremental volumes and concentrations.

For the period from t = 0 to t = τ, corresponding to the inflow of sample into the cell, the expression of material balance is given by Equation VII-2.

$$V_{cell}dC = C_o dV - [C(t)dV + dN_{elec}] \qquad \text{(VII-2)}$$

Division of both members of Equation VII-2 by dt, the period of time corresponding to the incremental accumulation of analyte, yields Equation VII-3. The derivative dV/dt is equivalent to the volume flow rate, v_f.

$$V_{cell}dC/dt = C_o v_f - [C(t)v_f + (dN/dt)_{elec}] \qquad \text{(VII-3)}$$

Substitution of the expression for the flux of analyte to the electrode results in Equation VII-4:

$$V_{cell}dC/dt = C_o v_f - [C(t)v_f + Ak_m C(t)] \qquad \text{(VII-4)}$$

Algebraic transformation of this equation yields Equation VII-5:

$$dC/dt + [(v_f + Ak_m)/V_{cell}]C(t) = C_o v_f/V_{cell} \qquad \text{(VII-5)}$$

Equation VII-5 is a first-order linear differential equation of the form $dy/dt + py(t) = q$, where $y(t)$ is a function of time and p and q are constants. Such equations are most expeditiously solved (156) by multiplication of all terms by an integrating factor, $\exp(pt)$. The entire left member becomes an exact derivative of $\exp(pt)y(t)$, and the solution is readily obtained by integration of the right member followed by algebraic manipulation. The solution is of the form given in Equation VII-6:

$$y(t) = q/p + k \exp(-pt) \qquad \text{(VII-6)}$$

The constant k results from the integration of the right member. Substitution of the variables and constants in Equation VII-5 corresponding to $y(t)$, p, and q in the general solution gives Equation VII-7, the solution to Equation VII-5.

$$C(t) = C_o v_f/(v_f + Ak_m) + k \exp[-(v_f + Ak_m)/V_{cell}]t \qquad \text{(VII-7)}$$

At the point when the leading edge of the sample plug reaches the cell, the concentration of analyte in the cell is zero. This initial condition, which together with Equation VII-5 constitutes an ideal value problem (156), is expressed by Equation VII-8:

$$C(t) = 0 \text{ at } t = 0. \qquad \text{(VII-8)}$$

This initial condition determines the value of k in Equation VII-7.

Evaluation of k in this manner followed by substitution of the calculated value back into Equation VII-7 completes the solution of the initial value problem. The solution is given in Equation VII-9.

$$C(t) = [C_o v_f/(v_f + Ak_m)] \left\{1 - \exp [- (v_f + Ak_m)/V_{cell}]t\right\} \quad \text{(VII-9)}$$

Equation VII-9 describes the concentration of analyte in the cell as a function of time for the period from t = 0 to t = τ, during which the sample plug is entering the cell.

To derive the equation describing the concentration of analyte in the cell after t = τ, the point at which the trailing edge of the sample plug passes into the cell, it is necessary to return to the basic material balance for the system. Since no new analyte is entering the cell, the material balance in this case is given by Equation VII-10, which is analogous to Equation VII-1.

$$dN_{cell} = - (dN_{out} + dN_{elec}) \quad \text{(VII-10)}$$

Development of this equation in a manner paralleling that shown in Equations VII-2 through VII-4 yields Equation VII-11:

$$V_{cell} dC/dt = - [C(t)v_f + Ak_m C(t)] \quad \text{(VII-11)}$$

Algebraic transformation results in an equivalent form:

$$dC/C(t) = - [(v_f + Ak_m)/V_{cell}]dt \quad \text{(VII-12)}$$

Integration of both members of Equation VII-12 between limits of t = τ and t = t for the right member and the corresponding limits of C(τ)

and C(t) for the left member gives Equation VII-13.

$$\ln[C(t)/C(\tau)] = - [(v_f + Ak_m)/V_{cell}](t - \tau) \qquad \text{(VII-13)}$$

Exponentiation of both members followed by multiplication of both sides of the resultant equation by $C(\tau)$ yields Equation VII-14.

$$C(t) = C(\tau) \exp \left\{- [(v_f + Ak_m)/V_{cell}](t - \tau)\right\} \qquad \text{(VII-14)}$$

$C(\tau)$ is given by Equation VII-9 for $t = \tau$. Equation VII-14 describes the concentration of analyte in the cell for all times after $t = \tau$.

When combined with Equation I-6, Equations VII-9 and VII-14 also define the limiting current observed in FIA, $I_l(t)$, for the injection of a sample peak of concentration C_o. The value of $I_l(t)$ is calculated from Equation I-6 using the corresponding value of C(t) calculated from Equation VII-9 or VII-14.

A significant observation regarding both Equations VII-9 and VII-14 is that the value of C(t), and therefore $I_l(t)$, is directly proportional to C_o, the concentration of analyte in the sample. Hence, the desired linear relationship between I_l and the concentration of analyte in the sample is also valid for the vibrating electrode in FIA.

Cursory inspection of Equation VII-9 reveals that the right member is composed of 2 primary factors. The first factor is independent of time and describes the concentration of analyte attained in the cell after steady-state conditions have been established. The second factor describes the exponential increase in concentration which occurs during the period that the sample plug is entering the cell. Steady-state conditions are attained when the value of the second factor becomes

unity, i.e., at times approaching infinity for a plug of infinite length. Experimentally, such conditions are produced by substitution of a solution of analyte at concentration C_o for the supporting electrolyte postulated in the second assumption of the theoretical treatment.

The steady-state values for the concentration, C_{ss}, and the limiting current, $I_{l,ss}$, are defined by Equations VII-15 and VII-16, respectively.

$$C_{ss} = v_f C_o/(v_f + Ak_m) \qquad \text{(VII-15)}$$

$$I_{l,ss} = nFAk_m v_f C_o/(v_f + Ak_m) \qquad \text{(VII-16)}$$

The fractional conversion, ϵ, for the vibrating electrode in FIA is defined as the fraction of analyte entering the cell which reacts at the electrode. It is most readily calculated by dividing the steady-state flux of analyte to the electrode, $Ak_m C_{ss}$, by the total influx of analyte into the cell, $v_f C_o$. Substitution of the expression given in Equation VII-15 for C_{ss} in this ratio yields Equation VII-17, which is used to calculate the value of ϵ. It is significant that the fractional conversion of the electrode is independent of the value of V_{cell}.

$$\epsilon = Ak_m/(v_f + Ak_m) \qquad \text{(VII-17)}$$

Experimentally, ϵ is calculated from the ratio of $I_{l,ss}$ to I_{coul}, the current which would result from quantitative (coulometric) reaction of the analyte at the electrode. I_{coul} is defined by Equation VII-18.

$$I_{coul} = nFv_f C_o \qquad \text{(VII-18)}$$

The product 100ϵ is referred to as the conversion efficiency of the electrode.

Equations corresponding to Equations VII-15 and VII-17 are given by Pickett in his discussion of the continuously stirred tank electrochemical reactor (CSTER) (155). However, Pickett only considers the equations relating to steady-state, continuous operation of the CSTER, which are of primary interest in chemical engineering. Pickett defines the ideal CSTER as

> "a flow reactor which operates at a steady state with perfect mixing of the contents. The composition of the solution leaving the reactor is constant and is the same as that of the solution within the reactor."

From this definition, it is evident that the vibrating electrode and flow system, when operated under steady-state conditions, constitute a CSTER. The vibrating electrode combines the functions of electrode and stirrer.

Analysis of Equations VII-9, VII-14, and VII-17 shows that 2 parameters may be independently varied for a given electrode and flow system, viz., v_f and k_m. The value of v_f is governed by the flow system and that of k_m (and thus Ak_m) by the vibrational parameters. It is instructive to consider the limiting cases defined by the relative magnitudes of v_f and Ak_m.

For $v_f \gg Ak_m$, Equations VII-9 and VII-17 reduce to the forms given in Equations VII-19 and VII-20, respectively:

$$C(t) = C_o\left\{1 - \exp\left[-\left(v_f/V_{cell}\right)t\right]\right\} \qquad \text{(VII-19)}$$

$$\epsilon = 0 \qquad \text{(VII-20)}$$

Equation VII-19 is equivalent to the corresponding equation derived by Pungor, et al. (149) for potentiometric electrodes in flowing systems in which the electrode is preceded by a mixing chamber. Potentiometric electrodes, by definition, operate at zero current and consequently consume no analyte. The conversion efficiency is thus 0%, and the value of Ak_m is thus zero. Therefore, the conditions set forth for the derivation of Equations VII-19 and VII-20 are satisfied. Equation VII-19 should also be applicable to amperometric electrodes of low efficiency (e.g., tubular electrodes) in similar systems, where a mixing chamber precedes the electrode.

In their derivation, Pungor and co-workers did not consider the use of amperometric electrodes in flowing streams, and the equations described in the present work constitute a significant extension of those derived by Pungor, et al. It is interesting to note that the consumption of analyte by the electrode affects both the concentration of analyte in the cell at steady-state conditions and the "time constant" of the response of the cell to a plug of injected analyte.

For $Ak_m \gg v_f$, Equations VII-9 and VII-17 reduce to the forms given in Equations VII-21 and VII-22, respectively.

$$C(t) = 0 \qquad \text{(VII-21)}$$

$$\epsilon = 1.0 \qquad \text{(VII-22)}$$

These trivial results indicate that the electrode in this hypothetical system operates at 100% efficiency and that the analyte quantitatively reacts at the electrode. Both results indicate that the electrode is coulometric. Also, Equation VII-16 reduces to Equation VII-18. This

is the equation for a coulometric electrode, as previously noted.

If the concentration of analyte in the cell is $C(t) = C_{init}$ and the flow of solution through the cell is suddenly stopped, the current decays according to Equation VII-14, where C_{init} replaces $C(\tau)$. However, $v_f = 0$ and therefore may be eliminated from the equation. Hence, Equation VII-14 reduces to the form shown in Equation VII-23:

$$C(t) = C_{init} \exp [- (Ak_m/V_{cell})t] \qquad \text{(VII-23)}$$

Equation VII-23 is identical to that derived by Meites (p. 516 of 141) for the bulk electrolysis of the contents of an electrolytic cell. The constant Ak_m/V_{cell} is equal to $AD/V_{cell}\delta$, the cell constant.

The preceding arguments have illustrated that the equations derived in this section comprise a generalization of several previously known equations which apply to seemingly unrelated systems. They also show the relationship of the vibrating electrode in FIA to other, more familiar methods.

The equations derived in this section should also apply to systems employing RDEs in FIA, because the rate of mass transport to the RDE is independent of the flow rate and the contents of the cell are mixed by the RDE. The negative deviations from proportionality between the peak current and $\omega_r^{1/2}$ noted by Oosterhuis, et al. (152) are likely due to the significant consumption of analyte by the RDE with consequent lowering of C(t) in the cell. This effect would increase at larger values of ω_r, due to the resultant increase in k_m for the RDE.

The equations also should apply to the turbulent tubular electrode (153), although the definition of V_{cell} for this system is vague.

However, these equations are not valid for cases such as the packed bed (157) and reticulated vitreous carbon (158) electrodes, in which the assumptions of perfect mixing and homogeneity of the contents of the cell are not satisfied.

C. Engineering and Instrumentation

The experimental studies of vibrating electrodes in FIA were all conducted with Electrode B, which was constructed, mounted, and operated as described in Chapter III of this dissertation. Recordings of the limiting currents, designated as $I_l(t)$ and $\Delta I_l(t)$ for the DC and HMVE(AM) studies, respectively, were obtained using a Speedomax XL-680 strip-chart recorder, manufactured by the Leeds and Northrup Co., North Wales, PA. The remaining electronic instrumentation employed in these experiments has been presented in Chapter IV.

In the absence of analyte, background potentials on the order of 50 mV were observed at the current output of the potentiostat. These background potentials, which originated from the bias currents of the operational amplifiers comprising the instrumentation amplifier and from the residual current at the working electrode, were offset to zero by the circuit depicted in Figure VII-1. When connected between the potentiostat and recorder as shown, this circuit permitted cancellation of background potentials up to 85 mV. Negative potentials were offset by reversal of the 2 leads to the offset circuit. The 20 KΩ resistor and 10-μF capacitor comprised an LP filter with a time constant of 0.2 sec, which filtered out the high-frequency noise produced by

Figure VII-1. Schematic diagram of offset circuit

B1 – Hg cell, 1.35 V; P1 – 10-turn precision potentiometer; S1 – SPST switch.

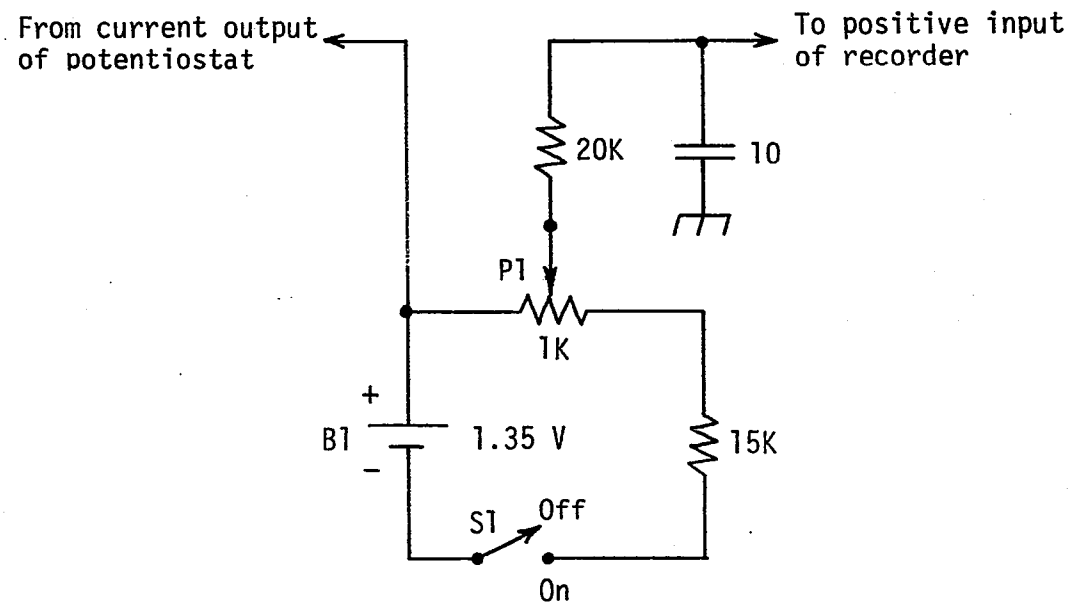
From current output
of potentiostat
To positive input
of recorder
20K
10
P1
1K
+
B1
1.35 V
-
15K
S1
Off
On

the potentiostat. The 10-μF capacitor was connected across the input leads to the recorder and was used only when required.

Insertion of this offset circuit and LP filter allowed recordings of $I_1(t)$ to be obtained at current sensitivities as high as 500 pA $in.^{-1}$, a twenty-fold improvement over the most sensitive value previously attained in this laboratory. At this sensitivity, adjustment of P1 was still readily performed.

The flow-through cell for the vibrating electrode was constructed in the machine shop at Iowa State University. The central portion of this cell is depicted in Figure VII-2. The body of the cell was constructed from silica-loaded Teflon and had a central compartment for the vibrating electrode, an inlet channel, an outlet channel, and 2 separate compartments for the reference and counter electrodes, respectively. The front and rear sides of the compartment for the vibrating electrode were made from 2.5 x 3.5-cm plates of glass obtained from microscope slides. Sheets of transparent Teflon tape were sandwiched between the cell body and the glass plates to minimize seepage of electrolyte from the electrode compartment. The transparent sides of the electrode compartment permitted <u>in situ</u> observation of the electrode during operation. The glass plates and Teflon tape were tightly clamped to the cell body by means of 2 U-shaped metal plates.

The compartment for the vibrating electrode had a cross section of 4.0 x 2.4 mm and during operation was filled to the level of the outlet channel, 17.5 mm above the inlet. The lowermost 2.0 mm of the compartment, when viewed from the side, were semicircular in shape. The volume of the compartment as calculated from these dimensions was

Figure VII-2. Cross section of central portion of flow-through cell showing vibrating electrode

Area within rectangle PQRS is covered by Teflon tape and glass plate.

H = holes (6) for screws used to mount U-shaped clamp; CE = counter electrode; SCE = saturated calomel electrode.

Scale = 2.5:1.

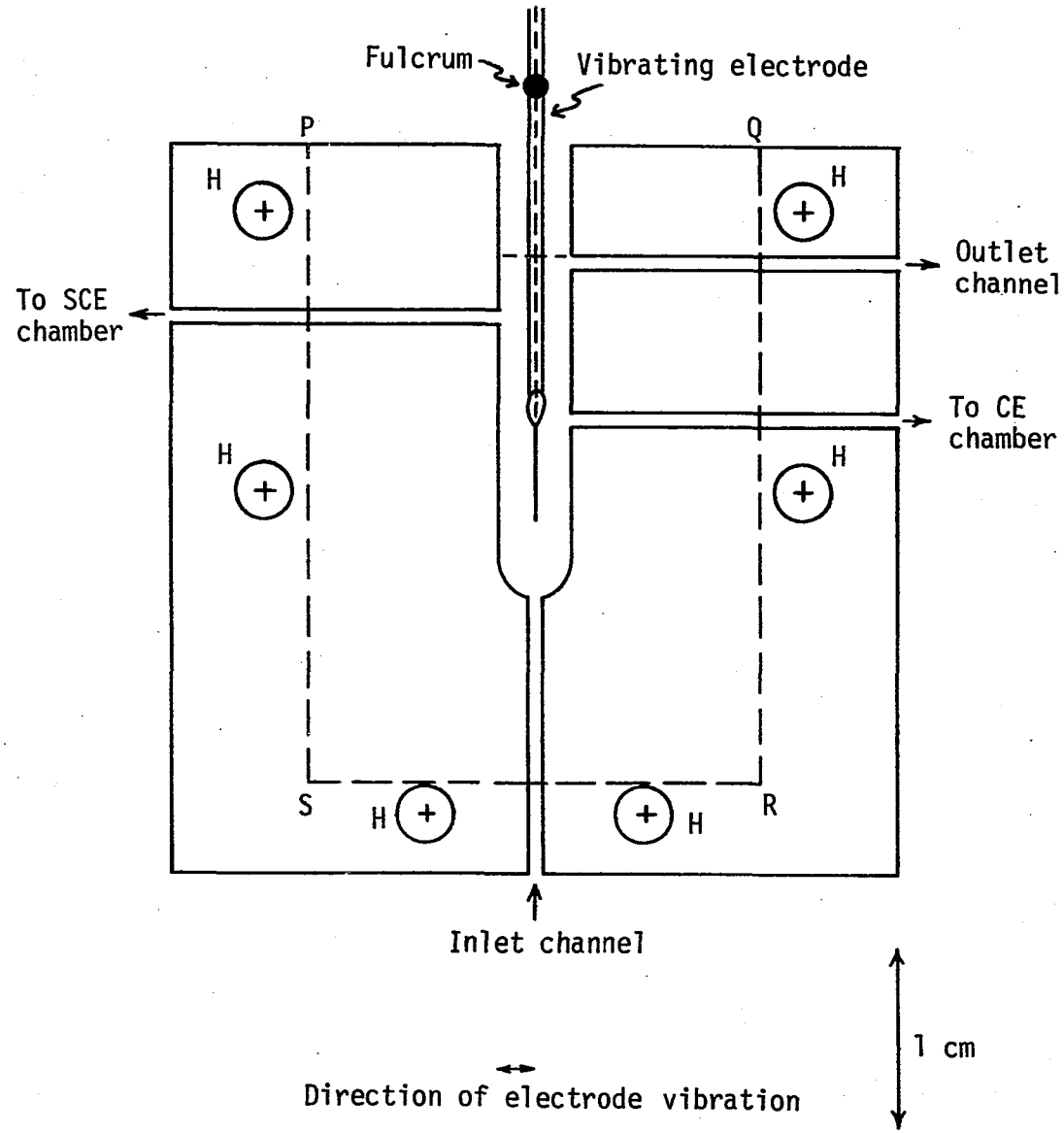
Fulcrum
Vibrating electrode
P
Q
H
H
To SCE chamber
Outlet channel
To CE chamber
H
H
S
H
H
R
Inlet channel
1 cm
Direction of electrode vibration

164 μL. This calculated value agreed, within experimental error, with the measured value, 165 μL, which was obtained by direct measurement of the volume of water required to fill the compartment to the level of the outlet channel. With the vibrating electrode positioned in this central compartment, the measured volume was 155 μL, indicating that a volume of 10 μL was displaced by the electrode.

Prior to operation, it was necessary to fill the chambers for the reference and counter electrodes with electrolyte. Care was taken to ensure that the narrow passages connecting these 2 chambers with the central compartment were free from bubbles. The outlet channel of the flow-through cell was connected to a waste bottle, which in turn was connected to an aspirator. The waste bottle was provided with an air-tight cover, and maintenance of a partial vacuum in the bottle ensured flow of solution through the outlet channel.

The flow-through cell was mounted on a miniature lab jack, manufactured by Precision Scientific, Chicago, IL. This lab jack permitted precise vertical positioning of the flow-through cell without alteration of the horizontal position of the cell. The vibrating electrode was inserted into the central compartment of the flow-through cell by vertically raising the cell until the electrode was positioned in the center of the compartment. In its final position, the tip of the electrode was situated 4 mm above the end of the inlet channel. The tubing connected to the inlet of the flow-through cell passed through a hole in the upper platform of the lab jack.

The flow system consisted of 4 basic components: the flow-through cell described above, a sample injection valve, a source bottle, and

a waste bottle. Interconnections between these components were made with 0.9-mm i.d. Teflon tubing. The source bottle was connected to the inlet of the injection valve with a 1.5-m length of tubing, which was shielded with Al foil to reduce pickup of electrical noise. The flow-through cell and sample injection valve were both enclosed in a single Faraday cage, and the source bottle was similarly shielded. All shielding was directly connected to a water-pipe ground.

Dispersion of the sample plug was minimized by utilization of a minimal length of tubing, 11 cm, between the injection valve and the inlet to the cell. The waste bottle, which was located external to the Faraday cage, was connected to the outlet channel of the cell with a 35-cm length of tubing.

Connections of Teflon tubing to the basic components of the flow system were made with Cheminert tube-end fittings and hardware, manufactured by Laboratory Data Controls, Riviera Beach, FL. The sample injection valve, Laboratory Data Controls model SVA8031, was a 4-way pneumatically actuated unit. Application of compressed air (70 psi) was controlled by an electrically operated solenoid valve. This automatic injection technique ensured reproducible sample injections. The volume of the sample loop used with the injection valve was 0.955 mL.

The value of v_f for the flow system was governed by the head of pressure of the solution in the source bottle. In this system, the head of pressure was equal to the height of the surface of the solution above the outlet channel of the cell. Discrete, reproducible values of v_f were obtained by placing the source bottle, filled to a standard level, on any of 4 separate shelves located above the laboratory bench.

The level of the solution was maintained within a tolerance of $\pm$ 0.5 cm from the standard level, corresponding to a maximum variation of $\pm$ 2% in the head of pressure. The experimental values of v_f were measured by recording the time required for a known volume of solution, 2.00 or 3.00 mL, to accumulate in a 10-mL buret. For this measurement, an 11-cm length of tubing was substituted for the connection to the cell, and the end of this tubing was situated at the same level as the outlet of the cell.

Experimental values of v_f measured at each of the 4 levels are tabulated in Table VII-1. At each head of pressure, the observed values of v_f differ significantly for the 2 positions of the injection valve. This effect arises from the nature of the driving force for the flow. Because this flow system relies on gravity feed and not on a positive displacement pump, the additional resistance presented by the sample loop reduces the flow rate from the value observed with the shorter bypass loop in the flow system. In both cases, however, the value of v_f is directly proportional to the head of pressure.

For the evaluation of experimental data obtained with this flow system, the value of v_f used in the calculations was that prevailing at the time of measurement of $I_1(t)$. In most cases the applicable value of v_f was that measured with the sample injection valve in the On position, because the valve remained in this position during recording of the entire peak.

Table VII-1. Flow rate as a function of head of pressure

Head of pressure (cm)	Flow rate at indicated position of injection valve[a]			
	Off (mL min^{-1})	On (mL min^{-1})	Off (mL sec^{-1})	On (mL sec^{-1})
37.7	0.800	0.632	0.0133	0.0105
65.1	1.38	1.09	0.0229	0.0182
97.8	2.09	1.69	0.0348	0.0281
133.5	2.85	2.32	0.0475	0.0386

[a]Off: bypass loop in flow stream; On: sample loop (V_s = 0.955 mL) in flow stream.

D. Experimental Evaluation of Equations

Residual voltammograms of Electrode B in the flow system are illustrated in Figure VII-3. Both voltammograms were obtained in air-saturated 0.01 M H_2SO_4 at v_f = 0.63 mL min^{-1}, and the electrode was either held stationary or vibrated at Re_v = 66.5, as designated in the figure. Mass-transport limited currents were observed at potentials of less than + 0.1 V vs. SCE, corresponding to the reduction of dissolved O_2. These currents increased ten-fold upon vibration of the electrode. The increased value of the mass-transport limited current noted at the vibrating electrode dramatically illustrates the enhancement of mass transport resulting from the vibration of the electrode. These results show that the sensitivity and conversion efficiency of the vibrating electrode are each approximately 10 times greater than the corresponding values for the same electrode when stationary.

The measured values of $I_{l,ss}$ at the vibrating electrode were approximately 3.5% greater at v_f = 2.09 mL min^{-1} than at v_f = 0.80 mL min^{-1}. At first glance, these data appear to contradict the assumption that the value of k_m for the vibrating electrode is independent of v_f. However, more careful theoretical analysis reveals that the value of $I_{l,ss}$ does exhibit a dependence on v_f, as predicted by Equation VII-16. The increased value of $I_{l,ss}$ at higher flow rates results not from an increase in the value of k_m, but, rather, from the increased value of C_{ss} characteristic of the higher flow rate.

The results of a study designed to test the validity of Equations VII-15 and VII-16 under experimental conditions are presented in

Figure VII-3. Effect of vibration of the electrode on mass transport in FIA

Scan rate = 5.0 V min^{-1}; f = 240.0 Hz; Re_v = 66.5; a_{pp} = 0.481 mm; v_f = 0.800 mL min^{-1}; Electrode B; air-saturated 0.01 M H_2SO_4.

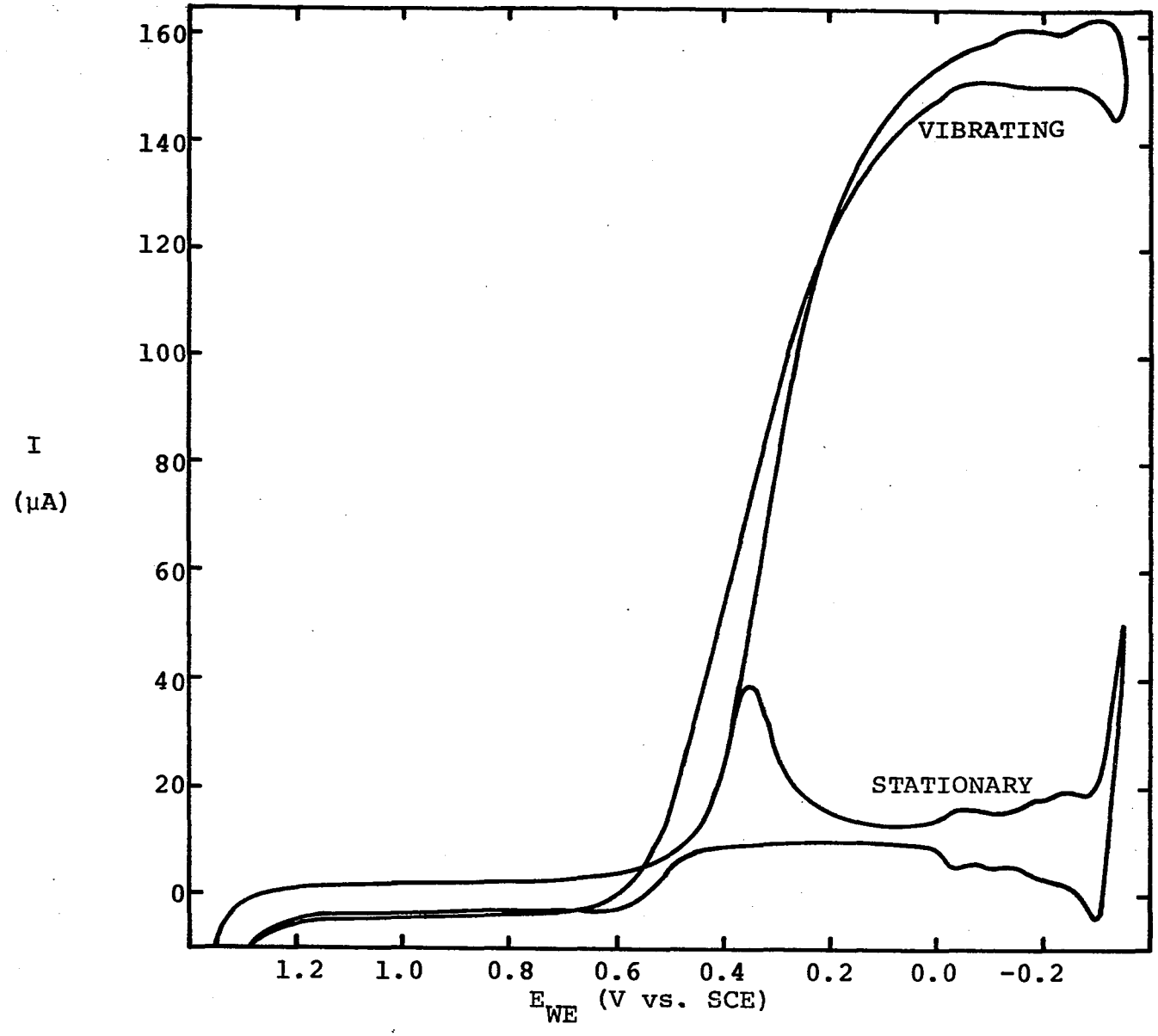
160
140
120
100
80
60
40
20
0
I
(μA)
VIBRATING
STATIONARY
1.2
1.0
0.8
0.6
0.4
0.2
0.0
-0.2
E_WE (V vs. SCE)

Table VII-2. Steady-state values of I_l were measured at 8 known flow rates for the oxidation of 0.500 mM I^- in 0.02 M HCl. The values of I_{coul} shown in the table were calculated from the experimental values of v_f and C_o using Equation VII-18. The fractional conversion, ϵ, was calculated for each flow rate from the ratio of the tabulated values of $I_{l,ss}$ and I_{coul}. From the experimental values of ϵ, the product Ak_m was calculated for each flow rate by means of Equation VII-24, which was obtained by algebraic manipulation of Equation VII-17.

$$Ak_m = v_f \epsilon/(1 - \epsilon) \qquad \text{(VII-24)}$$

When expressed in equivalent units, the values of Ak_m and v_f represent the relative magnitudes of the flux of analyte to the electrode and the outflow of unreacted analyte from the cell, respectively.

Division of Ak_m by the geometric area of the electrode, 0.05052 cm^2, yielded the value of k_m for the electrode. The thickness of the diffusion layer, δ, was calculated from this value of k_m using Equation VII-25.

$$\delta = D/k_m \qquad \text{(VII-25)}$$

The value used for D was that employed previously, 1.56×10^{-5} $cm^2 sec^{-1}$.

The calculated values of k_m and δ are constant within 3% over the range of flow rates studied, 0.63 to 2.85 mL min^{-1}. This result supports the validity of the seventh assumption set forth in Section A of this chapter and lends credibility to Equations VII-15 and VII-16, which characterize the steady-state behavior of the vibrating electrode in FIA.

Table VII-2. Study of vibrating electrodes in FIA: steady-state conditions[a]

Flow rate ($mL\ min^{-1}$)	Flow rate ($mL\ sec^{-1}$)	$I_{1,ss}$ (μA)	I_{coul} (μA)	ϵ	Ak_m ($cm^3 sec^{-1}$)	k_m ($cm\ sec^{-1}$)	δ (μm)
0.632	0.0105	79.0	508	0.156	0.00194	0.0384	4.06
0.800	0.0133	80.9	644	0.126	0.00192	0.0380	4.10
1.09	0.0182	82.8	878	0.0944	0.00190	0.0376	4.15
1.38	0.0229	84.2	1107	0.0761	0.00189	0.0374	4.17
1.69	0.0281	85.2	1357	0.0628	0.00188	0.0372	4.19
2.09	0.0348	86.3	1679	0.0514	0.00189	0.0374	4.17
2.32	0.0386	86.5	1862	0.0465	0.00188	0.0372	4.19
2.85	0.0475	87.9	2293	0.0383	0.00190	0.0376	4.15

[a] $f = 240.0$ Hz; $Re_v = 66.5$; $a_{pp} = 0.481$ mm; Electrode B; 0.500 mM I^- in 0.02 M HCl; $E_{WE} = +0.800$ V vs. SCE.

The conversion efficiencies calculated for the vibrating electrode in this study varied from 15.6% at v_f = 0.63 mL min^{-1} to 3.83% at v_f = 2.85 mL min^{-1}. These values compare with conversion efficiencies of 0.93% at v_f = 2.0 mL min^{-1} (2) and 0.35% at v_f = 3.15 mL min^{-1} (159) calculated from typical data quoted for tubular electrodes of similar area by Blaedel and co-workers. Hence, the vibrating electrode operates at conversion efficiencies 5 to 10 times greater than those obtained under corresponding conditions at the tubular electrode. As a result of this increased conversion efficiency, the detection limits observed at the vibrating electrode are expected to be 1/5 to 1/10 those noted by Blaedel for the tubular electrode, assuming that the background currents, which are proportional to the area of the electrode, are of equal magnitude.

Repetition of this experiment at v_f = 0.632 mL min^{-1} and v_f = 1.69 mL min^{-1} yielded the results shown in Table VII-3. Values are also given for Ak_m, k_m, and δ calculated on the basis of I_l observed at the same electrode in the batch cell, which is described in Section F of Chapter III. Since the batch cell was filled with the same solution employed for the sample plugs in the FIA experiments, Ak_m and k_m were calculated from Equation I-6 for $C^b = C_o$.

The decreased value of $I_{l,ss}$ in FIA relative to I_l in the batch cell is a direct consequence of the depletion of analyte in the flow-through cell. This depletion was not observed in the batch cell on the time scale employed in this experiment, due to the much larger cell volume, 28 mL. The values of Ak_m, k_m, and δ calculated at the 2 flow rates in FIA and in the batch cell agree to within 3%, showing

Table VII-3. Comparison of calculated values for k_m and δ for Electrode B in flow-through and batch cells[a]

Flow rate (mL min^{-1})	Flow rate (mL sec^{-1})	$I_{1,ss}$ (μA)	I_{coul} (μA)	ϵ	Ak_m ($cm^3 sec^{-1}$)	k_m (cm sec^{-1})	δ (μm)
0.632	0.0105	84.3	508	0.166	0.00209	0.0414	3.77
1.69	0.0281	91.2	1357	0.0672	0.00203	0.0402	3.88
Batch cell		100.0	n.a.[b]	n.a.[b]	0.00207[c]	0.0410	3.80

[a] f = 240.0 Hz; Re_v = 66.5; a_{pp} = 0.481 mm; Electrode B; C_o = 0.500 mM I^- in 0.02 M HCl; E_{WE} = + 0.800 V vs. SCE.

[b] Not applicable to batch cell (Chapter III, Section F).

[c] Calculated using Equation I-6 for $C^b = C_o$.

that these parameters are essentially independent of both the flow rate and the cell volume.

This experiment also illustrated a particular advantage of the vibrating electrode over other types of electrodes, namely, that the vibrating electrode may be operated under identical conditions in both the batch and flow-through cells. The vibrating electrode and flow-through cell employed in these experiments were both designed to facilitate application of the vibrating electrode to batch analysis and FIA. This study represents the first application of a particular electrode to both batch analysis and FIA under identical hydrodynamic conditions.

The values of Ak_m shown in Table VII-3 are approximately 10% greater than those presented in Table VII-2. The smaller values in Table VII-2 likely result from partial fouling of the electrode by silicone stopcock grease, which was used to seal capillary leaks between the Teflon tape and the cell body. The value of I_1 was restored to the original value, observed in Table VII-3, by dipping the electrode into a concentrated solution of KOH in ethanol, which dissolved the silicone grease.

Having shown that the steady-state portions of Equations VII-9 and VII-14 are valid, it is now possible to study the time dependence of $I_1(t)$ predicted by these equations. From inspection of Equations I-6, VII-9, and VII-16, it is evident that Equation VII-9 may be expressed in an alternate form, Equation VII-26, in which $C(t)$ and $C_o v_f/(v_f + Ak_m)$ are replaced by $I_1(t)$ and $I_{1,ss}$, respectively:

$$I_1(t) = I_{1,ss} \left\{1 - \exp\left[-(v_f + Ak_m)/V_{cell}\right]t\right\} \qquad \text{(VII-26)}$$

Algebraic transformation of Equation VII-26 produces an equivalent form:

$$1 - [I_1(t)/I_{1,ss}] = \exp\left\{\left[-(v_f + Ak_m)/V_{cell}\right]t\right\} \qquad \text{(VII-27)}$$

The ratio $I_1(t)/I_{1,ss}$ represents the relative, time-dependent current and is consequently designated as I_r.

$$I_r = I_1(t)/I_{1,ss} \qquad \text{(VII-28)}$$

Combination of Equations VII-27 and VII-28 followed by removal of the exponential portion yields Equation VII-29:

$$\ln (1 - I_r) = -[(v_f + Ak_m)/V_{cell}]t \qquad \text{(VII-29)}$$

For the rising portion of an observed peak, a graph of experimental values of $\ln (1 - I_r)$ vs. time should be linear with a slope of $-(v_f + Ak_m)/V_{cell}$. Hence, an effective value for V_{cell} may be calculated from Equation VII-30.

$$V_{cell} = -(v_f + Ak_m)/\text{slope} \qquad \text{(VII-30)}$$

From inspection of Equations I-6 and VII-14, it is evident that Equation VII-14 may similarly be expressed in an alternate form, shown in Equation VII-31.

$$I_1(t) = I_1(\tau) \exp\left\{\left[-(v_f + Ak_m)/V_{cell}\right](t - \tau)\right\} \qquad \text{(VII-31)}$$

For the injection of a large sample plug, $I_1(\tau)$ approaches $I_{1,ss}$. Under such conditions, the portion of the peak during which $I_1(t)$ is

decaying is described by Equation VII-32.

$$I_1(t) = I_{1,ss} \exp \left\{ [- (v_f + Ak_m)/V_{cell}](t - \tau) \right\} \qquad \text{(VII-32)}$$

Substitution of I_r, defined by Equation VII-28, followed by simplification yields Equation VII-33.

$$\ln I_r = - [(v_f + Ak_m)/V_{cell}](t - \tau) \qquad \text{(VII-33)}$$

A plot of experimental values of $\ln I_r$ vs. time for the falling portion of an observed peak should also be linear with a slope of $- (v_f + Ak_m)/V_{cell}$. Again, the effective value of V_{cell} for this portion of the peak may be calculated from Equation VII-30.

Experimentally obtained data for both the rising and falling portions of the current peaks observed for the injection of 0.500 mM I^- in 0.020 M HCl are presented in Table VII-4 for v_f = 0.632 mL min^{-1}. In contrast to the theoretical treatment, the time t = 0 in these experiments was defined as the time that the injection valve was switched to the On position. Due to the 11-cm length of tubing between the injection valve and the cell, these experimental times were greater than the theoretical times by $(0.070/v_f)$sec, for v_f in mL sec^{-1}. The calculated values of $\ln (1 - I_r)$ for the rising portion and $\ln I_r$ for the falling portion of the peak are graphed as a function of time in Figures VII-4 and VII-5, respectively. The slopes of these graphs are - 0.161 sec^{-1} for the rising portion of the peak and - 0.0924 sec^{-1} for the falling portion of the peak. These slopes were measured from the line determined by the lattermost 5 points shown on each graph; points corresponding to smaller values of t lay below the extrapolated

Table VII-4. Study of vibrating electrodes in FIA: plug injection at v_f = 0.632 mL min^{-1} [a]

Rising portion of peak			Falling portion of peak		
t (sec)	$I_1(t)$ (μA)	ln $(1 - I_r)$	t (sec)	$I_1(t)$ (μA)	ln I_r
0	0.0	0.000	72	84.3	0.000
6	0.0	0.000	78	83.7	- 0.00716
9	4.5	- 0.0550	84	80.3	- 0.0487
12	20.4	- 0.278	90	73.3	- 0.139
15	35.5	- 0.546	96	62.5	- 0.298
18	48.4	- 0.854	102	49.6	- 0.530
21	58.7	- 1.193	108	37.0	- 0.824
24	66.8	- 1.576	114	26.1	- 1.174
27	72.6	- 1.981	120	17.4	- 1.576
30	76.9	- 2.431	126	11.0	- 2.034
33	79.8	- 2.928	132	6.5	- 2.560
36	81.5	- 3.402	138	3.7	- 3.124
39	82.6	- 3.901	144	2.1	- 3.690
42	83.4	- 4.537	150	1.2	- 4.250

[a] f = 240.0 Hz; Re_v = 66.5; a_{pp} = 0.481 mm; Electrode B; V_s = 0.955 mL; C_o = 0.500 mM I^- in 0.020 M HCl; E_{WE} = + 0.800 V vs. SCE; $I_{1,ss}$ = 84.3 μA.

Figure VII-4. Graph of ln $(1 - I_r)$ vs. time for rising portion of peak

For data and experimental conditions, see Table VII-4.

Slope = - 0.1608 sec^{-1}.

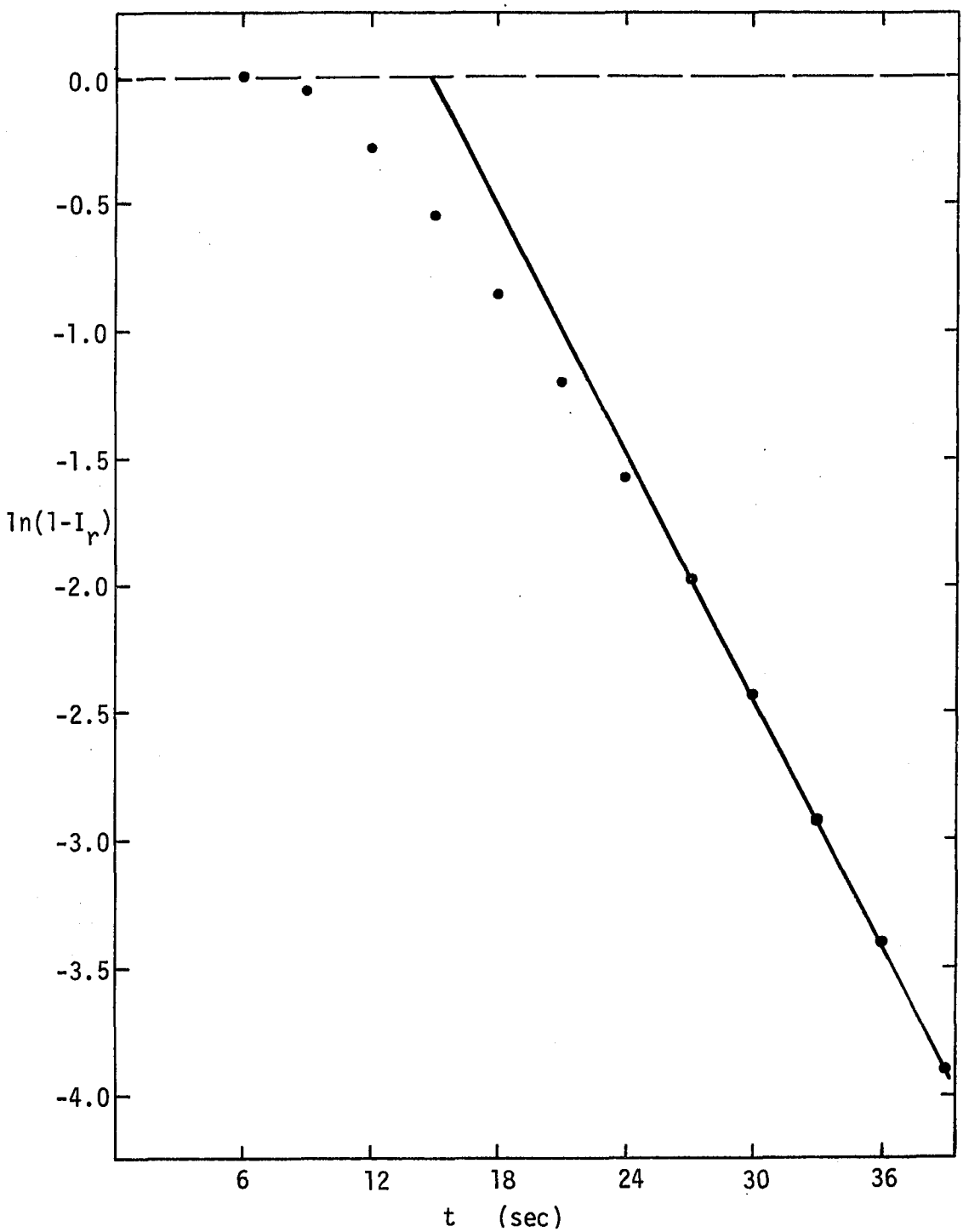
0.0
-0.5
-1.0
-1.5
ln(1-I_r)
-2.0
-2.5
-3.0
-3.5
-4.0
6
12
18
24
30
36
t (sec)

Figure VII-5. Graph of ln I_r vs. time for falling portion of peak

For data and experimental conditions, see Table VII-4.

Slope = - 0.0924 sec^{-1}.

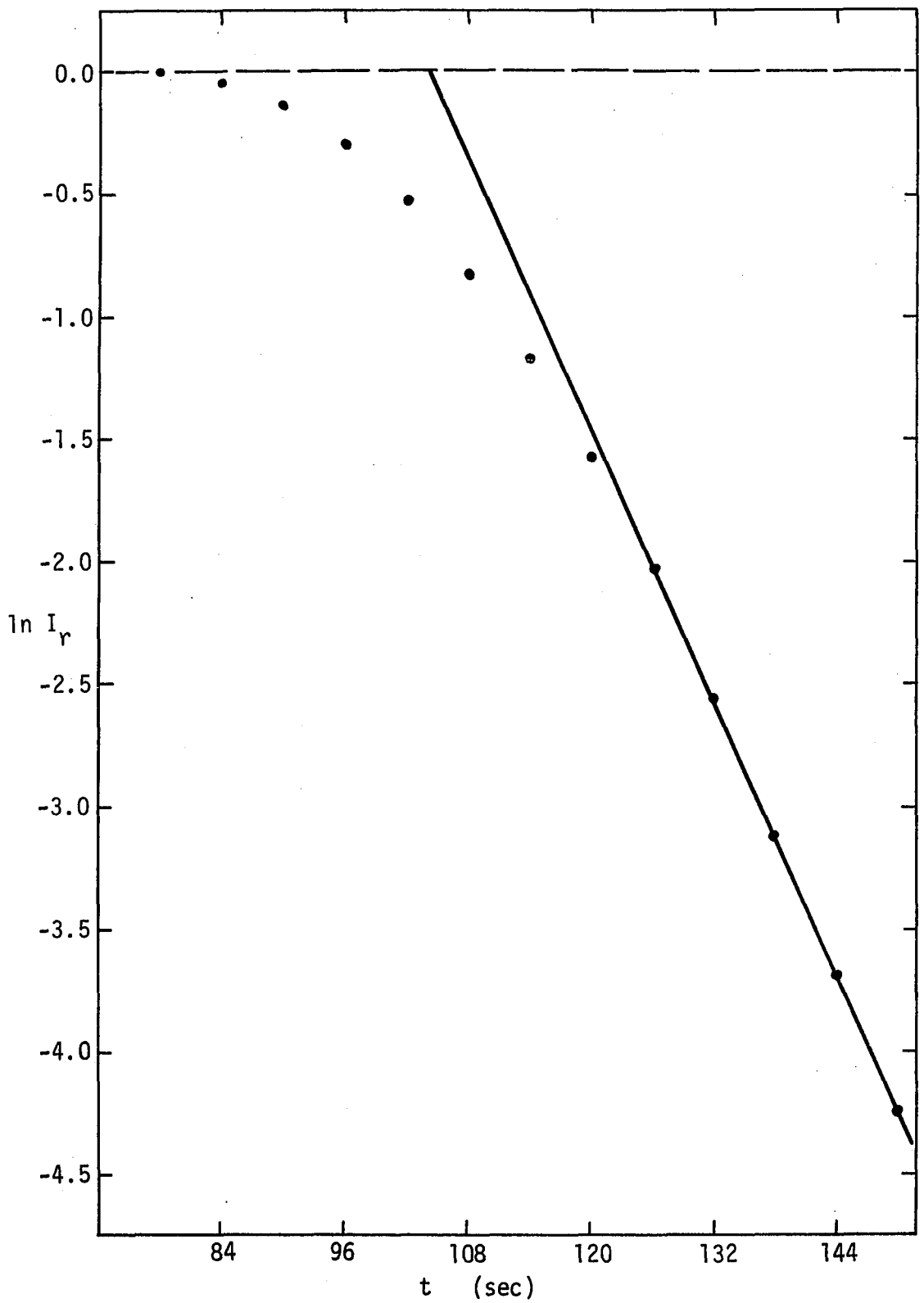
0.0
-0.5
-1.0
-1.5
-2.0
-2.5
-3.0
-3.5
-4.0
-4.5
ln I_r
84
96
108
120
132
144
t (sec)

Table VII-5. Study of vibrating electrodes in FIA: plug injection at v_f = 1.69 mL min^{-1} [a]

Rising portion of peak			Falling portion of peak		
t (sec)	$I_1(t)$ (μA)	ln $(1 - I_r)$	t (sec)	$I_1(t)$ (μA)	ln I_r
0	0.0	0.000	27	91.2	0.000
3	0.0	0.000	30	88.3	- 0.0324
6	40.6	- 0.589	33	81.0	- 0.119
9	69.2	- 1.424	36	68.0	- 0.293
12	83.0	- 2.407	39	52.4	- 0.554
15	88.1	- 3.379	42	36.4	- 0.919
18	90.1	- 4.416	45	23.2	- 1.367
21	90.8	- 5.427	48	13.7	- 1.893
			51	7.5	- 2.496
			54	3.8	- 3.176
			57	1.9	- 3.869
			60	0.9	- 4.616

[a] f = 240.0 Hz; Re_v = 66.5; a_{pp} = 0.481 mm; Electrode B; V_s = 0.955 mL; C_o = 0.500 mM I^- in 0.020 M HCl; E_{WE} = + 0.800 V vs. SCE; $I_{1,ss}$ = 91.2 μA.

line. From these slopes, effective cell volumes were calculated using Equation VII-30. The values for v_f and Ak_m were taken from Table VII-3. Data in this table were obtained concurrently with the data shown in Tables VII-4 and VII-5, thus assuring consistency of results. The calculated values of V_{cell} at v_f = 0.632 mL min^{-1} were 78.5 μL for the rising portion of the peak and 137 μL for the falling portion of the peak.

Data from an analogous experiment conducted at v_f = 1.69 mL min^{-1} are presented in Table VII-5. The slopes of the graphs of ln (1 - I_r) and ln I_r vs. t for these data were - 0.395 sec^{-1} for the rising portion of the peak and - 0.230 sec^{-1} for the falling portion, respectively. These slopes corresponded to effective cell volumes of 76.3 μL for the rising portion of the peak and 131 μL for the falling portion. The graphs were similar in appearance to those shown for v_f = 0.632 mL min^{-1}.

For times between the rising and falling portions shown in Tables VII-4 and VII-5, the value of $I_1(t)$ was within 1% of the steady-state value, $I_{1,ss}$.

The effective cell volumes calculated in these experiments are significantly lower than the actual cell volumes calculated and measured in Section C of this chapter. A likely explanation for this divergence is that the mixing effects do not extend over the entire cell. Most notably, that portion of V_{cell} above the passage to the counter electrode is not instantaneously mixed with the solution below the electrode. The fifth assumption set forth in Section B of this chapter is therefore not strictly valid.

The values of V_{cell} calculated for the falling portions of the

current peaks are approximately 72% larger than those calculated for the rising portions. This variance most likely results from dispersion of the trailing edge of the sample plug. The trailing edge must pass through the entire sample loop, 1.5 m in length, prior to reaching the cell. Hence, the dispersion of the trailing edge of the sample plug is significant, whereas that of the leading edge, which passes through but 11 cm of tubing before reaching the cell, is negligible.

Observation of the central compartment of the flow-through cell during injection of a plug of 0.05% $KMnO_4$ into H_2O verified that the mixing effect of the vibrating electrode did not immediately extend over the entire central compartment. However, mixing in the lower portion of the cell was very rapid, and the composition of the region surrounding the working electrode, as estimated visually from the depth of color of the solution, appeared to be homogeneous. Significant dispersion of the trailing edge of the sample plug was also noted in this experiment. It is concluded that the assumption of instantaneous, perfect mixing is substantially valid for most of the lower portion of the central compartment of the flow-through cell, although not for the entire cell volume. In addition, the assumption of zero dispersion in the injected sample plug is definitely not valid for the trailing edge of the plug, although it is a good approximation for the leading edge. The values of 78.5 μL and 76.3 μL for the effective cell volume are therefore considered as indicative of the actual mixing conditions prevailing in the cell.

The effect of time dependence of the mixing process on the peak shapes was not investigated in this research. However, it is likely that backmixing of analyte from the upper to the lower portion of the

electrode compartment occurs during the falling portion of the current peak and contributes to the observed increase in the effective cell volume.

E. Analytical Application

A calibration curve of the response of Electrode B to injected sample plugs containing I^- is shown in Figure VII-6. The concentration of I^- in the sample plugs ranged from 1.00×10^{-3} M to 5.00×10^{-10} M, and the corresponding peak currents, I_{peak}, observed at the vibrating electrode ranged from 159 μA to 138 pA. The supporting electrolyte in both the sample plugs and the carrier solution was 0.020 M HCl, made from a single bottle of Fisher analytical grade HCl and triply-distilled water (TDW). The flow rate was 0.632 mL min^{-1} for all injections. All sample plugs had a volume of 0.955 mL, and the vibrational parameters were identical to those employed in the previous section, f = 240.0 Hz, Re_v = 66.5, and a_{pp} = 0.481 mm. The electrode was maintained at a potential of + 0.800 V vs. SCE. The experimental results were obtained over a period of 5 days, and triplicate injections were performed at each concentration level. Long-term variations in the electrode response, as evaluated from the daily variation in the peak current noted for multiple preliminary injections of 0.500 mM I^-, were less than 1% relative. These preliminary injections also served to precondition the electrode prior to the actual analytical determinations. Peak currents observed following removal and reinsertion of the electrode into the cell were also reproducible within 1% relative, provided that the

Figure VII-6. Calibration curve for response of Electrode B in FIA to I^-

$f = 240.0$ Hz; $Re_v = 66.5$; $a_{pp} = 0.481$ mm; $v_f = 0.632$ mL min^{-1}; $V_s = 0.955$ mL; $C_o = 5.00 \times 10^{-10}$ to 1.00×10^{-3} M I^- in 0.020 M HCl; $E_{WE} = +0.800$ V vs. SCE.

$pI^- = -\log I^-$; $pI_{peak} = -\log$ (peak current).

Equation of line: $pI_{peak} = (0.956 \pm 0.011)pI^- + (0.878 \pm 0.071)$. Uncertainties calculated at 90% confidence intervals.

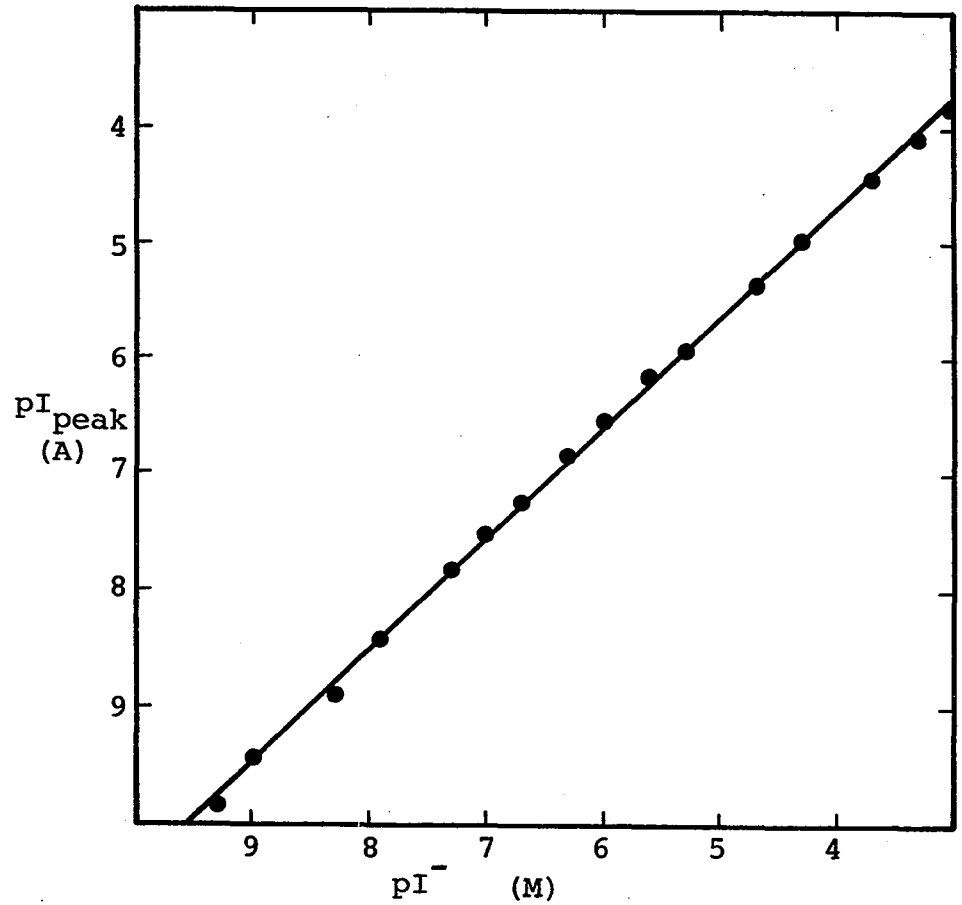
4
5
6
7
8
9
pI_{peak} (A)
9
8
7
6
5
4
pI^- (M)

electrode did not touch the sides of the compartment.

At all concentrations, the observed current peaks were similar in form to the peaks analyzed in the preceding section of this chapter. The peak currents, I_{peak}, noted for triplicate injections were reproducible within 1% relative at all concentrations above 5.00×10^{-9} M I^-. The relative variations noted for multiple injections at 1.00×10^{-9} M and 5.00×10^{-10} M I^- were 5% and 15%, respectively. Representative current peaks are illustrated in Figure VII-7; the response of the FIA system to an injected plug of 0.020 M HCl containing no added I^- is also shown. The slope of the log-log calibration curve shown in Figure VII-6 is 0.956, with an uncertainty of $\pm$ 0.011, calculated at the 90% confidence interval.

The data shown in Figure VII-7 indicate that the detection limit for I^- in this system is approximately 5×10^{-10} M I^-, for a signal-to-noise ratio of 2. This value is 1/20th the value of 1×10^{-8} M cited by Blaedel and Boyer (159) for the tubular electrode. The indicated dynamic range of the vibrating electrode in FIA, as demonstrated by these results, is 2,000,000 to 1, or more than 6 decades of concentration. These results represent both the lowest detection limit and the greatest dynamic range reported to date with electrochemical flow-through detectors. The only instances of lower detection limits reported in electroanalysis are those cited for differential pulse anodic stripping voltammetry, in which the sensitivity is greatly increased by virtue of the preconcentration of analyte inherent in the method.

The slope of 0.956 for the log-log calibration curve shown in Figure VII-6 indicates that the current observed at the vibrating

Figure VII-7. Observed response of Electrode B to injected I^-

A $C_o = 5.00 \times 10^{-6}$ M I^- in 0.020 M HCl;

B $C_o = 1.00 \times 10^{-9}$ M I^- in 0.020 M HCl;

C $C_o = 5.00 \times 10^{-10}$ M I^- in 0.020 M HCl;

D $C_o = 0$ (blank, 0.020 M HCl).

Experimental conditions shown in Figure VII-6.

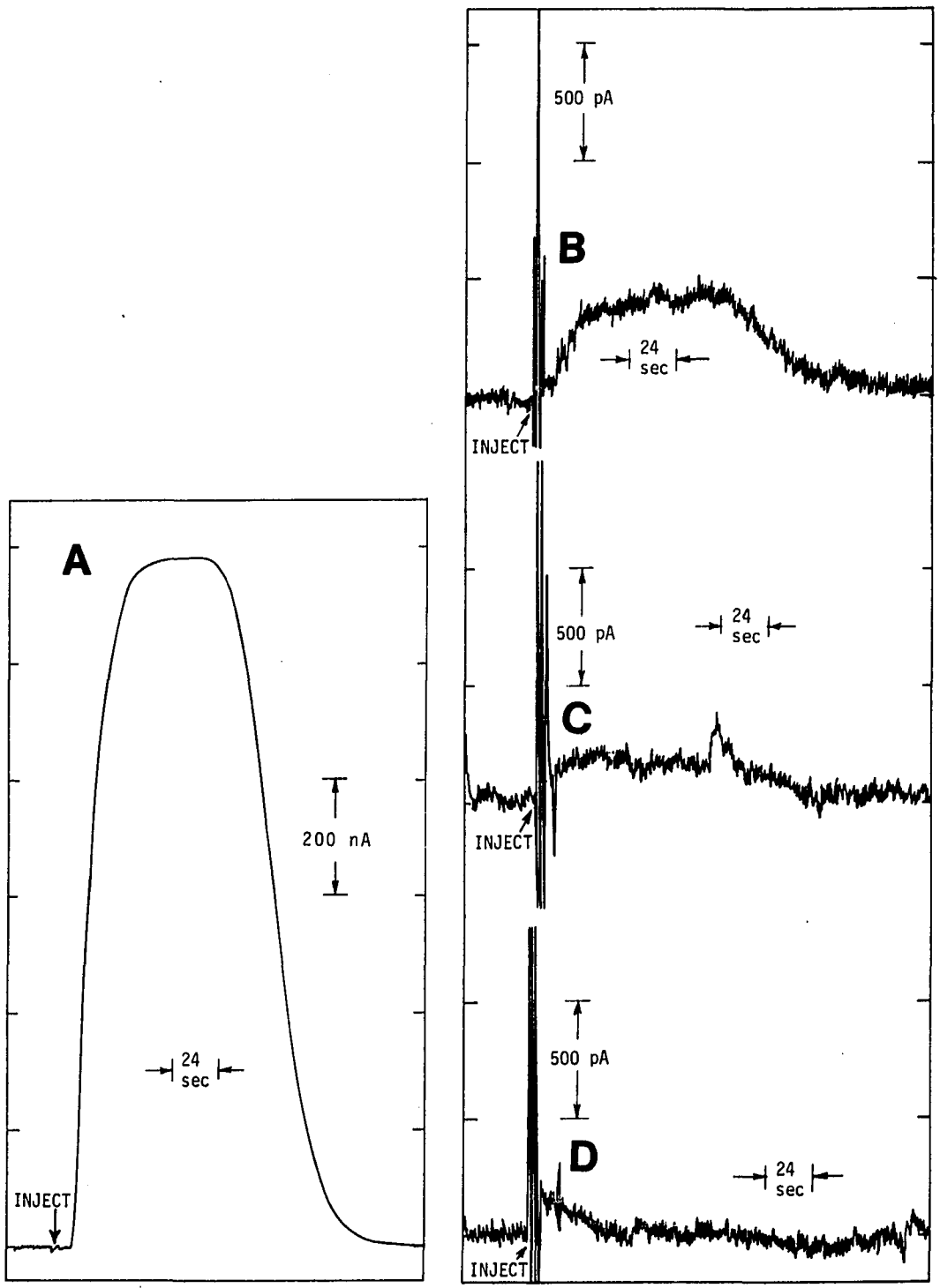
A
200 nA
24
sec
INJECT
B
500 pA
24
sec
INJECT
C
500 pA
24
sec
INJECT
D
500 pA
24
sec
INJECT

electrode, in contrast to theory, is not strictly proportional to concentration. This same property was observed with the response of this and other electrodes to O_2 and I^- in the batch cell. Therefore, it is a property of the electrode and is not related to the use of the vibrating electrode in FIA. Similar nonlinear response was noted by Küster (26) in the amperometric determination of O_2 at a vibrating electrode, and slight nonlinearity is evident in the calibration curves ($I_{peak} - C^b$) published by Harris and Lindsey for the reduction of I_2 (20) and Br_2 (21) at Pt vibrating electrodes. Because the nonlinearity is very slight, it is not evident in calibration curves ($I_{peak} - C^b$) covering concentration ranges of less than 1 decade and therefore may have been overlooked by other investigators. The reason for the nonlinearity is unknown.

Tests of HMVE(AM) in the flow-through cell indicated that the detection limit for HMVE(AM) at 95% modulation in FIA is approximately 3×10^{-9} M, a value considerably higher than that demonstrated for DC amperometry at the vibrating electrode. The detection limit for HMVE(AM) was calculated from comparison of the noise level observed at high sensitivity to the signal level, ΔI_{peak}, observed for the injection of 0.5 mM I^-. The sole advantage of HMVE(AM) in FIA is that the value of ΔI_1 decays to a constant value within less than 15 sec following any change of the potential of the electrode, as contrasted with the waiting period of up to 30 min required for the same electrode in DC amperometry. As noted in Chapter VI, HMVE(AM) discriminates against charging currents, which are the cause of the time-dependent background currents noted in DC amperometry.

The vibrating electrode was also applied to the determination of I^- in household iodized salt. Morton iodized salt was dried for 3 hr at 110 C and stored in a desiccator. A 2.4565-g sample of the dried salt was dissolved in 0.020 M HCl and diluted to volume in a 100-mL volumetric flask. From this stock solution, 5 5.00-mL aliquots were transferred to separate 100-mL volumetric flasks, and 5.00-mL, 10.00-mL, 15.00-mL, and 20.00-mL aliquots of a 10.55-μM I^- solution were added to 4 of these 5 flasks, respectively. All 5 flasks were then diluted to volume with 0.020 M HCl. These 5 solutions were then analyzed for I^- using the flow system as described above. The results of triplicate injections were averaged to give the value of I_{peak} cited for each solution. These data and the equation of the least-squares line determined by these points are given in Table VII-6. The absolute value of the x-intercept of this line, 0.449 ± 0.066 μM I^-, represents the concentration of I^- in the flask containing no standard addition. Accounting for the 1:20 dilution factor in the preparation of this solution, this value is equivalent to 149 ± 22 μg KI in the 2.4565-g sample, or 60.7 ± 9.0 ppm KI. The uncertainties in these data were all calculated at the 90% confidence interval. The comparatively large values for these uncertainties are a direct result of the nonlinearity in the electrode response, which was noted previously. The final result of 60.7 ± 9.0 ppm KI compares to the value of 85 ppm KI quoted by the manufacturer (160).

Small background currents were noted at the vibrating electrode in FIA. At a potential of + 0.750 V vs. SCE in the absence of adsorbed I^-, a constant anodic background current of 2.7 to 3.0 nA was observed

Table VII-6. Analysis of iodized salt[a]

Solution[b,c]	Added $[I^-]$ (μM)	I_{peak} (nA)[c,d]
Sample	0.000	103
1	0.527	241
2	1.055	372
3	1.582	500
4	2.110	616

[a] f = 240.0 Hz; Re_v = 66.5; a_{pp} = 0.481 mm; v_f = 0.632 mL min^{-1}; Electrode B; V_s = 0.955 mL; E_{WE} = + 0.800 V vs. SCE.

[b] Number of standard additions.

[c] Equation of line determined by least-squares program:

$$I_{peak} = (243.6 \pm 9.3)[I^-] + (104.9 \pm 12.0);$$

$$\text{x-intercept} = (109.4 \pm 12.0)/(243.6 \pm 9.3) = 0.449 \pm 0.066\ \mu M$$

$$= [I^-] \text{ in sample.}$$

All uncertainties calculated at 90% confidence intervals.

[d] Average for triplicate injections.

at Electrode B in the flow-through cell at v_f = 0.632 mL min^{-1}, f = 240.0 Hz, and Re_v = 66.5. At these same conditions but in the presence of adsorbed I^-, the corresponding background current was 1.2 nA. Injection of deaerated 0.020 M HCl into a carrier stream of air-saturated 0.020 M HCl failed to produce any measurable change in the observed current, thus showing that a cathodic contribution arising from the reduction of dissolved O_2 was not present. These background currents displayed a significant dependence on the amplitude of vibration; reduction of a_{pp} from 0.481 mm to 0.120 mm caused an immediate change in the background current from 2.7 nA to 1.4 nA. The dependence on the flow rate was much smaller. The background currents observed in 0.010 M H_2SO_4 were approximately 3 times larger than those observed in 0.020 M HCl. From these data, it is not possible to ascertain whether the background currents arise from oxidation of impurities in the supporting electrolyte or from oxidation, i.e., corrosion, of the Pt electrode. However, experiments conducted at lower values of v_f, i.e., higher values of ϵ, should be able to distinguish between these alternatives. In such experiments, significant dependence of the background current on v_f would indicate the presence of a contaminant in the supporting electrolyte.

F. Conclusion

Theoretical equations have been derived which describe the performance of the vibrating electrode in FIA for both steady-state conditions and plug injection of samples. These equations have been verified by experi-

mental studies, and the validity of the fundamental assumptions, upon which the equations are based, has been critically evaluated. It was found that the mixing process in the flow-through cell is not actually instantaneous and does not cover the entire cell volume. However, the assumption of perfect, instantaneous mixing was shown to be valid for the lower portion of the cell. Dispersion of the trailing edge of the sample plug had a noticeable effect on the nature of the falling portion of the observed current peak. The value of the mass transport coefficient for the vibrating electrode, k_m, was substantially the same for identical values of the vibrational parameters in both the batch and flow-through cells. Also, it was found to be independent of the value of v_f in the flow-through cell. It was therefore concluded that the reduced value of I_l observed in the flow-through cell resulted solely from the depletion of the concentration of analyte in the cell effected by the reaction at the electrode.

The basic equations developed in this chapter have been shown to reduce to previously known equations for the limiting cases of $Ak_m \gg v_f$, $v_f \gg Ak_m$, $v_f = 0$, and $t \rightarrow \infty$. The applicability of the basic equations, developed for vibrating electrodes, to other systems, notably the RDE in FIA, has been evaluated. However, the data presented in the literature were not sufficient to permit quantitative calculations, although the equations derived in this work were shown to explain the qualitative deviations from the Levich equation, which were noted by the authors.

The vibrating electrode has been applied to the determination of I^- by FIA. The method was found to possess the lowest detection limit and

largest dynamic range reported to date for a flow-through electrochemical detector, 5×10^{-10} M and 6.3 decades of concentration, respectively. The reproducibility and reliability of the method were evaluated, and the technique was applied to the analysis of a real sample, iodized salt. The method was also employed in an investigation of the background currents observed at amperometric electrodes. The applicability of HMVE(AM) to FIA was also investigated. It was concluded that the sole advantage of HMVE(AM) in FIA is its ability to discriminate against charging currents, thus enabling the electrode to be used immediately following a change in the electrode potential.

VIII. ANODIC BEHAVIOR OF GOLD

A. Literature

The salient features of the residual voltammogram obtained at Au electrodes in acidic, chloride-free media have been discussed by Bélanger and Vijh (86) and by Nicol (161). For voltammograms obtained in such media with voltage limits of + 1.50 V and 0.00 V vs. SCE, the authors noted a complex anodic wave commencing at + 1.10 V vs. SCE on the positive scan, corresponding to the oxidation of the Au surface to a monolayer of Au_2O_3, and a single, sharp cathodic peak at + 0.90 V vs. SCE on the negative scan, corresponding to the reduction of this oxide to Au metal. During the negative scan of applied potential, the anodic current decreased approximately 50% at E_{WE} = + 1.40 to + 1.50 V vs. SCE, relative to the value observed at E_{WE} = + 1.20 to + 1.35 V vs. SCE. In addition, Nicol (161) noted that the potentials corresponding to the onset of oxidation of the Au metal and to the reduction of the oxide film both move 60 mV in a negative direction for each unit increase in the pH.

Significant increases in the double-layer capacity of Au electrodes, based on the geometric surface area, were noted following more severe anodization of the electrodes (162). In 2.0 M Na_2SO_4, the measured double-layer capacity of a Au electrode which had no prior history of electrochemical anodization was 22.4 $\mu F\ cm^{-2}$. Anodization of this electrode at + 1.75 V vs. SCE for several minutes followed by electrochemical reduction of the oxide layer increased the observed double-layer capacity to final values of 131 to 300 $\mu F\ cm^{-2}$, with the higher

values corresponding to longer periods of anodization. These increases in the double-layer capacity were attributed to the formation of gold black and consequent roughening of the surface of the electrode, which greatly increased its electrochemical surface area.

Rand and Woods (163) described the changes in appearance noted for Au electrodes during severe anodization and subsequent reduction of the resultant oxide film:

> "The process [anodization] forms a visible deep orange layer on the electrode surface which turns black on reduction: this layer is phase oxide and its formation causes a severe roughening of the gold surface."

These authors also conducted measurements of the quantities of charge, Q_{ox}, corresponding to the oxidation of the electrode surface. The value of Q_{ox} obtained for anodization at + 1.62 V vs. SCE, prior to the formation of phase oxide, was 0.50 mcoul cm^{-2}. However, the value of Q_{ox} measured for an anodization of 1000 sec at + 1.92 V vs. SCE, corresponding to the formation of orange phase oxide, was 11.8 mcoul cm^{-2}. The authors concluded that this anodization increased the roughness of the surface of the electrode by a factor of 20.

Frankenthal and Thompson (164) conducted investigations of the film of oxide formed at Au electrodes under conditions of severe anodization. By means of interrelated gravimetric measurements, they established that the formula of the oxide forming the film was $Au(OH)_3$ and not Au_2O_3. The data were also used to calculate the current densities corresponding to formation of the oxide film, under the assumption that the film contained only Au(III). The results of these calculations indicated that film growth in excess of 1 monolayer of

oxide occurred only at potentials greater than + 1.75 V vs. SCE in 1.0 M H_2SO_4. Frankenthal and Thompson also studied the effects of trace Cl^- on the anodic behavior of Au. They observed that the anodic currents occurring at potentials between + 1.10 V and + 1.40 V vs. SCE were greatly increased in the presence of Cl^- at concentrations of 1 and 10 mM. In addition, they noted that the onset of the anodic wave occurred at potentials as low as + 0.85 V vs. SCE in the presence of Cl^-.

B. Experimental Results

The experimental evidence gathered in this research supported the conclusions reported in the literature. These studies were conducted with vibrating electrodes made from Au wire with no prior history of electrochemical anodization. Residual voltammograms were obtained at voltage limits of + 1.70 V and + 0.20 V vs. SCE. Extended anodization of such electrodes at potentials greater than + 1.75 V vs. SCE in 1.0 M H_2SO_4 changed the surface of the Au electrode from the characteristic yellow, metallic color to a duller, red-orange color, presumably owing to the formation of phase oxide. Following this anodization, the appearance of the electrode changed radically during the course of a scan of applied potential initiated at the potential of anodization, + 1.8 to + 2.0 V vs. SCE, and terminated at 0.00 V vs. SCE. The red-orange color noted during anodization persisted until the potential of the electrode reached the value corresponding to the reduction of the oxide layer, ca. + 0.90 V vs. SCE. At this point, the color of the electrode changed through a fleeting, lighter stage to a uniform black

color, which persisted at potentials more negative than + 0.90 V vs. SCE. In contrast to the single, sharp peak noted in the normal voltammogram, the cathodic reduction peak obtained following severe anodization was much broader and displayed fragmentation into minor peaks on the positive side of the main peak, as noted previously by Rand and Woods (163). With respect to the present research, the most important change resulting from severe anodization of these Au electrodes was the tremendous increase in the magnitude of the residual currents noted subsequent to such anodization and reduction of the surface oxide. The residual currents noted in the voltammograms of a given Au electrode in 1.0 M H_2SO_4, following anodization at potentials in excess of + 1.75 V vs. SCE, were approximately 10 times greater than the corresponding currents observed in the voltammogram of the same electrode prior to its first severe anodization. However, the overall features of the 2 voltammograms were identical. Anodization of Au electrodes at potentials of + 1.70 V vs. SCE or less for periods of up to 24 hr did not change the magnitude of the observed residual currents.

In contrast to the ten-fold increase in the magnitude of the residual currents observed subsequent to severe anodization, the magnitude of mass-transport controlled currents, such as the reduction of $Cr_2O_7^{2-}$ at + 0.30 V vs. SCE, remained unchanged following anodization of these Au electrodes.

The above observations are consistent with a ten-fold increase in the microscopic surface area of the electrode resulting from the anodization, since the surface-controlled currents observed in the residual voltammograms are directly proportional to the microscopic surface

area of the electrode. Although mass-transport controlled currents are also related to the area of the electrode (see Equation I-6), microscopic roughening of the electrode does not affect the flux of electroactive species to the electrode. This is because the thickness of the diffusion layer, typically 4 μm for a vibrating electrode, is much greater than the dimensions associated with surface roughening. Hence, the area of the electrode, as "seen" by the diffusing ions, remains unchanged following anodization.

Residual voltammograms of Au obtained in 1.0 M H_2SO_4 and 2.0 M HNO_3 were identical in form. However, the anodic wave in the residual voltammogram was found to be highly sensitive to the presence of Cl^- ions. This observation is in agreement with previous work (164).

In preparation for the determinations of Hg described in the following chapter, the rest potentials of Electrode E were obtained under conditions of zero current in both air-saturated 1.0 M H_2SO_4 and 2.0 M HNO_3. This measurement was performed by disconnecting the counter electrode from the potentiostat at a chosen potential, E_{dis}, during the recording of the residual voltammogram and allowing the working electrode to drift to a constant potential. This rest potential was then measured at the voltage output of the potentiostat. In both H_2SO_4 and HNO_3, the rest potentials measured at values of E_{dis} from 0.00 to 1.10 V vs. SCE, corresponding to a reduced Au surface, were + 0.45 $\pm$ 0.02 V vs. SCE, and the rest potentials measured at values of E_{dis} from 1.5 to 1.7 V vs. SCE, corresponding to an oxidized Au surface, were + 1.06 $\pm$ 0.01 V vs. SCE. Repetition of these experiments in a solution containing 0.05% $KMnO_4$ in 1.0 M H_2SO_4 indicated that the rest

potentials obtained in this solution were + 1.26 ± 0.01 V vs. SCE, regardless of the value of E_{dis}. From these experiments, it was concluded that electrodeposited Hg, which is stripped from a Au electrode at E_{WE} = + 0.9 V vs. SCE, could not be chemically stripped from the electrode under open-circuit conditions in air-saturated H_2SO_4 or HNO_3, but that it would be chemically stripped in acidic media containing $KMnO_4$.

C. Conclusion

Anodization of Au electrodes in H_2SO_4 and HNO_3 at potentials greater than + 1.75 V vs. SCE causes severe microscopic roughening of the Au surface. This surface roughening increases the residual, or background, currents observed at Au electrodes without producing corresponding increases in the currents associated with mass-transport limited reactions, such as the reduction of Hg(II). As a result, the detection limit for the voltammetric determination of species which react at a mass-transport limited rate at Au electrodes is degraded significantly by severe anodization, and optimum detection limits are expected for electrodes with no prior history of electrochemical anodization at potentials above + 1.75 V vs. SCE.

Studies of the rest potentials of Au electrodes at conditions of zero current indicate that air-saturated H_2SO_4 or HNO_3 will not chemically strip electrodeposited Hg from the electrode. However, Hg will be chemically stripped from Au electrodes in acidic solutions of $KMnO_4$.

IX. DETERMINATION OF MERCURY IN LAKE SUPERIOR WATER

A. Introduction

The application of vibrating Au electrodes to the determination of Hg at ultratrace levels in Lake Superior water (LSW) is described in this chapter. The method as presented here is applicable to aqueous samples containing Hg(II) at part per trillion (pptr) levels. The sensitivity and detection limit for this method are compared to those attainable with cold-vapor atomic absorption spectroscopy (AAS) (165), the accepted method for the determination of Hg at trace levels. Problems associated with contamination of reagents and with loss of analyte from the samples are also discussed.

Numerous analytical methods have been developed in recent years for the determination of Hg at trace concentrations, primarily as a result of justified concern for the effects of trace Hg in the environment. The reader is referred to the 1978 report by the Panel on Mercury of the National Academy of Sciences (USA) (166) for an in-depth review of the environmental, toxicological, and analytical aspects of Hg at trace levels. Analytical methods for the determination of Hg have also been reviewed by Allen (167).

The electrochemical method employed in this research for the determination of Hg is based on the method developed by Allen (167) and by Andrews, et al. (168), and refined by Lindstrom (148). In the first phase of the procedure, the mercury, present as Hg(II) in LSW, is electrochemically deposited onto the vibrating Au electrode. In the second phase, the electrode is transferred to a 1 M H_2SO_4 solution prepared

with triply distilled water (TDW), where the deposited Hg atoms are stripped from the electrode using differential pulse anodic stripping voltammetry (DPASV). These 2 portions of the procedure are referred to as the "deposition phase" and the "stripping phase," respectively. The extreme sensitivity afforded using this technique is a result of 3 factors. First, the vibration of the electrode during the deposition phase results in an extremely high rate of mass transport to the surface of the electrode. This means that a larger quantity of Hg(II) is deposited from a solution of a given concentration onto the vibrating electrode than would be deposited from the same solution onto a tubular electrode or a RDE of the same area, when applied under the normal conditions of convective mass transport. The analytical signal, which results from the reoxidation of these deposited Hg atoms, is proportional to the number of deposited atoms. A larger analytical signal is thus obtained at the vibrating electrode.

The second factor resulting in increased sensitivity for this method is the preconcentration of analyte, which is characteristic of anodic stripping voltammetry. The Hg atoms are deposited onto the electrode over a comparatively long period, 600 sec, and are stripped from the electrode during a single scan of applied potential. The long period of preconcentration increases the quantity of deposited Hg and, consequently, increases the analytical signal obtained for a given concentration of Hg(II) in the sample.

The third factor, which decreases the detection limit obtained with this method, is the use of DPASV in the stripping phase. To a great extent, DPASV discriminates against the nonfaradaic current

associated with the charging of the double layer at the surface of the electrode during the scan of applied potential. This charging current constitutes a significant source of unwanted background signal in linear-sweep stripping voltammetry, in which the potential applied to the electrode increases linearly with time. Since the use of DPASV decreases the value of this charging current relative to the analytical signal, the detection limit for the determination of Hg by this procedure is decreased.

The positive potential employed in the deposition, + 0.45 V vs. SCE, results in a high degree of selectivity for Hg relative to other electroactive species. The only species which interferes seriously with the determination of Hg(II) in this procedure is Ag(I). Ag(I) does not interefere unless present at a concentration greater than 100 times the concentration of Hg(II). The deposition of Hg occurs at a potential which is 50 mV more positive than the reversible thermodynamic potential for the Hg(II)/Hg(0) couple in this medium and is consequently referred to as "underpotential deposition." At the concentration levels employed in this determination, Hg is deposited at quantities less than 1 monolayer. Under these conditions, the deposited Hg is stripped at a potential of + 0.90 V vs. SCE, forming Hg(II). A single, sharp stripping peak is observed at this potential (148, 167).

B. Engineering and Instrumentation

The analyses for Hg were conducted with Electrodes E and F, which were constructed, mounted, and operated as described in Chapter III.

The electronic instrumentation used to drive the speaker has been described in Section G of Chapter IV. Potential control and current measurement for the vibrating electrode were performed with the model 174A Polarographic Analyzer, manufactured by Princeton Applied Research (PAR), Princeton, NJ. The PAR 174A was modified according to the procedure given by Lindstrom (p. 112 of 148), to permit the operation of the instrument at periods of 0 to 0.5 sec for the differential pulse waveform, which was employed during the stripping analysis.

A transfer apparatus was constructed to facilitate the transfer of the Au electrode from the cell containing LSW to the cell containing TDW. This transfer apparatus consisted of a 5-3/4 x 2-5/8 x 1-in. stainless steel tray, a plastic insert with inside dimensions of 4-1/8 x 2-3/8 x 2 in., and 2 mounting brackets. The mounting brackets were attached to the sides of the speaker support, described in Section C of Chapter III, with the bottom edge of each bracket parallel to the base of the speaker support. Each of the mounting brackets was constructed from 14-gauge Al sheet and was provided with 3 slots, 3/16 in. in width and 1-5/16 in. in height. The slots were perpendicular to the bottom edges of the brackets and were spaced 1-1/8 in. apart. The plastic insert fit snugly into the tray and was designed to hold 2 glass cells, constructed as described in Section F of Chapter III, such that the central compartments of the 2 cells were adjacent to each other, with each cell centered with respect to the longest dimension of the steel tray. A pair of 3/16-in. diameter steel rods, 1 in. in length, was soldered to each of the 2-3/8-in. sides of the tray, with the 2 rods centered 3/4 in. from either edge of the tray and 1/2 in. above the

bottom. These pairs of rods fit into the mating slots in the mounting brackets and supported the tray in either a forward or a rear position, such that the vibrating electrode was immersed in the corresponding cell. In the forward position, the 2 rods on each side of the tray fit into the foremost 2 of the 3 slots; in the rear position, the rods fit into the rearmost 2 slots. The upper end of each slot was provided with a recess, into which the corresponding steel rod could be placed. The positions of the 3 slots on the mounting brackets were located such that the Au electrode was centered in the corresponding cell in both the forward and rear positions of the tray, with the rods placed in these recesses.

The speaker support, vibrating electrode, cells, and transfer apparatus were all placed within a 8-1/2 x 8-1/2 x 14-in. plastic box, the front cover of which was hinged to permit access to the transfer apparatus. This box served to minimize contamination of the electrode and solutions during analysis and also reduced the acoustical noise level produced in the laboratory. Due to the contamination of the cell solutions with mercury and/or Cl^- from the SCE, isolation of the SCE from the cell was found to be necessary in ultratrace determinations of Hg at Au electrodes. This isolation was effected by means of a Luggin capillary made from a 1-mm bore stopcock. Each arm of this stopcock was bent 90 deg such that the outermost 6 cm lengths of the 2 arms were parallel. When the stopcock was closed and both arms were filled with 1 M H_2SO_4, ionic conductivity was provided between the reference sidearm of the cell and a 50-mL beaker placed at the rear of the box. The SCE was placed into this beaker, which was partially

filled with 1 M H_2SO_4. A dual Pt counter electrode was immersed into the CE sidearms of the 2 cells and was connected to the CE connection on the PAR 174A. With the Luggin capillary positioned as described in the following section, both the Au working electrode and the reference electrode were simultaneously and automatically switched from one cell to the other by changing the position of the tray from the forward to the rear position or vice versa. Since the arm of the Luggin capillary remained in the sidearm of the cell longer than the Au electrode remained in the central compartment, saturation of the potentiostat could not occur during the period that the Au electrode was immersed in the solution. Hence, damage to the Au electrode by severe anodization was not possible. This procedure also avoided the need for a second Luggin capillary and SCE, and it eliminated the DPDT switch which normally would be required in a dual-cell experiment.

The initial potential, + 1.700 V, and scan direction, Negative, employed with the PAR 174A in this experiment were chosen to minimize the possibility of damage to the electrode through carelessness on the part of the operator. With these controls set as shown, it was impossible to expose the electrode to potentials greater than + 1.700 V vs. SCE.

C. Procedure

The step-by-step procedure employed in the analyses of LSW is given below:

1) Place the speaker and its mount in the plastic enclosure, with

the cone and protruding wire facing the front. The base will fit into the limiting stops on the plastic box. The connection to the speaker (terminated in a 1/4-in. phone plug) should come out through the rear hole.

2) Carefully mount one of the vibrating electrodes (in its Cu holder) onto the speaker by using brass hardware (supplied), using 1 nut and bolt for each of the 4 holes in the vertical aluminum strip.

3) Put the signal generator and amplifier on top of the PAR 174A. Connect the signal generator to the amplifier (either amplifier input — they are connected in parallel, as supplied) with the probe which terminates in banana plugs and an RCA phono plug. The black and red banana plugs should be plugged into the correspondingly colored jacks on the generator. Plug the speaker connector (1/4-in. phone plug) into the desired channel output (1 or 2) on the amplifier. Connect the cell probe to the PAR 174A and clip the 4 alligator clips to the 3 banana plugs (bare metal) and the frame of the speaker mount (right bracket), as follows: Red (CE) to red jack; White (Ref.) to white jack; Blue (WE) to blue jack; black alligator clip through front hole in plastic box to speaker mount. All instruments should be off at this time.

4) Fill the 2 glass cells; one with the sample solution (LSW made 1.0 M in H_2SO_4) and the other with 1 M H_2SO_4 in TDW. The sidearms of both cells should also be filled (to approximately 1 cm from the top) with 1 M H_2SO_4. Place the 2 cells into one of the plastic trays. Put the plastic tray into the stainless steel cell holder. Holding the 2 sides of the stainless steel tray with the hands, outside of the mounting

brackets, lift the tray in the forward position (rods in the 2 forward slots) straight up and level until it can be moved backwards and into the recesses provided for holding the tray. The vibrating electrode should now be immersed in the 1 M H_2SO_4 solution, with the seal at least 3 mm below the surface.

5) Add 25 mL of 1 M H_2SO_4 to a 50-mL beaker, and place the beaker on a wooden block (supplied) in the right rear corner of the plastic enclosures. Make certain that the block is not sitting on this speaker lead. Place the SCE (reference electrode) into this beaker.

6) Fill a reference bridge (Luggin capillary) with 1 M H_2SO_4 completely, making certain that there are no bubbles in either arm. The stopcock should be in the open position during the filling process. After filling both arms completely, turn the stopcock 90 deg and carefully invert the entire assembly. Place the 2 ends of the reference electrode bridge into the 50-mL beaker and the right sidearm of the rear cell. Check carefully for bubbles in the bridge; repeat this procedure as necessary until no bubbles are observed in the bridge as finally installed. Brace the bridge in a vertical position with the grounding (black) alligator clip of the PAR 174A cell probe.

7) Insert the counter electrode into the 2 left sidearms of the 2 cells. The 2 helical portions of the counter electrode should be immersed in the solution of each sidearm.

8) Set the signal generator to 1 V_{pp} output (fine attenuation control at maximum clockwise position). Set the frequency to 210 Hz. Turn both Channel switches on the amplifier to the Off position (down). Turn the signal generator on; then turn the amplifier on (rocker switch

on generator; Power switch on amplifier). Momentarily turn the Channel switch on the amplifier to the on (up) position and adjust the corresponding Level control such that E_{in}, as measured across the speaker terminals with the digital voltmeter (DVM) on the 20 V AC range, is equal to 3.00 V RMS. The electrode should vibrate at about 1.3 mm peak-to-peak, and a 210 Hz tone should be heard. Following this adjustment, return the Channel switch to the Off position.

9) Set the PAR 174A controls as follows, with the Power switch Off.

Rate: 100 mV sec^{-1}

Direction: -

Range: 1.5 V

Initial Potential: + 1.700 V

Modulation Amplitude: 100 mV

Initial Button: depressed

Operating Mode: DC

Selector: Off

Current Range: 1 mA

Output Offset: - , 0.000 V

Display Direction: +

Clock: 0-0.5 sec. position

50 msec/turn potentiometer: 2.58 turns

Low Pass Filter: Off.

10) Connect the PAR 174A to the X-Y recorder; preferably such that the current (Y on PAR 174A) axis is on the longer axis of the chart paper (usually X axis on recorder). Set both axes' sensitivities to

100 mV $in.^{-1}$ or 100 mV cm^{-1} (depending on chart size). The voltage axis may need to be set to 150 mV $in.^{-1}$ (or cm) to fit a 1.5 V range onto the paper. Connect the DVM across the X-axis output of the PAR 174A (DVM on 2 V DC range).

11) Turn the Power switch on the PAR 174A to the On position. Then turn the X-Y recorder on. This prevents transients from the PAR 174A from possibly damaging the recorder.

12) Turn the Selector switch on the PAR 174A to the Ext. Cell position. The X-Y recorder may go temporarily off scale, but should return within 5 sec to a value on scale. If not, switch the Selector switch on the PAR 174A to the Off position and check all connections and control settings. Also check the reference electrode for low KCl level and the reference electrode bridge for bubbles.

This completes the preliminary setup and alignment for analysis. Having completed the preliminary setup and alignment, the apparatus is now set for actual analytical measurements. The procedure is given below.

13) Scan the Au electrode over the range of + 1.7 to + 0.2 V vs. SCE by alternately depressing the Scan and Scan Rev. button on the PAR 174A. Repeat this procedure until a reproducible residual voltammogram for Au is obtained. Adjust the Current Range switch on the PAR 174A and/or the recorder sensitivity to keep the residual curve to scale if necessary. The electrode should be vibrating (amplifier Channel switch for appropriate channel in On (up) position) during this step.

Note: Au tends to absorb Hg from the air if stored for long periods. The absorbed Hg will show up on the stripping curve as a peak which is undistinguishable from the stripping peak obtained from Hg deposited from solution. The electrode may be cleaned of such absorbed Hg by repeated cycling and anodization at + 1.700 V vs. SCE (Initial button depressed for anodization), with the electrode vibrating. The cell solution should be changed prior to performing analyses, after this cleaning procedure is performed.

14) With the Initial button on the PAR 174A depressed (electrode at + 1.7 V vs. SCE) and the electrode stationary (Channel switch on amplifier in Off (down) position), transfer the electrode to the sample cell by lowering the electrode tray and setting the tray on the aluminum base, sliding the tray with cells backwards for 1-1/8 in. until the 2 rods on each side are directly below the rearmost 2 slots in the side supports, and lifting the tray upwards (level!) until the rods can be lowered into the rear holding position. The Au microelectrode should now be immersed in the sample (front) solution, with the seal 3 mm below the surface of the solution. The reference electrode bridge should contact the solution in the sidearm of the sample cell prior to the Au electrode coming into contact with the sample solution. Otherwise the electrode may be ruined by anodization, as described in Chapter VIII.

15) Switch the Channel switch on the amplifier to the On (up) position (electrode vibrating). Cycle the electrode twice over the range + 1.7 to + 0.2 V vs. SCE. At the beginning portion of the third cathodic scan, press the Hold button on the PAR 174A to stop the cathodic scan at a point as close to + 0.450 V vs. SCE (indicated on the DVM as

+ 1.250 V) as possible. The initial DVM reading should be 1.240 to 1.265 V. As soon as the Hold button is depressed, switch the Operating Mode switch on the PAR 174A from the DC position to the Diff. Pulse position (far right). The Overload light on the PAR 174A may light up for a period, but should go out within 10 sec. Simultaneously with switching the Operating Mode switch, start a stopwatch to time the deposition period, t_{dep}. Also, after switching to Diff. Pulse mode and starting the stopwatch, switch the Current Range switch to 0.02 mA or 0.05 mA. The entire procedure should be completed, from stopping the scan to final setting of the Current Range, within 10 to 15 sec. Continue the deposition for 600 sec. During the deposition, switch the Scan Rate switch on the PAR 174A from 100 mV sec^{-1} to 20 mV sec^{-1}. The deposition voltage may normally be corrected to exactly + 0.450 V vs. SCE (DVM reading + 1.250 V) by juggling the Hold, Scan, and Scan Rev. buttons to shift the Hold potential (indicated on DVM) to 1.250 $\pm$ 0.002 V.

16) When the stopwatch reaches 10 min 0.0 sec, switch the Channel switch on the amplifier to the Off (down) position. The electrode will be stationary. Lower the transfer tray and slide it 1-1/8 in. forward on the aluminum base. Raise the tray (level!) so that the electrode is now immersed, as before, in the stripping cell. Important: Observe the same precautions noted in step 14 of this procedure. The reference bridge, after this second transfer, should again be in the right sidearm of the stripping (rear) cell.

17) Switch the Channel switch on the amplifier twice for 2 sec each time. This mixes any transferred solution into the bulk of the

solution in the stripping cell. Be certain that the electrode is stationary before proceeding.

18) Lower the recorder pen on the X-Y recorder and press the Scan Rev. button on the PAR 174A. The stripping scan is now being recorded. It may be necessary to adjust the Offset knob on the PAR 174A to ensure that the stripping peak for Hg is on scale. The correct position for the Offset knob and best procedure for adjustment (which must be performed during the stripping scan) are determined empirically and by practice.

19) Raise the recorder pen at the onset of the oxidation wave for Au (recorder pen will go off scale and Overload light may light on PAR 174A). Turn the Current Sens. switch to the 1 mA position and turn the Offset switch to the Off position. Switch the Scan Rate switch to 100 mV/sec and the Operating Mode switch to the DC position. Switch the Channel switch on the amplifier to the On (up) position; the electrode will again be vibrating.

20) Cycle the electrode again as described in step 13 above until a reproducible DC residual voltammogram is obtained. Usually 2 or 3 scans will be sufficient.

21) Add an appropriate amount of a freshly prepared standard Hg^{2+} solution (20 to 50 μL typically) to the sample (front) cell using a glass micropipette. If the pipette is calibrated to contain, rinse the pipette with the cell solution 3 times to ensure quantitative transfer. Stir the sample cell with a small glass stirring rod.

22) Repeat steps 13 through 20 for each standard addition, followed by addition of the next aliquot of standard Hg^{2+} solution

as per step 21.

23) Determine the peak differential stripping current, ΔI_{strip}, obtained for each addition and for the sample solution using the desired procedure from the 2 described in the following section.

24) Make a standard plot and determine the concentration of Hg in the sample solution.

Between analyses, the Au electrodes were stored with the active Au surface immersed in TDW. This reduced absorption of Hg from the air onto the electrode, a process which has been noted both in this work and in the literature (169).

D. Experimental Results

Determinations of Hg(II) by DPASV were performed on a LSW sample and also following each of 8 successive standard additions of 50.0-μL aliquots containing freshly prepared 2.07×10^{-7} M Hg(II) to the 28.5-mL LSW sample. The stripping voltammograms were obtained at Electrode F in accordance with the procedure detailed in the preceding section. From these representative voltammograms, those obtained for the LSW sample and for LSW with 1.47 nM (294 pptr) added Hg(II) are depicted in Figure IX-1. Residual voltammograms of Au in 1.0 M H_2SO_4 made using TDW and LSW are shown for reference, and the voltammogram for the preliminary determination of Hg(II) in the solution containing 1.0 M H_2SO_4 in TDW, which was employed in the stripping cell, is also illustrated. In this latter determination, the deposition and stripping phases were both performed in the stripping cell, and the procedural

Figure IX-1. Representative voltammograms for the determination of Hg in Lake Superior water by DPASV

A — Residual voltammogram of Electrode F in TDW blank; B — Residual voltammogram of Electrode F in LSW sample; C — DPASV of TDW blank (1.0 M H_2SO_4 in TDW); D — DPASV of LSW sample (1.0 M H_2SO_4 in LSW); E — DPASV of LSW sample plus 1.47 nM Hg(II) (294 pptr).

DC and differential pulse voltammograms depicted by broken and solid lines, respectively. Geometric constructions for determination of peak height by horizontal and sloping baseline methods shown for voltammogram C (F — horizontal baseline; G — sloping baseline).

Voltammograms C, D, E vertically offset for clarity.

Electrode F; f = 210 Hz; Re_v = 152; a_{pp} = 1.28 mm.

DPASV parameters: Scan rate = 20 mV sec^{-1}; Modulation amplitude = 100 mV; Period of DPASV waveform = 0.129 sec.

t_{dep} = 600 sec.

Scan rate for DC voltammograms = 100 mV sec^{-1}.

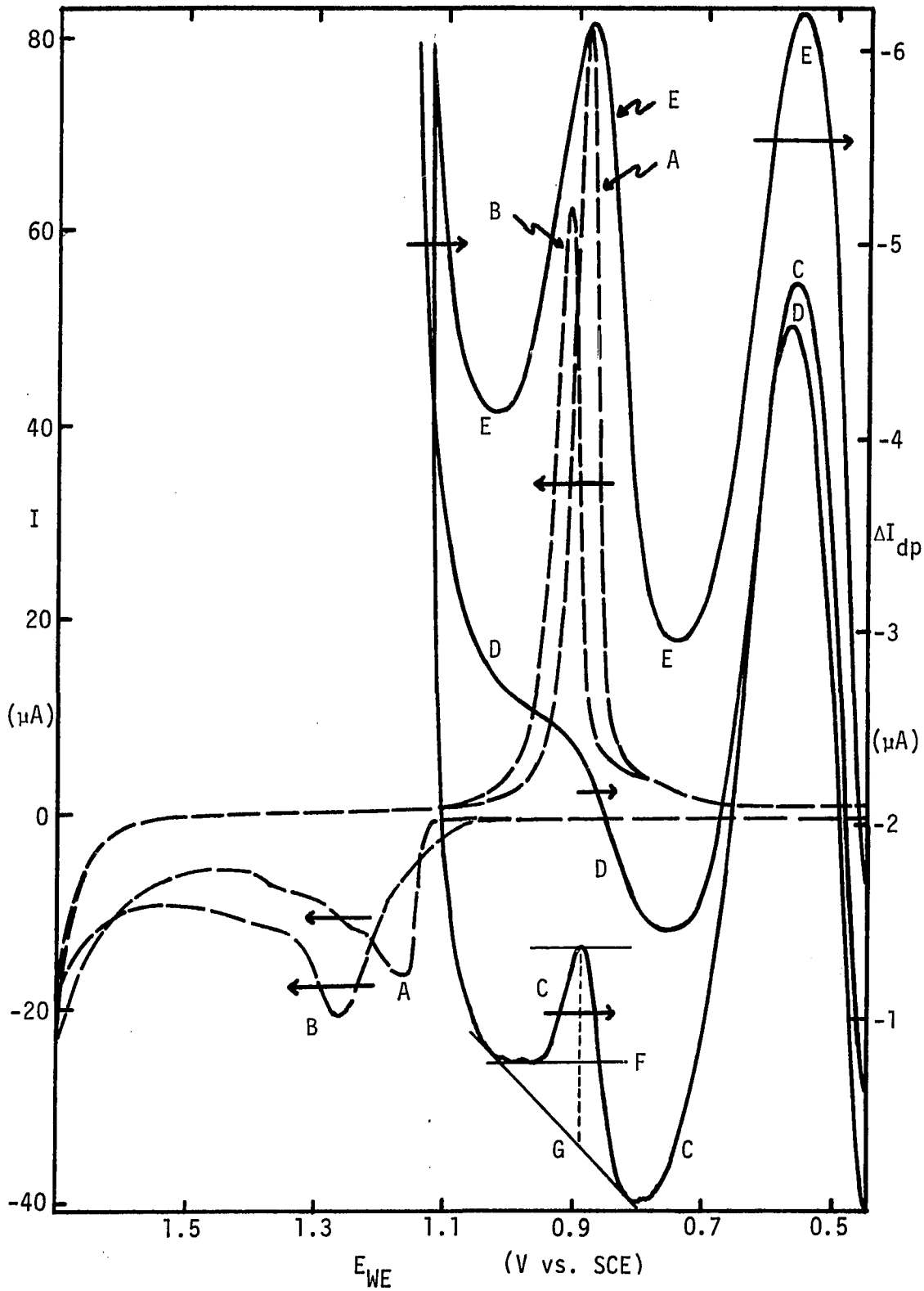
80
60
40
I
20
(μA)
0
-20
-40
-6
-5
-4
ΔI dp
-3
(μA)
-2
-1
1.5
1.3
1.1
0.9
0.7
0.5
E WE
(V vs. SCE)
A
B
C
D
E
F
G

steps pertaining to the transfer of the electrode were deleted. The peak noted at + 0.575 V vs. SCE in the stripping voltammograms is characteristic of Au electrodes and is not indicative of an impurity in the solution nor of a leaky Au electrode. The altered form of the oxidation wave noted in the residual voltammogram recorded in the LSW sample is likely due to the presence of trace Cl^-.

The stripping cell and Luggin capillary were both filled with 1.0 M H_2SO_4, which was made up from TDW and from a freshly opened bottle of Ultrex® grade H_2SO_4, purchased from the J. T. Baker Chemical Co., Phillipsburg, NJ. This solution, hereafter referred to as the "TDW blank," was stored in a 2-L volumetric flask which had previously been employed exclusively for the storage of 1.0 M H_2SO_4 free from Hg. All glassware was rinsed thoroughly with TDW and with the TDW blank solution prior to the experiment. The cells had no prior history of exposure to solutions containing Hg.

The observed values of ΔI_{strip} for the 10 determinations are summarized in Table IX-1. For each voltammogram, ΔI_{strip} was calculated by means of 2 different techniques. In the first technique, ΔI_{strip} was measured from a horizontal tangent to the top of the stripping peak for Hg down to a horizontal tangent to the minimum value of the differential current, ΔI_{dp}, observed on the positive side of the Hg peak, prior to the onset of the wave for Au oxidation.

In the second technique, ΔI_{strip} was measured from a sloping tangent to the 2 minima located on each side of the stripping peak for Hg. The greatest difference noted along a vertical line from the peak down to the point directly below, on the sloping tangent, was taken as

Table IX-1. Calibration curves for Hg(II) at Electrode F: ΔI_{strip} vs. concentration of Hg(II) in Lake Superior water[a]

Added Hg(II) (nM)[b,c]	Added Hg(II) (pptr)	Horiz. baseline ΔI_{strip} (μA)[b]	Sloping baseline ΔI_{strip} (μA)[c]
TDW blank		0.610	1.04
LSW sample		n.a.[d]	0.295
0.367	73.6	0.215	0.755
0.733	147	0.830	1.41
1.10	221	1.36	1.99
1.47	294	2.00	2.62
1.83	368	2.58	3.15
2.20	441	3.11	3.71
2.57	515	3.69	4.30
2.93	588	4.26	4.84

[a]Experimental conditions and representative voltammograms given in Figure IX-1. All uncertainties calculated at the 90% confidence interval.

[b]Equation of line:

$$\Delta I_{strip} = 1.574 \pm 0.008)[Hg(II)] - (0.343 \pm 0.016)$$

[c]Equation of line:

$$\Delta I_{strip} = (1.572 \pm 0.026)[Hg(II)] + (0.257 \pm 0.046)$$

$$\text{x-intercept} = (0.257 \pm 0.046)/(1.572 \pm 0.026)$$

$$= 0.163 \pm 0.032 \text{ nM Hg(II) in LSW sample.}$$

[d]n.a. = not applicable.

ΔI_{strip}. These 2 techniques were designated as the "horizontal baseline" and "sloping baseline" methods, respectively. The horizontal baseline method is easier to use and produces calibration curves of greater linearity, but it is not applicable to voltammograms in which the required minimum between the stripping peak for Hg and the wave for Au oxidation is absent, e.g., in the LSW blank. In addition, the horizontal baseline method is not suited to the determination of Hg by the method of standard additions, because a portion of the peak is "lost" in the measurement procedure. The sloping baseline method yields slightly less precise calibration curves, but it is the only applicable method for cases in which the horizontal tangents required for the former method are not defined. The sloping baseline technique is also better suited to the determination of Hg by the method of standard additions, because the measurement results in a better approximation of the peak height.

In Figure IX-1, the stripping peak for Hg depicted for the TDW blank corresponds to a Hg(II) concentration of 0.67 nM in the solution. This value is equivalent to a concentration of 1.3 parts per billion (ppb) in the Ultrex® H_2SO_4, assuming that the Hg(II) originated solely from the H_2SO_4. However, this background value was observed to vary widely from experiment to experiment, even when using the same solution of 1.0 M H_2SO_4 prepared from TDW in the stripping cell. The observed stripping peaks indicated the presence of Hg(II) at concentrations of 0.2 to 0.7 nM (20 to 140 pptr) in the 1.0 M H_2SO_4 solution employed in the stripping cell. These concentrations corresponded to Hg(II) levels from 0.4 to 1.4 ppb (w/w) in the Ultrex® acid. In addition, repeated analyses of a single aliquot of this solution generally produced

stripping peaks of increasing height for successive determinations, indicating that the concentration of Hg(II) was increasing with time. Isolation of the SCE from the cell, using the Luggin capillary as described above, reduced but did not totally eliminate this latter problem. Repetition of the experiment under identical conditions, but with the Au electrode held stationary during the deposition step, decreased the height of the stripping peak for Hg by a factor of 20. This result indicated that the deposition of Hg was mass-transport dependent, thus proving that the Hg originated from the solution and not from the electrode.

Although the concentration of 1.3 ppb Hg(II) calculated for the Ultrex® H_2SO_4 agrees well with the label value of 1 ppb, the variability of peak heights observed in separate aliquots taken from the same solution indicates that the Hg contamination arose in great part not from the Ultrex® H_2SO_4, nor from the TDW, but rather from external sources. The most likely sources of this contamination were adsorbed Hg on the walls of the glassware or Hg vapor in the laboratory. However, the cells and glassware had no prior history of exposure to solutions containing Hg, and experiments performed with the same apparatus at the laboratory of the U.S. Environmental Protection Administration in Duluth, MN, yielded similar background concentrations. In these latter experiments, the phenomenon of increased levels of Hg in successive analyses of a single aliquot of solution was also observed. From these results, it was not possible to localize definitively the source of the Hg contamination. The background levels of Hg(II) observed in this work were of comparable magnitude and showed similar variations to the values measured

by Glass and Sandberg (170) in LSW samples, using an optimized version of the cold-vapor AAS technique and acids of equal purity.

Analyses of 1.0 M H_2SO_4 solutions made from TDW and from analytical-grade H_2SO_4 manufactured by J. T. Baker Chemical Co., Fisher Scientific Co., Fair Lawn, NJ, and by Mallinckrodt, Inc., Paris, KY, indicated that the Mallinckrodt acid contained the lowest concentration of Hg, comparable to J. T. Baker Ultrex® acid, followed by J. T. Baker analytical-grade and Fisher H_2SO_4, both with considerably higher values. These relative levels were estimated from the heights of the Hg stripping peaks noted for the first determination of Hg(II) in a freshly prepared solution, in which the possibility of contamination was at a minimum.

The concentration of standard solutions containing Hg(II) at levels at or below 1 μM was observed to decrease significantly following storage for extended periods. The height of the Hg stripping peak obtained in a 1.8 nM Hg(II) solution in LSW prepared from a standard solution containing 1.045 μM Hg(II) decreased 30% upon storage of the 1.045-μM solution for 24 hours. A 75% decrease was noted for 1.0 nM Hg(II) upon storage for 48 hours. Similar results have been noted in the literature (171, 172), and the use of $KMnO_4$ and $K_2Cr_2O_7$ as preservatives for dilute solutions of Hg(II) has been suggested. In this work, the presence of $K_2Cr_2O_7$ in the LSW was found to interfere with the deposition of Hg onto the electrode. However, the presence of 18 ppm $KMnO_4$ did not affect the deposition of Hg. Chemical stripping of the deposited Hg was not observed, in contrast to the prediction stated in Chapter VIII. Possibly the small quantity of solution which adhered to the electrode during the transfer process, together with the short period

of exposure to this solution at open-circuit conditions and the low concentration of $KMnO_4$, mitigated against the chemical stripping of the electrode. However, in view of the results cited in Chapter VIII, caution is advised in the use of $KMnO_4$ as a preservative in samples to be analyzed by this electrochemical method.

Experiments conducted with LSW containing added Hg(II) at a level of 1.3 nM (260 pptr) indicated that the LSW apparently contained a species which complexed or chelated the Hg(II) at this concentration level. The potential of the stripping peak for Hg obtained following transfer of the electrode to the solution in the stripping cell, 1.0 M H_2SO_4 in TDW, was + 0.90 V vs. SCE, in agreement with the value obtained for deposition and stripping of Hg in the TDW blank, without transfer of the electrode. However, the potential of the stripping peak for Hg obtained in the same LSW sample without transfer of the electrode, i.e., with both deposition and stripping performed in the LSW sample, was + 0.78 V vs. SCE. This value represents a - 120 mV shift in the potential of the stripping peak for Hg. Chelation or complexation of Hg(II) stripped from the Au electrode would cause such a negative shift in the peak potential in a manner analogous to the process which causes the negative shift in the polarographic half-wave potential of a metal ion in the presence of a complexing agent (pp. 209-10 of 141). Although the peak potential was shifted - 120 mV in this latter experiment, the values for the peak current, ΔI_{strip}, measured by the horizontal and sloping baseline techniques, respectively, were 92% and 97% of the values obtained for deposition in the same LSW sample and stripping in the TDW blank following transfer of the electrode.

Chelation of Hg(II) in natural waters has been investigated by Kritsotakis, et al. (173), who determined the speciation of Hg(II) present at a level of 6.4 ppb in the water of the Ginsheimer Altrhein, a notoriously highly polluted secondary channel of the Rhein at Mainz-Ginsheim, Germany. The authors ascertained that the Hg(II) was completely chelated in the original samples and remained 70% chelated at a pH of 3. The binding capacity of the water was 55 ppb Hg(II). Calibration curves prepared from synthetic Hg^{2+} solutions were found to be unsuitable for the determination of Hg(II) in this matrix, and the authors recommended application of the method of standard additions for the analysis of these water samples. Although the Ginsheimer Altrhein is more highly polluted than Lake Superior, the findings of these studies are likely applicable to other natural waters, with a reduction in the binding capacity of the water for Hg(II).

The sensitivity ($\mu A\ nM^{-1}$) of the analytical method described in this chapter was defined as the least-squares slope of the calibration curve of ΔI_{strip} vs. [Hg(II)]. For the determination of Hg in TDW without transfer of the electrode and in LSW with transfer of the electrode, these sensitivities were 1.572 $\mu A\ nM^{-1}$ and 1.557 $\mu A\ nM^{-1}$, respectively. These values agree to within 1% relative, indicating that the complexation of Hg(II) mentioned previously did not affect the efficiency of deposition of Hg from the LSW onto the electrode. In addition, the agreement of these sensitivities indicates that loss of deposited Hg did not occur during the transfer of the electrode.

The concentration of Hg(II) present in the LSW solution, as determined by the results of the analysis summarized in Table IX-1, was

0.163 ± 0.032 nM (32.8 ± 6.4 pptr), with the uncertainty calculated at the 90% confidence interval. This value is equivalent to a concentration of 34.7 ± 6.8 pptr Hg(II) in the LSW prior to the addition of H_2SO_4, assuming that the H_2SO_4 contained no Hg. This latter assumption is false, however, and it is therefore necessary to know the true concentration of Hg(II) in the H_2SO_4 in order to calculate the level present in the LSW.

The detection limit for Hg(II) using this electrochemical method is 2×10^{-11} M Hg(II) (4 pptr), in the absence of the external contamination noted above. This detection limit was defined as the concentration of Hg(II) which would produce a value of ΔI_{strip} equal to twice the uncertainty of the baseline. Preliminary work with Electrode E in TDW solutions indicated a lower detection limit, 5×10^{-12} M (1 pptr); however, this electrode was inadvertently subjected to severe anodization and was unsuited to further trace-level work following this unfortunate incident. These detection limits are significantly lower than the detection limit of 1 ppb generally reported for cold-vapor AAS (165, 174-177) and are similar to the value cited by Hawley and Ingle (178) for an optimized version of the cold-vapor method. The detection limits for the vibrating electrode are 2.5 to 10 times lower than those cited for the same electrochemical method using a Au RDE and an equivalent deposition time (168) and 25 to 100 times lower than those found by Lindstrom (148) for the same method at a Au flow-through disc electrode.

E. Conclusion

The vibrating Au electrode has been applied to the ultratrace determination of Hg(II) in LSW samples by DPASV. Using a deposition time of 600 sec, the estimated detection limit in the absence of external contamination was 2×10^{-11} M Hg(II) (4 pptr), and linear calibration curves were obtained for Hg(II) concentrations from 0.37 to 2.9 nM (74 to 590 pptr). Evidence has been presented which supports the hypothesis that Hg(II) at these levels exists in LSW as a complexed or chelated species; however, this complexation did not affect the efficiency of deposition of Hg onto the Au electrode.

Problems associated with contamination of the reagents and glassware by trace Hg have been investigated, and the relative levels of Hg(II) present in analytical-grade H_2SO_4 obtained from different manufacturers have been determined. The limiting factor in practical analyses was found to be the highly variable background level of Hg(II) present in the 1.0 M H_2SO_4 solutions employed in the analytical procedure. Similar background levels were observed using this electrochemical method both at this laboratory and at the laboratory of the U.S. Environmental Protection Administration at Duluth, MN. These results were also similar in magnitude to those noted in independent determinations of the background levels of Hg(II) in LSW performed at Duluth, MN, using cold-vapor AAS, and similar random variations in these levels were noted with both methods.

Standard solutions containing Hg(II) at concentrations below 1 μM (200 ppb) were found to be unstable upon storage for extended periods,

with the concentration of Hg(II) decreasing with the time of storage. This instability was attributed to the adsorption of Hg(II) onto the walls of the borosilicate glassware, in which the solutions were prepared and stored, and/or the loss of Hg as Hg(0) vapor following reduction. $K_2Cr_2O_7$ was found to be unsuitable as a preservative for samples to be analyzed by this method, but the presence of $KMnO_4$ at low concentrations did not affect the deposition and stripping of Hg. Caution in the use of $KMnO_4$ as a preservative is advised, however, due to the possibility of chemical stripping of Hg from the electrode during the transfer process.

The analytical method described in this chapter is presently being applied at the laboratory of the U.S. Environmental Protection Administration in Duluth, MN, in studies of the background levels of Hg present in Lake Superior water. Due to its electrochemical basis, this analytical method constitutes an ideal confirmatory technique, when applied in conjunction with the optimized cold-vapor AAS procedure developed at that laboratory.

X. CONCLUSION

The design and construction of Au and Pt vibrating electrodes was presented. These electrodes were vibrated by means of a louspeaker at peak-to-peak amplitudes up to 3.3 mm and frequencies up to 510 Hz. Electronic instrumentation was described which permitted automatic recording of the limiting current as a function of the vibrational amplitude. This instrumentation also facilitated the use of hydrodynamic modulation through sinusoidal, 10-Hz modulation of the vibrational amplitude or frequency, with phase-selective detection of the 10-Hz component of the electrode current.

Hydrodynamic transitions in the flow patterns prevailing at vibrating electrodes from Re_v = 0 to 150 were studied both visually and electrochemically. Visual evidence of such transitions was noted at Re_v = 11, ca. 25, 78, ca. 90, and 103, with evidence from the electrochemical studies for transitions at Re_v = 25 and 90.

The exponential dependence of the limiting current on the vibrational amplitude was determined, with values from 0.5 to 1.0 noted for different electrodes. The exponential dependences of the limiting current on the vibrational amplitude and frequency for a given electrode were 0.620 and 0.664, respectively. Studies of the mass transport to vibrating electrodes indicated an improvement of at least 50% in the sensitivity of vibrating electrodes over RDEs of equivalent area.

Detection limits of 4×10^{-7} M for Br^-, 1×10^{-8} M for $Cr_2O_7^{2-}$, and 2×10^{-8} M for O_2 were observed for a signal-to-noise ratio of 2 using hydrodynamic modulation at a vibrating Pt electrode. These

limits were 10 to 100 times lower than the corresponding values observed in DC cyclic voltammetry at the same electrode. Background currents noted at Pt electrodes using hydrodynamic modulation were attributed to dissolution of Pt from the electrode.

The vibrating electrode was employed in flow-injection analysis for the determination of I^-. A detection limit of 5×10^{-10} M I^- was demonstrated for a signal-to-noise ratio of 2, and a dynamic range from 1×10^{-3} M to 5×10^{-10} M I^- was observed. The method was applied to the determination of I^- in household iodized salt. Equations were derived which describe the performance of the vibrating electrode in flow-injection analysis for both steady-state conditions and plug injection of samples. The validity of the fundamental assumptions, upon which these equations are based, was evaluated. The equations were also predicted to be applicable to the RDE in flow-injection analysis. Hydrodynamic modulation at the vibrating electrode in flow-injection analysis was shown to discriminate against the charging current normally observed at amperometric flow-through electrodes following a change in potential.

Determinations of Hg(II) in Lake Superior water were performed at the part-per-trillion level, using a vibrating electrode in differential pulse anodic stripping voltammetry with a deposition time of 600 sec. A linear calibration curve was obtained from 3.6×10^{-10} M to 2.9×10^{-9} M Hg(II) (74 to 590 pptr). The estimated detection limit for a signal-to-noise ratio of 2 was 2×10^{-11} M Hg(II) (4 pptr). The limiting factor in the analytical determination was the highly variable background level of Hg noted in the reagents employed in the procedure.

This background level was similar in magnitude to that noted in cold-vapor atomic absorption spectroscopy, and similar variations in the background level were observed with both methods. Standard solutions of Hg^{2+} were observed to decrease in concentration upon storage. The use of $K_2Cr_2O_7$ as a preservative was found to be incompatible with this electrochemical method, but $KMnO_4$ was suitable if present in the deposition solution at part-per-million levels. However, chemical stripping of the deposited Hg was shown to be possible in the presence of $KMnO_4$. Complexation of Hg(II) in Lake Superior water was observed.

XI. SUGGESTIONS FOR FUTURE WORK

The research for the Ph.D. dissertation generally raises more questions than it answers. Such is also the case with the present work. In view of this fact, several avenues of possible future research are suggested below.

The topic of the hydrodynamic flow patterns induced by vibrating cylinders is extremely complex and could benefit from future research with vibrating electrodes. The exact relationship between the macroscopic flow pattern induced by the electrode and the nature of the microscopic diffusion layer should be investigated more closely. The frequency and phase responses of the diffusion layer should be studied in greater detail and at different Re_v values, and an attempt should be made to correlate the frequency and phase responses to the hydrodynamic properties of the electrode. The effects of minor changes in the geometry of the electrode on the hydrodynamic transitions should be investigated. The dependence of the 3-bumped graphs of I_1 vs. Re_v on the vibrational frequency should be studied in greater detail, and the significance of the bumps should be elucidated. The variations noted between different electrodes are worthy of further investigation.

The nonlinearity noted in the calibration curves of I_1 vs. C^b is of basic importance to the analytical application of vibrating electrodes and deserves closer study. Viewed from the perspective of Equation I-5, it is likely that this nonlinearity results from a failure of the basic assumption of this equation, viz., that the value of C^s is zero at all points on the electrode surface.

Construction of a smaller vibrating electrode would permit the operation of the vibrating electrode at higher frequencies and the use of a smaller flow-through cell in FIA. This smaller cell would decrease the response time of the vibrating electrode in FIA.

Application of a miniature RDE to FIA in a manner analogous to that employed with the vibrating electrode in the present work shows much promise for future work. Provided that the RDE displays the same hydrodynamic behavior in batch and flow-through cells, the value of k_m in Equations VII-9 and VII-14 could be calculated *a priori* using Equation I-8. The major problem with the RDE in this application is that it would have to be rotated at a very high speed to obtain the values of k_m, and thus, the analytical sensitivities, attained with the vibrating electrode.

Further investigation of the background currents noted in FIA and with hydrodynamic modulation at vibrating electrodes is of fundamental importance to the attainment of lowered detection limits for electroanalytical determinations. It is most important to ascertain the degree to which these currents result from contamination of the supporting electrolyte and to what extent they originate from other causes.

Future application of the electrochemical technique described in Chapter IX for the ultratrace determination of Hg(II) in water samples should provide greater confidence in the results obtained from concurrent analyses of the same samples by cold-vapor AAS. Also, the concurrent application of both techniques should provide more information regarding the sources of the Hg contamination noted in this work.

XII. BIBLIOGRAPHY

1. Nernst, W. Z. Physik. Chem. 1904, 47, 52.

2. Blaedel, W. J.; Olson, C. L.; Sharma, L. R. Anal. Chem. 1963, 35, 2100.

3. Levich, V. G. "Physicochemical Hydrodynamics;" Prentice-Hall, Inc.: Englewood Cliffs, NJ, 1962, Page 296.

4. Delahay, P. "New Instrumental Methods in Electrochemistry;" Interscience Publishers: New York, NY, 1954, Pages 248-9.

5. Facsko, G. Rev. Roum. Chim. 1966, 11, 191.

6. Harris, E. D.; Lindsey, A. J. Nature (London) 1948, 162, 413.

7. Roberts, E. R.; Meek, J. S. Analyst (London) 1952, 77, 43.

8. Dirscherl, W.; Otto, K. Leybold Polarogr. Ber. 1953, 1 (3), 49.

9. Dirscherl, W.; Otto, K. Chem.-Ing.-Tech. 1954, 26, 321.

10. Oehme, F.; Noack, D. Chem. Tech. (Leipzig) 1955, 7, 270.

11. Vlček, A. Coll. Czech. Chem. Comm. 1959, 24, 1748.

12. Leon'tev, V. M.; Fedotov, N. A. Zavod. Lab. 1960, 26, 276; Ind. Lab. (Engl. Transl.) 1960, 26, 291.

13. Kalvoda, R. Chem. Zvesti 1962, 16, 245.

14. Facsko, G.; Poraicu, M. Bul. Stiint. Teh. Inst. Politeh. Timisoara, Ser. Chim. 1973, 18, 205.

15. Facsko, G.; Poraicu, M. Bul. Stiint. Teh. Inst. Politeh. Timisoara, Ser. Chim. 1974, 19, 247.

16. Pint, P.; Flengas, S. N. J. Electrochem. Soc. 1976, 123, 1042.

17. Magjer, T.; Branica, M. Croat. Chim. Acta 1977, 49, L1.

18. Moorhead, E. D.; Stephens, M. M.; Bhat, G. A. Anal. Lett. 1980, 13 (A3), 167.

19. Rosenberg, S.; Perrone, J. C.; Kirk, P. L. Anal. Chem. 1950, 22, 1186.

20. Harris, E. D.; Lindsey, A. J. Analyst (London) 1951, 76, 647.

21. Harris, E. D.; Lindsey, A. J. Analyst (London) 1951, 76, 650.

22. Alimarin, I. P.; Gallai, Z. A. Zavod. Lab. 1955, 21, 244.

23. Jenšovský, L. Chem. Listy 1956, 50, 1313.

24. Ray Sarkar, B. C.; Sivaraman, R. Analyst (London) 1956, 81, 668.

25. Tikhomirova, V. I. Izv. Akad. Nauk Tadzh. SSR, Otd. Geol-Khim. Tekh. Nauk 1962, 1 (7), 62.

26. Küster, H. Ber. Dtsch. Botan. Ges. 1955, 68, 183.

27. Liese, W.; Kunz, W.; Jahn, E. Z. Med. Labortech. 1969, 10, 20.

28. Shurukhin, Yu. V.; Gusev, L. F.; Samoilov, P. M.; Antonovskii, V. L. Appl. Biochem. Microbiol. 1973, 9, 261.

29. Rudichenko, M. F.; Rudichenko, V. F. Patol. Fiziol. Eksp. Ter. 1975 (4), 87; Chem. Abstr. 1975, 83, 174965x.

30. Passwaters, W. R. Ph.D. Dissertation, University of West Virginia, Morgantown, WV, 1978.

31. Popov, S. Ya.; Rybyanets, K. A. Zh. Prikl. Khim. 1965, 38, 1766; J. Appl. Chem. USSR 1965, 38, 1728.

32. Facsko, G.; Radoi, I. Bul. Stiint. Teh. Inst. Politeh. Timisoara 1969, 14, 519.

33. Radoi, I. Bul. Stiint. Teh. Inst. Politeh. Timisoara, Ser. Chim. 1971, 16, 193.

34. Gibert, H.; Angelino, H. Can. J. Chem. Eng. 1973, 51, 319.

35. Ross, T. K.; Aspin, A. F. Corros. Sci. 1973, 13, 53.

36. Podesta, J. J.; Paus, G. F.; Arvia, A. J. Electrochim. Acta 1974, 19, 583.

37. Blackman, L. C. F.; Wall, R. Nature (London) 1964, 202, 285.

38. Rama Raju, C. V.; Ramalinga Sastry, A.; Jagannadha Raju, G. J. V. Indian J. Technol. 1969, 7, 35.

39. Al-Taweel, A. M.; Ismail, M. I.; El-Abd., M. Z. Chem.-Ing.-Tech. 1974, 46, 861.

40. Al-Taweel, A. M.; Ismail, M. I. J. Appl. Electrochem. 1976, 6, 559.

41. Rowe, W. E.; Nyborg, W. L. J. Acoust. Soc. Am. 1966, 39, 965.

42. Somasundara Rao, K.; Jagannadha Raju, G. J. V.; Venkata Rao, C. Indian J. Technol. 1965, 3, 38.

43. Rama Raju, C. V.; Jagannadha Raju, G. J. V.; Venkata Rao, C. Indian J. Technol. 1967, 5, 305.

44. Rayapa Raju, S. G. V. V.; Jagannadha Raju, G. J. V. Indian J. Technol. 1974, 12, 307.

45. Lindsey, A. J. J. Phys. Chem. 1952, 56, 439.

46. Facsko, G. Galvanotechnik 1975, 66, 391; Chem. Abstr. 1976, 84, 11715x.

47. Facsko, G. Acad. Repub. Pop. Rom., Baza Cercet. Stiint., Timisoara, Stud. Cercet. Stiint. Chim. 1955, 2, 143; Chem. Abstr. 1956, 50, 15330e.

48. Facsko, G.; Radoi, I. Bul. Stiint. Teh. Inst. Politeh. Timisoara 1960, 5, 391.

49. Facsko, G.; Radoi, I. Acta Chim. Acad. Sci. Hung. 1961, 27, 31.

50. Bondarenko, A. V.; Popov, S. Ya. Tr. Novocherk. Politekhn. Inst. 1962, 134, 45; Chem. Abstr. 1963, 58, 8635f.

51. Radoi, I.; Facsko, G. Studia Univ. Babes-Bolyai, Ser. Chim. 1963, 8, 443; Chem. Abstr. 1965, 62, 3660g.

52. Radoi, I.; Julean, I.; Facsko, G. Studia Univ. Babes-Bolyai, Ser. Chim. 1963, 8, 451; Chem. Abstr. 1965, 62, 3661b.

53. Kvyatkovskii, A. N.; Vdovkin, G. G.; Kudinov, B. V. Sb. Tr. Nauch.-Issled. Proekt. 1971, 2, 64; Chem. Abstr. 1973, 78, 78952s.

54. Facsko, G.; Nartea, E. Bul. Stiint. Teh. Inst. Politeh. Timisoara, Ser. Chim. 1974, 19, 257.

55. Facsko, G.; Nartea, E. Lucr. Teh.-Stiint. Chim. Tehnol. Chim., Ses. Comun. Festivalului "Cintarea Rom." 1977, 17; Chem. Abstr. 1979, 91, 183823s.

56. Petrov, D.; Shentov, I.; Genevski, V. Fr. Demande 2,286,892, 1976; Chem. Abstr. 1977, 86, P62725z.

57. Facsko, G.; Radoi, I. Acad. Repub. Pop. Rom., Baza Cercet. Stiint., Timisoara, Stud. Cercet. Stiint. Chim. 1957, 4, 107; Chem. Abstr. 1959, 53, 14831d.

58. Müller, F.; Kuss, H. Helv. Chim. Acta 1950, 33, 217.

59. Facsko, G.; Golumbioschi, F. Bul. Stiint. Teh. Inst. Politeh. Timisoara 1963, 8, 43.

60. Hoover, A. E. Ph.D. Dissertation, University of Michigan, Ann Arbor, MI, 1968.

61. Facsko, G. Acad. Repub. Pop. Rom., Baza Cercet. Stiint, Timisoara, Stud. Cercet. Stiint. Chim. 1957, 4, 91; Chem. Abstr. 1959, 53, 11104i.

62. Facsko, G.; Golumbioschi, F. Rev. Roum. Chim. 1966, 11, 207.

63. Facsko, G.; Radoi, I.; Golumbioschi, F. Bul. Stiint. Teh. Inst. Politeh. Timisoara 1962, 7, 45.

64. Facsko, G.; Radoi, I. Bul. Stiint. Teh. Inst. Politeh. Timisoara, Ser. Chim. 1970, 15, 23.

65. Facsko, G. Acad. Repub. Pop. Rom., Baza Cercet. Stiint., Timisoara, Stud. Cercet. Stiint. Chim. 1961, 8, 255; Rev. Roum. Chim. 1966, 11, 191.

66. Facsko, G.; Radoi, I. Acad. Repub. Pop. Rom., Baza Cercet. Stiint., Timisoara, Stud. Cercet. Stiint. Chim. 1961, 8, 265; Rev. Roum. Chim. 1966, 11, 191.

67. Nakayama, T. Light Metals Jpn. 1959, 1, 53; Rev. Roum. Chim. 1966, 11, 191.

68. Nakayama, T. Light Metals Jpn. 1959, 9, 10; Rev. Roum. Chim. 1966, 11, 191.

69. Nakayama, T. Light Metals Jpn. 1959, 9, 13; Rev. Roum. Chim. 1966, 11, 191.

70. Nakayama, T. Light Metals Jpn. 1959, 9, 38; Rev. Roum. Chim. 1966, 11, 191.

71. Nakayama, T. Light Metals Jpn. 1959, 9, 52; Rev. Roum. Chim. 1966, 11, 191.

72. Khnykin, A. P.; Ogol, A. P. Otkritiya, Izobret., Prom. Obraztsy, Tovarnye Znaki 1976, 53, 136; Chem. Abstr. 1976, 85, 136908q.

73. Facsko, G.; Poraicu, M. Bul. Stiint. Teh. Inst. Politeh. Timisoara, Ser. Chim. 1976, 21, 111.

74. Facsko, G.; Poraicu, M. Bul. Stiint. Teh. Inst. Politeh. Timisoara, Ser. Chim. 1977, 22, 306.

75. Radoi, I. Rev. Roum. Chim. 1966, 11, 909.

76. Radoi, I. Rev. Roum. Chim. 1966, 11, 919.

77. Radoi, I. Bul. Stiint. Teh. Inst. Politeh. Timisoara, Ser. Chim. 1972, 17, 83.

78. Facsko, G.; Poraicu, M. Rev. Roum. Chim. 1964, 19, 341.

79. Facsko, G.; Poraicu, M. Bul. Stiint. Teh. Inst. Politeh. Timisoara, Ser. Chim. 1975, 20, 233.

80. Küster, H. Ber. Dtsch. Botan. Ges. 1954, 67, 365.

81. Jenšovský, L. Chem. Tech. (Leipzig) 1956, 8, 360.

82. Shevtsov, V. E. Zavod. Lab. 1972, 38, 923; Ind. Lab. (Engl. Transl.) 1972, 38, 1175.

83. Lindsey, A. J. Anal. Chim. Acta 1955, 13, 200.

84. Petrov, D. A.; Shentov, I. P.; Genevski, V. V. S. African 75 06,140, 1976; Chem. Abstr. 1977, 86, P129998m.

85. Parr, L. M.; Hendley, C. A. "Laboratory Glassblowing;" Chemical Publishing Co.: New York, NY, 1957; Chapter 8, Pages 97-8.

86. Bélanger, G.; Vijh, A. K. In "Oxides and Oxide Films," Vijh, A. K., Ed.; Marcel Dekker, Inc.: New York, NY, 1977; Volume V, Chapter 1.

87. Wagner, J. Z. Phys. Chem. 1890, 5, 31.

88. Deboo, G. J.; Burrous, C. N. "Integrated Circuits and Semiconductor Devices: Theory and Applications," 2nd ed.; McGraw-Hill Book Co.: New York, NY, 1977; Chapter 4.

89. Bard, A. J.; Faulkner, L. R. "Electrochemical Methods;" John Wiley and Sons: New York, NY, 1980; Chapter 13.

90. Melen, R.; Garland, H. "Understanding IC Operational Amplifiers;" Howard Sams and Co., Inc.: Indianapolis, IN, 1976; Page 120.

91. Analog Devices, Inc., Analog Devices Product Guide, Norwood, MA, 1975; Pages 175-6.

92. Bowditch, N. Memoirs of the American Academy of Arts and Sciences 1815, 3 (Article LII), 413.

93. Malmstadt, H. V.; Enke, C. G.; Crouch, S. R. "Instrumentation for Scientists Series: Digital and Analog Data Conversions;" W. A. Benjamin, Inc.: Menlo Park, CA, 1973; Module 3.

94. Miaw, L. L.; Bordreau, P. A.; Pichler, M. A.; Perone, S. P. Anal. Chem. 1978, 50, 1988.

95. Buck, R. P.; Eldridge, R. W. Anal. Chem. 1963, 35, 1829.

96. Sherwood, W. G. Anal. Chem. 1975, 47, 84.

97. Miller, B.; Bruckenstein, S. Anal. Chem. 1974, 46, 2026.

98. Williams, A. B. "Active Filter Design;" Artech House, Inc.: Dedham, MA, 1975; Chapter 4, Pages 75-88.

99. Motorola, Inc., Motorola Linear Integrated Circuits Data Book, 2nd ed., December 1972; Page 7-385, Figure 23.

100. Malmstadt, H. V.; Enke, C. G.; Crouch, S. R.; Horlick, G. "Instrumentation for Scientists Series: Optimization of Electronic Measurements;" W. A. Benjamin, Inc.: Menlo Park, CA, 1973; Module 4.

101. Hilburn, J. L.; Johnson, D. E. "Manual of Active Filter Design;" McGraw-Hill Book Co.: New York, NY, 1973; Chapter 4.

102. Mills, T. B. The PLL as a Communications Building Block, Application Note AN-46, National Semiconductor Corp., June 1971.

103. National Semiconductor Corp., National Linear Data Book, June 1976, Page 9-36.

104. Smith, E. B.; Barnes, C. S.; Carr, P. W. Anal. Chem. 1972, 44, 1663.

105. National Semiconductor Corp., FET Circuit Applications, Application Note AN-32, February 1970.

106. American Radio Relay League. "The Radio Amateur's Handbook;" 52nd ed.; Newington, CT, 1975; Chapters 12, 14.

107. Intersil, Inc., Data Sheet for Intersil 8038 Integrated Circuit.

108. Zeltex, Inc., Data Conversion and Linear Products, Concord, CA, Fall 1973; Pages 32-3.

109. West, G. D. Proc. Phys. Soc., London, Sect. B. 1951, 64, 483.

110. Radoi, I. Rev. Roum. Chim. 1971, 16, 3.

111. Radoi, I. Bul. Stiint. Teh. Inst. Politeh. Timisoara, Ser. Chim. 1970, 15, 85.

112. Radoi, I. Rev. Roum. Chim. 1972, 17, 1367.

113. Eck, B. "Technische Strömungslehre;" 5th ed., Springer Verlag: Berlin, Germany, 1957; Pages 238-242.

114. Homann, F. Forsch. Geb. Ingenieurwes. 1936, 7, 10.

115. Blevins, R. D. "Flow-Induced Vibration;" Van Nostrand Reinhold Co.: New York, NY, 1977; Page 14.

116. Ulsamer, J. Forsch. Geb. Ingenieurwes. 1932, 3, 94.

117. Hilpert, R. Forsch. Geb. Ingenieurwes. 1933, 4, 215.

118. Johnson, D. C.; Pratt, K. W., Operating Instructions for RDE-3 Potentiostat, Pine Instrument Co., Grove City, PA, 1979; Pages 32-34.

119. Kolthoff, I. M.; Lingane, J. J. "Polarography;" 2nd ed., Interscience Pub.: New York, NY, 1965; Volume 1, Page 52.

120. Welty, J. R.; Wicks, C. E.; Wilson, R. E. "Fundamentals of Momentum, Heat, and Mass Transfer;" John Wiley and Sons, Inc.: New York, NY, 1969; Pages 536-546.

121. Fortuna, G.; Hanratty, T. J. J. Heat Mass Transfer 1971, 14, 1499.

122. Hanratty, T. J.; Chorn, L. G. In "Turbulence in Liquids," Zakin, J. L.; Patterson, G. K., Eds., Proc. 4th Biennial Symposium on Turbulence in Liquids, Dept. Chem. Eng., U. Missouri at Rolla, Science Press: Princeton, NJ, 1975; Pages 244-253.

123. Koile, R. C.; et al. Chemistry Dept., Iowa State University, Ames, IA, 1978; personal communication.

124. Tokuda, K.; Bruckenstein, S.; Miller, B. J. Electrochem. Soc. 1975, 122, 1316.

125. Miller, B.; Bellavance, M. I.; Bruckenstein, S. Anal. Chem. 1972, 44, 1983.

126. Miller, B.; Bruckenstein, S. J. Electrochem. Soc. 1974, 121, 1558.

127. Tokuda, T.; Bruckenstein, S. J. Electrochem. Soc. 1979, 126, 431.

128. Kanzaki, Y.; Bruckenstein, S. J. Electrochem. Soc. 1979, 126, 437.

129. Albery, W. J.; Hillman, A. R.; Bruckenstein, S. J. Electroanal. Chem. 1979, 100, 687.

130. Bruckenstein, S.; Miller, B. Acc. Chem. Res. 1977, 10, 54.

131. Blaedel, W. J.; Engstrom, R. C. Anal. Chem. 1978, 50, 476.

132. Blaedel, W. J.; Iverson, D. G. Anal. Chem. 1977, 49, 11.

133. Blaedel, W. J.; Kim, Z. Anal. Chem. 1978, 50, 1722.

134. Blaedel, W. J.; Kim, Z. Anal. Chem. 1980, 52, 564.

135. Blaedel, W. J.; Wang, J. Anal. Chem. 1981, 53, 78.

136. Miller, B. Bell Laboratories, Murray Hill, NJ, 30 August 1978; personal communication.

137. Johnson, D. C. Ph.D. Dissertation, Univ. of Minnesota, Minneapolis, MN, 1967.

138. Larochelle, J. H.; Johnson, D. C. Anal. Chem. 1978, 50, 240.

139. Johnson, D. C. J. Electrochem. Soc. 1972, 119, 331.

140. Chemical Rubber Co. "Handbook of Chemistry and Physics," 46th ed.; Weast, R. C., Ed.; Cleveland, OH, 1965; Page F-116.

141. Meites, L. "Polarographic Techniques," 2nd ed.; Interscience Pub.: New York, NY, 1967.

142. Stone, H. W. J. Am. Chem. Soc. 1936, 58, 2591.

143. Betteridge, D. Anal. Chem. 1978, 50, 832A.

144. Ranger, C. B. Anal. Chem. 1981, 53, 20A.

145. Müller, O. H. J. Am. Chem. Soc. 1947, 69, 2992.

146. Fleet, B.; Gunesingham, H.; de Damia, G. G.; Berger, T. A.; das Gupta, S.; Little, C. J. Physicochemical Hydrodynamics 1977, 1, 373.

147. Koile, R. C. Ph.D. Dissertation, Iowa State Univ., Ames, IA, 1980.

148. Lindstrom, T. R. Ph.D. Dissertation, Iowa State Univ., Ames, IA, 1980.

149. Pungor, E.; Feher, Z.; Nagy, G.; Toth, K.; Horvai, G.; Gratzl, M. Presented at the 176th National Meeting of the American Chemical Society, Miami Beach, FL, Sept. 1978.

150. Wang, J.; Ariel, M. Anal. Chim. Acta 1978, 99, 89.

151. Wang, J.; Ariel, M. Anal. Chim. Acta 1978, 101, 1.

152. Oosterhuis, B.; Brunt, K.; Westerink, B. H. C.; Doornbos, D. A. Anal. Chem. 1980, 52, 203.

153. Blaedel, W. J.; Schieffer, G. W. Anal. Chem. 1974, 46, 1564.

154. Johansson, G. Talanta 1965, 12, 163.

155. Pickett, D. J. "Electrochemical Reactor Design," 2nd ed.; Elsevier Scientific Pub. Co.: Amsterdam, 1979; Chapter 6, Pages 283-90.

156. Boyce, W. E.; DiPrima, R. C. "Introduction to Differential Equations;" John Wiley and Sons, Inc.: New York, NY, 1970; Chapter 2, Pages 7-18.

157. Johnson, D. C.; Larochelle, J. H. Talanta 1973, 20, 959.

158. Blaedel, W. J.; Wang, J. Anal. Chem. 1979, 51, 799.

159. Blaedel, W. J.; Boyer, S. L. Anal. Chem. 1971, 43, 1538.

160. Morton Salt Company, Chicago, IL, March 1979; personal communication.

161. Nicol, M. J. Gold Bulletin 1980, 13, 46.

162. Hoare, J. P. Electrochim. Acta 1964, 9, 1289.

163. Rand, D. A. J.; Woods, R. J. Electroanal. Chem. 1971, 31, 29.

164. Frankenthal, R. P.; Thompson, D. E. J. Electrochem. Soc. 1976, 123, 799.

165. Hatch, W. R.; Ott, W. L. Anal. Chem. 1968, 40, 2085.

166. "An Assessment of Mercury in the Environment;" Panel on Mercury of the Coordinating Committee for Scientific and Technical Assessments of Environmental Pollutants, Environmental Studies Board, Commission on Natural Resources, National Research Council, National Academy of Sciences: Washington, DC, 1978.

167. Allen, R. E. Ph.D. Dissertation, Iowa State University, Ames, IA, 1974.

168. Andrews, R. W.; Larochelle, J. H.; Johnson, D. C. Anal. Chem. 1976, 48, 212.

169. Siemer, D. D.; Hageman, L. Anal. Chem. 1980, 52, 105.

170. Glass, G. E.; Sandberg, C. U.S. Environmental Protection Administration, Duluth, MN, September 1980; personal communication.

171. Litman, R.; Finston, H. L.; Williams, E. T. Anal. Chem. 1975, 47, 2354.

172. Feldman, C. Anal. Chem. 1974, 46, 99.

173. Kritsotakis, K.; Rubischung, P.; Tobschall, H. J. Fresenius Z. Anal. Chem. 1979, 296, 358.

174. Lindstedt, G. Analyst 1970, 95, 264.

175. Toffaletti, J.; Savory, J. Anal. Chem. 1975, 47, 2091.

176. Ure, A. M. Anal. Chim. Acta 1975, 76, 1.

177. Lawrence, K. E.; White, M.; Potts, R. A.; Bertrand, R. D. Anal. Chem. 1980, 52, 1391.

178. Hawley, J. E.; Ingle, J. D. Anal. Chem. 1975, 47, 719.

XIII. ACKNOWLEDGMENTS

I am indebted foremost to Dr. Dennis C. Johnson for his support, training, and electrochemical expertise during the last 4 years. His policy of encouraging freedom and independence in the research of his graduate students is much appreciated.

I am also grateful to Dr. Gary E. Glass of the U.S. Environmental Protection Administration, Duluth, MN, for expressing interest in this project, for funding the research described in Chapter IX, and for sharing the data for the determinations of Hg by cold-vapor AAS. The assistance of Craig Sandberg in the procurement of LSW samples and during my visit to Duluth is much appreciated. I thank the staff of that laboratory for an interesting and educational visit to the Twin Ports.

The financial assistance from Pine Instrument Co., Grove City, PA, and from Phillips Petroleum, Inc., Bartlesville, OK, is gratefully acknowledged.

The assistance of Eldon E. Ness in the design of the transfer apparatus is appreciated, as is the assistance of Scott Hughes in the calculation of uncertainties.

The technical and emotional support of the past and present members of the electrochemistry group has been much appreciated.

Special thanks go out to those who run the railroads, bus lines, trolleys, ferries, cable cars, Amtrak, VIA Rail Canada, and the Alaska Marine Highway, and to those whom I met during my travels, for they showed me the world beyond Ames, from Grand Isle to Grand Marais and from Tillamook to Tottenville.